

# Self-organized Growth in Developing Epithelia

DISSERTATION

zur Erlangung des akademischen Grades

Doctor rerum naturalium  
(Dr. rer. nat.)

vorgelegt

der Fakultät Mathematik und Naturwissenschaften  
der Technischen Universität Dresden

von

Peer Mumcu

geboren am 27. April 1982 in Marl



MAX-PLANCK-INSTITUT FÜR PHYSIK KOMPLEXER SYSTEME

Dresden, 2011

---

## **Gutachter**

Prof. Dr. Frank Jülicher  
Prof. Dr. Dr. Karsten Kruse

## **Tag der Einreichung bei der Fakultät**

14. Juni 2011

## **Tag der Verteidigung**

19. Oktober 2011

# Abstract

The development of a multicellular organism, such as a human or an animal, begins with the fertilization of an egg cell. Thereupon the organism grows by repeated cell divisions until the adult size is reached and growth stops. Although it is known that intrinsic mechanisms determine the final size of developing organs and organisms, the basic principles of growth control are still poorly understood. However, there is strong evidence that certain morphogens, which are a special class of signaling molecules, act as growth factors and play a key role in growth control.

In this work, growth control is studied from a mainly theoretical viewpoint. A discrete vertex model describing the organization of cells by a network of polygons is used, including a description of the cell cycle and a description of dynamical morphogen distributions. Self-organized growth is studied by introducing growth rules that govern cell divisions based on the local morphogen level. This discrete description is complemented by a continuum theory to gain further insight into the dynamics of self-organized growth processes.

The theoretical description is applied to the developing wing of the fruit fly *Drosophila melanogaster*. In the developing wing, which is an epithelium consisting of single-layered cell sheets, the morphogen Decapentaplegic (Dpp) acts as a key growth factor. Experimental data shows that the Dpp distribution is dynamic and adapts to the size of the developing wing. Two mechanisms that rely on a regulatory molecule species and lead to such a dynamic behaviour of the Dpp distribution are studied. Several growth rules are tested and the resulting growth behaviour is quantitatively compared to experimental data of the developing wing. A particular growth rule, that triggers a cell division when the local morphogen level has increased by a certain relative amount, is found to be consistent with experimental observations under normal and several perturbed conditions. It is shown that mechanical stresses that arise due to spatial growth inhomogeneities can have a stabilizing effect on the growth process.



# Acknowledgements

Here I want to express my gratitude to those who contributed to this thesis. First and foremost I thank my supervisor Frank Jülicher for guiding my work. I learned much from this brilliant scientist. Furthermore, I especially want to thank Ortrud Wartlick and her supervisor Marcos González-Gaitán for performing the biological experiments that made this thesis possible. The continuous exchange of ideas in countless video conferences connecting Dresden and Genève was a true source of inspiration throughout my work. I want to thank Anna Kicheva and Thomas Bittig who also contributed to our interdisciplinary project. I wish to express my gratitude to Reza Farhadifar for many fruitful discussions and valuable hints regarding the vertex model. Furthermore, I am indebted to my friends and colleagues Douglas Staple and Jöbin Gharakhani for critical reading of the manuscript and for their efforts to improve my mastery of English. Finally, I want to thank my dear parents. Without their support this thesis would not exist.



# Contents

<b>1. Introduction</b>	<b>1</b>
1.1. The Development of Multicellular Organisms . . . . .	1
1.1.1. Morphogens and Pattern Formation . . . . .	1
1.1.2. Morphogens and Growth Control . . . . .	3
1.2. The Fruit Fly <i>Drosophila Melanogaster</i> . . . . .	3
1.2.1. Development of the Fly . . . . .	3
1.2.2. The Wing Imaginal Disc . . . . .	5
1.3. Theoretical Approaches . . . . .	9
1.3.1. Formation of Morphogen Gradients . . . . .	9
1.3.2. Growth of Epithelia . . . . .	10
1.3.3. Growth Control in the Wing Imaginal Disc . . . . .	11
1.4. Overview of This Work . . . . .	12
<b>2. Morphogen Gradients and Tissue Growth in a Vertex Model</b>	<b>15</b>
2.1. Tissue Mechanics . . . . .	15
2.2. Compartments and Their Interfaces . . . . .	16
2.3. Morphogen Dynamics . . . . .	17
2.3.1. Rules for Morphogen Production . . . . .	17
2.3.2. Rules for Morphogen Degradation . . . . .	18
2.4. The Cell Cycle . . . . .	19
2.4.1. Cell Cycle States . . . . .	19
2.4.2. Cell Divisions . . . . .	20
2.5. Initial System Configuration . . . . .	20
<b>3. Scaling of Morphogen Gradients in Growing Tissues</b>	<b>23</b>
3.1. Experimental Evidence for Scaling . . . . .	23
3.2. Mechanisms for Scaling of Morphogen Gradients . . . . .	25
3.2.1. Expander Dilution . . . . .	28
3.2.2. Expansion-repression Feedback . . . . .	30
<b>4. Self-organized Growth Described by Cellular Growth Rules</b>	<b>37</b>
4.1. Temporal Growth Rules . . . . .	38
4.1.1. Deterministic Temporal Rule . . . . .	39
4.1.2. Stochastic Temporal Rule . . . . .	43
4.1.3. Clone Size Distributions . . . . .	46

---

4.2. Spatial Growth Rules . . . . .	49
4.2.1. Instantaneous Spatial Rule . . . . .	50
4.2.2. Time-averaged Spatial Rule . . . . .	50
<b>5. Continuum Description of Self-organized Growth</b>	<b>55</b>
5.1. Continuum Description of the Dpp Dynamics . . . . .	55
5.2. Continuum Description of the Growth Dynamics . . . . .	56
5.2.1. Stochastic Temporal Growth Rule . . . . .	57
5.2.2. Deterministic Temporal Growth Rule . . . . .	60
5.2.3. Spatial Growth Rules . . . . .	64
<b>6. Relationship Between Tissue Growth and Mechanical Stresses</b>	<b>71</b>
6.1. Influence of Proliferation on Mechanical Stresses . . . . .	72
6.1.1. Homogeneous Proliferation . . . . .	72
6.1.2. Inhomogeneous Proliferation . . . . .	73
6.2. Influence of Mechanical Stresses on Self-organized Growth . . . . .	76
<b>7. Self-organized Growth Under Perturbed Conditions</b>	<b>83</b>
7.1. Kinetic Parameters Estimated from Haltere Imaginal Discs . . . . .	83
7.2. Local Production of Permanently Active Dpp Receptors . . . . .	85
7.3. Changes in the Maximum Growth Rate . . . . .	91
7.4. Fixed Dpp Source Width . . . . .	94
7.5. System-wide Dpp Production . . . . .	96
7.6. Nonlinear Dpp Auto-repression . . . . .	98
<b>8. Conclusion</b>	<b>101</b>
<b>A. Scaling Behaviour of Non-exponential Morphogen Gradients</b>	<b>105</b>
<b>B. Sensitivity of the Growth Rules with Respect to Initial Conditions</b>	<b>109</b>
B.1. Deterministic Temporal Rule . . . . .	109
B.2. Stochastic Temporal Rule . . . . .	111
B.3. Time-averaged Spatial Rule . . . . .	113
<b>C. Dynamic Range and Uncertainty of Local Dpp Levels</b>	<b>115</b>
<b>D. Estimation of the Mechanical Forces in the Wing Imaginal Disc</b>	<b>117</b>
<b>E. Growth and Apoptosis Rates</b>	<b>119</b>
E.1. Continuous System . . . . .	119
E.1.1. Definitions . . . . .	119
E.1.2. Relationship Between Doubling Time and Growth Rate . . . . .	119
E.2. Discrete System . . . . .	120
E.2.1. Definitions . . . . .	120
E.2.2. Relationship Between Cell Cycle Time and Growth Rate . . . . .	120



E.2.3. Temporally and Spatially Resolved Growth Rate . . . . .	122
<b>F. Relaxation of the Cellular Network in the Vertex Model</b>	<b>127</b>
F.1. Global Relaxation of the Network . . . . .	127
F.2. Local Relaxation of the Network . . . . .	127
F.2.1. Relaxation of the Cellular Neighbourhood . . . . .	128
F.2.2. Relaxation of the Simulation Box . . . . .	129
F.3. Comparison Between Global and Local Relaxation . . . . .	129
<b>G. Continuum Description of the Dpp Morphogen Gradient</b>	<b>133</b>
G.1. Finite System Size . . . . .	133
G.1.1. Time-dependent Solution . . . . .	133
G.1.2. Steady State Solution . . . . .	135
G.2. Infinite System Size . . . . .	136
G.2.1. Time-dependent Solution . . . . .	137
G.2.2. Steady State Solution . . . . .	140
<b>H. The Hedgehog Morphogen Gradient</b>	<b>141</b>
H.1. Experimental Observations . . . . .	141
H.2. Continuum Description . . . . .	141
H.2.1. Finite Hedgehog Degradation in the Hedgehog Source . . . . .	141
H.2.2. Vanishing Hedgehog Degradation in the Hedgehog Source . . . . .	143
<b>I. The Dpp Source</b>	<b>147</b>
I.1. Generation of the Dpp Source in the Wing Imaginal Disc . . . . .	147
I.2. Continuum Description . . . . .	147
I.3. Comparison of Theory and Experimental Data . . . . .	147
<b>J. Analysis of Experimental Data</b>	<b>149</b>
J.1. Analysis of GFP-Dpp and Dad-nRFP Gradients . . . . .	149
J.1.1. Measurement of the Gradients . . . . .	149
J.1.2. Data Fitting . . . . .	150
J.2. Estimation of the Temporal Variation of Kinetic Dpp Parameters . . . . .	155
J.2.1. Wing Imaginal Disc . . . . .	156
J.2.2. Haltere Imaginal Disc . . . . .	157
<b>Bibliography</b>	<b>159</b>



# 1. Introduction

## 1.1. The Development of Multicellular Organisms

The development of a multicellular organism from a single cell is an intriguing form of self-organization. Although nearly all cells within an organism are genetically identical [5], internal processes lead to the emergence of highly organized structures such as eyes, hearts, and brains. An adult human body, for example, consists of roughly  $10^{13}$  cells, and is characterized by more than 200 different cell types and 11 major organ systems, each consisting of various specialized organs [5, 167]. To generate such high complexity, several developmental processes such as growth, pattern formation, and cell differentiation act in concert [182]. Growth is achieved by an increase in cell size, an increase in cell number, and by deposition of extracellular materials such as bone and shell. The emergence of spatio-temporal patterns of cell activities that lead to regular structures is called pattern formation. An important function of pattern formation is to define the main body axes, for example the axis which runs from the head to the tail of the organism. Cell differentiation is the process that renders cells structurally and functionally different from each other, leading to distinct cell types such as muscle or skin cells. How growth, pattern formation, and cell differentiation are coordinated during development is largely unknown. However, there is evidence that special signaling molecules, which are known as *morphogens*, play a key role for the coordination of these processes.

### 1.1.1. Morphogens and Pattern Formation

In 1952, the mathematician Alan Turing suggested that systems of reacting and diffusing chemicals could account for pattern formation during development [170]. He termed these chemicals morphogens. Turing showed that stable spatial patterns can evolve from initially homogeneous morphogen distributions due to a diffusion driven instability. Many patterns which are generated by this mechanism bear a striking resemblance to coat patterns found on animals like the zebra or leopard. It has therefore been suggested that Turing's mechanism underlies most of the observed coat markings [122]. Whether this is actually true has not yet been confirmed experimentally. However, Turing's idea has inspired extensive research on pattern formation in reaction-diffusion systems [68, 113, 131, 96, 123].

The contemporary morphogen concept was established by Lewis Wolpert in 1969 [181]: morphogens are signaling molecules that spread from localized sources and

form graded concentration profiles in a tissue, so that the local morphogen concentration contains positional information. Such concentration profiles are called morphogen gradients. The response of target cells, for example the expression of a certain gene, directly depends on the local morphogen concentration. The French flag model provides a clear illustration of Wolpert's idea (see figure 1.1). Many morphogens that match the contemporary definition have been found in developing organisms. Well known examples are Bicoid [45, 46, 47, 48], Activin [70, 72], Hedgehog [12, 85, 80], Decapentaplegic [59, 179, 102, 126], Squint [34], and Sonic hedgehog [140]. Morphogens are highly conserved in evolution, so that the same type of morphogen is usually found in different organisms.

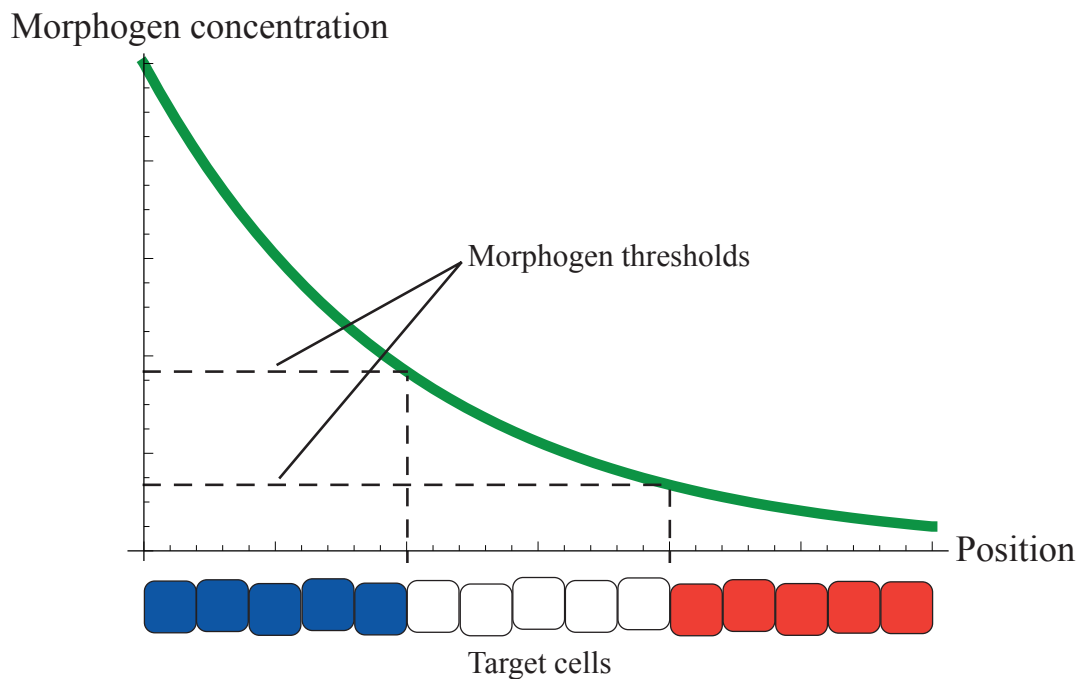


**Figure 1.1.:** The French flag model of pattern formation. The cells are exposed to a decaying morphogen gradient. Each cell can differentiate into one of three different cell types, which are indicated by the colors blue, white, and red. The cell type is determined by the local morphogen concentration in a threshold dependent manner.

Binding to receptors on the cell surface, morphogens can trigger intracellular signaling cascades that lead to the expression of target genes [77, 151, 172, 143]. Theoretical analysis of signaling systems has shown that feedback loops can generate bistability with well-defined input thresholds for the transition between states [18, 8]. Indeed, the expression of target genes often behaves like a switch, changing discontinuously at certain morphogen thresholds [71]. However, it has also been observed that cellular responses depend on the exposure time to the morphogen [40, 74], or on the combination of several morphogen signals [54].

Recently it was proposed that certain morphogen gradients adapt to the size of the tissue. This behaviour, which is called gradient scaling, has been suggested for the BMP (Bone Morphogenetic Protein) activity gradient in *Xenopus* embryos [15], and for the Dpp (Decapentaplegic) gradient in the *Drosophila* wing imaginal disc [174, 175]. Such scaling behaviour has also been reported for the concentration profiles of molecules that act downstream in morphogen signaling cascades [163, 81, 175]. Gradient scaling is an important feature because it can ensure that patterns are appropriately scaled and proportions are preserved if the size of an organism deviates from the usual size, for example due to lack of food [10]. For the mechanism underlying scaling of the BMP activity gradient a simple model has been proposed [15]. However, neither the role of gradient scaling nor the mechanism underlying it are understood in the case of the Dpp morphogen in the *Drosophila* wing imaginal disc. Scaling of the Dpp gradient is the subject of chapter 3.

### 1.1.2. Morphogens and Growth Control

In contrast to pattern formation, little is known about the principles of growth control. How the sizes of animals or organs are determined still remains an open question [36]. For the normal growth of organs during development, extrinsic factors such as nutrients and hormones are essential. However, these extrinsic factors do not determine the size under normal conditions. Instead, it has been suggested that the size of organs is determined by organ-intrinsic mechanisms [27]. Strong evidence for such mechanisms is provided by experiments in which developing organs grow to their characteristic sizes after the transplantation into adult hosts [171, 114, 42, 153, 27]. Because growth and pattern formation are closely interrelated, it is not surprising that many morphogens are crucial for growth regulation. Growth promoting effects have for instance been observed for Sonic hedgehog in the chick wing [168] and in the vertebrate neural tube [32], and for Hedgehog in the developing *Drosophila* eye [49]. Other examples are morphogens belonging to the TGF- $\beta$  superfamily (Transforming Growth Factor  $\beta$ ) or to the FGF family (Fibroblast Growth Factor) [94].

The best studied model system for growth control is the developing wing of the fruit fly *Drosophila melanogaster*, on which we will focus in the following. There, the morphogen Decapentaplegic plays a key role for the organ-intrinsic growth control mechanism [4, 145]. Because it is most likely that growth control mechanisms are similar in different species, it is expected that the understanding of wing development is of great value.

## 1.2. The Fruit Fly *Drosophila Melanogaster*

### 1.2.1. Development of the Fly

The fruit fly *Drosophila melanogaster* has been used as a biological model system for a century, starting with the first *Drosophila* research paper published in 1910 by

Thomas Morgan [120]. He was awarded the Nobel Prize in Physiology or Medicine 1933 for his discoveries concerning the role played by the chromosome in heredity. Today, the fruit fly is one of the best studied organisms, in particular concerning its genetics and developmental biology. The genome of *Drosophila* has been sequenced and is thought to contain roughly 13,600 genes [2].

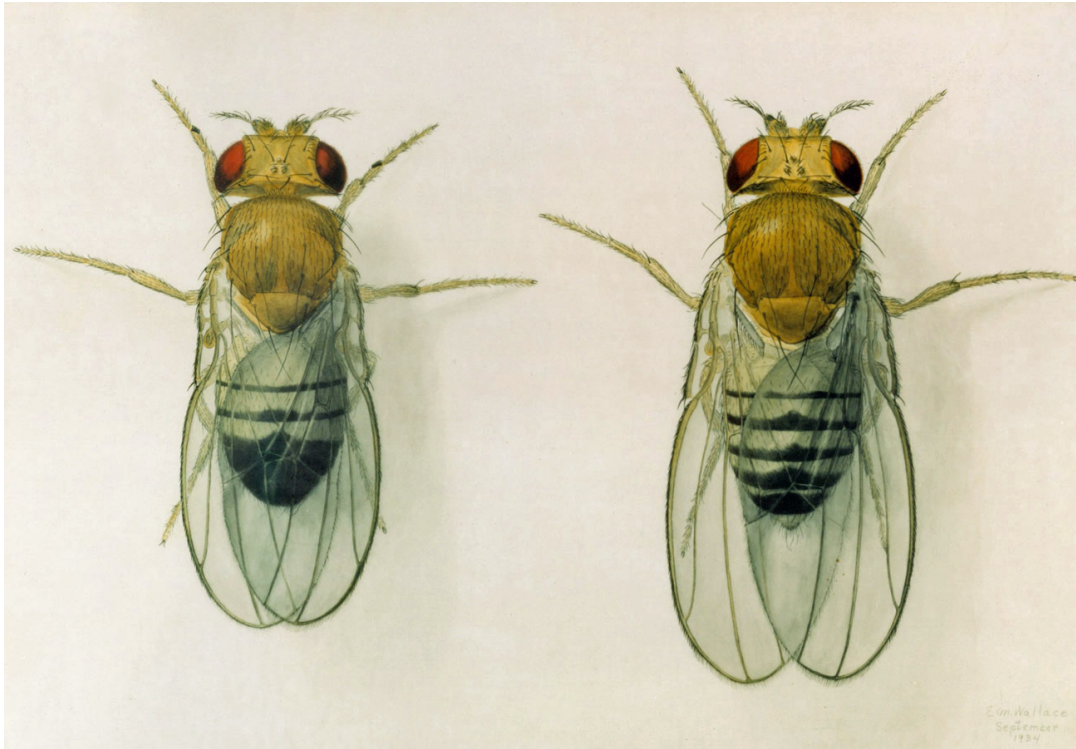


**Figure 1.2.:** Drawings of a male (left) and female (right) wild type *Drosophila melanogaster* by E. M. Wallace (1934). Courtesy of the Archives, California Institute of Technology.

Development of the fly begins with the fertilization of the egg, which is approximately 0.5 mm long and oval in shape [50]. The embryo develops inside the egg, until a larva hatches after one day. Larval life, during which most growth takes place, is divided into three stages between which molts occur. Each stage is called an *instar*. The larva grows from 0.5 mm at hatching to 4.5 mm at the end of the third instar. Five days after fertilization, the larva encapsulates in the puparium and undergoes metamorphosis, during which an extensive morphological transformation occurs. The adult fly, which is about 2.5 mm long, emerges from the pupal case after approximately four additional days. The speed of development depends on temperature; the given timings correspond to  $T = 25^{\circ}\text{C}$ .

### 1.2.2. The Wing Imaginal Disc

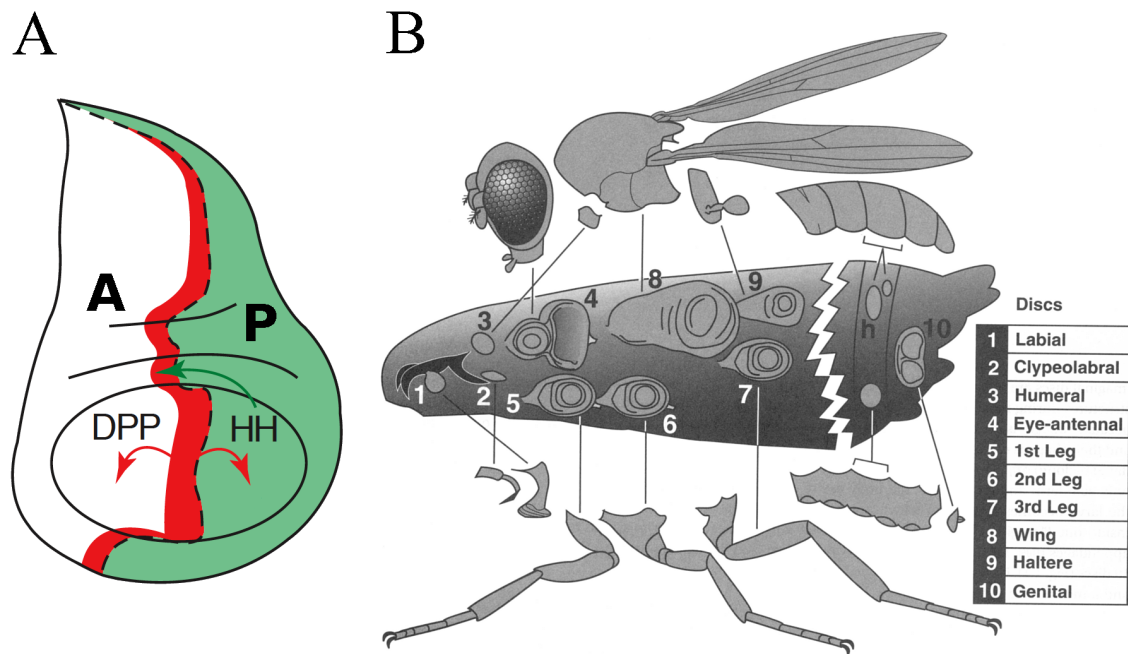


**Figure 1.3.:** (A) Cartoon of a wing imaginal disc. The oval region in the lower part indicates the wing pouch, which forms the wing blade during metamorphosis. The expression domains of Hh (green) and Dpp (red) are shown. The dashed line indicates the compartment boundary, which separates the anterior compartment (**A**) from the posterior compartment (**P**). Figure reprinted from [38], with permission from Elsevier. (B) Imaginal discs in the *Drosophila* larva, and the corresponding adult body parts formed during metamorphosis. The discs are drawn to the same scale, and are oriented to show their mature shapes and folding. Placements are approximate and half of the larval midsection is omitted here. There exist two discs of each type 1-9, so in total, a larva contains 19 imaginal discs. Figure reprinted from [76], with permission from Cambridge University Press.

#### Structure of the Wing Imaginal Disc

Many body parts of the adult fly that are formed during metamorphosis, for example the wings, legs, or eyes, develop inside the larva as imaginal discs (see figure 1.3). Imaginal discs are composed of single-layered sheets of epithelial cells. The two imaginal discs that form the wings during metamorphosis are called the wing imaginal discs, or simply wing discs. A wing disc is essentially a two-sided epithelial sac. One side is composed of elongated, columnar cells and the other side, which is known as the peripodial membrane, consists of flat cells (see figure 1.4). The columnar side of the disc forms the wing blade, wing hinge, and parts of the body

wall during metamorphosis. The wing blade is formed by the wing pouch, which is an oval-shaped part of the columnar epithelium (see figure 1.3).

Epithelial cells form characteristic cell packings due to adhesive junctions in their apical region. The predominantly hexagonal cell pattern was already noted in early microscopic analyses of epithelia [147]. However, due to geometric disorder induced by cell divisions [103, 104], the growing wing disc does not exhibit a regular hexagonal pattern. Instead, the cell packing geometry in the wing disc can be described by a distribution of polygons with different neighbour numbers [58, 157, 67].

The wing disc consists of two different cell populations, anterior cells and posterior cells, which remain separated during development [65]. Each of these two cell populations is called a compartment. The straight interface that separates the anterior and posterior compartments is called a compartment boundary [38]. During the second larval instar, another perpendicular compartment boundary forms, separating the dorsal and ventral compartments [66, 41, 128]. Compartments are relevant for growth control because they determine where morphogens are produced.

### **Growth Behaviour of the Wing Imaginal Disc**

The wing disc initially consists of approximately 40 cells [105]. During the four days of larval development, the number of cells increases approximately 1000-fold due to cell divisions [55, 64, 69], which occur approximately homogeneously in space [69, 64, 146]. It has been observed that cell divisions have a preferred orientation with respect to the dorsal-ventral compartment boundary [9], and that growth is weakly anisotropic [20]. Like other developing organs, the wing disc is thought to possess an organ-intrinsic growth control mechanism [27]. Strong evidence for such a mechanism is provided by experiments in which developing wing discs grow to normal sizes when transplanted into adult flies [63, 26].

Damaging some of the imaginal discs in the larva can retard the pupal stage of development. Although the intact imaginal discs have additional time for growth under such conditions, the discs develop into organs of normal size [154]. This experiment demonstrates that the available time for growth does not determine the final size of an organ.

It has also been shown that the maximum speed of growth does not determine the final organ size. This has been shown using experiments involving the group of *Minute* mutations, which owes its name to the abnormally small bristles on the adult body. In cells carrying a *Minute* mutation, growth is slowed down as compared to non-*Minute* cells due to reduced ribosome levels [119, 144, 112]. It is possible to generate wing discs with a *Minute* anterior compartment and a non-*Minute* posterior compartment. Although the *Minute* compartment grows slower than the non-*Minute* compartment, the final size of both compartments is normal at the end of larval development [108]. This experiment also demonstrates that the sizes of the two compartments are controlled separately.

In two other experiments it is shown that the number of cells can be altered



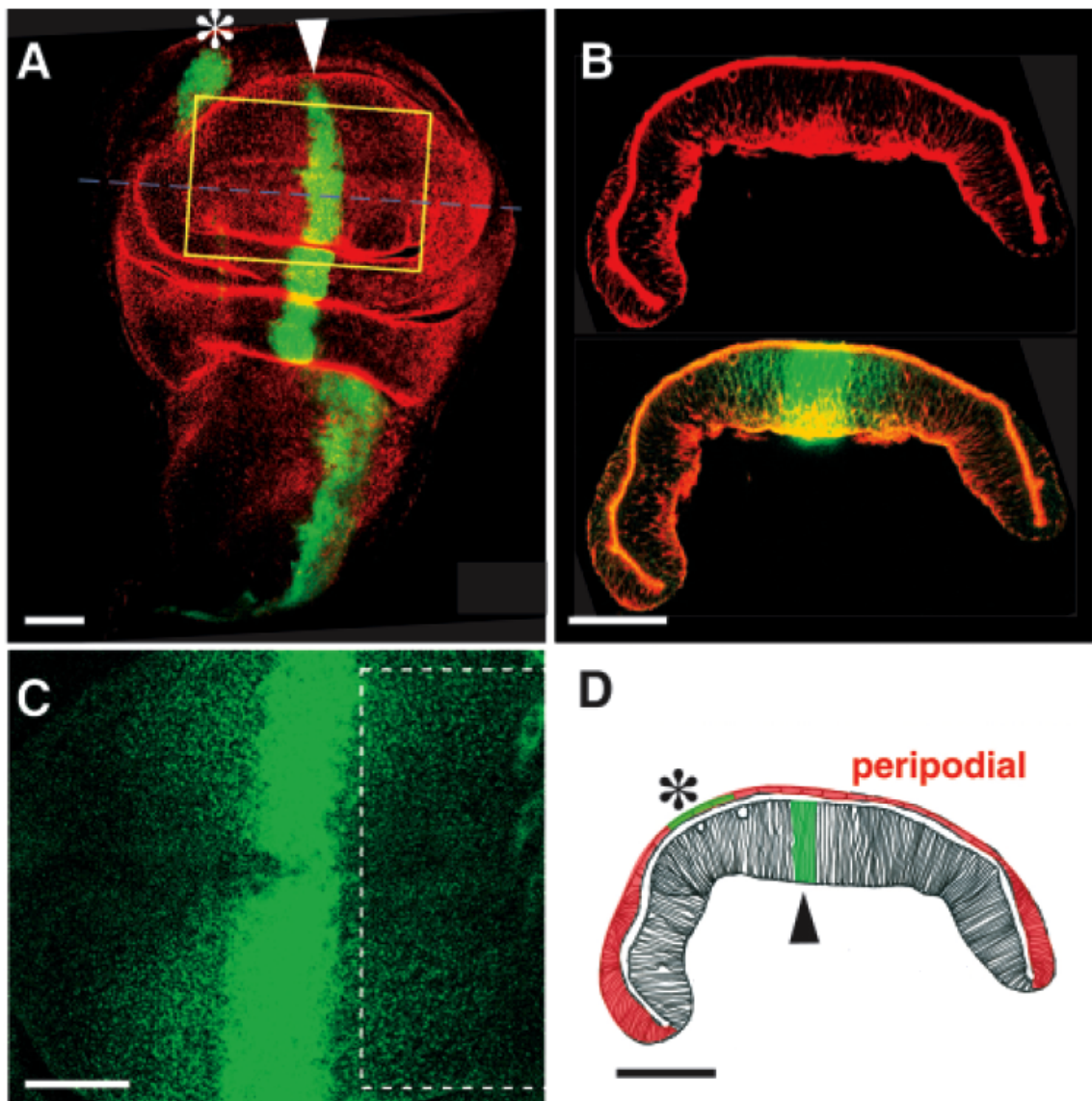


**Figure 1.4.:** Dpp gradient in a grown wing disc. The scale bars correspond to  $50 \mu\text{m}$ . The anterior compartment is on the left side in these pictures. (A) Double staining of the wing disc showing Dpp in green and cell profiles in red. The arrowhead points to the Dpp source in the columnar epithelium and the asterisk indicates the Dpp source in the periopodial membrane. (B) Double staining of a cross section of the wing disc along the dashed blue line in A, showing cell profiles in red, superimposed by GFP-Dpp expression (green) in the lower panel. (C) Magnified view of GFP-Dpp localization in a region of the wing disc corresponding to the yellow box in A. (D) Schematic representation of the wing disc section shown in B. Here, the green color indicates the location of the Dpp source (arrowhead: columnar epithelium, asterisk: periopodial membrane). The periopodial membrane is colored red elsewhere. Figure adapted from [98], with permission from The Company of Biologists.

without significantly affecting the size. In the first experiment, two rounds of cell divisions are blocked in a compartment without changing its size. The affected compartment contains fewer but larger cells [177]. In the second experiment, the number of cells in a compartment is changed by manipulating the expression of cell cycle genes. Nevertheless, compartment sizes are not changed significantly [127].

Apoptosis (cell death) is a rather rare phenomenon in wild type wing discs. Approximately 1.4% of the cells are dead at any instant. Dead cells remain in the epithelium for 2–4 hours before they are engulfed by other cells [116]. Apoptosis becomes considerable in experiments with Minute mutants, where a phenomenon known as cell competition has been observed: slow growing Minute cells next to fast growing non-Minute cells exhibit an increased apoptosis rate, which leads to the complete elimination of Minute clones in a non-Minute background [119, 155, 159]. It was thought that cell competition is important to ensure the proper final size of the organ under such conditions. However, recently it was shown that cell competition plays no significant role in growth control [107]. This conclusion was drawn from the observation that compartment sizes are unchanged if cell competition is inhibited by an antiapoptotic protein.

The described growth behaviour suggests that the mechanism that controls the size of the wing disc neither relies on counting cell numbers nor on measuring time.

### **Morphogens Produced in the Wing Imaginal Disc**

Four morphogens are known to play a role in wing development: Hedgehog (Hh), Decapentaplegic (Dpp), Wingless (Wg), and Glass bottom boat (Gbb). Hh is only produced in the posterior compartment [162, 12]. The Hh receptor Patched (Ptc) is in turn only expressed in the anterior compartment. Thus, only anterior cells can respond to Hh [79, 125, 132]. Hh is degraded in the anterior compartment, such that it forms a decaying morphogen gradient there [166, 35]. Anterior cells respond to Hh by producing Dpp if the Hh concentration is sufficiently high [12, 85, 183]. As a result, Dpp is produced in a narrow stripe along the anteroposterior compartment boundary (see figure 1.3). Dpp molecules are degraded while spreading in the whole wing disc, which leads to a decaying morphogen gradient [93]. The Dpp gradient has been visualized by labeling Dpp with green fluorescent protein (GFP), see figure 1.4 [53, 163]. The genes *spalt* and *optomotor-blind* are transcriptionally activated at different Dpp concentrations [126, 102]. *Spalt* is only expressed close to the Dpp source, whereas *optomotor-blind* has a broader expression domain. Like Dpp, Gbb also belongs to the TGF- $\beta$  superfamily [180, 73]. The expression domain of Gbb essentially comprises the whole wing disc [92]. The expression pattern of Wg changes during development. From the late third larval instar on, Wg is produced in a narrow stripe at the dorsoventral compartment boundary and in rings that outline the wing pouch [184, 110]. Whether or not Wg is a classical morphogen is controversial because there is evidence that Wg only maintains the expression of its target genes instead of initiating it [110].

## Effects of Morphogen Signaling on Growth

The morphogen Dpp plays a major role in growth control [4, 145]. The name Decapentaplegic was coined because mutations in the corresponding gene cause defects in 15 of the 19 imaginal discs [156]. If Dpp production is defective, the wing disc fails to grow sufficiently and forms a small stump instead of a wing [183, 156]. Clones lacking the Dpp receptors Punt or Thickveins also fail to grow [28]. Furthermore, the inhibition of Dpp signaling slows cell growth and division [109]. Conversely, ectopic expression of Dpp in the wing disc causes additional growth [30, 183]. Clones expressing a permanently active Dpp receptor overgrow as well [126, 102, 109, 141].

Compared to Dpp, the other morphogens seem to play a less important role in growth control in the wing disc. A direct influence of the morphogen Hh onto cell proliferation has not been observed in the wing disc. The morphogen Wingless (Wg) owes its name to the fact that mutations in the corresponding gene give rise to wingless flies [150]. Instead, these mutant flies show a symmetric duplication of body wall structures [118]. The absence of wings in Wg mutants is not due to insufficient growth as in Dpp mutants. Rather, the explanation seems to be that Wg signaling is required to specify which cells will form the wing [129]. Without this Wg signal, cells that normally would form the wing will form body wall parts instead. It has also been shown that Wg signaling inhibits apoptosis in the wing. Furthermore, Wg signaling represses growth in the wing pouch during the third larval instar [88]. Little is known about the role of Gbb in growth control. However, mutations in the Gbb gene have mild effects as compared to Dpp mutations [92, 73].

## 1.3. Theoretical Approaches

### 1.3.1. Formation of Morphogen Gradients

Several different models for the formation of morphogen gradients have been proposed. Shortly after the contemporary morphogen concept was introduced by Wolpert [181], Francis Crick suggested in a theoretical study, that morphogen gradients are formed by simple diffusion of the morphogens in the tissue [37]. Indeed, there is experimental evidence that the Dpp and Wg gradients in the wing disc form via extracellular diffusion [13, 161]. In another model, extracellular propagation guided by receptors on the cell surface is proposed as a mechanism for the formation of morphogen gradients [91]. Another suggestion is that cytonemes, actin-based extensions which project from the cells to the Dpp source, play a role in Dpp transport [138, 82]. The suggested role of cytonemes in Dpp transport has little experimental support.

Contrary to the suggestion that the Dpp gradient forms via extracellular diffusion [100], it has been argued that diffusion alone cannot account for the dynamics of the Dpp gradient in the wing disc. Instead, it is thought that active transport of Dpp via endocytosis and re-secretion is essential [98, 53]. Because morphogens

move from cell to cell in a planar fashion in this model, the mechanism is known as planar transcytosis. It has been shown that transcytosis leads to robust morphogen gradients, which are insensitive to the morphogen production rate [24, 25, 23]. On length scales large compared to a cell diameter, planar transcytosis can be described by nonlinear reaction-diffusion equations. The kinetic parameters governing Dpp spreading in the wing disc have been determined experimentally, using a linearized equation of the form

$$\frac{\partial c(x, t)}{\partial t} = \nu(x, t) - kc(x, t) + D \frac{\partial^2 c(x, t)}{\partial x^2} \quad (1.1)$$

to describe the dynamics of the Dpp gradient [93]. Here,  $c(x, t)$  is the Dpp area concentration,  $\nu(x, t)$  is the production rate per unit area,  $k$  is the degradation rate, and  $D$  is the effective diffusion coefficient of Dpp molecules. Which model provides the best description of the morphogen gradients in the wing disc is still an open question. Therefore, details of morphogen gradient formation are not taken into account in this work: the dynamics of morphogen gradients is either described by equations of the form (1.1) or by spatially discrete versions of it. In other studies, systems of partial differential reaction-diffusion equations have been used to investigate the robustness of morphogen gradients with respect to gene expression levels [51, 52]. Furthermore, scaling of morphogen gradients with tissue size has been studied using this approach [15, 10, 14].

### 1.3.2. Growth of Epithelia

Many biological tissues behave as soft, elastic materials on short timescales and as viscous liquids on long timescales [139, 61, 164]. Furthermore, active processes such as the chemically driven dynamics of the cytoskeleton characterize biological tissues, which are therefore in a thermodynamic non-equilibrium state. Hydrodynamic theories can describe the physical properties of such complex materials on large length scales and long timescales [97, 75]. Such hydrodynamic theories have been used to show that oriented cell divisions can lead to anisotropic tissue growth and thus influence tissue shape [21, 20, 19].

Growth of epithelia can also be described by representing each cell individually [22, 117, 44, 43]. In vertex models, which were originally introduced to study the evolution of cellular structures such as foams, each cell is represented by a polygon [158, 176, 124]. To describe growth of epithelia, vertex models have been developed that take the mechanical properties of cells into account by means of a work function [58, 83]. Simulations of a particular vertex model have shown excellent agreement with experimental data with respect to the cell packing topology, morphology, and the rate of apoptosis [57, 58, 157]. This vertex model, which is described in chapter 2, is used to describe the cell packing geometry of growing epithelia in this thesis.

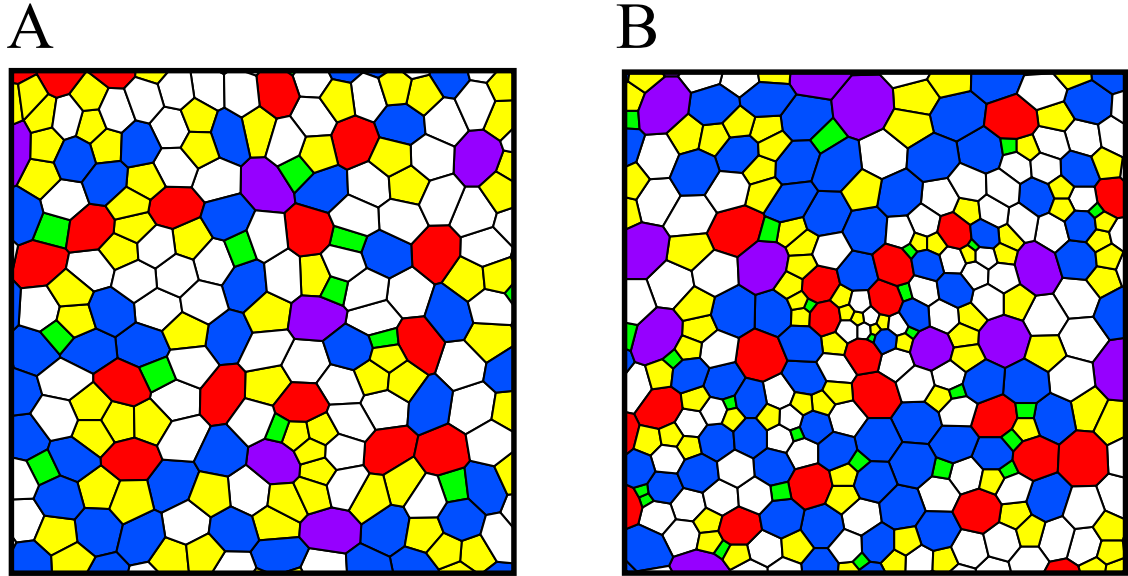


**Figure 1.5.:** Simulation results of the vertex model that is used to describe the cell packing geometry of growing epithelia in this work (see chapter 2). The number of neighbours is indicated for each cell by a color code. Green: 4, yellow: 5, white: 6, blue: 7, red: 8, violet: 9 or more. (A) Parameter values:  $\Gamma/K A^{(0)} = 0.04$ ,  $\Lambda/K(A^{(0)})^{3/2} = 0.12$  (B) Parameter values:  $\Gamma/K A^{(0)} = 0.1$ ,  $\Lambda/K(A^{(0)})^{3/2} = 0$

### 1.3.3. Growth Control in the Wing Imaginal Disc

Many different models for growth control in the wing disc have been formulated [4, 145]. In all of them, Dpp plays a key role. However, almost all of these models are vague, lack experimental support, and have not been formulated in a mathematical form. None of the existing models have been compared with quantitative experimental data.

One difficulty in developing a model is to explain how the spatially inhomogeneous distribution of Dpp molecules can induce spatially homogeneous growth in the wing disc. It has been suggested that a gradient of a growth inhibitor that parallels the Dpp gradient leads to spatially homogeneous growth [148]. This explanation seems unlikely because no such growth inhibitor has been identified [4].

Another suggestion is that a mechanical feedback ensures growth homogeneity [152]. According to this model, higher Dpp levels lead to faster growth. However, a locally increased growth rate causes local compression of the tissue, which generates mechanical stress. Sufficiently high mechanical stress in turn leads to a decrease of the local growth rate. A simulation of this feedback mechanism using a vertex model indeed yields approximately homogeneous growth [83]. Yet, experimental observations that indicate that mechanical stress influences cell proliferation in the wing disc are lacking. To explain the termination of growth, two crucial assumptions

are made in this model: the Dpp gradient is radially symmetric and has a fixed decay length [83]. From these assumptions it follows that a cell that is sufficiently far away from the point-like Dpp source receives too little Dpp and thus stops growing. This fact combined with the assumed radial symmetry of the Dpp gradient results in a ring of non-proliferating cells, which leads to the compression of the growing inner cells. The compression of the inner cells leads to the termination of growth. A similar mechanism has been proposed in [3]. However, the assumed radial symmetry and fixed decay length of the Dpp gradient are inconsistent with experimental observations [175].

Another well known model assumes that the Dpp gradient is linear and that the Dpp levels in the center and at the margin of the wing disc are fixed [39]. The growth rate is assumed to be dependent on the slope of the gradient, which is position-independent. As the disc grows, the slope of the linear gradient decreases until growth finally terminates when the slope is sufficiently small. This model is unsatisfactory because the assumption of a linear Dpp gradient is inconsistent with reports of an exponentially decaying Dpp gradient [93]. Concerning whether or not proliferation depends on the slope of the Dpp gradient, experimentalists have made contradictory claims [141, 142, 146].

## 1.4. Overview of This Work

How can a morphogen gradient control epithelial growth in a self-organized manner? Still, there exists no model that has substantial experimental support. In addition to biological experiments, physical concepts are essential to develop a satisfying model. Therefore, we have taken an interdisciplinary approach to the problem of growth control. This work represents the theoretical viewpoint. The theoretical description that is developed is general and can be applied to essentially any two-dimensional tissue. However, most parts of this work are focused on a particular model system, the *Drosophila* wing disc, for which quantitative experimental data is available thanks to a collaboration with the biochemistry group of M. González-Gaitán. The remainder of this thesis is organized as follows.

In chapter 2, a general description of morphogen gradients and growth in epithelial tissues is developed. This description is based on a vertex model in which cells are represented as polygons and mechanical tissue properties are taken into account. In chapter 3, mechanisms that may underlie the scaling of morphogen gradients with tissue size are explored. We study two different mechanisms that both require a regulatory molecule species to achieve scaling of the Dpp gradient. In chapter 4 we explore how growth of developing tissues can be controlled in a self-organized way. We introduce local cellular growth rules that are based on a morphogen signal and study the resulting growth behaviour of the system. We find temporal growth rules that generate largely homogeneous growth and are consistent with experimental data of the wing disc. In chapter 5, we develop mean field descriptions of the

systems studied in chapter 4. It is shown that essential features are captured by nonlinear dynamical systems. In chapter 6, the relationship between tissue growth and mechanical stresses is investigated. We show that mechanical stresses can have a stabilizing effect on tissue growth. The growth behaviour of perturbed systems, most of which correspond to mutant wing discs, is studied in chapter 7 in order to gain further insight into the properties of the cellular growth rules. We conclude in chapter 8 with a discussion of what has been achieved in this work.





## 2. Morphogen Gradients and Tissue Growth in a Vertex Model

### 2.1. Tissue Mechanics

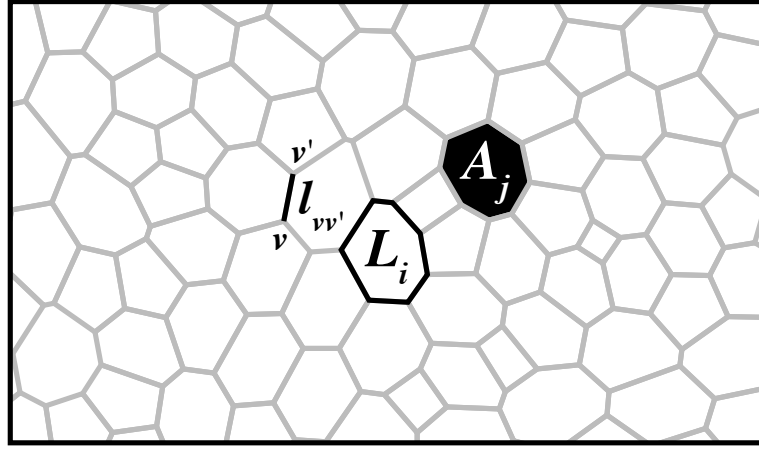


**Figure 2.1.:** Cellular packing obtained by a simulation of the vertex model. The area  $A_j$  of cell  $j$ , the perimeter  $L_i$  of cell  $i$ , and the length  $l_{vv'}$  of the bond  $\langle v, v' \rangle$  are indicated.

The vertex model describes the network of adherens junctions of an epithelium as a two-dimensional network of polygons [57, 58, 157]. Each polygon represents a cell and the configuration of the network is characterized by the positions of the vertices, and the connections between them. The mechanical properties of the cells are captured by the work function

$$\mathcal{F} = \sum_i \frac{K}{2} \left( A_i - A_i^{(0)} \right)^2 + \sum_i \frac{\Gamma}{2} L_i^2 + \sum_{\langle v, v' \rangle} \Lambda_{vv'} l_{vv'}, \quad (2.1)$$

where the sum extends over all cells in the first two terms and over all bonds in the third term. The first term describes area elasticity of cells with an elastic coefficient  $K$ . Here  $A_i$  is the area and  $A_i^{(0)}$  is the preferred area of cell  $i$ . We choose the value  $A_i^{(0)} = A^{(0)}$  as the preferred area for all cells  $i$  that are not undergoing cell division. The second term in (2.1) describes the stiffness of the cell perimeter  $L_i$  by

a coefficient  $\Gamma$ , and the third term accounts for the line tensions  $\Lambda_{vv'}$  of the bonds separating the cells. The bond connecting vertex  $v$  and  $v'$  is denoted by  $\langle v, v' \rangle$  and  $l_{vv'}$  is the length of the bond.

We assign the constant line tension  $\Lambda_{vv'} = \Lambda$  to all bonds, except those that separate different cell populations (see section 2.2). We consider stable and stationary network configurations, which satisfy mechanical force balance and correspond to local minima of the work function. The relaxation to the force balanced state is performed numerically by minimizing  $\mathcal{F}$  with respect to the vertex positions using a conjugate gradient algorithm (see appendix F) [133, 136]. During the relaxation process, bonds may shrink and vanish if it is energetically favourable. If a bond vanishes it may form again and expand, such that it results in a cell boundary rearrangement (T1 process). If the area of a triangular cell reduces below a threshold it is replaced by a single vertex (T2 process). This topological change corresponds to extrusion of an apoptotic cell from the epithelium.



**Figure 2.2.:** Topological changes in the vertex model. (A) Cell boundary rearrangement between four cells (T1 process). (B) Elimination of a small triangular cell (T2 process).

We choose a simulation box of variable size and periodic boundary conditions. The linear dimensions  $L_x$  and  $L_y$  of the periodic simulation box are determined by the minimum of  $\mathcal{F}$  for a given number of cells. This choice corresponds to a situation where no external force is applied to the tissue. Note that periodic boundary conditions are appropriate to describe the topology of the wing disc, which consists of two cell layers that are connected at the edges.

## 2.2. Compartments and Their Interfaces

We introduce two different cell populations by assigning a population variable  $\rho_i$  to each cell  $i$ . The variable  $\rho_i$  can assume two discrete states which are denoted  $A$  and  $P$ , corresponding to the anterior ( $A$ ) and posterior ( $P$ ) compartments of the wing disc. In order to generate sharp interfaces between the populations we set the line tension at bonds that separate cells from different populations to  $\Lambda_{vv'} = \kappa\Lambda$ , which is increased by a factor  $\kappa$  as compared to other bonds. The increased mechanical tension at the interface prevents mixing of the  $A$  and  $P$  populations when the system is growing [101]. Due to the periodic boundary conditions there exist two  $AP$ -interfaces in the system.

## 2.3. Morphogen Dynamics

In a continuum description, the dynamics of the Dpp gradient with diffusion coefficient  $D$  and degradation rate  $k$  can be described by the following reaction-diffusion equation (see appendix G) [175, 93],

$$\frac{\partial c(x, t)}{\partial t} = \nu(x, t) - kc(x, t) + D \frac{\partial^2 c(x, t)}{\partial x^2}. \quad (2.2)$$

Here,  $c(x, t)$  is the Dpp area concentration and  $\nu(x, t)$  is the Dpp production rate per unit area;  $x$  denotes position and  $t$  denotes time. The steady state solutions of (2.2) are given by exponential functions with decay length  $\lambda = \sqrt{D/k}$ . In the vertex model, we describe the distribution of the morphogens Dpp and Hh by assigning molecule numbers  $n_i^{(D)}$  and  $n_i^{(H)}$  to each cell  $i$ , respectively. Production, degradation, and transport of morphogen molecules are described by spatially discrete versions of equation (2.2):

$$\frac{d}{dt} n_i^{(D)} = p_i^{(D)} - k_i^{(D)} n_i^{(D)} + d^{(D)} \sum_j b_{ij} \left( n_j^{(D)} - n_i^{(D)} \right), \quad (2.3)$$

$$\frac{d}{dt} n_i^{(H)} = p_i^{(H)} - k_i^{(H)} n_i^{(H)} + d^{(H)} \sum_j b_{ij} \left( n_j^{(H)} - n_i^{(H)} \right). \quad (2.4)$$

Here,  $p_i$  is the production rate and  $k_i$  is the degradation rate of the respective morphogen in cell  $i$ . The third term on the right hand side of (2.3) and (2.4) accounts for morphogen spreading by a diffusion process. The sum extends over all neighbour cells  $j$  of cell  $i$ . The length of the bond separating cell  $j$  and  $i$  is denoted  $b_{ij}$ . The parameter  $d$  and the diffusion coefficient  $D$  are related by  $D \simeq A_c^{3/2} d$ , where  $A_c$  is the area of a cell. The solutions of (2.3) and (2.4) are determined numerically using a fifth-order Runge-Kutta method with adaptive stepsize control [31, 136].

### 2.3.1. Rules for Morphogen Production

The Hh source is represented by the rule

$$p_i^{(H)} = \begin{cases} 0 & \text{if } \rho_i = A, \\ p^{(H)} & \text{if } \rho_i = P, \end{cases} \quad (2.5)$$

and consists thus of the whole  $P$  population. The Dpp source is generated by the rule

$$p_i^{(D)} = \begin{cases} p^{(D)} \Theta \left( n_i^{(H)} - n_T^{(H)} \right) & \text{if } \rho_i = A, \\ 0 & \text{if } \rho_i = P. \end{cases} \quad (2.6)$$

Here,  $\Theta$  denotes the Heaviside step function, and  $n_T^{(H)}$  is the Hh threshold above which Dpp production is switched on in the  $A$  population. The parameters  $p^{(H)}$

and  $p^{(D)}$  characterize the production of morphogens in the system. The rules (2.5) and (2.6) generate stripes of Dpp producing cells along the  $AP$ -interfaces. Due to the choice of periodic boundary conditions, two  $AP$ -interfaces exist and two Dpp sources are generated. However, it is more convenient to deal with only one Dpp source. Therefore, we eliminate one Dpp source by imposing that one of the two  $AP$ -interfaces is impenetrable for Hh molecules. The width of the Dpp source is defined by

$$w = \frac{1}{L_y} \sum_{p_i^{(D)} \neq 0} A_i, \quad (2.7)$$

where the sum extends over all Dpp producing cells.

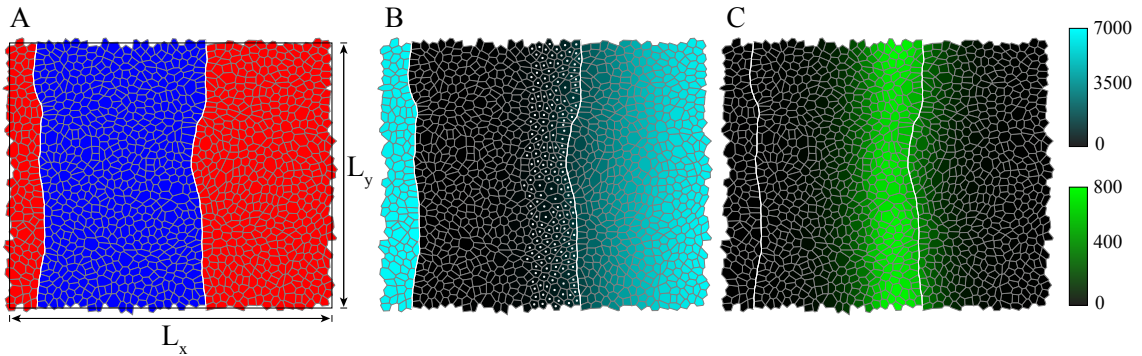


**Figure 2.3.:** Configuration of a system consisting of 1300 cells. (A) Cell population variable  $\rho_i$  indicated for each cell by a color code.  $\rho_i = A$ : blue,  $\rho_i = P$ : red. The  $AP$ -interfaces are indicated by white lines. The periodic simulation box is drawn in black. (B) Hh level  $n_i^{(H)}$  indicated for each cell by a color code. Cells from the  $A$  population in which the Hh level exceeds the threshold for Dpp production are marked with white dots ( $n_T^{(H)} = 250$ ). (C) Dpp level  $n_i^{(D)}$  indicated for each cell by a color code.

### 2.3.2. Rules for Morphogen Degradation

For the degradation rate of Hh we choose the following rule,

$$k_i^{(H)} = \begin{cases} k^{(H)} & \text{if } \rho_i = A, \\ 0 & \text{if } \rho_i = P. \end{cases} \quad (2.8)$$

Due to this rule, the width  $w$  of the Dpp source grows logarithmically with system size (see appendix I), consistent with experimental observations. Regulating  $k_i^{(D)}$  appropriately leads to scaling of the Dpp gradient, which we discuss in chapter 3.

## 2.4. The Cell Cycle

In this section, cell cycle states and cell divisions are introduced. The residence times in the cell cycle states and the angles of cell division are chosen to be random. Therefore the vertex model simulations are stochastic. Most simulation results presented in this work are therefore averages over several realizations.

### 2.4.1. Cell Cycle States

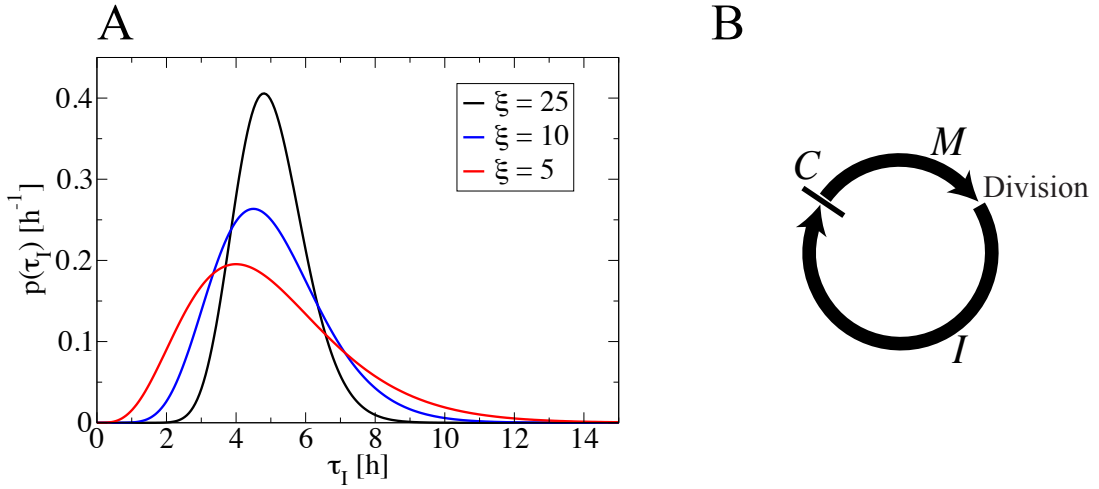


**Figure 2.4.:** (A) Probability distribution of the residence time  $\tau_I$  in cell cycle state  $I$ , shown for  $\bar{\tau}_I = 5$  h and different choices of the parameter  $\xi$ . The gamma distribution  $p(\tau_I)$  is defined in equation (2.9). (B) Schematic representation of the cell cycle states. State  $C$  behaves like a checkpoint in the cycle.

We introduce a cell cycle variable  $\sigma_i$  for each cell  $i$ . The variable  $\sigma_i$  can assume three discrete states, which are denoted  $M$ ,  $I$ , and  $C$ . They correspond to mitosis ( $M$ ), a part of interphase with fixed duration ( $I$ ), and a part of interphase with variable duration ( $C$ ). The cell switches its state in the order  $M \rightarrow I \rightarrow C \rightarrow M$  in a cyclic fashion. The transition  $M \rightarrow I$  is accompanied by a cell division (see section 2.4.2). The cell cycle states  $M$  and  $I$  are characterized by stochastic, gamma distributed residence times  $\tau_M$  and  $\tau_I$  with probability densities

$$p(\tau_M) = \tau_M^{\xi-1} \frac{\exp(-\xi\tau_M/\bar{\tau}_M)}{(\bar{\tau}_M/\xi)^\xi \Gamma(\xi)}, \quad p(\tau_I) = \tau_I^{\xi-1} \frac{\exp(-\xi\tau_I/\bar{\tau}_I)}{(\bar{\tau}_I/\xi)^\xi \Gamma(\xi)}. \quad (2.9)$$

Here,  $\Gamma$  denotes the gamma function and  $\xi > 0$  is the shape parameter of the gamma distributions. The average residence times are denoted  $\bar{\tau}_M$  and  $\bar{\tau}_I$ . The standard deviations  $\Delta\tau_M$  and  $\Delta\tau_I$  of the distributions obey  $\Delta\tau_M/\bar{\tau}_M = \xi^{-\frac{1}{2}}$ ,  $\Delta\tau_I/\bar{\tau}_I = \xi^{-\frac{1}{2}}$ . The quantity  $\xi^{-\frac{1}{2}}$  is thus a measure for the degree of randomness of the residence

times. The randomness of  $\tau_M$  and  $\tau_I$  ensures that cell divisions occur asynchronously. In contrast to state  $M$  and  $I$ , the residence time in state  $C$  is determined by a growth rule. Growth rules are introduced in chapter 4. If the residence time in state  $C$  vanishes and if no T2 processes occur, the system reaches its maximum growth rate  $\hat{g}$  and number of cells  $N$  increases exponentially for sufficiently long times,  $N(t) \sim \exp(\hat{g}t)$ . The maximum growth rate  $\hat{g}$  can be determined using equation (E.15). We obtain

$$\hat{g} = \frac{\xi}{2\bar{\tau}_M\bar{\tau}_I} \left( \sqrt{4\bar{\tau}_M\bar{\tau}_I 2^{1/\xi} + (\bar{\tau}_M - \bar{\tau}_I)^2} - \bar{\tau}_M - \bar{\tau}_I \right). \quad (2.10)$$

The function  $\hat{g}(\xi)$  is strictly decreasing if  $\bar{\tau}_M$  and  $\bar{\tau}_I$  are fixed. In the limiting cases,  $\hat{g}$  behaves as follows,

$$\lim_{\xi \rightarrow 0} \hat{g} = \infty, \quad \lim_{\xi \rightarrow \infty} \hat{g} = \frac{\ln 2}{\bar{\tau}}, \quad (2.11)$$

where  $\bar{\tau} = \bar{\tau}_M + \bar{\tau}_I$  is the average cell cycle time. The limiting value  $\frac{\ln 2}{\bar{\tau}}$  is a good approximation for the maximum growth rate  $\hat{g}$  if the parameter  $\xi$  is not too small. For example, the relative difference between  $\frac{\ln 2}{\bar{\tau}}$  and  $\hat{g}$  is less than 1.4% if  $\xi \geq 25$ . In most simulations we choose  $\xi = 25$ , in which case  $\hat{g} \approx \frac{\ln 2}{\bar{\tau}}$  is thus an excellent approximation (the black curve in figure 2.4A corresponds to  $\xi = 25$ ).

### 2.4.2. Cell Divisions

Tissue growth is generated by cell divisions, which are described in the vertex model in the following way. While a cell is in cell cycle state  $M$ , its preferred area  $A_i^{(0)}$  is doubled quasistatically. When a cell switches from state  $M$  to  $I$ , a new bond is created, passing through the cell center at a random angle. This process transforms the cell into two new cells and corresponds to a cell division (see figure 2.5). The preferred areas  $A_j^{(0)}$  of the two new cells are set to the value  $A^{(0)}$ , the cell cycle variables  $\sigma_j$  are set to  $I$ , and the values of the cell population variables  $\rho_j$  are inherited from the precursor cell. The molecule numbers  $n_i$  are shared equally between the two new cells.

## 2.5. Initial System Configuration

We choose a hexagonal network consisting of  $N_0$  cells as an initial configuration, with the  $A$  and  $P$  populations each constituting one half of the network. The initial values of the cell cycle variables  $\sigma_i$  are chosen randomly from  $\{M, I\}$  with probabilities

$$p(M) = \frac{\bar{\tau}_M}{\bar{\tau}_M + \bar{\tau}_I}, \quad p(I) = 1 - p(M). \quad (2.12)$$

A random initial residence time is assigned to cell  $i$ , which is denoted by  $\tau_M^{(0)}$  for state  $M$  and  $\tau_I^{(0)}$  for state  $I$ . We choose piecewise constant probability distributions

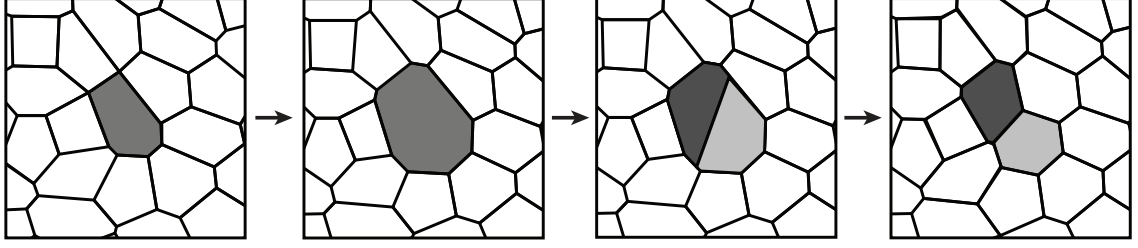


**Figure 2.5.:** Cell division in the vertex model. The preferred area  $A_i^{(0)}$  of the dividing cell, which is colored in grey, is doubled before a new bond is inserted, transforming the cell into two cells. Figure adapted from [58].

for the initial residence times,

$$p(\tau_M^{(0)}) = \frac{1}{\bar{\tau}_M} \Theta(\tau_M^{(0)}) \Theta(\bar{\tau}_M - \tau_M^{(0)}), \quad p(\tau_I^{(0)}) = \frac{1}{\bar{\tau}_I} \Theta(\tau_I^{(0)}) \Theta(\bar{\tau}_I - \tau_I^{(0)}). \quad (2.13)$$

As initial condition for the morphogen distributions we choose for all cells  $i$ ,

$$n_i^{(D)} = 0, \quad n_i^{(H)} = 0. \quad (2.14)$$

In general, there is an initial non-exponential growth phase in simulations of the described vertex model. After this complicated non-exponential growth phase, the system grows exponentially with the maximum growth rate  $\hat{g}$ , as long as the residence time in cell cycle state  $C$  vanishes. We choose initial conditions for the cell cycle states and residence times that exhibit a high degree of randomness, because this choice ensures that the exponential growth phase is reached quickly, which permits to easily fit simulated growth curves to experimental data.

In the following chapters the vertex model is used to study gradient scaling and self-organized growth. An example of a growth curve obtained by simulating the vertex model is shown in figure 3.4 on page 26.





# 3. Scaling of Morphogen Gradients in Growing Tissues

## 3.1. Experimental Evidence for Scaling

The Dpp morphogen gradient in the wing disc decays on a characteristic length scale  $\lambda$  [93]. In recent experiments it has been observed that  $\lambda$  is not constant during development. Instead,  $\lambda$  is approximately proportional to the linear dimension of the wing disc, which is shown in the following [175]. This dynamic property of the Dpp gradient is denoted by the term *scaling*.

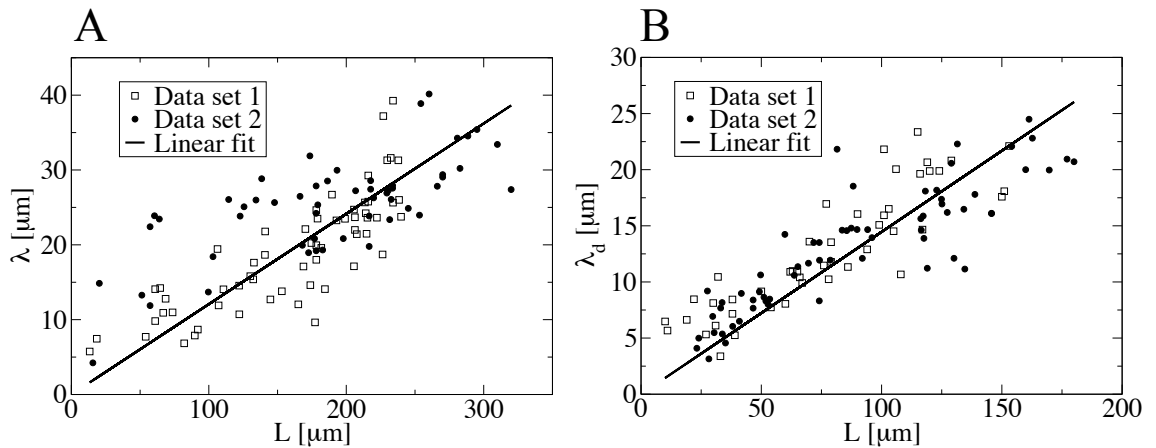


**Figure 3.1.:** (A) Decay length  $\lambda$  of the GFP-Dpp gradient shown as a function of the disc width  $L$ . A fit of the function  $\lambda = mL$  yields  $m = 0.121 \pm 0.003$ . (B) Decay length  $\lambda_d$  of the dad-nRFP gradient shown as a function of  $L$ . A fit of the function  $\lambda_d = m_d L$  yields  $m_d = 0.145 \pm 0.003$ .

We used a fluorescent GFP-Dpp fusion protein [53, 163] to quantify GFP-Dpp gradients in the posterior compartment of the wing disc as a function of the distance  $x$  from the Dpp source at different times during larval development (see appendix J). To obtain the decay length of the gradients, we fitted the function

$$c(x) = c_0 \exp(-x/\lambda) \quad (3.1)$$

to the data, where  $c_0$  and  $\lambda$  are fit parameters. We found that  $\lambda$  is approximately proportional to the width  $L$  of the posterior compartment (figure 3.1A). We also

determined the decay length  $\lambda_d$  of the dad-nRFP gradient, which shows the expression of the Dpp target gene *daughters against dpp* (dad) [169, 111, 165, 178] using nuclear red fluorescent protein (nRFP). The dad-nRFP gradient can be regarded as a measure of the Dpp signaling level. We observed that the decay length  $\lambda_d$  has the same magnitude as  $\lambda$  and that it is also approximately proportional to  $L$  (figure 3.1B). The GFP-Dpp and dad-nRFP experiments were performed by Ortrud Wartlick.

The scaling property of the GFP-Dpp and the dad-nRFP gradients can also be shown in a way that does not require any curve fitting. Instead, the gradients are normalized to unity amplitude and are displayed as a function of the relative position  $r = x/L$ . In these plots, the gradients measured at different times collapse into one single curve, which indicates scaling (figure 3.2). The normalization of the gradients is necessary because the amplitudes increase with time.

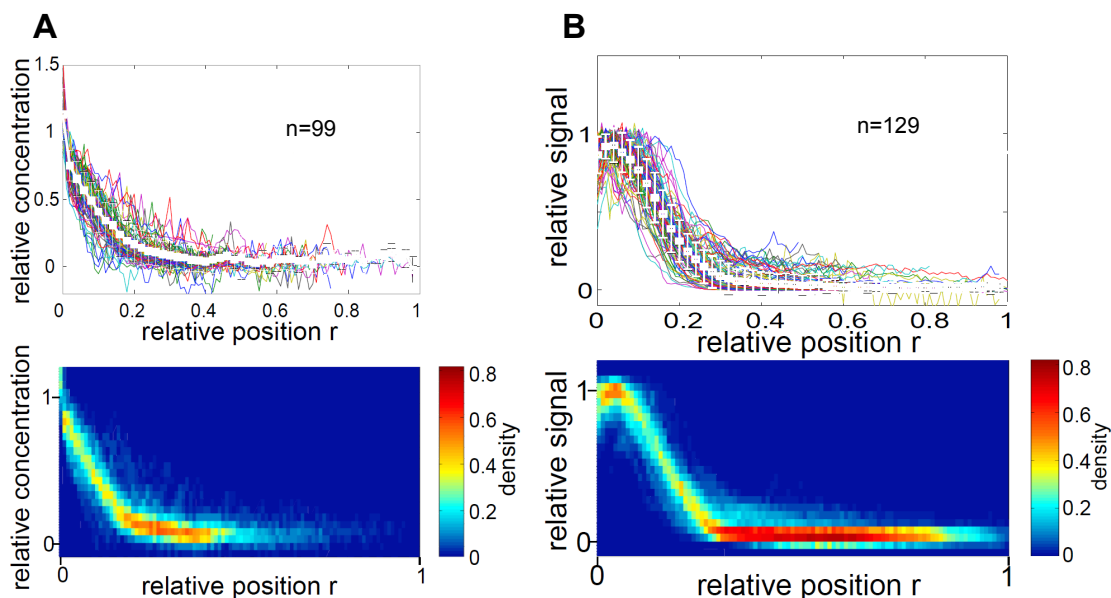


**Figure 3.2.:** (A) GFP-Dpp gradients from  $t = 48$  h to  $t = 130$  h (representing the whole growth period of the wing disc), normalized to unity amplitude and displayed as a function of the relative position  $r = x/L$ . The gradients collapse into one single curve due to the scaling property. Below, a density plot is shown (arbitrary units). (B) Corresponding normalized dad-nRFP gradients, with density plot below. Figure reproduced from [175], with permission from the American Academy of Arts and Sciences.

In a continuum description, the decay length of the steady state GFP-Dpp gradient is given by  $\lambda = \sqrt{D/k}$ , where  $D$  is the diffusion coefficient and  $k$  is the degradation rate (see appendix G). Either an increase of  $D$  or a decrease in  $k$  could account for the observed scaling. To determine which of these processes causes the scaling of the GFP-Dpp gradient,  $D$  and  $k$  were measured in wing discs of two different sizes

using fluorescence recovery after photobleaching (FRAP) experiments (performed by Anna Kicheva) [93]. Additionally, we used a reporter assay that allowed us to estimate the temporal changes of these parameters (experiments performed by Ortrud Wartlick, see appendix J.2). The results of these analyses indicate that the diffusion coefficient  $D$  is roughly constant whereas the degradation rate  $k$  decreases substantially during development (figure 3.3). We find that the degradation rate is inversely proportional to the wing disc area. Recently a secreted molecule species called Pentagone was found, which is thought to play an important role in scaling of the Dpp gradient [173]. Our results suggest that Pentagone affects the Dpp gradient by regulating the degradation rate  $k$ .

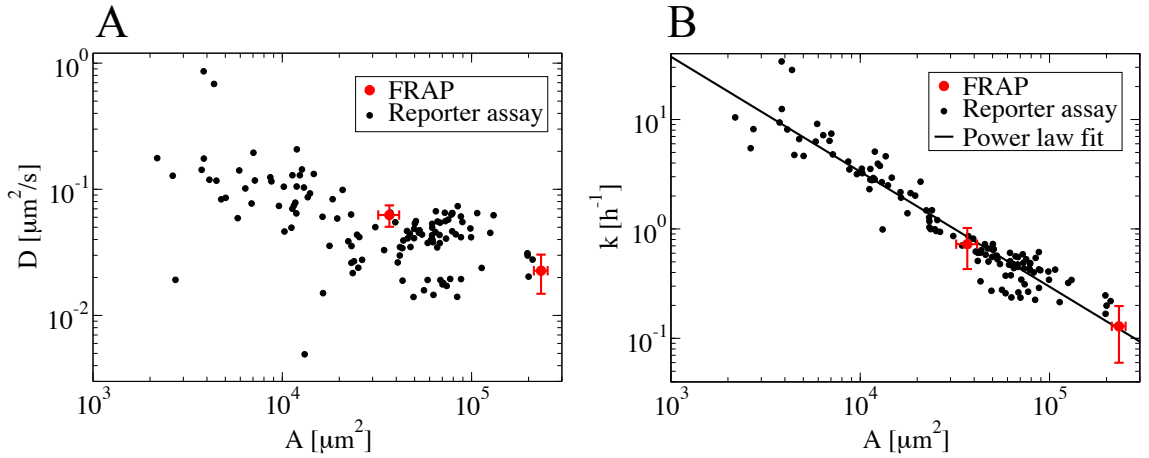


**Figure 3.3.:** (A) Effective GFP-Dpp diffusion coefficient  $D$  shown as a function of the disc area  $A$ . (B) Effective GFP-Dpp degradation rate  $k$  shown as a function of the area  $A$ . A fit of the power law  $k \sim A^\gamma$  yields  $\gamma = -1.05 \pm 0.03$ .

## 3.2. Mechanisms for Scaling of Morphogen Gradients

In this section, we study two mechanisms that may underlie the scaling of the Dpp gradient. For that purpose we use vertex model simulations in which the growth rate is predetermined and consistent with experimental data (see figure 3.4). In the simulations the Dpp decay length  $\lambda$  is determined by fitting exponential functions to the Dpp distribution in the  $P$  population (see figure 3.5). To quantify scaling,  $\lambda$  is displayed as a function of the width  $L$  of the  $P$  population, which is defined by

$$L = \frac{1}{L_y} \sum_{\rho_i=P} A_i. \quad (3.2)$$

Here the sum extends over all cells belonging to the  $P$  population. Additionally, normalized Dpp gradients are displayed as a function of the relative position at

different times. In these plots, scaling is indicated by a collapse of the gradients into one single curve. The parameter values used in the simulations are given in the tables 3.1, 3.2, and 3.3 at the end of this chapter.

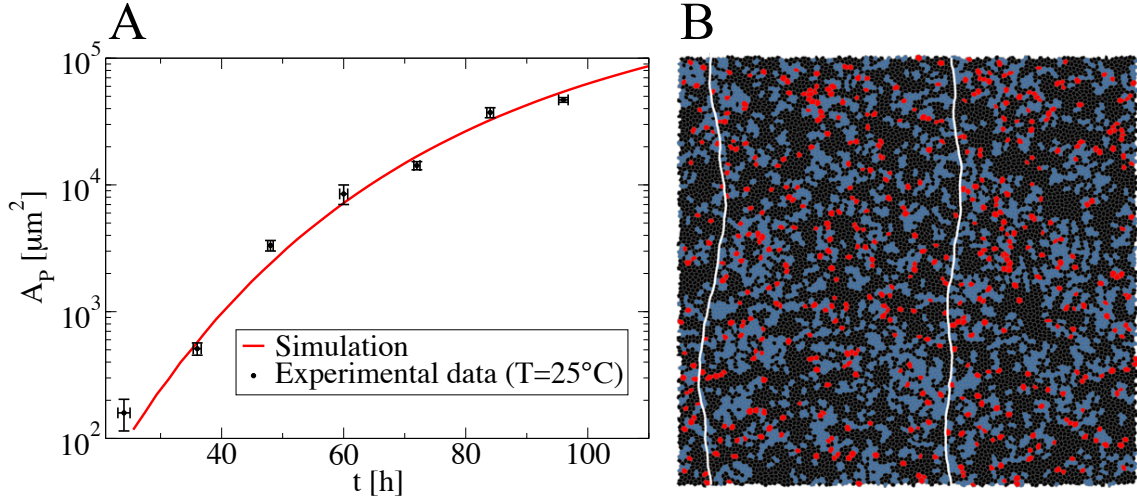


**Figure 3.4.:** (A) Area of the  $P$  population shown as a function of time. Here the residence time  $\tau_C$  in cell cycle state  $C$  is also chosen to be gamma distributed. The probability density  $p(\tau_C)$  has the form given in equation (2.9), but the mean  $\bar{\tau}_C$  increases with time as follows:  $\bar{\tau}_C = (\bar{\tau}_M + \bar{\tau}_I) (\exp[(t - t_0)/\tau_g] - 1)$ . Here  $\bar{\tau}_M$ ,  $\bar{\tau}_I$ ,  $t_0$ , and  $\tau_g$  are parameters (see table 3.3 on page 35). The temporal increase of  $\bar{\tau}_C$  leads to a temporal decrease of the growth rate. (B) Configuration of the cell cycle variables  $\sigma_i$  at  $t = 85$  h ( $N = 1.2 \cdot 10^4$  cells). The state of  $\sigma_i$  is indicated by a color code for each cell. Red:  $M$ , blue:  $I$ , black:  $C$ . The  $AP$ -interfaces are indicated by white lines. Cell proliferation, represented by cell cycle state  $M$  (red), is stochastic, spatially homogeneous on average, and occurs either in single cells or in small clusters, as observed in experiments [115].

The growth rate of the system is much smaller than the Dpp degradation rate, which determines the relaxation rate of the Dpp gradient (see appendix G). Therefore convection of Dpp molecules due to the movement of cells can be neglected: the gradient is renewed faster than growth occurs. Consequently, the decay length is approximately given by  $\lambda = \sqrt{D/k}$  and the Dpp gradient does not scale if the diffusion coefficient  $D$  and degradation rate  $k$  are constant parameters. However scaling can be achieved if the degradation rate of Dpp is allowed to change dynamically while the system is growing. The two mechanisms that we study require an additional molecule species that regulates the degradation of Dpp. We denote this molecule species by the name *expander*, which was introduced by Danny Ben-Zvi and Naama Barkai [10, 14]. Analogous to equations (2.3) and (2.4), we describe the dynamics of expander molecules by

$$\frac{d}{dt}n_i^{(E)} = p_i^{(E)} - k_i^{(E)}n_i^{(E)} + d^{(E)} \sum_j b_{ij} (n_j^{(E)} - n_i^{(E)}), \quad (3.3)$$

where  $n_i^{(E)}$  is the number of expander molecules,  $p_i^{(E)}$  is the expander production rate, and  $k_i^{(E)}$  is the expander degradation rate in cell  $i$ . The parameter  $d^{(E)}$  and the expander diffusion coefficient  $D^{(E)}$  are related by  $D^{(E)} \simeq A_c^{3/2} d^{(E)}$ , where  $A_c$  is the area of a cell. The length of the bond separating cell  $j$  and  $i$  is denoted  $b_{ij}$ .

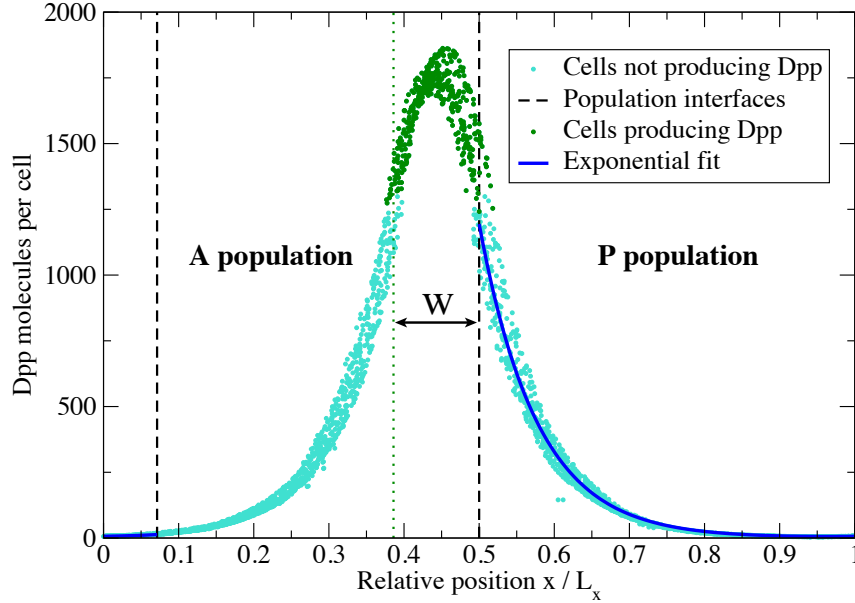


**Figure 3.5.:** Projection of the Dpp gradient on the  $x$ -axis at  $t = 64$  h ( $N = 3600$  cells). Each point corresponds to a cell. The decay length  $\lambda$  is determined by fitting the function  $n(x) = B_1 \exp(-x/\lambda) + B_2 \exp(x/\lambda)$  to the gradient in the  $P$  population using the Levenberg-Marquardt algorithm and  $B_1$ ,  $B_2$ , and  $\lambda$  as fit parameters [136]. The amplitude of the Dpp gradient is defined by  $n_0 = n(x_0)$ , where  $x_0$  is the  $x$ -coordinate of the  $AP$ -interface adjacent to the Dpp source. The  $x$ -coordinates of the  $AP$ -interfaces are defined by the average vertex position of the corresponding interface, accounting for periodic boundary conditions. Due to random fluctuations, the  $P$  population is larger than the  $A$  population here. The width of the Dpp source,  $w$ , is defined in equation (2.7).

The first mechanism that we study, the expander dilution mechanism, is related to mechanisms that have been proposed previously in the context of Turing-type reaction-diffusion systems of pattern formation. It has been shown that scale invariant patterns can be generated in such systems by introducing a regulatory molecule species whose concentration depends on the system size [130, 84, 87]. The second mechanism, the expansion-repression feedback, was originally proposed and analyzed in [10, 14]. However this analysis focused on systems of different sizes that are not growing. Here we study the expansion-repression mechanism, but we take growth of the system into account. In appendix A we furthermore show that the assumption of a nonlinear Dpp degradation term does not provide a simpler explanation for the experimentally observed scaling of the Dpp gradient.

### 3.2.1. Expander Dilution

The dilution mechanism requires that expander molecules are neither degraded nor produced,

$$k_i^{(E)} = 0, \quad p_i^{(E)} = 0, \quad (3.4)$$

but initially supplied at a fixed amount in each cell. The total number of expander molecules in the system  $n_S^{(E)} = N_0 n_0^{(E)}$  is thus constant but the cellular levels drop due to dilution. The initial number of expander molecules per cell is denoted  $n_0^{(E)}$ , and  $N_0$  is the initial number of cells. We impose a linear relationship between the Dpp degradation rate  $k_i^{(D)}$  in cell  $i$  and the local expander level  $n_i^{(E)}$ ,

$$k_i^{(D)} = \gamma n_i^{(E)}. \quad (3.5)$$

Here,  $\gamma$  is a constant parameter. Cell divisions cause a dilution of expander molecules so that spatially homogeneous growth leads to a spatially homogeneous Dpp degradation rate, which is inversely proportional to the total number of cells  $N$ .

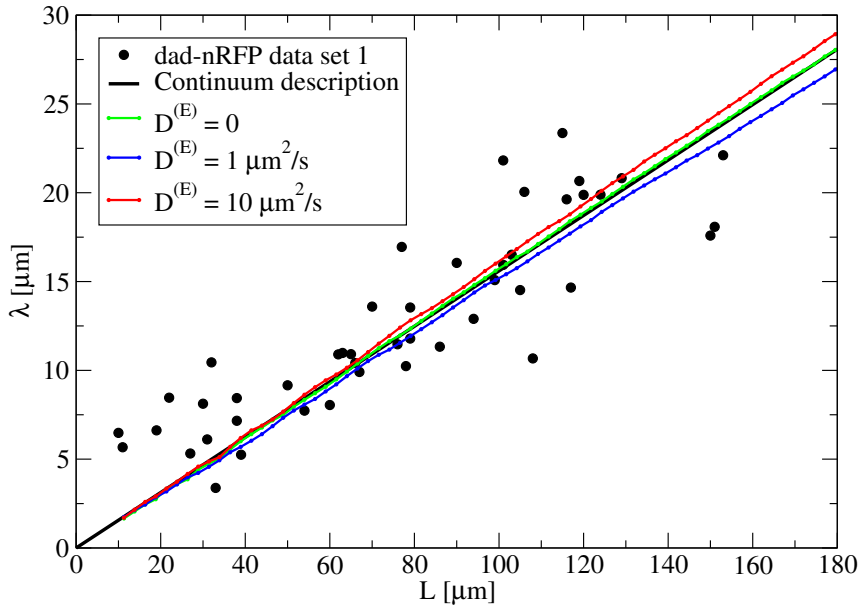


**Figure 3.6.:** Decay length  $\lambda$  as a function of  $L$  for different choices of  $D^{(E)}$  in the dilution mechanism. There is no significant difference between the three different simulation results. The deviations are due to random fluctuations.

Because growth is isotropic,  $k \sim L^{-2}$  holds. From this relationship,  $\lambda \sim L$  follows (see figure 3.6), because the Dpp gradient can be approximated as being in a steady state. For the rectangular system geometry in the simulation, a continuum description yields

$$\lambda = \sqrt{\frac{4D^{(D)}}{\gamma n_S^{(E)} A_c}} L, \quad (3.6)$$

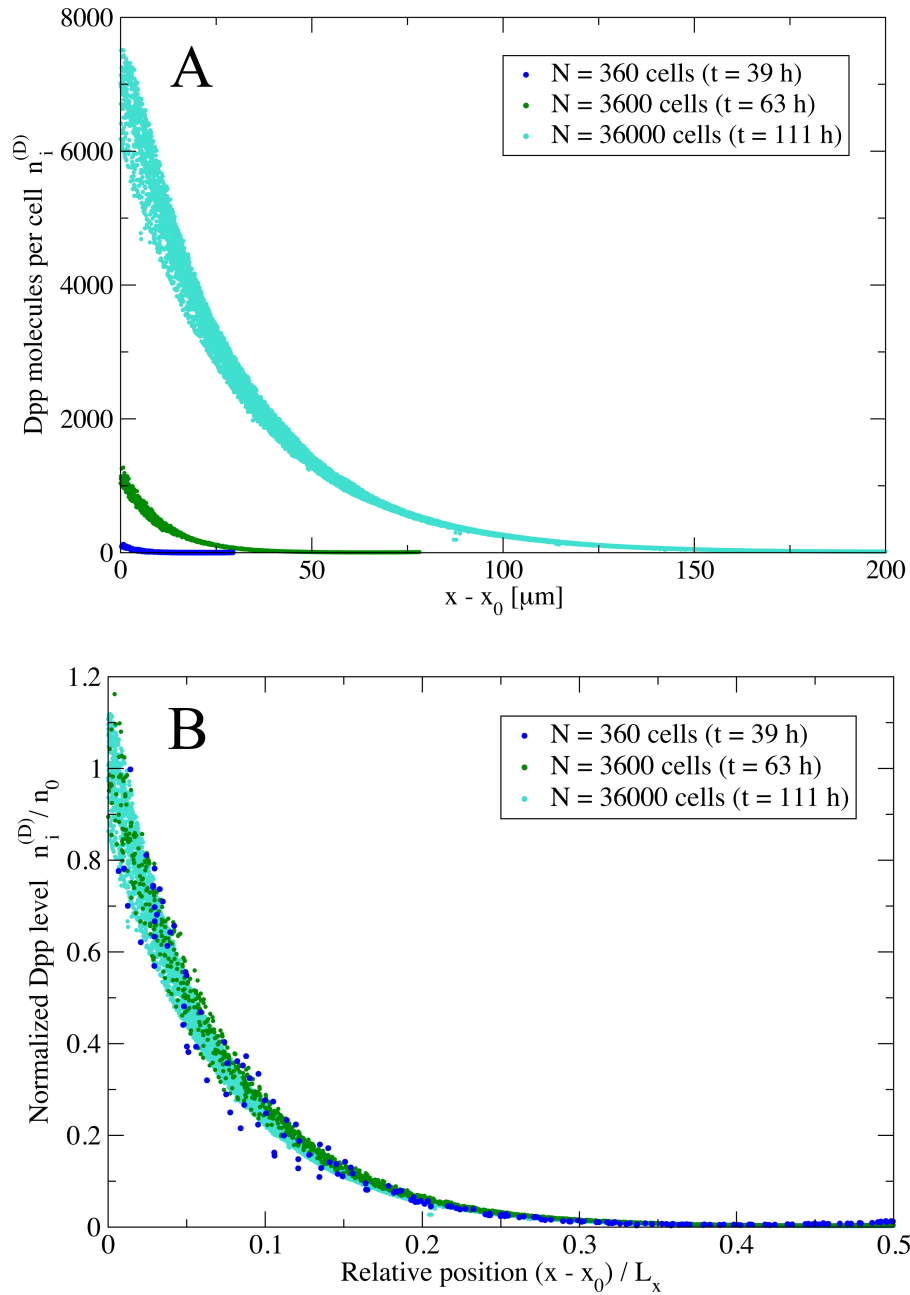


**Figure 3.7.:** Dpp gradients in a growing system shown at three different times. Each point corresponds to a cell. In this simulation the dilution scaling mechanism is used and the expander diffusion coefficient is chosen to be  $D^{(E)} = 1 \mu\text{m}^2/\text{s}$ . The  $x$ -coordinate of the  $AP$ -interface adjacent to the Dpp source is denoted  $x_0$ . Top (A): The amplitude and the decay length of the Dpp gradient increases with time due to the decrease in the degradation rate. Bottom (B): Normalized Dpp gradients shown as a function of the relative position. The normalized Dpp gradients collapse into one curve because  $\lambda \sim L$  (see figure 3.6).

where  $A_c$  is the average cell area. Thus, the proportionality between  $\lambda$  and  $L$  is exact in a steady state approximation. Therefore, normalized Dpp gradients at different times collapse into one curve if they are plotted as function of the relative position (see figure 3.7B), in agreement with experimental data (see figure 3.2).

Because growth and consequently dilution of the expander molecules is spatially homogeneous on average, the dilution mechanism does not require that expander molecules are diffusible. Even if the expander is non-diffusible, the Dpp gradient scales consistently with experimental data.

### 3.2.2. Expansion-repression Feedback

In this section we discuss the expansion-repression feedback mechanism for gradient scaling. This mechanism requires that expander production is repressed by high levels of Dpp, so that only cells with sufficiently low Dpp levels produce expander molecules [10, 14]. Additionally, increasing expander levels have to cause a decrease in the Dpp degradation rate. Here, we consider an idealized case in which the expander is not degraded. Moreover, we impose that expander production in cell  $i$  depends on the local Dpp level and behaves like a switch,

$$k_i^{(E)} = 0, \quad p_i^{(E)} = p^{(E)} \Theta \left( n_T^{(D)} - n_i^{(D)} \right). \quad (3.7)$$

The Dpp threshold, below which the production of expander molecules with rate  $p^{(E)}$  is switched on, is denoted  $n_T^{(D)}$ . The required decrease of the Dpp degradation rate with increasing expander concentration is taken into account by choosing a suitable functional relationship between these two quantities. We choose a Hill function, which was already used in previous works to describe a repression effect [14, 15],

$$k_i^{(D)} = \frac{\omega}{\left( n_C^{(E)} \right)^h + \left( n_i^{(E)} \right)^h}. \quad (3.8)$$

Here  $k_i^{(D)}$  is the Dpp degradation rate in cell  $i$ ,  $n_i^{(E)}$  is the number of expander molecules in cell  $i$ , and  $\omega$ ,  $h$ , and  $n_C^{(E)}$  are constant parameters. The parameter  $n_C^{(E)}$  determines a cutoff for the Dpp degradation rate and is chosen such that it is small as compared to the typical number of expander molecules per cell.

The steady state expander distribution is flat because expander molecules are diffusible but not degraded. However, because the system grows continuously and is not in a steady state, the diffusion coefficient  $D^{(E)}$  has to be sufficiently large to ensure an approximately homogeneous expander distribution. Let  $\tau$  be the time interval during which the system size doubles. Considering that expander molecules have to diffuse a distance of the order  $L$  within the time interval  $\tau$ , one obtains the following condition for an approximately homogeneous expander distribution,

$$D^{(E)} \gg \frac{L^2}{2\tau}. \quad (3.9)$$



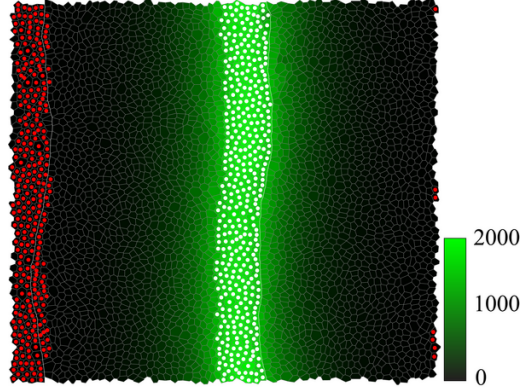


**Figure 3.8.:** Snapshot of a system ( $t = 64$  h,  $N = 3600$ ) with expansion-repression feedback. Cells producing expander molecules due to low Dpp levels are marked with red dots. Dpp producing cells are marked with white dots. The distribution of Dpp molecules is indicated by a color code. Parameter values:  $D^{(E)} = 1 \mu\text{m}^2/\text{s}$  and  $p^{(E)}/\omega = 1$ .

Inserting typical values ( $L = 150 \mu\text{m}$ ,  $\tau = 25$  h) into (3.9) yields  $D^{(E)} \gg 0.1 \mu\text{m}^2/\text{s}$ . To ensure a spatially homogeneous distribution, the expander must thus diffuse fast as compared to Dpp, which is characterized by  $D^{(D)} = 0.1 \mu\text{m}^2/\text{s}$  [93].

Furthermore, the production rate  $p^{(E)}$  has to be sufficiently high to ensure that gradient scaling can keep up with tissue growth (see figure 3.9). Within the time interval  $\tau$ , additional expander molecules have to be produced to achieve gradient scaling. The required magnitude of  $p^{(E)}$  can be estimated by comparing the number of required expander molecules with the maximum number of expander molecules that can be produced, which is given by  $N\tau p^{(E)}$ . Here the number of cells is denoted  $N$ . Generally, the necessary magnitude of  $p^{(E)}$  depends on the relationship between  $k_i^{(D)}$  and  $n_i^{(E)}$ . For the choice given in equation (3.8), the average number of expander molecules per cell  $\bar{n}^{(E)}$  has to increase by a factor of  $2^{1/h}$  during the time interval  $\tau$ , because  $\lambda \approx (D^{(D)}(\bar{n}^{(E)})^h/\omega)^{1/2}$  must approximately increase by a factor of  $2^{1/2}$  to achieve scaling. Taking dilution into account, we therefore obtain the following condition for the production rate,

$$p^{(E)} \gg \frac{2^{1+1/h} - 1}{\tau} \left( \frac{\omega \lambda^2}{D^{(D)}} \right)^{1/h}. \quad (3.10)$$

For the choice  $h = 1$  and typical values ( $\lambda = 20 \mu\text{m}$ ,  $\tau = 25$  h,  $D^{(D)} = 0.1 \mu\text{m}^2/\text{s}$ ) the condition becomes  $p^{(E)}/\omega \gg 10^{-1}$ . If the production rate does not fulfill this condition, scaling of the Dpp gradient is insufficient (see figure 3.9). However, if  $p^{(E)}/\omega$  is too large ( $\gg 1$ ), we observe a significant overshooting of  $\lambda$  in the early stages of the simulation. This overshooting of  $\lambda$  is due to an overshooting production of expander molecules at the onset of the simulation, when almost no Dpp molecules are present. Subsequently, the excess expander molecules are diluted due to growth so that  $\lambda$  decreases temporarily.

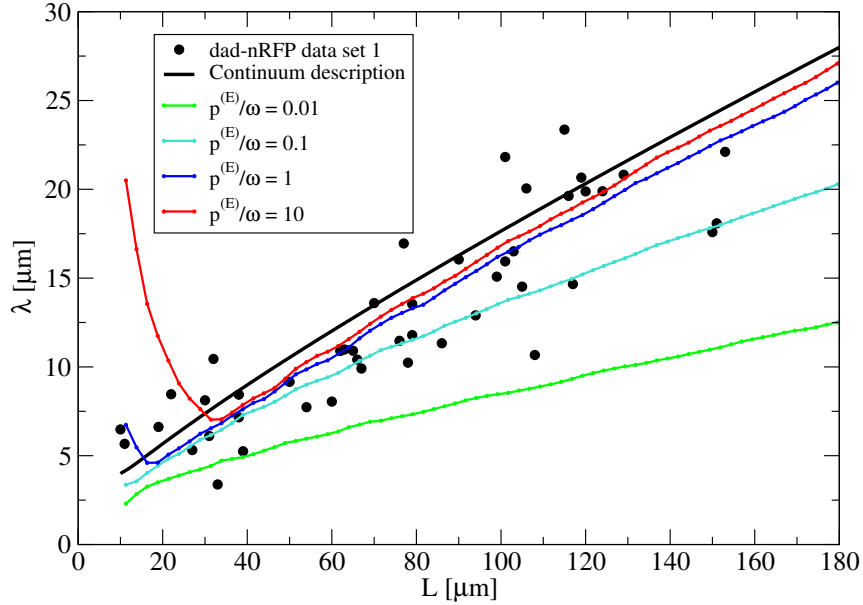


**Figure 3.9.:** Decay length  $\lambda$  as a function of  $L$  for different choices of  $p^{(E)}$  in the expansion-repression mechanism ( $D^{(E)} = 1 \mu\text{m}^2/\text{s}$ ). For high production rates there is a considerable overshooting effect at the onset of the simulation.

If  $D^{(E)}$  obeys (3.9) and  $p^{(E)}/\omega$  has an appropriate magnitude ( $\approx 1$ ), the system is close to the steady state and the Dpp level in the minimum of the gradient is approximately equal to the repression threshold. Using a continuum description and approximating the Dpp gradient by the single exponential steady state solution given in equation (G.24), one obtains the following equation describing scaling,

$$\lambda = \frac{L}{\ln\left(c_0 A_c / n_T^{(D)}\right)}, \quad (3.11)$$

$$c_0 = \frac{\nu \lambda^2}{2D^{(D)}} \left(1 - \exp\left(-\frac{w}{\lambda}\right)\right). \quad (3.12)$$

Here,  $c_0$  is the amplitude of the Dpp gradient and  $\nu$  is the Dpp production rate per unit area. The width  $w$  of the Dpp source, which increases as the system grows, is parametrized by  $w = b_1 \ln(L/b_2)$  (see appendix I). The proportionality between  $\lambda$  and  $L$  is not exact in the continuum description because  $c_0$  depends both on  $\lambda$  and  $L$ . Therefore, normalized Dpp gradients at different times do not collapse to one curve if they are plotted as a function of the relative position (see figure 3.10B). However, since the dependence on  $c_0$  is only logarithmic in equation (3.11),  $\lambda$  is roughly proportional to  $L$ . Consequently there is an approximate collapse of the gradients in figure 3.10B.

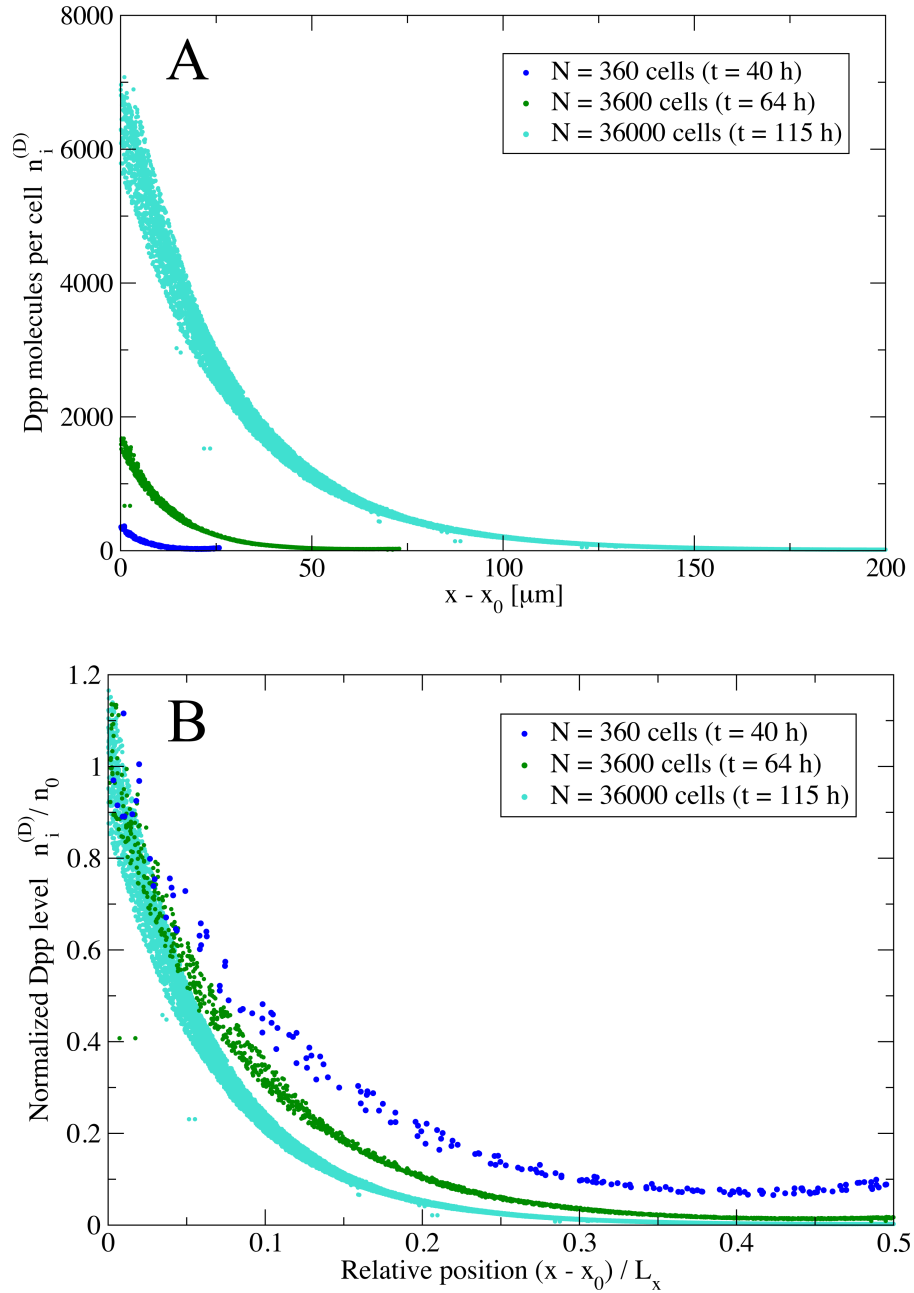


**Figure 3.10.:** Dpp gradients in a growing system shown at three different times. Each point corresponds to a cell. In this simulation the expansion-repression scaling mechanism is used and the following parameter values are chosen,  $D^{(E)} = 1 \mu\text{m}^2/\text{s}$  and  $p^{(E)}/\omega = 1$ . The  $x$ -coordinate of the  $AP$ -interface adjacent to the Dpp source is denoted  $x_0$ . Top (A): The amplitude and the decay length of the Dpp gradient increases with time due to the decrease in the degradation rate. Bottom (B): Normalized Dpp gradients shown as a function of the relative position. The normalized Dpp gradients do not collapse to one curve because the proportionality between  $\lambda$  and  $L$  is not exact, see equation (3.11).

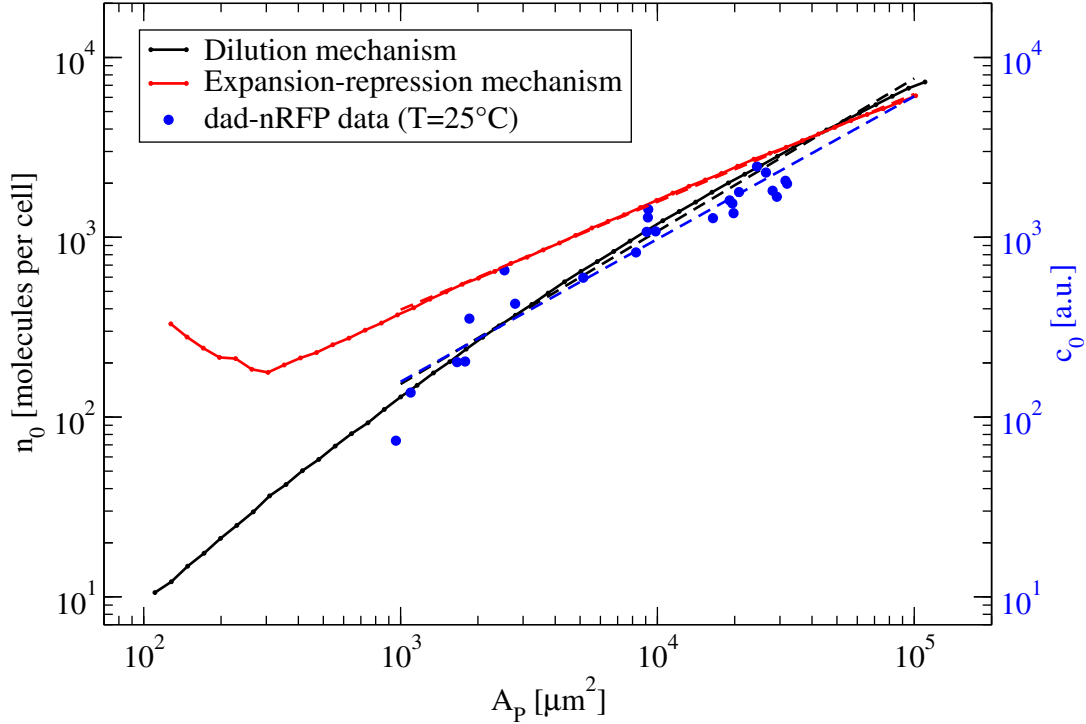


**Figure 3.11.:** Dpp gradient amplitude  $n_0$  shown as a function of the area  $A_P$  of the  $P$  population. Fits of the power law  $n_0 \sim A_P^\beta$  to the simulation data, excluding data points with  $A_P < 10^3 \mu\text{m}^2$ , yield  $\beta = 0.85 \pm 0.01$  for the dilution mechanism, and  $\beta = 0.600 \pm 0.003$  for the expansion-repression mechanism. The power law fits are indicated by dashed lines. For comparison, the experimentally determined amplitude  $c_0$  of the dad-nRFP gradient is shown, for which the scale with arbitrary units on the right side applies. The fit to the experimental data yields the exponent  $\beta = 0.79 \pm 0.05$ . Thus only the dilution scaling mechanism leads to an agreement with the experimental data. Parameter values of the simulations:  $D^{(E)} = 1 \mu\text{m}^2/\text{s}$  and  $p^{(E)}/\omega = 1$ . As long as the growth rate is comparable to the growth rate used in these simulations, the exponents  $\beta$  are essentially determined by the scaling mechanism. Therefore the exponents given here are also valid for the simulations in chapter 4, where the growth rate is determined by cellular growth rules.

Parameter	Meaning	Value
$n_0^{(E)}$	Initial number of expander molecules per cell	$3 \cdot 10^4$
$\gamma$	Rate constant	$10^{-2} \text{h}^{-1}$
$d^{(E)}$	Parameter describing expander diffusion	$(0 - 2600) \mu\text{m}^{-1}\text{h}^{-1}$
$D^{(E)}$	Corresponding expander diffusion coefficient	$(0 - 10) \mu\text{m}^2\text{s}^{-1}$

**Table 3.1.:** Parameter values used for the expander dilution mechanism.

Parameter	Meaning	Value
$n_0^{(E)}$	Initial number of expander molecules per cell	0
$n_T^{(D)}$	Dpp threshold for expander production	10
$\omega$	Rate constant	$10^4 \text{ h}^{-1}$
$n_C^{(E)}$	Cutoff parameter	30
$h$	Hill coefficient	1
$d^{(E)}$	Parameter describing expander diffusion	$(0 - 2600) \mu\text{m}^{-1}\text{h}^{-1}$
$D^{(E)}$	Corresponding expander diffusion coefficient	$(0 - 10) \mu\text{m}^2\text{s}^{-1}$
$p^{(E)}$	Expander production rate	$(10^2 - 10^5) \text{ h}^{-1}$

**Table 3.2.:** Parameter values used for the expansion-repression feedback mechanism.

Parameter	Meaning	Value
$\Gamma/KA^{(0)}$	Dimensionless cell perimeter stiffness	0.04
$\Lambda/K(A^{(0)})^{3/2}$	Dimensionless cell bond tension	-0.12
$A^{(0)}$	Preferred cell area	$6.83 \mu\text{m}^2$
$\kappa$	$AP$ -interface tension factor	-5
$N_0$	Initial number of cells	36
$\bar{\tau}_M$	Mean residence time in cell cycle state $M$	0.75 h
$\bar{\tau}_I$	Mean residence time in cell cycle state $I$	3.12 h
$t_0$	Starting time of the simulation	24.6 h
$\tau_g$	Timescale on which $\bar{\tau}_C$ increases	42 h
$\xi$	Gamma distribution shape parameter	25
$p^{(H)}$	Hh production rate	$10^4 \text{ h}^{-1}$
$k^{(H)}$	Hh degradation rate in $A$ cells	$36 \text{ h}^{-1}$
$d^{(H)}$	Parameter describing Hh diffusion	$130 \mu\text{m}^{-1}\text{h}^{-1}$
$D^{(H)}$	Corresponding Hh diffusion coefficient	$0.5 \mu\text{m}^2\text{s}^{-1}$
$n_T^{(H)}$	Hh threshold for Dpp production	250
$p^{(D)}$	Dpp production rate	$10^4 \text{ h}^{-1}$
$\nu$	Dpp production rate per unit area	$1800 \mu\text{m}^{-2}\text{h}^{-1}$
$d^{(D)}$	Parameter describing Dpp diffusion	$26 \mu\text{m}^{-1}\text{h}^{-1}$
$D^{(D)}$	Corresponding Dpp diffusion coefficient	$0.1 \mu\text{m}^2\text{s}^{-1}$
$b_1$	Parameter describing the Dpp source	$7.1 \mu\text{m}$
$b_2$	Parameter describing the Dpp source	$6.4 \mu\text{m}$

**Table 3.3.:** Parameter values used in this chapter. For the mechanical parameter values given here, T2 processes do not occur, and the average cell area is given by  $A_c \approx 0.8A^{(0)} \approx 5.5 \mu\text{m}^2$ .

**Summary** In this chapter we have shown experimental evidence for the scaling of the Dpp gradient and discussed two possible scaling mechanisms. Both mechanism, the dilution mechanism and the expansion-repression mechanism, rely on a regulatory molecules species, the expander. The expansion-repression scaling mechanism can achieve an approximate proportionality between the Dpp decay length  $\lambda$  and the growing system size  $L$ , if the parameters are chosen appropriately (figure 3.9). Because the proportionality is not exact, normalized Dpp gradients displayed as a function of the relative position do not collapse into one curve (figure 3.10B). In contrast, the dilution scaling mechanism leads to an exact proportionality between  $\lambda$  and  $L$  (figure 3.6). As a result, normalized Dpp gradients displayed as a function of the relative position do collapse into one curve (figure 3.7B), as observed experimentally for both the GFP-Dpp and the dad-nRFP gradients (figure 3.2). Despite the simplicity of the dilution scaling mechanism, the agreement with experimental data is thus better than in the case of the expansion-repression mechanism. In a plot showing the gradient amplitude as a function of the posterior area, the agreement with experimental data is also better for the dilution scaling mechanism (figure 3.11).

## 4. Self-organized Growth Described by Cellular Growth Rules

In this chapter we explore how growth of developing tissues can be controlled in a self-organized way. Growth control and the mechanisms by which the final sizes of animals and organs are determined are still poorly understood [36]. Growing organs have to be supplied with essential extrinsic factors such as nutrients and hormones during development. Therefore developing organs can apparently not be considered as closed systems. However there is strong evidence that many organs possess organ-intrinsic growth control mechanisms [27]. Essentially, these mechanisms control growth and determine the final organ size if the tissue is provided with a sufficient amount of the necessary extrinsic factors. In the following we want to consider this situation, in which it is justified to consider growth control in the developing organ as an internal process.

An appropriate theoretical description of such systems should not depend on any functions with explicit time-dependence, because such functions correspond to external control. External growth control was for example used in the last chapter. There the cell cycle time was determined by an explicitly time-dependent function (see caption of figure 3.4). In our description of growth control in this chapter we do not use such functions. Instead, the timing of cell divisions is determined by cellular growth rules that only depend on the local neighbourhood of the cell. In our description, the growth behaviour of the system is thus not controlled externally but emerges from local growth rules. We therefore speak of self-organized growth and argue that organ-intrinsic growth control mechanisms are appropriately described in this way.

In our study we again use the vertex model and focus on the *Drosophila* wing imaginal disc, for which experimental data is available. In the vertex model, a growth rule defines a condition on which the transition from cell cycle state  $C$  to cell cycle state  $M$  occurs. Thus a growth rule essentially defines when a cell should divide. Because the morphogen Dpp plays a major role in growth control in the wing disc (see section 1.2.2), we introduce cellular growth rules that couple the decision to divide a cell to the local Dpp level. The goal of our study is to find the mechanism by which Dpp controls growth. In particular we want to answer the question how the inhomogeneous Dpp distribution can stimulate homogeneous growth.

The Dpp gradient is not static but it adapts to the size of the tissue. Both the decay length and the amplitude of the gradient increase during development (see figures 3.1 and 3.11 in the previous chapter). This behaviour suggests two plausible

types of growth rules: one that depends on temporal changes of the cellular Dpp concentration and one that depends on the slope of the Dpp gradient. The growth rules that are based on temporal changes of the cellular Dpp concentration are denoted *temporal* growth rules and are discussed in section 4.1. The growth rules that depend on the slope of the Dpp gradient are denoted *spatial* growth rules and are discussed in section 4.2. The idea that the growth rate depends on the slope of the Dpp gradient has been proposed previously [39].

It turns out that the growth behaviour does not only depend on the growth rule, but also on the choice of the scaling mechanism. Therefore we discuss the growth behaviour for the dilution mechanism as well as for the expansion-repression mechanism. Furthermore, it turns out that the temporal growth rules are sensitive to initial conditions and fluctuations at the onset of the simulation. However, the initial configuration of the wing disc is unknown and experimental data for very small discs is not available. Therefore we introduce a cell number threshold  $N_g$  that determines when the growth rules are switched on. As long as the number of cells  $N$  is smaller than  $N_g$ , the transition  $C \rightarrow M$  occurs instantaneously for any cell so that the system is forced to grow exponentially in the beginning. By choosing  $N_g$  sufficiently large, we are able to study the behaviour of the growth rules independent of details concerning the initial conditions. The growth behaviour that results if the rules are applied from the beginning on, when the system is small and fluctuations are strong, is discussed in appendix B. In appendix C we discuss further details. We estimate the dynamic range that a signaling system would have to cover to make growth control by the Dpp gradient possible. Moreover we estimate the minimum number of Dpp molecules in the wing disc, and the uncertainties in the Dpp signal due to molecule number fluctuations.

Two important quantities characterizing a growth rule are the resulting system size as a function of time, and the growth rate  $g$ , which is defined as the number of cell divisions per cell per unit time (see appendix E). The growth curves obtained by the vertex model simulations are compared to growth curves of wing discs measured by Ortrud Wartlick. The parameter values used in the simulations are given in the tables 4.1, 4.2, and 4.3 on pages 52 and 53. In all figures shown in this chapter, error bars indicate the standard error of the mean if not stated otherwise.

## 4.1. Temporal Growth Rules

The temporal growth rules discussed in this section are based on the idea that the Dpp signaling pathway is sensitive to relative changes of the input signal [175]. A sensitivity to relative temporal changes rather than absolute values might be a general property of cellular signaling systems. Such a behaviour is typical for adaptive sensory systems and is known to exist in other signaling scenarios such as bacteria and sperm chemotaxis [11, 6, 62]. There, the determination of relative temporal changes is achieved by combining adaptation with a dynamic response



[11, 6, 62]. The Dpp signaling pathway is a dynamic network of signal transduction components, which may generate an adaptive response by combining feed-forward and feedback elements in its pathway structure.

### 4.1.1. Deterministic Temporal Rule

The deterministic temporal rule is defined as follows: the transition  $C \rightarrow M$  occurs in cell  $i$  if the relative temporal difference of the Dpp level exceeds a threshold,

$$\frac{n_i^{(D)}(t) - n_{i,0}^{(D)}}{n_{i,0}^{(D)}} \geq \alpha. \quad (4.1)$$

The parameter  $\alpha$  is equal to the relative increase of the Dpp level that is necessary to trigger the transition. The number of Dpp molecules that were in the precursor cell of cell  $i$  when the transition  $C \rightarrow M$  occurred there is denoted  $n_{i,0}^{(D)}$ . In figure 4.1, a time series of the Dpp concentration in a cell is shown. Cell division events are indicated by vertical lines in this figure. The growth behaviour that results from the deterministic temporal rule depends on which scaling mechanism is chosen. Therefore we discuss the growth behaviour separately for the dilution scaling mechanism and for the expansion-repression scaling mechanism.

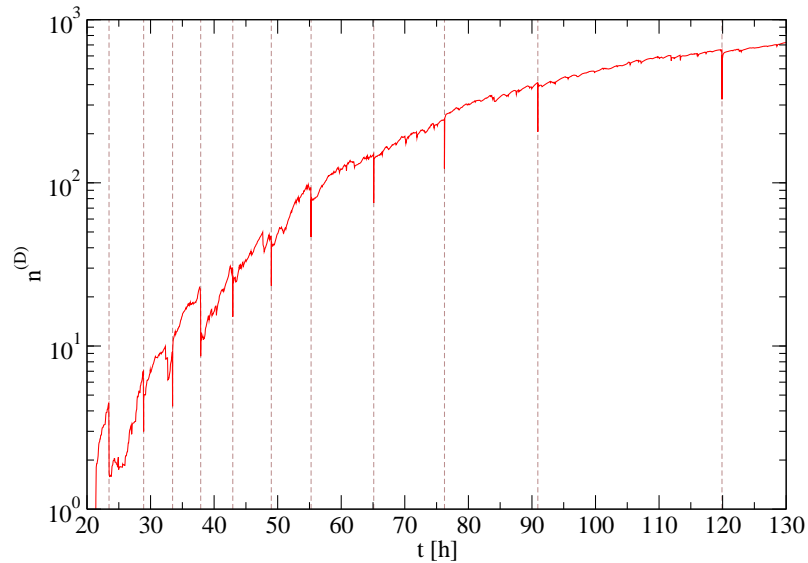


**Figure 4.1.:** Number of Dpp molecules  $n^{(D)}$  in an individual cell during a simulation of self-organized growth (deterministic temporal rule,  $\alpha = 64\%$ ), shown as a function of time. When the cell divides, the time series is continued with one of the two daughter cells. Here, the dilution scaling mechanism is used. The growth rule is switched on at  $t \approx 40$  h. Cell division events are indicated by dashed lines. Directly after a cell division, the cellular Dpp level drops by 50% due to dilution.

### Dilution Scaling Mechanism

If the dilution scaling mechanism is chosen, the growth curve can be matched to experimental data well by choosing the parameter  $\alpha$  appropriately ( $\alpha = 64\%$ ), see figure 4.2. For this choice, the system still grows slowly ( $g \approx 0.02 \text{ h}^{-1}$ ) at the time of pupariation ( $t \approx 110 \text{ h}$ ), corresponding to a cell cycle time of  $\tau \approx 35 \text{ h}$ , which is consistent with experimental studies [107].

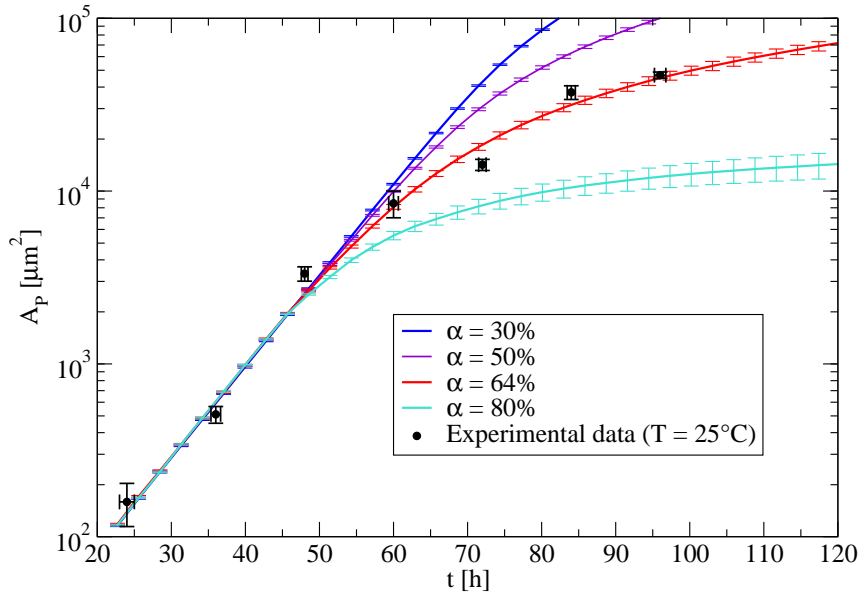


**Figure 4.2.:** Area  $A_P$  of the  $P$  population shown as a function of time for the deterministic temporal rule. The dilution scaling mechanism is used in these simulations.

Growth is largely homogeneous in space on average, see figures 4.3 and 4.10C, consistent with experimental observations [69, 64, 146]. The homogeneity of growth can be understood using the following simplified continuum description. The Dpp concentration  $c_i$  perceived by cell  $i$  at position  $x_i$  is given by

$$c_i(t) = c_0(t) \exp\left(-\frac{x_i(t)}{\lambda(t)}\right), \quad (4.2)$$

and the relative time derivative is given by

$$\frac{\dot{c}_i}{c_i} = \frac{\dot{c}_0}{c_0} - \frac{d}{dt} \left( \frac{x_i}{\lambda} \right), \quad (4.3)$$

where  $c_0$  is the Dpp gradient amplitude and  $\lambda$  is the Dpp decay length. Because the deterministic temporal rule essentially depends on the relative time derivative of the cellular Dpp concentration,  $\dot{c}_i/c_i$ , this growth rule generates spatially homogeneous growth if  $\dot{c}_i/c_i$  is independent of the cellular position  $x_i$ . Indeed, we can show that

the assumption of spatially homogeneous growth is self-consistent if the gradient scales. From the assumption of homogeneous growth it follows that the relative position of a cell  $r_i = x_i/L$  is time-independent. Because of the scaling property  $\lambda \sim L$ , which is ensured by the dilution scaling mechanism, it follows that the ratio  $x_i/\lambda$  is time-independent as well. According to equation (4.3), the relative time derivative of the cellular Dpp level is then independent of  $x_i$ ,

$$\frac{\dot{c}_i}{c_i} = \frac{\dot{c}_0}{c_0}, \quad (4.4)$$

which leads to spatially homogeneous growth. The assumption of spatially homogeneous growth is thus self-consistent in this simplified continuum description, which applies to the  $P$  population.

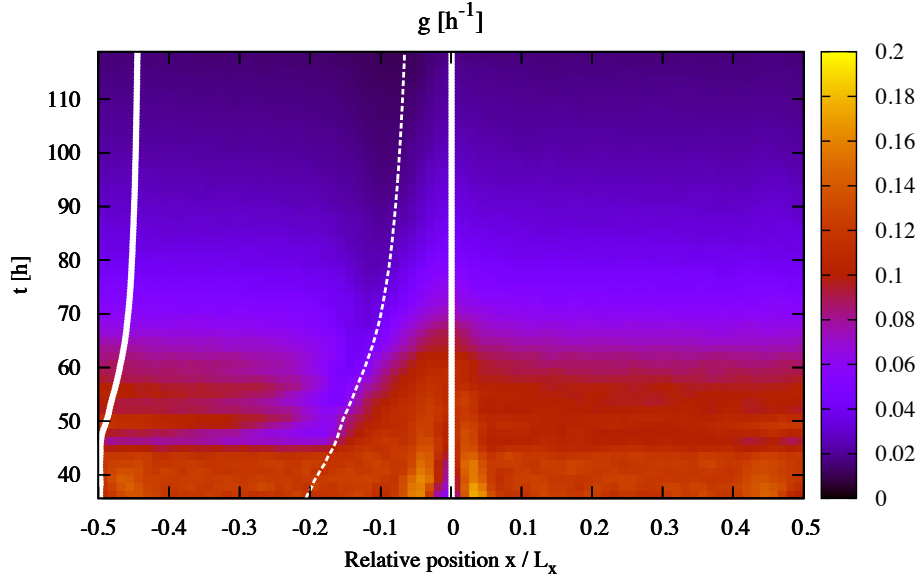


**Figure 4.3.:** Local growth rate  $g$ , generated by the deterministic temporal rule together with the dilution scaling mechanism, shown as a function of time and position using a color code ( $\alpha = 64\%$ , average over 400 simulations). The average positions of the  $AP$ -interfaces are indicated by solid lines. The Dpp source is located between the dashed line and the central solid line.

In the  $A$  population, next to the anterior border of the Dpp source, there is however slightly less proliferation than elsewhere (see figure 4.3). This inhomogeneity is due to the asymmetry caused by the Dpp source. Whether or not a cell produces Dpp molecules depends on the local Hh concentration. Cells in the  $A$  population that move away from the  $AP$ -interface due to growth may stop Dpp production if the local Hh concentration becomes too small. In cells that stop Dpp production, the temporal increase of the Dpp concentration is attenuated, leading to fewer cell divisions. As a result, the  $A$  population grows less than the  $P$  population. The

growth asymmetry of the two cell populations is in agreement with experimental data (see figure 4.4). For vanishing expander diffusion coefficient  $D^{(E)}$  the growth asymmetry is more pronounced.

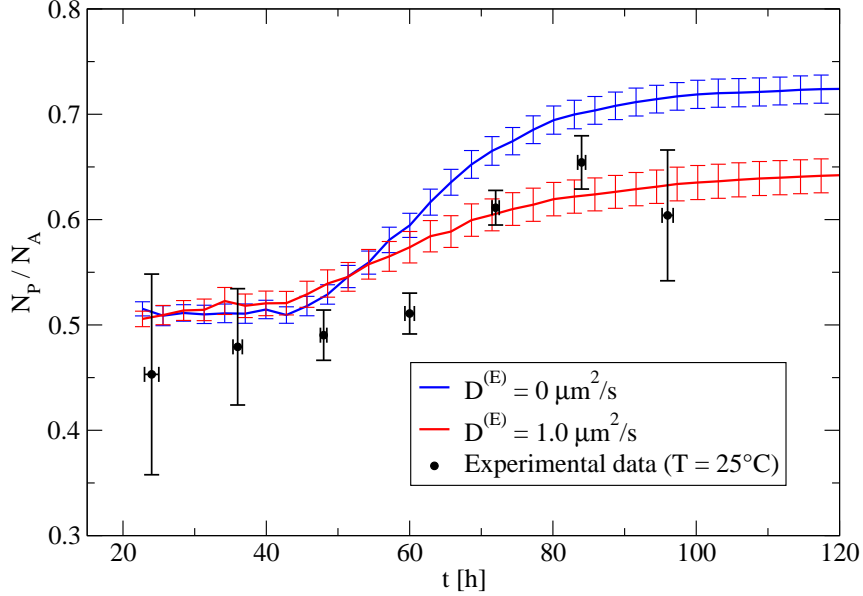


**Figure 4.4.:** Ratio of the cell number in the  $P$  population ( $N_P$ ) to the cell number in the  $A$  population ( $N_A$ ). The solid lines are simulations of the deterministic temporal rule with the dilution scaling mechanism ( $\alpha = 64\%$ ). As initial condition, an asymmetric configuration with  $N_P = 14$  and  $N_A = 28$  is chosen here to compare the simulation results with experimental data measured by Ortrud Wartlick. The ratio  $N_P/N_A$  is calculated from the measured compartment areas assuming a constant cell density.

### Expansion-repression Scaling Mechanism

If the expansion-repression scaling mechanism is chosen instead of the dilution mechanism, the parameter  $\alpha$  must be chosen smaller ( $\alpha \lesssim 10\%$ ) to cause substantial growth. Growth is strongly inhomogeneous in space, and most cell divisions occur in the Dpp source (see figures 4.5 and 4.10E). Growth is inhomogeneous because the expansion-repression mechanism does not achieve perfect scaling: the proportionality between the Dpp decay length  $\lambda$  and the system size  $L$  is only approximate. Hence, the argument explaining the homogeneity of growth for the dilution scaling mechanism, which was given in the previous section, does not hold for the expansion-repression mechanism. The assumption of homogeneous growth is not self-consistent because the ratio  $x_i/\lambda$  is not time-independent in this case.

According to equation (4.2) there are two factors that determine the Dpp concentration in cell  $i$ : the Dpp concentration profile, which is determined by  $c_0$  and  $\lambda$ , and the position of the cell,  $x_i$ . Due to growth, cells move away from the Dpp

source, which would cause a decrease in the cellular Dpp concentration if the Dpp concentration profile was fixed. However, changes in the Dpp concentration profile can compensate for this decrease. The expansion-repression scaling mechanism is designed such that the Dpp concentration in cells located in the minimum of the gradient is essentially fixed (see section 3.2.2): the loss in Dpp concentration due to the movement of the cell is compensated by the increase in the Dpp gradient amplitude. However, cells that are located closer to the Dpp source do experience an increase in the cellular Dpp concentration. The closer a cell is located to the Dpp source, the smaller is the effect of the movement of the cell, and the larger is the relative temporal increase in the cellular Dpp concentration. Therefore most cell divisions occur in the Dpp source.

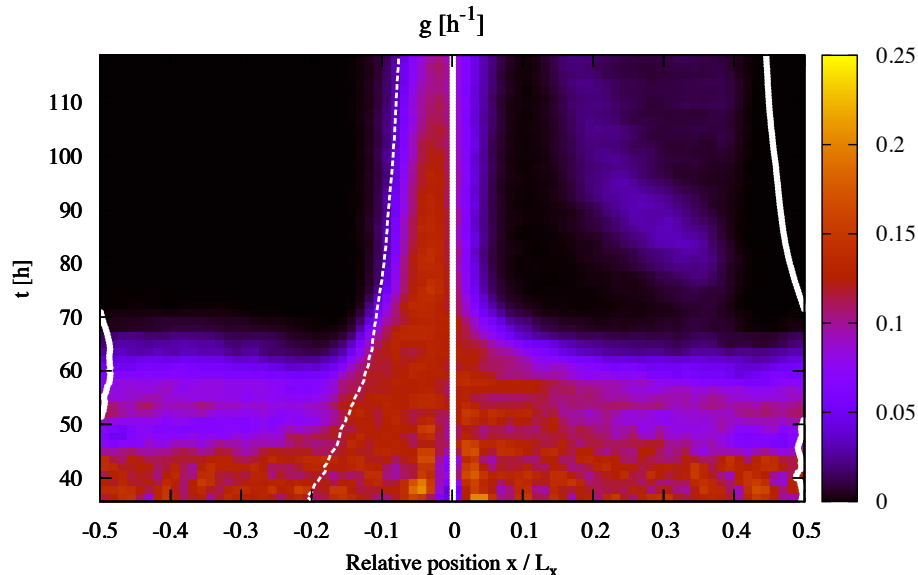


**Figure 4.5.:** Local growth rate  $g$ , generated by the deterministic temporal rule together with the expansion-repression scaling mechanism, shown as a function of time and position using a color code ( $\alpha = 5\%$ , average over 25 simulations). The average positions of the  $AP$ -interfaces are indicated by solid lines. The Dpp source is located between the dashed line and the central solid line. Most cell divisions occur in the Dpp source (see also figure 4.10E on page 48).

### 4.1.2. Stochastic Temporal Rule

The stochastic temporal rule is related to a model describing cell replenishment in the epidermis [89, 95]. The main features shared by this model and the growth rule are the distinction between proliferating and non-proliferating cells, and the stochastic transition between the two cell types. Here, the proliferating cells are denoted type A cells, and the non-proliferating cells are denoted type B cells. The

transition  $C \rightarrow M$  occurs instantaneously for type A cells. In contrast, the transition  $C \rightarrow M$  never occurs for type B cells, which implies that these cells cannot divide. Initially all cells are of type A. However, whether a new cell that is generated by a cell division is of type A or B is determined as follows. When the transition  $C \rightarrow M$  occurs in cell  $i$ , which initiates a cell division, the probability  $\varrho_i(t)$  that a daughter cell of cell  $i$  is of type A is determined. The probabilities of the three possible kinds of cell divisions are thus given by

$$A \rightarrow \begin{cases} A + A & \text{probability } \varrho_i^2 \\ A + B & \text{probability } 2\varrho_i(1 - \varrho_i) \\ B + B & \text{probability } (1 - \varrho_i)^2 \end{cases}. \quad (4.5)$$

We choose a piecewise linear relationship between  $\varrho_i(t)$  and the relative time derivative of the Dpp level in cell  $i$ :

$$\varrho_i(t) = \begin{cases} 1 & \text{if } 1 \leq \theta\zeta_i(t), \\ \theta\zeta_i(t) & \text{if } 0 < \theta\zeta_i(t) < 1, \\ 0 & \text{if } \theta\zeta_i(t) \leq 0. \end{cases} \quad \zeta_i(t) = \frac{n_i^{(D)}(t) - n_{i,0}^{(D)}}{(t - t_{i,0})n_{i,0}^{(D)}}. \quad (4.6)$$

Here,  $\theta$  is a parameter,  $t_{i,0}$  is the time when the transition  $C \rightarrow M$  occurred in the precursor cell of cell  $i$ , and  $n_{i,0}^{(D)}$  is the number of Dpp molecules in the precursor cell at that time. The quantity  $\zeta_i(t)$  is thus a measure for the average relative time derivative of the Dpp level in cell  $i$ . For this growth rule the parameter  $N_g$  has the following meaning: all cells are of type A as long as the number of cells satisfies  $N < N_g$ . The growth behaviour resulting from the stochastic temporal rule is also qualitatively different for the dilution scaling mechanism and for the expansion-repression scaling mechanism.

### Dilution Scaling Mechanism

The growth curves can be matched to experimental data by choosing the parameter  $\theta$  appropriately (see figure 4.6), as in the case of the deterministic temporal rule. However, there is a significant difference between the two rules. In case of the stochastic temporal rule, growth has stopped completely at the time of pupariation ( $t \approx 110$  h, see figures 4.6 and 4.7), whereas the system still grows with a small rate at that time if the deterministic temporal rule is used (figures 4.2 and 4.3). However, we cannot use this difference to exclude one of the two rules because there is no conclusive evidence from experimental studies as to whether or not growth in the wing disc has stopped at the time of pupariation.

Growth is roughly homogeneous in space (see figure 4.7), which can be understood using the argument given in section 4.1.1. However, compared to the deterministic temporal rule, the stochastic temporal rule leads to growth that is less homogeneous. The reduced proliferation in the region directly anterior to the Dpp source is also

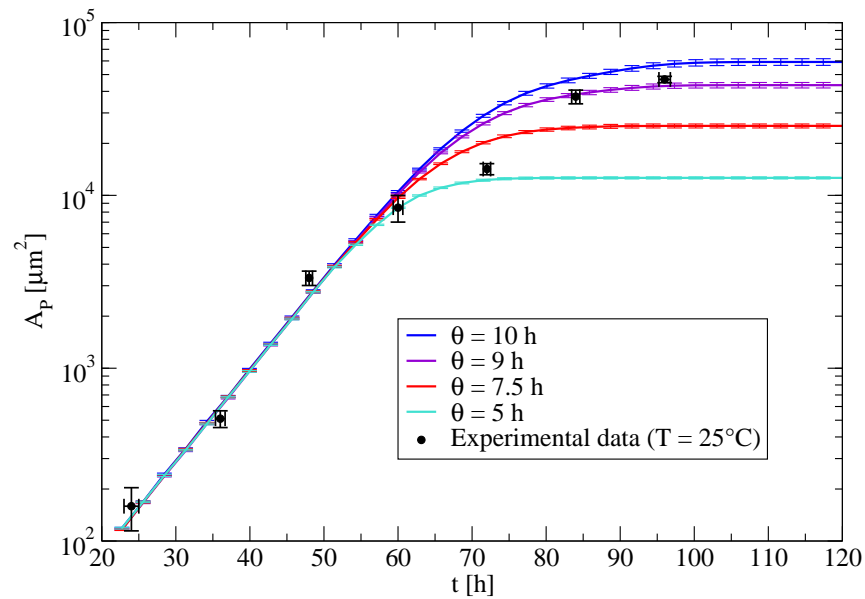


**Figure 4.6.:** Area  $A_P$  of the  $P$  population shown as a function of time for the stochastic temporal rule. The dilution scaling mechanism is used in these simulations.

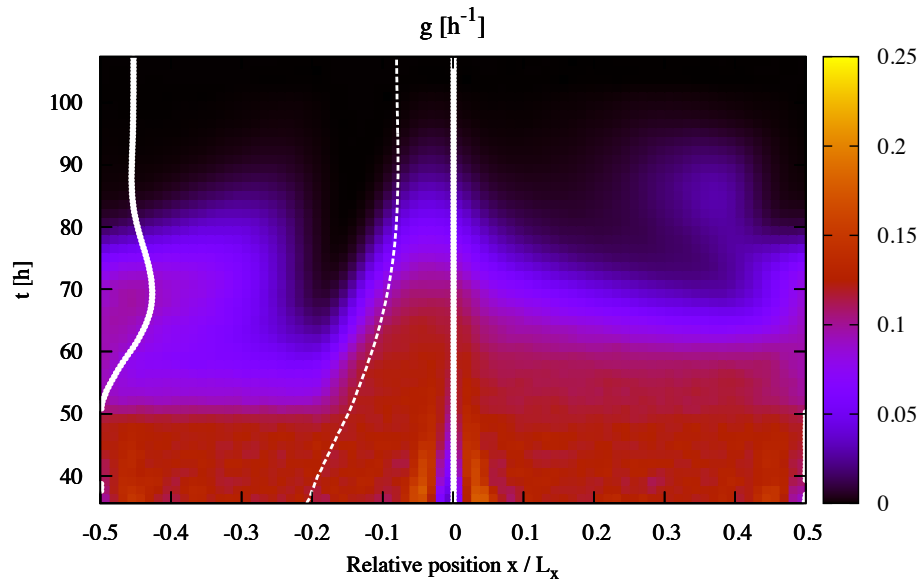


**Figure 4.7.:** Local growth rate  $g$ , generated by the stochastic temporal rule together with the dilution scaling mechanism, shown as a function of time and position using a color code ( $\theta = 9$  h, average over 400 simulations). The average positions of the  $AP$ -interfaces are indicated by solid lines. The  $Dpp$  source is located between the dashed line and the central solid line.

due to the asymmetry caused by the Dpp source (see section 4.1.1). However, for the stochastic temporal rule this growth inhomogeneity is more pronounced, so that it is even visible in figure 4.10D. Additionally, proliferation in the  $P$  population exhibits a weak spatial dependence.

### Expansion-repression Scaling Mechanism

Growth is strongly inhomogeneous in space, and most cell divisions occur in the Dpp source if the expansion-repression scaling mechanism is chosen (see figures 4.8 and 4.10F). Growth is inhomogeneous because the expansion-repression mechanism does not achieve perfect scaling: the proportionality between the Dpp decay length  $\lambda$  and the system size  $L$  is only approximate (see section 4.1.1).

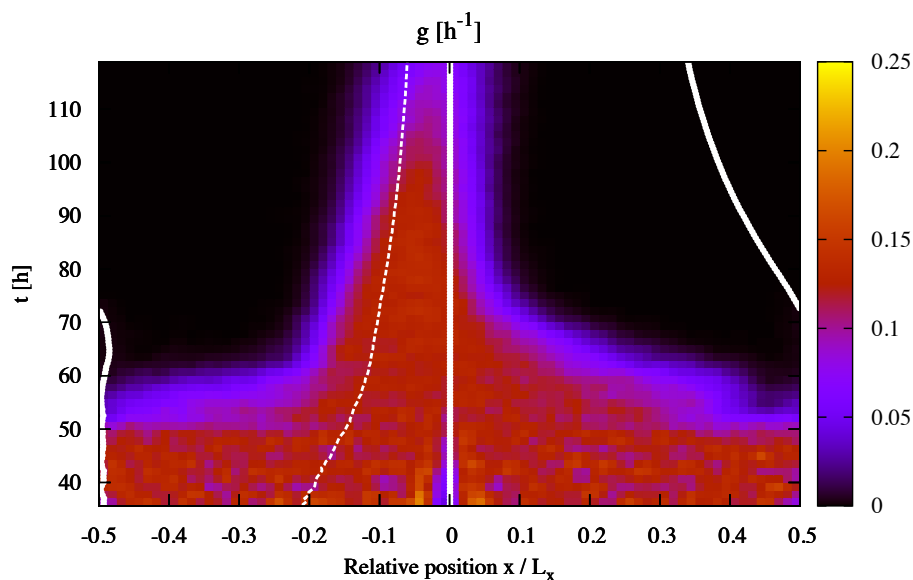


**Figure 4.8.:** Local growth rate  $g$ , generated by the stochastic temporal rule together with the expansion-repression scaling mechanism, shown as a function of time and position using a color code ( $\theta = 100$  h, average over 25 simulations). The average positions of the  $AP$ -interfaces are indicated by solid lines. The Dpp source is located between the dashed line and the central solid line. Most cell divisions occur in the Dpp source (see also figure 4.10F on page 48).

### 4.1.3. Clone Size Distributions

To obtain an experimental criterion to discriminate between the stochastic temporal rule and the deterministic temporal rule, we analyze clone size distributions for both growth rules. Any cell that is selected at an arbitrary point in time gives rise to a clone, which consists of the progeny of the selected cell. The initial cell giving rise to



the clone is denoted founder cell. The number of cells  $N_c(t)$  that constitute a clone is a stochastic quantity because the simulations are stochastic, for example due to the stochastic cell cycle times. The clone size distributions are obtained by determining clone sizes at a fixed time in many simulations. If the founder cells of the clones are selected at the onset of the simulation, the resulting clone size distributions are similar for both growth rules, because the initial phase of the simulation, when all cells divide with the maximum rate, is the same in both cases.

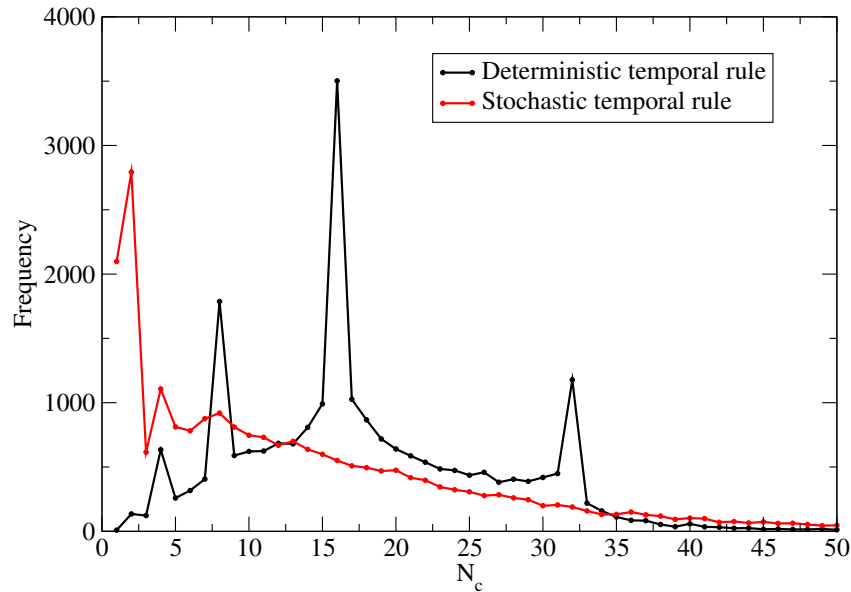


**Figure 4.9.:** Distributions of the clone size  $N_c$  for the deterministic temporal rule and the stochastic temporal rule. The clone size distributions are obtained by determining clone sizes at  $t = 96$  h in many simulations. The founder cells of the clones are selected at  $t = 48$  h. The dilution scaling mechanism and the following growth rule parameters are used here:  $\alpha = 64\%$ ,  $\theta = 9$  h.

If the founder cells are selected at a later time point, after the initial exponential growth phase, the resulting clone size distributions are clearly different for the two growth rules (see figure 4.9). The deterministic temporal rule generates distributions with pronounced peaks at powers of 2 (4, 8, 16, 32), and almost no clones consist of just 1 or 2 cells. The distribution exhibits peaks due to the deterministic nature of the growth rule. If the cells in a clone would divide perfectly synchronized, then the number of cells constituting a clone would double after each cell cycle, and the clone size would always be a power of 2. Due to fluctuations, the synchrony of cell divisions is not perfect in the simulations of the deterministic temporal growth rule. Therefore the peaks at the powers of 2 are broadened. In contrast to the deterministic temporal rule, the stochastic temporal rule generates clone size distributions that have a peak at  $N_c = 2$ , but no pronounced peaks at higher powers of 2.

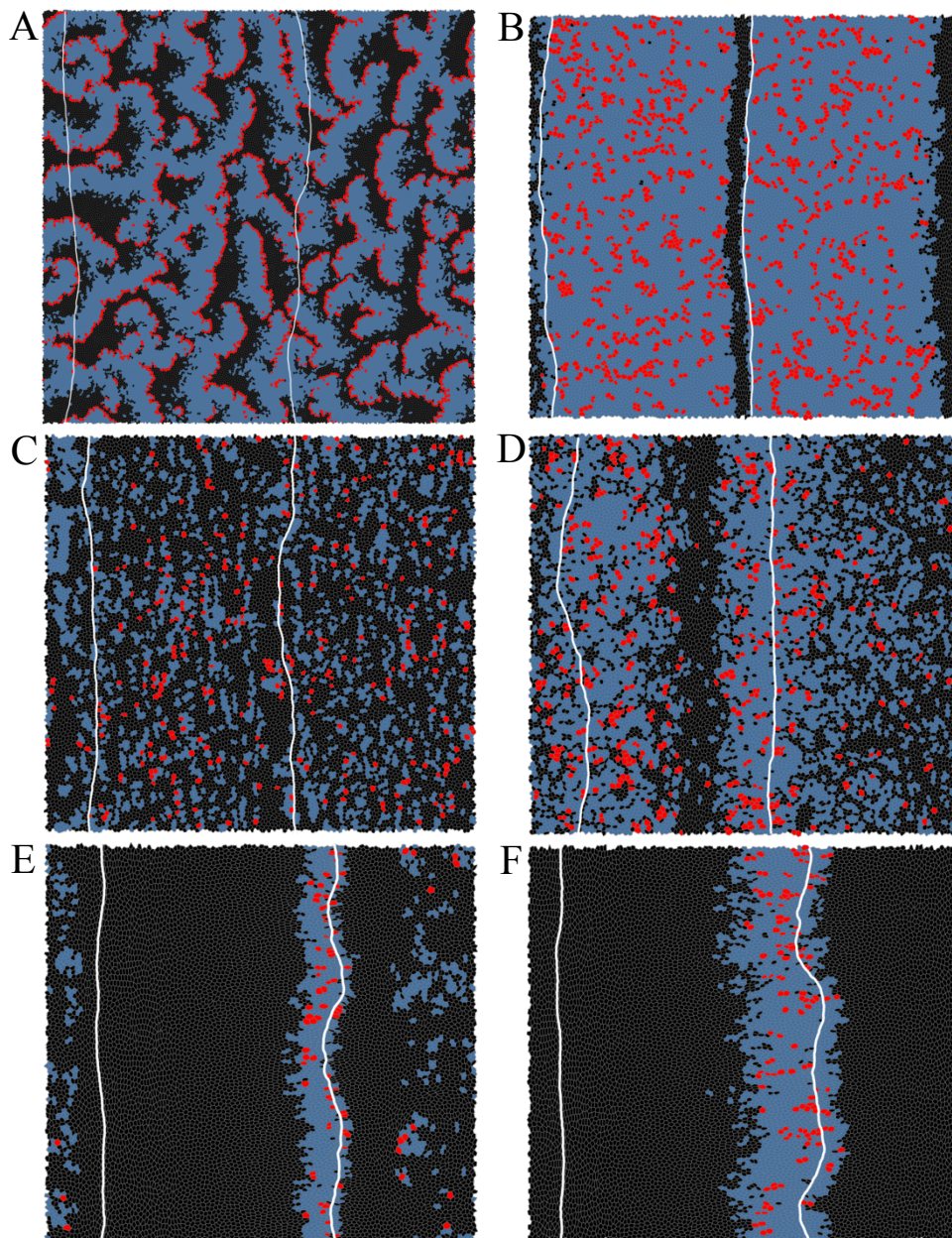


**Figure 4.10.:** Configuration of the cell cycle variables  $\sigma_i$  generated by different growth rules. The state of  $\sigma_i$  is indicated by a color code for each cell. Red:  $M$ , blue:  $I$ , black:  $C$ . The  $AP$ -interfaces are indicated by white lines. (A-D) Dilution scaling mechanism. (E-F) Expansion-repression scaling mechanism. (A) Instantaneous spatial rule ( $t = 95$  h,  $N = 5 \cdot 10^4$ ,  $u_T = 0.6$ ). (B) Time-averaged spatial rule ( $t = 73$  h,  $N = 1.5 \cdot 10^4$ ,  $u_T = 0.375$ ,  $\tau_u = 5$  h). (C) Deterministic temporal rule ( $t = 93$  h,  $N = 1.3 \cdot 10^4$ ,  $\alpha = 64\%$ ). (D) Stochastic temporal rule ( $t = 75$  h,  $N = 1.1 \cdot 10^4$ ,  $\theta = 9$  h). (E) Deterministic temporal rule ( $t = 116$  h,  $N = 1.0 \cdot 10^4$ ,  $\alpha = 5\%$ ). (F) Stochastic temporal rule ( $t = 92$  h,  $N = 1.0 \cdot 10^4$ ,  $\theta = 100$  h).

## 4.2. Spatial Growth Rules

The two spatial growth rules are based on a vectorial measure  $\vec{u}_i$  for the local, relative slope of the Dpp gradient. For each cell  $i$  we define

$$\vec{u}_i = \frac{1}{n_i^{(D)}} \int_0^{2\pi} d\varphi \begin{pmatrix} \cos \varphi \\ \sin \varphi \end{pmatrix} n_{j_i(\varphi)}^{(D)}, \quad (4.7)$$

where the angle  $\varphi$  is measured relative to the cell center (see figure 4.11). The index of the neighbour cell of cell  $i$  that is located in the direction  $\varphi$  is denoted  $j_i(\varphi)$ . For an exponential gradient with decay length  $\lambda \gg \delta$  in a network of hexagonal cells the modulus  $u_i = |\vec{u}_i|$  is given by

$$u_i = \frac{3\delta}{\lambda}, \quad (4.8)$$

where  $\delta$  is the distance between the centers of two neighbouring cells. Because the decay length increases in the growing system due to gradient scaling (see chapter 3), the quantity  $u_i$  decreases with time. The growth behaviour generated by the spatial growth rules is qualitatively the same for the dilution scaling mechanism and the expansion-repression scaling mechanism, because the Dpp gradient is exponential regardless of the scaling mechanism.

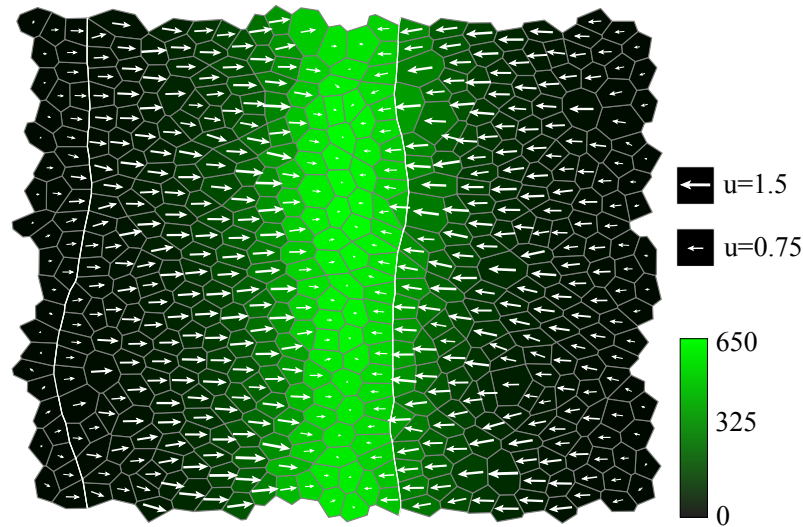


**Figure 4.11.:** Dpp level  $n_i^{(D)}$  (color coded) and vectors  $\vec{u}_i$ , shown for each cell  $i$  in an exponential Dpp gradient scaled with the expansion-repression mechanism ( $t = 43$  h,  $N = 500$  cells). The arrow length is proportional to the modulus  $u_i$ , which goes to zero in the maximum and minimum of the Dpp gradient. The  $AP$ -interfaces are indicated by white lines.

### 4.2.1. Instantaneous Spatial Rule

The instantaneous spatial rule is defined as follows: the transition  $C \rightarrow M$  occurs in cell  $i$  if the local relative slope of the Dpp gradient exceeds a threshold value  $u_T$ ,

$$u_i(t) \geq u_T. \quad (4.9)$$

For both scaling mechanisms the resulting growth behaviour is qualitatively the same: for sufficiently small thresholds  $u_T$  the system stops to grow after an initial exponential growth phase. However, for larger values of  $u_T$  the system becomes unstable as travelling waves of proliferating cells appear (see figure 4.10A on page 48). These waves are caused by local perturbations of the Dpp gradient as a result of cell divisions. A cell division dilutes Dpp molecules which leads to large values of  $u_i$  in the vicinity. Therefore, cell divisions can trigger further cell divisions nearby. This instability generates travelling waves of proliferation that sustain growth. This growth behaviour is not consistent with experimental observations.

### 4.2.2. Time-averaged Spatial Rule

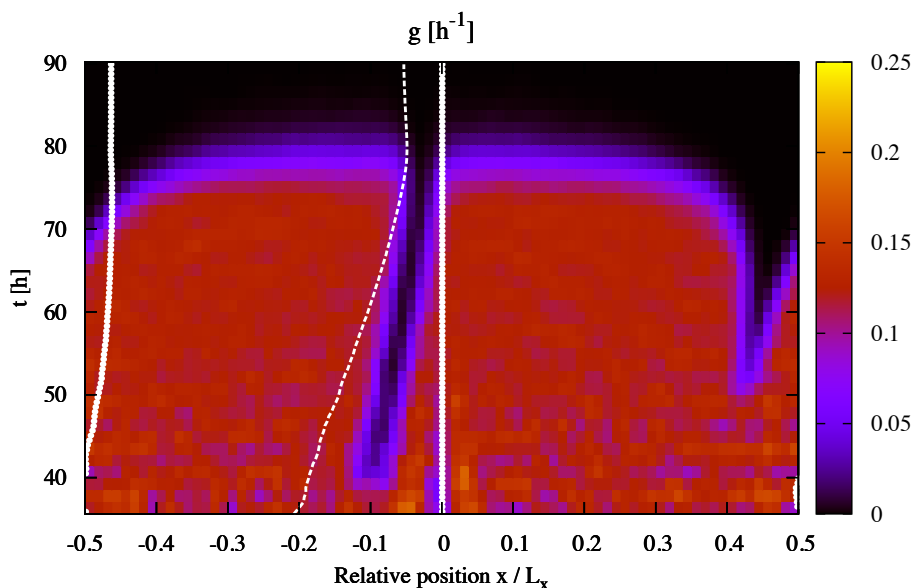


**Figure 4.12.:** Local growth rate  $g$  generated by the time-averaged spatial rule, shown as a function of time and position using a color code (average over 25 simulations,  $u_T = 0.375$ ,  $\tau_u = 5$  h). The average positions of the  $AP$ -interfaces are indicated by white beaded lines. The Dpp source is located between the dashed line and the central beaded line. Here the dilution scaling mechanism is used. The results for the expansion-repression scaling mechanism are qualitatively the same.

Due to the instability of the instantaneous growth rule we have considered an alternative spatial rule that involves time-averaging of the quantity  $u_i(t)$ . According to the time-averaged spatial rule, the transition  $C \rightarrow M$  occurs in cell  $i$  if

$$\bar{u}_i(t) \geq u_T, \quad (4.10)$$

where the time average  $\bar{u}_i(t)$  is defined as

$$\bar{u}_i(t) = \frac{1}{\tau_u} \int_{-\infty}^t dt' u_i(t') \exp\left(-\frac{t-t'}{\tau_u}\right). \quad (4.11)$$

The parameter  $\tau_u$  represents the averaging time. We determine  $\bar{u}_i(t)$  by solving the dynamic equation

$$\frac{d}{dt} \bar{u}_i = \frac{1}{\tau_u} (u_i - \bar{u}_i) \quad (4.12)$$

numerically using a Runge-Kutta method with adaptive stepsize control [31, 136]. When cell  $i$  divides, the two daughter cells inherit the value of  $\bar{u}_i$ .

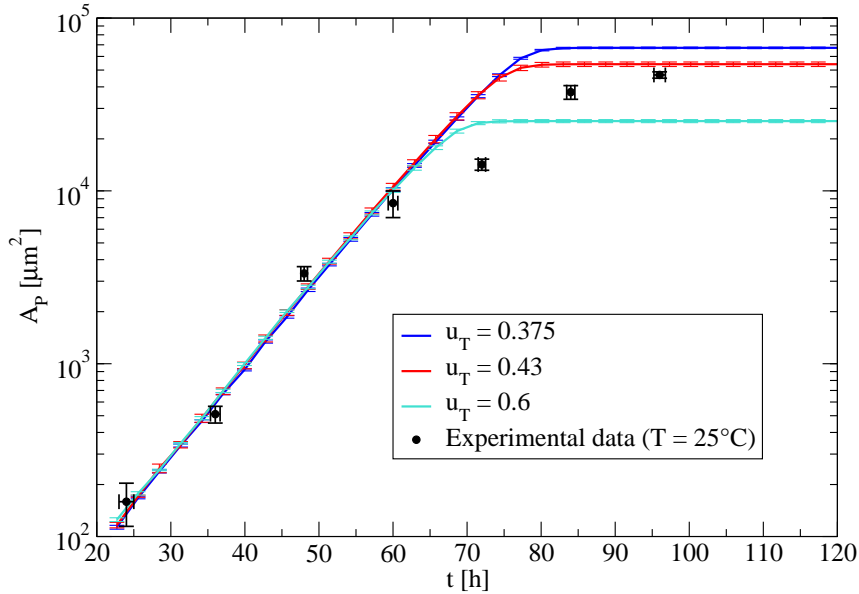


**Figure 4.13.:** Area  $A_P$  of the  $P$  population shown as a function of time for the time-averaged spatial rule ( $\tau_u = 5$  h). The dilution scaling mechanism is used here. The results for the expansion-repression scaling mechanism are qualitatively the same.

The effect of fluctuations caused by cell divisions is damped by considering the time-average in the growth rule, and the resulting growth behaviour is qualitatively the same for both scaling mechanisms. No waves of proliferating cells are observed for sufficiently long averaging times  $\tau_u \gtrsim 1$  h. Instead, the system grows exponentially until growth stops rather abruptly, due to the threshold-character of the

growth rule (see figure 4.13). During the growth phase, there is a pronounced inhomogeneity in the spatial pattern of proliferation: in the maximum and minimum of the Dpp gradient where the slope goes to zero, there is almost no proliferation at all (see figure 4.12 and 4.10B). Such a striking spatial growth inhomogeneity has not been reported in experimental studies of the wing disc, which suggests that the time-averaged spatial rule is inappropriate to describe growth control in that system.

Parameter	Meaning	Value
$\Gamma/KA^{(0)}$	Dimensionless cell perimeter stiffness	0.04
$\Lambda/K(A^{(0)})^{3/2}$	Dimensionless cell bond tension	-0.12
$A^{(0)}$	Preferred cell area	$6.83 \mu\text{m}^2$
$\kappa$	$AP$ -interface tension factor	-5
$N_0$	Initial number of cells	36
$N_g$	Cell number threshold for growth rules	360
$\bar{\tau}_M$	Mean residence time in cell cycle state $M$	0.75 h
$\bar{\tau}_I$	Mean residence time in cell cycle state $I$	5 h
$\xi$	Gamma distribution shape parameter	25
$p^{(H)}$	Hh production rate	$10^4 \text{h}^{-1}$
$k^{(H)}$	Hh degradation rate in $A$ cells	$36 \text{h}^{-1}$
$d^{(H)}$	Parameter describing Hh diffusion	$130 \mu\text{m}^{-1}\text{h}^{-1}$
$D^{(H)}$	Corresponding Hh diffusion coefficient	$0.5 \mu\text{m}^2\text{s}^{-1}$
$n_T^{(H)}$	Hh threshold for Dpp production	250
$p^{(D)}$	Dpp production rate	$10^4 \text{h}^{-1}$
$d^{(D)}$	Parameter describing Dpp diffusion	$26 \mu\text{m}^{-1}\text{h}^{-1}$
$D^{(D)}$	Corresponding Dpp diffusion coefficient	$0.1 \mu\text{m}^2\text{s}^{-1}$
$t_0$	Starting time of the simulation	21.3 h
$b_1$	Parameter describing the Dpp source	$7.1 \mu\text{m}$
$b_2$	Parameter describing the Dpp source	$6.4 \mu\text{m}$
$\alpha$	Parameter of the deterministic growth rule	64%
$\theta$	Parameter of the stochastic growth rule	9 h
$u_T$	Parameter of the spatial growth rules	0.375
$\tau_u$	Parameter of the time-averaged growth rule	5 h

**Table 4.1.:** Parameter values used in this chapter if not stated otherwise. For the mechanical parameter values given here, T2 processes do not occur, and the average cell area is given by  $A_c \approx 0.8A^{(0)} \approx 5.5 \mu\text{m}^2$ . The simulations are terminated if  $N > 5 \cdot 10^4$ , or if the growth rate satisfies  $g < 4 \cdot 10^{-3} \text{h}^{-1}$ , which corresponds to a cell cycle time of more than one week.

Parameter	Meaning	Value
$n_0^{(E)}$	Initial number of expander molecules per cell	0
$n_T^{(D)}$	Dpp threshold for expander production	25
$\omega$	Rate constant	$10^4 \text{ h}^{-1}$
$n_C^{(E)}$	Cutoff parameter	30
$h$	Hill coefficient	1
$d^{(E)}$	Parameter describing expander diffusion	$2600 \mu\text{m}^{-1}\text{h}^{-1}$
$D^{(E)}$	Corresponding expander diffusion coefficient	$10 \mu\text{m}^2\text{s}^{-1}$
$p^{(E)}$	Expander production rate	$10^4 \text{ h}^{-1}$

**Table 4.2.:** Parameter values used for the expansion-repression feedback mechanism in this chapter if not stated otherwise.

Parameter	Meaning	Value
$n_0^{(E)}$	Initial number of expander molecules per cell	$3 \cdot 10^4$
$\gamma$	Rate constant	$10^{-2} \text{ h}^{-1}$
$d^{(E)}$	Parameter describing expander diffusion	$260 \mu\text{m}^{-1}\text{h}^{-1}$
$D^{(E)}$	Corresponding expander diffusion coefficient	$1 \mu\text{m}^2\text{s}^{-1}$

**Table 4.3.:** Parameter values used for the expander dilution mechanism in this chapter if not stated otherwise.

**Summary** In this chapter we explored how growth of developing tissues can be controlled in a self-organized way. For that purpose we introduced cellular growth rules that govern cell divisions based on the local Dpp level. We formulated two spatial growth rules that are based on the slope of the Dpp gradient, and two temporal growth rules that depend on relative temporal changes of the cellular Dpp concentration. Both spatial growth rules lead to a growth behaviour that is inconsistent with experimental studies of the wing imaginal disc. The instantaneous spatial rule leads to a highly unstable behaviour. Growth cannot be reliably controlled with this rule due to travelling waves of cell divisions. The time-averaged spatial rule does not exhibit this instability for sufficiently long averaging times. However, this rule leads to a striking spatial growth inhomogeneity: in the maximum and minimum of the Dpp gradient almost no cell divisions occur. Furthermore, the shape of the growth curve does not fit the experimental data well. The growth behaviour resulting from the temporal growth rules depends on the scaling mechanism. If the expansion-repression mechanism is used, both temporal growth rules generate strongly inhomogeneous growth: most cell divisions occur inside the Dpp source. However, both temporal rules lead to a growth behaviour that is consistent with experimental observations if the expander dilution mechanism is used to scale the Dpp gradient. Then, growth is largely homogeneous and the growth curves agree well with experimental data. The deterministic temporal rule and the stochastic temporal rule can be distinguished by determining the distribution of clone sizes. In contrast to the stochastic rule, the deterministic rule generates several pronounced peaks in these distributions.



# 5. Continuum Description of Self-organized Growth

In this chapter we develop continuum descriptions of the systems studied in the previous chapter to gain a better understanding of the vertex model simulations. We only consider mean values and neglect fluctuations and cell death. Furthermore we only consider the dilution scaling mechanism because only this mechanism leads to largely homogeneous growth in case of the temporal growth rules. For simplicity, we describe the Dpp gradient by a single exponential function. In this approximation, the relative slope of the Dpp gradient, on which the spatial growth rules depend, is inversely proportional to the Dpp decay length and thus position-independent (see section 4.2 on page 49). Furthermore, we neglect any spatial growth inhomogeneities. In this case the relative temporal derivative of the Dpp concentration  $c_i$  perceived by cell  $i$ , on which the temporal growth rules depend, is also position-independent (see section 4.1.1 on page 40),

$$\frac{\dot{c}_i}{c_i} = \frac{\dot{c}}{c}. \quad (5.1)$$

Here,  $c$  is the Dpp gradient amplitude. Because the quantities that are relevant for the growth rules are position-independent, we can neglect the spatial extension of the system and describe it by ordinary differential equations.

## 5.1. Continuum Description of the Dpp Dynamics

Due to the dilution scaling mechanism, the Dpp degradation rate  $k$  is inversely proportional to the system size  $A$ , which is a continuous quantity in this chapter. The degradation rate thus obeys

$$\dot{k} = -gk, \quad (5.2)$$

where  $g = \dot{A}/A$  is the growth rate. In our continuum description we take into account that the Dpp gradient is not in a steady state as long as the system grows. During the growth process, the Dpp gradient relaxes towards the steady state. The timescale of relaxation is given by  $k^{-1}$ . One can understand this relationship by realizing that the lifetime of a Dpp molecule is given by  $k^{-1}$ . Furthermore, the diffusion time of a Dpp molecule for travelling a distance corresponding to the decay length  $\hat{\lambda} = \sqrt{D/k}$  is of the order  $k^{-1}$ . Another way of showing that  $k^{-1}$  is the relaxation time of the Dpp gradient is to solve the time-dependent diffusion equation for the

Dpp concentration  $c(x, t)$ . For constant parameters and a  $\delta$  shaped Dpp source that is concentrated at  $x = 0$ , the solution obeys (see appendix G.2.1),

$$c(x, t) \sim e^{-\frac{|x|}{\lambda}} \left( 1 - \frac{\exp(-kt) \exp(\frac{|x|}{\lambda})}{\sqrt{\pi kt}} \right) \quad \text{if } \sqrt{kt} \gg 1 \text{ and } \sqrt{kt} \gg \frac{|x|}{\lambda}, \quad (5.3)$$

which shows that the concentration profile relaxes exponentially with time constant  $k^{-1}$  towards the steady state. In this chapter we therefore use the approximation that the Dpp gradient amplitude  $c$ , which is defined as the concentration at the  $AP$ -interface, and the decay length  $\lambda$  relax towards the steady state values with relaxation time  $k^{-1}$ ,

$$\dot{c} = k(\hat{c} - c), \quad (5.4)$$

$$\dot{\lambda} = k(\hat{\lambda} - \lambda). \quad (5.5)$$

Here,  $\hat{c}$  is the steady state value of the gradient amplitude, and  $\hat{\lambda}$  is the steady state value of the decay length. These quantities are given by (see appendix G.2.2)

$$\hat{c} = \frac{\nu}{2k}(1 - e^{-w/\hat{\lambda}}), \quad (5.6)$$

$$\hat{\lambda} = \sqrt{D/k}, \quad (5.7)$$

where  $\nu$  is the production rate per unit area,  $k$  is the degradation rate,  $w$  is the width of the Dpp source, and  $D$  is the diffusion coefficient. The production rate and the diffusion coefficient are constant parameters, but the degradation rate and the source width are time-dependent. The width of the Dpp source  $w$  grows logarithmically with the width  $L$  of the system (see appendix I). Because the system grows isotropically,  $A \sim L^2$ , the temporal increase of  $w$  can be described by the dynamic equation

$$\dot{w} = \eta g, \quad (5.8)$$

where  $\eta \geq 0$  is a parameter that determines how fast the Dpp source widens.

## 5.2. Continuum Description of the Growth Dynamics

At early times, all growth rules generate exponential growth with the maximum growth rate  $\hat{g}$ , which can be determined using equation (2.10). Subsequently, the growth rate  $g$  decreases. To complete the continuum description of self-organized growth, we need to add an explicit expression for the growth rate, which depends on the growth rule. In general, the system size is determined by the growth rate according to

$$A(t) = A_0 \exp \left( \int_{t_0}^t dt' g(t') \right), \quad (5.9)$$

where  $A_0$  is the system size at the initial time  $t_0$ . Because  $k(t)$  obeys equation (5.2), the system size can also be determined using the equation

$$A(t) = \frac{A_0 k_0}{k(t)}. \quad (5.10)$$

Here,  $k_0$  is the initial degradation rate.

### 5.2.1. Stochastic Temporal Growth Rule

The stochastic growth rule, which is introduced in section 4.1.2, imposes that there are two different kinds of cells: proliferating cells (type A) and non-proliferating cells (type B). The growth rate of the proliferating cells is given by  $\hat{g}$ , and the mean growth rate of the system is given by

$$g = \hat{g}\phi, \quad (5.11)$$

where  $\phi$  is the expectation value of the relative fraction of proliferating cells,

$$\phi = \frac{N_A}{N_A + N_B}. \quad (5.12)$$

The expectation values of the number of proliferating and non-proliferating cells are denoted  $N_A$  and  $N_B$ . According to the stochastic rule (4.6), a new cell generated by a cell division is a proliferating cell with probability  $\varrho$ . This probability depends

Type of cells generated by a cell division	Probability
Two proliferating cells	$\varrho^2$
Two non-proliferating cells	$(1 - \varrho)^2$
One proliferating and one non-proliferating cell	$2\varrho(1 - \varrho)$

**Table 5.1.:** Probabilities of the three different kinds of cell divisions that are possible according to the stochastic growth rule.

on the average relative time derivative of the Dpp level in the precursor cell. Here, we approximate  $\varrho$  by

$$\varrho = \begin{cases} 0 & \text{if } \Delta \leq 0, \\ \Delta & \text{if } 0 < \Delta < 1, \\ 1 & \text{if } 1 \leq \Delta, \end{cases} \quad \Delta = \bar{\theta}k(\hat{c} - c)/c, \quad (5.13)$$

where we have used equation (5.4) to substitute  $\dot{c}$ , and where  $\bar{\theta}$  is an effective parameter corresponding to the parameter  $\theta$  in equation (4.6). The expectation values  $N_A$  and  $N_B$  obey

$$\dot{N}_A = \hat{g}(2\varrho - 1)N_A, \quad (5.14)$$

$$\dot{N}_B = \hat{g}(2 - 2\varrho)N_A, \quad (5.15)$$

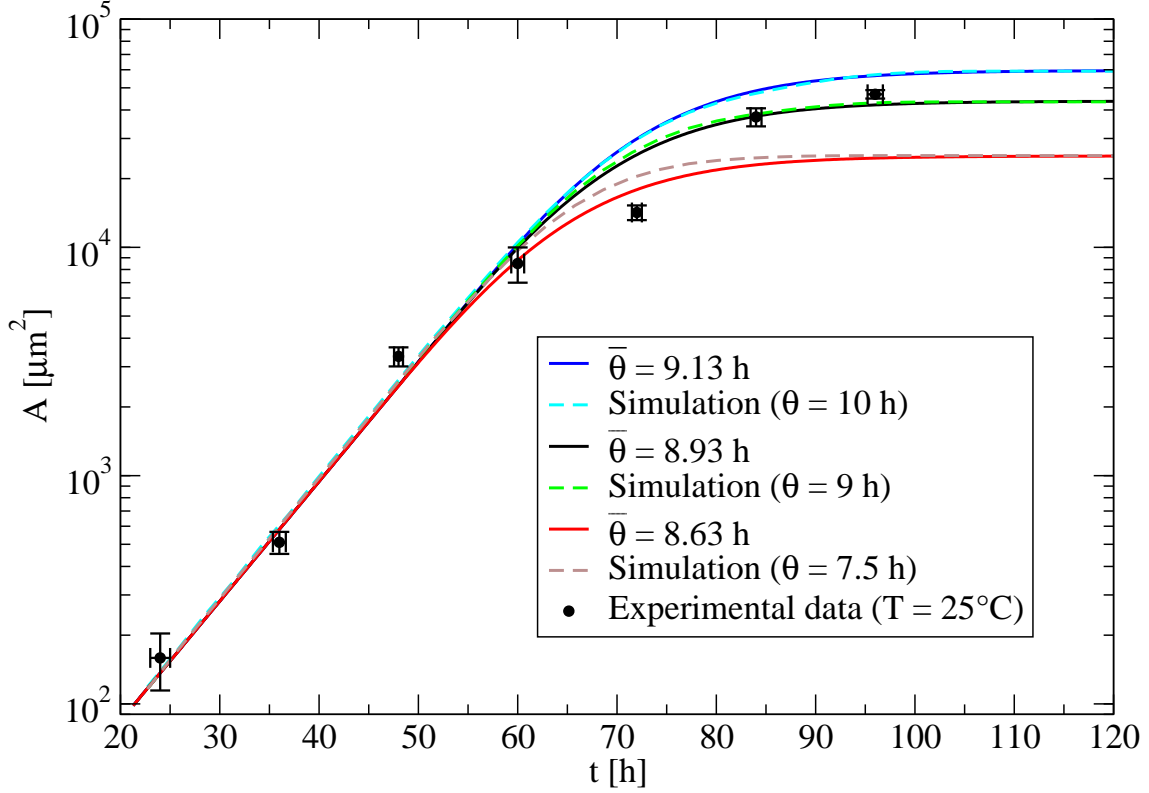


**Figure 5.1.:** System size  $A$  shown as a function of time. The solid lines are obtained by solving the nonlinear system (5.17) numerically using the initial conditions and parameter values given in table 5.2 on page 69. The system size is determined using equation (5.10). The dashed lines indicate the area of the  $P$  population obtained by vertex model simulations of the stochastic rule, using the parameter values given in the tables 4.1 and 4.3. Because the continuum approximation is an effective description, the growth rule parameter has to be chosen differently than in the simulations to obtain the same final size  $A^*$ . There is good agreement between the simulation and the continuum approximation with respect to the shape of the growth curve. The experimental data measured by Ortrud Wartlick shows the area of the posterior compartment. The Dpp production rate  $\nu$  does not influence the growth curve. The dependence of the final size  $A^*$  on the growth rule parameter  $\bar{\theta}$  is shown in figure 5.2. The dependence of  $A^*$  on the other parameters is shown in the figures 5.9, 5.10, 5.11, and 5.12.

from which the following equation describing the dynamics of  $\phi$  follows,

$$\dot{\phi} = \hat{g}\phi(2\rho - 1 - \phi). \quad (5.16)$$

Thus we obtain a four-dimensional, nonlinear dynamical system,

$$\frac{d}{dt} \begin{pmatrix} c \\ k \\ w \\ \phi \end{pmatrix} = \begin{pmatrix} k(\hat{c} - c) \\ -\hat{g}\phi k \\ \eta\hat{g}\phi \\ \hat{g}\phi(2\rho - 1 - \phi) \end{pmatrix}. \quad (5.17)$$

In figure 5.1 we show growth curves obtained by solving this system numerically. The system has infinitely many fixed points  $\mathbf{x}^*$ , which we parametrize using the

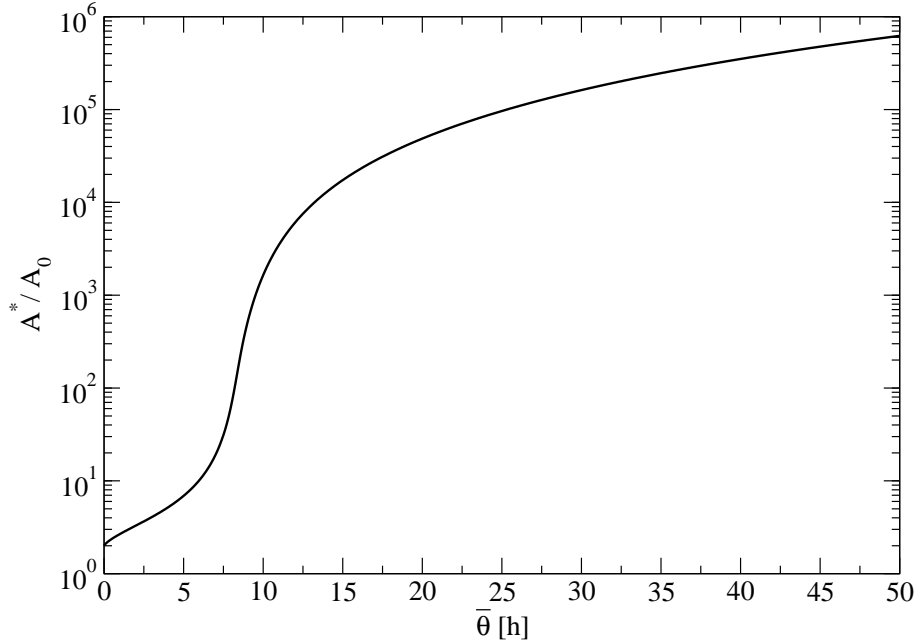


**Figure 5.2.:** Ratio of the final size  $A^*$  to the initial size  $A_0$  for the stochastic growth rule as a function of the parameter  $\bar{\theta}$ .

degradation rate  $k^*$  and the Dpp source width  $w^*$  at the fixed point. Both  $k^*$  and  $w^*$  are larger than zero for physical reasons. The Dpp gradient amplitude  $c^*$  at the fixed point is determined by the equation

$$c^* = \frac{\nu}{2k^*} (1 - e^{-w^* \sqrt{k^*/D}}). \quad (5.18)$$

Thus the fixed points have the form

$$\mathbf{x}^* = \begin{pmatrix} c^* \\ k^* \\ w^* \\ 0 \end{pmatrix}. \quad (5.19)$$

The Jacobian matrix, evaluated at the fixed point, reads

$$\mathbf{J}^* = \begin{pmatrix} -k^* & -c^* + \frac{\nu w^*}{4\sqrt{Dk^*}} e^{-w^* \sqrt{k^*/D}} & \frac{\nu \sqrt{k^*/D}}{2} e^{-w^* \sqrt{k^*/D}} & 0 \\ 0 & 0 & 0 & -k^* \hat{g} \\ 0 & 0 & 0 & \eta \hat{g} \\ 0 & 0 & 0 & -\hat{g} \end{pmatrix}. \quad (5.20)$$

The eigenvalues of this matrix are given by  $\lambda_1 = -\hat{g}$ ,  $\lambda_2 = -k^*$ , and  $\lambda_3 = 0$ . The stability of the nonlinear system cannot be determined using linear stability analysis because one eigenvalue is zero. However we can conclude that the linearized system is always stable because the eigenvalue  $\lambda_3 = 0$  has double algebraic and geometric multiplicity. The multiplicity of the zero eigenvalue is two because the set of fixed points is a two-dimensional manifold.

### 5.2.2. Deterministic Temporal Growth Rule

According to the deterministic temporal growth rule introduced in section (4.1.1), a cell division is triggered when the relative increase of the cellular Dpp level reaches a threshold. To obtain a continuum approximation, we rewrite this rule in the following form,

$$\frac{\Delta c}{c} \geq \bar{\alpha}, \quad (5.21)$$

where  $\Delta c$  is the increase in the Dpp amplitude  $c$  during the cell cycle time  $\tau$ , and  $\bar{\alpha} > 0$  is an effective parameter corresponding to the parameter  $\alpha$  in equation (4.1). We divide this inequality by  $\tau$  and use the approximations  $\dot{c} \approx \frac{\Delta c}{\tau}$  and  $g \approx \frac{\ln 2}{\tau}$ , which yields

$$g \leq \frac{\ln 2}{\bar{\alpha}} \frac{\dot{c}}{c}. \quad (5.22)$$

The approximation  $g \approx \frac{\ln 2}{\tau}$  is good as long as the cell cycle time  $\tau$  is small compared to the timescale on which  $\tau$  changes. The growth rate  $g$  is limited by the maximum value  $\hat{g}$ . Therefore the equal sign in the inequality (5.22) applies if the right-hand side is smaller or equal to  $\hat{g}$ . In that case, the gradient amplitude  $c$  and the system size  $A$  are related by the following power law (see figure 5.3),

$$c \sim A^\beta, \quad \beta = \frac{\bar{\alpha}}{\ln 2}. \quad (5.23)$$

Using the inequality (5.22), equation (5.4), and taking into account that  $\hat{g}$  is an upper bound for  $g$ , we get

$$g = \begin{cases} \frac{\ln 2}{\bar{\alpha}} k(\hat{c} - c)/c & \text{if } \frac{\ln 2}{\bar{\alpha}} k(\hat{c} - c)/c < \hat{g}, \\ \hat{g} & \text{otherwise.} \end{cases} \quad (5.24)$$

We finally obtain a three-dimensional, nonlinear dynamical system,

$$\frac{d}{dt} \begin{pmatrix} c \\ k \\ w \end{pmatrix} = \begin{pmatrix} k(\hat{c} - c) \\ -gk \\ \eta g \end{pmatrix}. \quad (5.25)$$

In figure 5.5 on page 63 we show growth curves obtained by solving this system numerically. The system has infinitely many fixed points  $\mathbf{x}^*$ , which we parametrize using the degradation rate  $k^*$  and the Dpp source width  $w^*$  at the fixed point,

$$\mathbf{x}^* = \begin{pmatrix} c^* \\ k^* \\ w^* \end{pmatrix}. \quad (5.26)$$

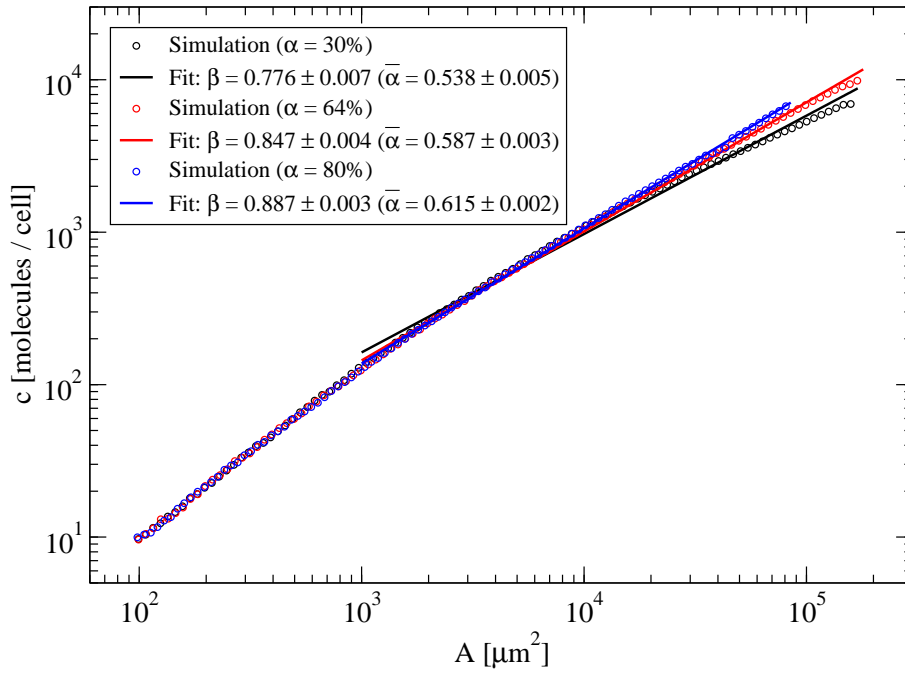


**Figure 5.3.:** Here, the Dpp gradient amplitude is shown as a function of the area of the  $P$  population. The data is averaged over 25 vertex model simulations in each case. The solid lines are fits of the power law  $c \sim A^\beta$ , see equation (5.23). Data points that satisfy  $A < 10^3 \mu\text{m}^2$  are excluded from the fit because small systems grow exponentially, independent of the Dpp dynamics. Using the fit results and the relation  $\bar{\alpha} = \beta \ln 2$ , we estimate values for the parameter  $\bar{\alpha}$  of the continuum approximation (see figure 5.5).

Both  $k^*$  and  $w^*$  are larger than zero for physical reasons. The Dpp gradient amplitude  $c^*$  at the fixed point is determined by equation (5.18). The Jacobian

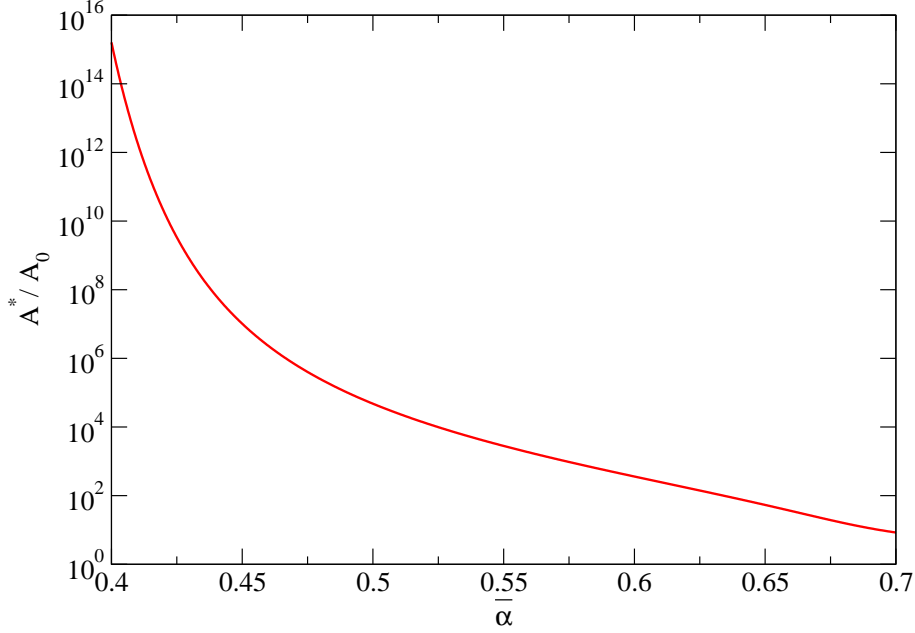


**Figure 5.4.:** Ratio of the final size  $A^*$  to the initial size  $A_0$  for the deterministic growth rule as a function of the parameter  $\bar{\alpha}$ .

matrix, evaluated at the fixed point, reads

$$\mathbf{J}^* = \begin{pmatrix} -k^* & -c^* + \frac{\nu w^*}{4\sqrt{Dk^*}} e^{-w^*\sqrt{k^*/D}} & \frac{\nu\sqrt{k^*/D}}{2} e^{-w^*\sqrt{k^*/D}} \\ \frac{(k^*)^2 \ln 2}{\bar{\alpha} c^*} & \frac{k^* \ln 2}{\bar{\alpha}} - \frac{\nu w^* \sqrt{k^*/D} \ln 2}{4\bar{\alpha} c^*} e^{-w^*\sqrt{k^*/D}} & -\frac{\nu k^* \sqrt{k^*/D} \ln 2}{2\bar{\alpha} c^*} e^{-w^*\sqrt{k^*/D}} \\ -\frac{\eta k^* \ln 2}{\bar{\alpha} c^*} & -\frac{\eta \ln 2}{\bar{\alpha}} + \frac{\nu \eta w^* \ln 2}{4\bar{\alpha} c^* \sqrt{k^* D}} e^{-w^*\sqrt{k^*/D}} & \frac{\nu \eta \sqrt{k^*/D} \ln 2}{2\bar{\alpha} c^*} e^{-w^*\sqrt{k^*/D}} \end{pmatrix}. \quad (5.27)$$

It has the eigenvalues  $\lambda_1 = k^* \left( \frac{\ln 2}{\bar{\alpha}} - 1 \right) - \frac{\nu \sqrt{k^*/D} (w^* - 2\eta) \ln 2}{4\bar{\alpha} c^*} e^{-w^*\sqrt{k^*/D}}$  and  $\lambda_2 = 0$ , which has double algebraic and geometric multiplicity. The fixed point is unstable if  $\lambda_1 > 0$ , which is equivalent to the following inequality,

$$\bar{\alpha} < \ln 2 \left( 1 - \frac{(w^* - 2\eta) \sqrt{k^*/D}}{2(e^{w^*\sqrt{k^*/D}} - 1)} \right). \quad (5.28)$$

The temporal increase of the Dpp source width, which is taken into account via the parameter  $\eta$ , has a destabilizing effect on the system because it increases the eigenvalue  $\lambda_1$ . In the limiting case  $\eta = 0$ , in which  $\lambda_1$  assumes its minimal value, the inequality (5.28) simplifies to

$$\bar{\alpha} < F \left( w^* \sqrt{k^*/D} \right) \ln 2, \quad (5.29)$$

$$F(x) = 1 - \frac{x}{2(e^x - 1)}. \quad (5.30)$$



The function  $F$  is strictly increasing on the interval  $(0, \infty)$  and behaves as follows,

$$\lim_{x \rightarrow 0} F(x) = \frac{1}{2}, \quad \lim_{x \rightarrow \infty} F(x) = 1. \quad (5.31)$$

From this it follows that all fixed points are unstable if  $\bar{\alpha} < \frac{\ln 2}{2} \approx 0.35$ , which leads to unbounded growth.

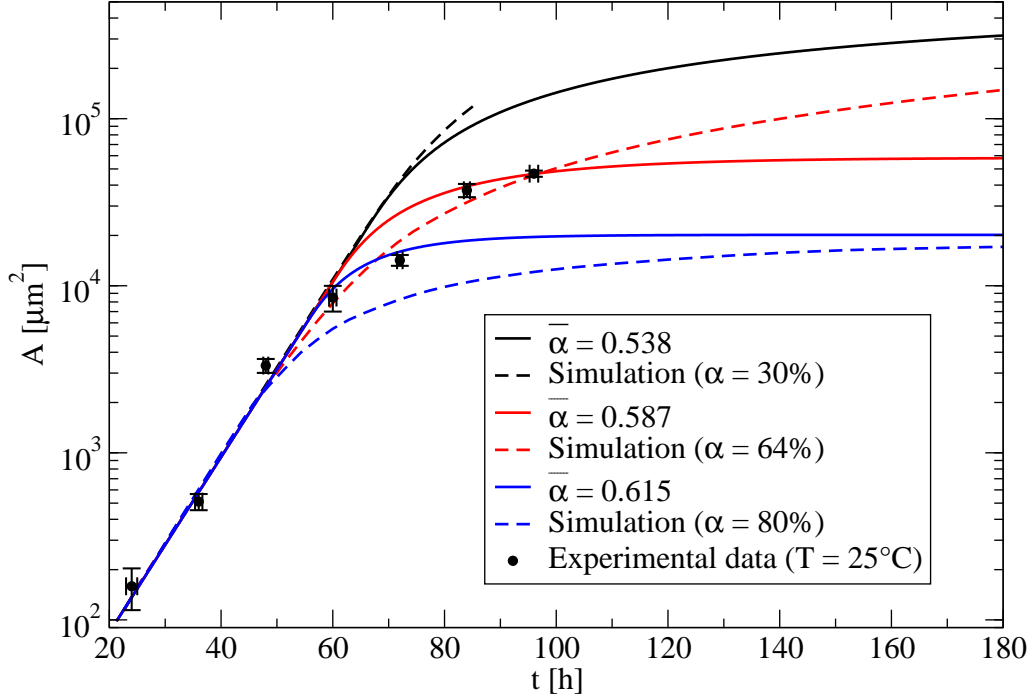


**Figure 5.5.:** System size  $A$  shown as a function of time. The solid lines are obtained by solving the nonlinear system (5.25) numerically using the initial conditions and parameter values given in table 5.2 on page 69. The system size is determined using equation (5.10). The values used for the parameter  $\bar{\alpha}$  are determined by power law fits to simulation results (see figure 5.3). The dashed lines indicate the area of the  $P$  population obtained by vertex model simulations of the deterministic temporal rule, using the parameter values given in the tables 4.1 and 4.3. If growth does not stop, the simulation has to be aborted at some point. Therefore the dashed black line ends at  $t = 85$  h. The agreement between simulation and continuum approximation is less good than in the case of the stochastic temporal rule, because here the continuum theory has been derived using the approximation  $g \approx \frac{\ln 2}{\tau}$ . This approximation is only valid as long as the cell cycle time  $\tau$  is small compared to the timescale on which  $\tau$  changes. The experimental data measured by Ortrud Wartlick shows the area of the posterior compartment. The Dpp production rate  $\nu$  does not influence the growth curve. The dependence of the final size  $A^*$  on the growth rule parameter  $\bar{\alpha}$  is shown in figure 5.4. The dependence of  $A^*$  on the other parameters is shown in the figures 5.9, 5.10, 5.11, and 5.12.

### 5.2.3. Spatial Growth Rules

According to the time-averaged spatial growth rule introduced in section (4.2.2), cell divisions stop when the time-averaged relative slope of the Dpp gradient falls below a threshold. We approximate this rule in the following way,

$$g = \begin{cases} \hat{g} & \text{if } \bar{\lambda} \leq \bar{\lambda}_T, \\ 0 & \text{otherwise.} \end{cases} \quad (5.32)$$

Here,  $\bar{\lambda}_T > 0$  is a parameter and  $\bar{\lambda}$  is the time-average of  $\lambda$ , which obeys

$$\frac{d}{dt}\bar{\lambda} = \tau_\lambda^{-1}(\lambda - \bar{\lambda}). \quad (5.33)$$

The averaging time is denoted  $\tau_\lambda$ . The limit  $\tau_\lambda \rightarrow 0$  corresponds to the instantaneous spatial growth rule introduced in section (4.2.1). We thus obtain a three-dimensional, nonlinear dynamical system,

$$\frac{d}{dt} \begin{pmatrix} k \\ \lambda \\ \bar{\lambda} \end{pmatrix} = \begin{pmatrix} -gk \\ k(\hat{\lambda} - \lambda) \\ \tau_\lambda^{-1}(\lambda - \bar{\lambda}) \end{pmatrix}. \quad (5.34)$$

In figure 5.6 we show growth curves obtained by solving this system numerically. The system has infinitely many fixed points  $\mathbf{x}^*$ , which we parametrize using the Dpp degradation rate  $k^*$  at the fixed point,

$$\mathbf{x}^* = \begin{pmatrix} k^* \\ \sqrt{D/k^*} \\ \sqrt{D/k^*} \end{pmatrix}. \quad (5.35)$$

Due to physical reasons,  $k^*$  must be larger than zero. In order that  $x^*$  is a fixed point,  $k^*$  must additionally fulfill  $k^* < D(\bar{\lambda}_T)^{-2}$ . The Jacobian matrix, evaluated at the fixed point, reads

$$\mathbf{J}^* = \begin{pmatrix} 0 & 0 & 0 \\ -\frac{\sqrt{D/k^*}}{2} & -k^* & 0 \\ 0 & \tau_\lambda^{-1} & -\tau_\lambda^{-1} \end{pmatrix}. \quad (5.36)$$

It has the eigenvalues  $\lambda_1 = -k^*$ ,  $\lambda_2 = -\tau_\lambda^{-1}$ , and  $\lambda_3 = 0$ . Due to the zero eigenvalue, the stability of the nonlinear system cannot be determined using linear stability analysis. However we can conclude that the linearized system is always stable.

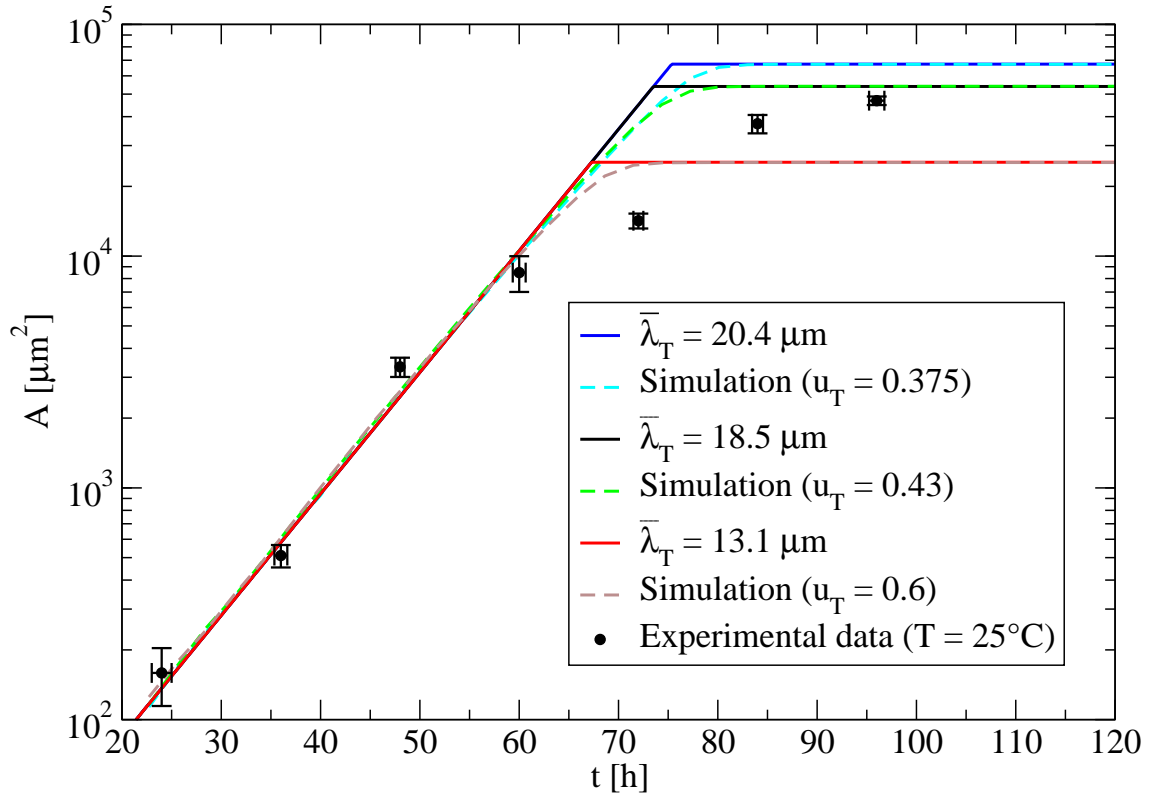


**Figure 5.6.:** System size  $A$  shown as a function of time. The solid lines are obtained by solving the nonlinear system (5.34) numerically using the initial conditions and parameter values given in table 5.2 on page 69. The system size is determined using equation (5.10). The dashed lines indicate the area of the  $P$  population obtained by vertex model simulations of the time-averaged spatial rule, using the parameter values given in the tables 4.1 and 4.3. The experimental data measured by Ortrud Wartlick shows the area of the posterior compartment. The dependence of the final size  $A^*$  on the growth rule parameters  $\bar{\lambda}_T$  and  $\tau_\lambda$  is shown in the figures 5.7 and 5.8. The dependence of  $A^*$  on the other parameters is shown in the figures 5.9, 5.10, and 5.11.

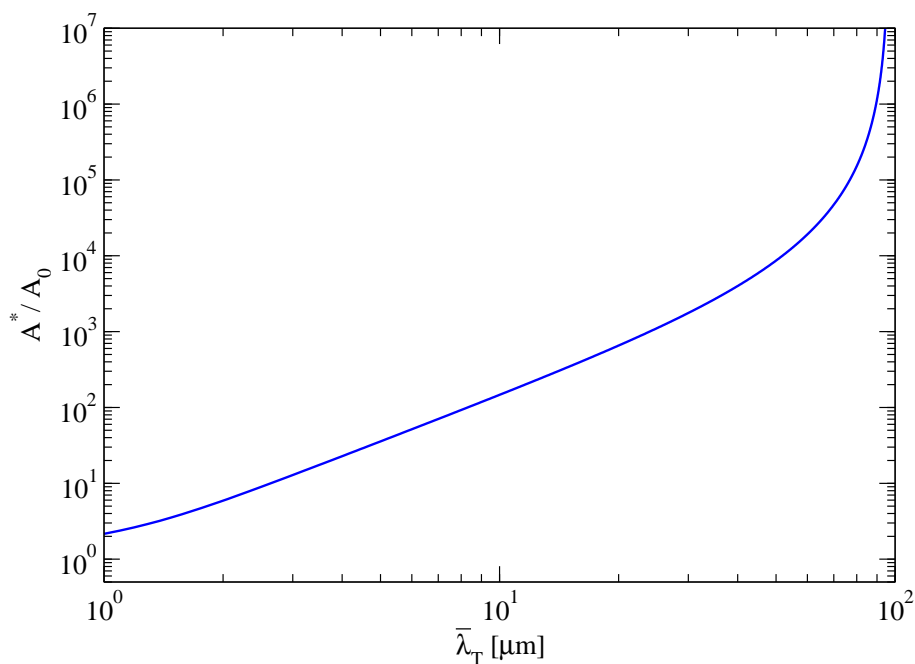


**Figure 5.7.:** Ratio of the final size  $A^*$  to the initial size  $A_0$  for the time-averaged spatial growth rule as a function of the parameter  $\bar{\lambda}_T$ .

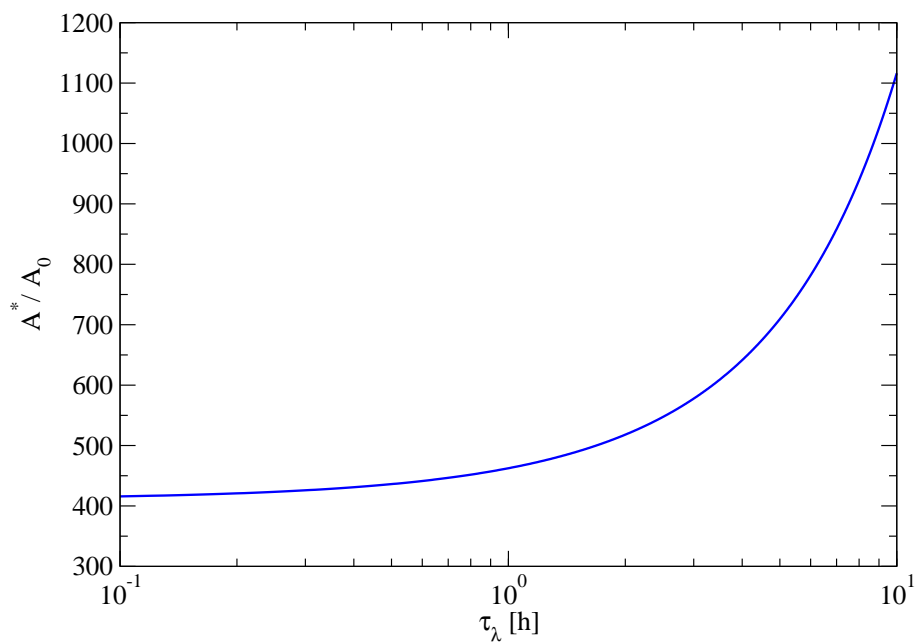


**Figure 5.8.:** Ratio of the final size  $A^*$  to the initial size  $A_0$  for the time-averaged spatial growth rule as a function of the parameter  $\tau_\lambda$ .

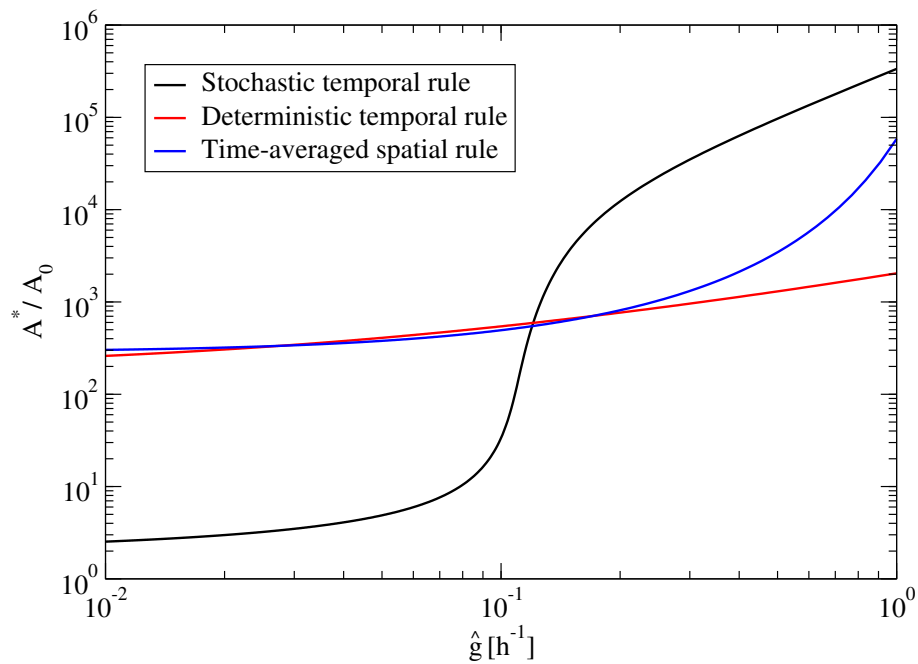


**Figure 5.9.:** Ratio of the final size  $A^*$  to the initial size  $A_0$  as a function of the maximum growth rate  $\hat{g}$ .

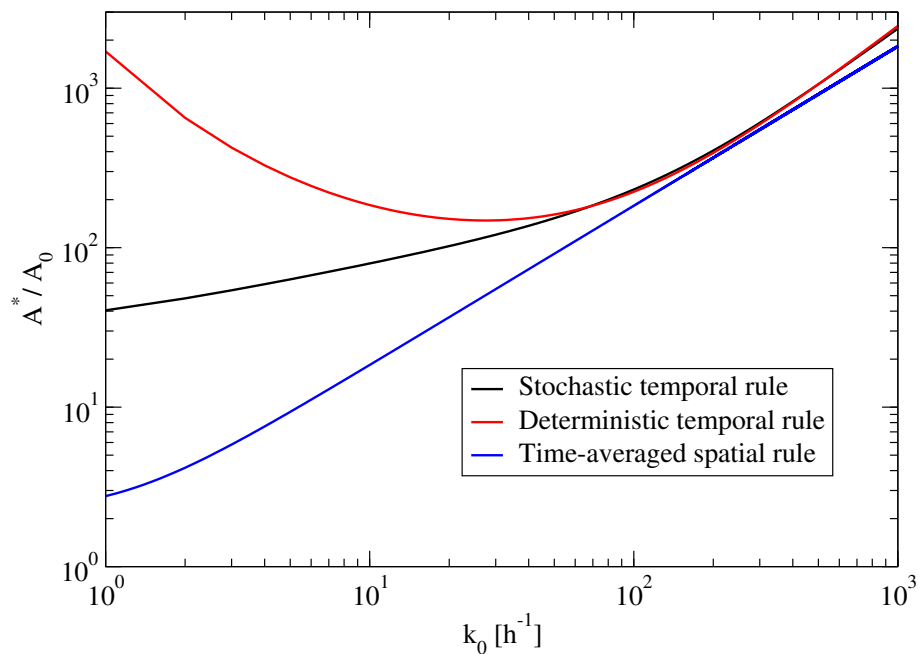


**Figure 5.10.:** Ratio of the final size  $A^*$  to the initial size  $A_0$  as a function of the initial Dpp degradation rate  $k_0$ .

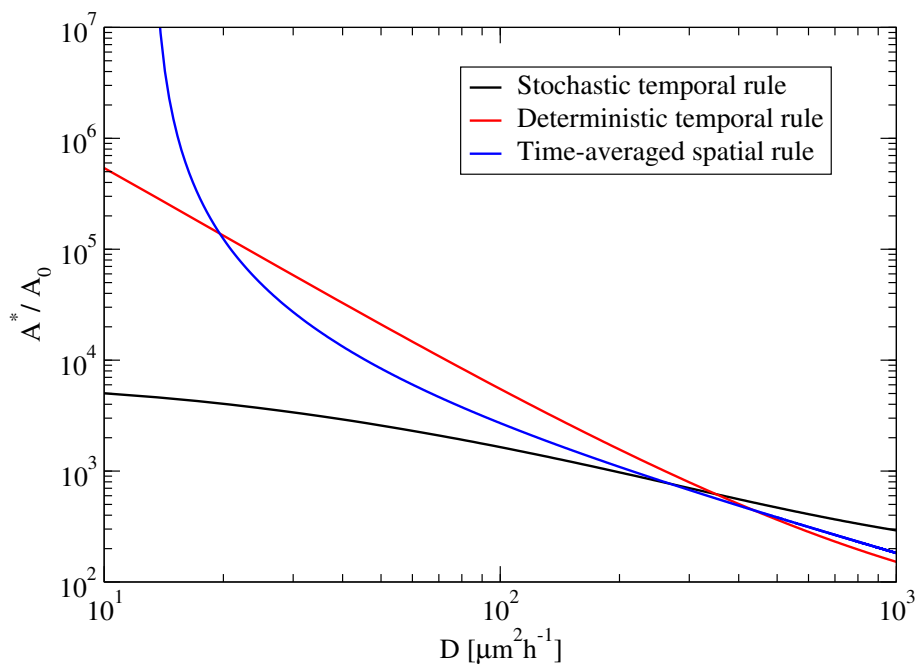


**Figure 5.11.:** Ratio of the final size  $A^*$  to the initial size  $A_0$  as a function of the Dpp diffusion coefficient  $D$ .

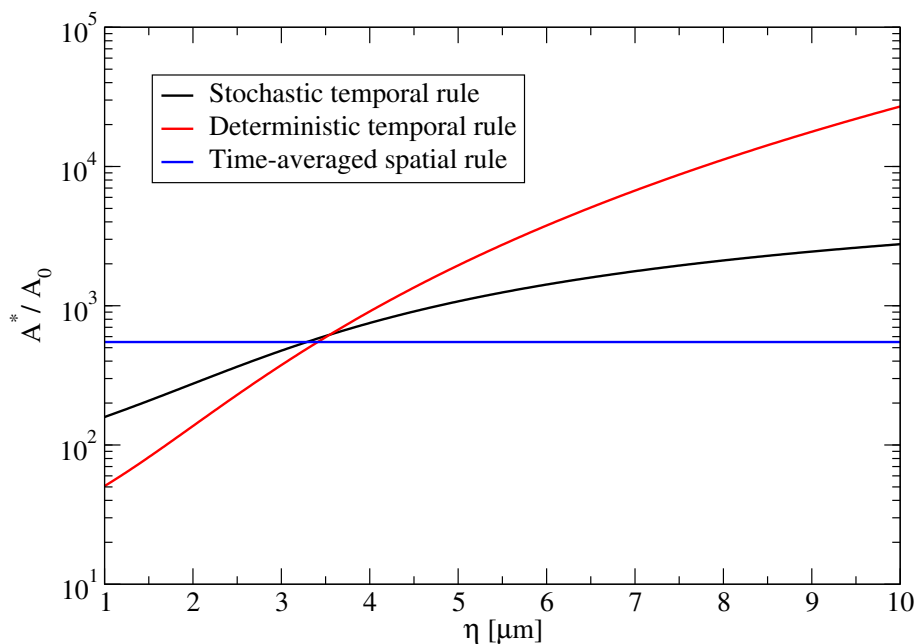


**Figure 5.12.:** Ratio of the final size  $A^*$  to the initial size  $A_0$  as a function of the parameter  $\eta$ , by which the widening of the Dpp source is taken into account.

Parameter	Meaning	Value
$A_0$	Initial system size	$98.3 \mu\text{m}^2$
$t_0$	Initial time	21.3 h
$c_0$	Initial Dpp gradient amplitude	$0 \mu\text{m}^{-2}$
$\lambda_0$	Initial Dpp decay length	$0 \mu\text{m}$
$\lambda_0$	Initial time-averaged Dpp decay length	$0 \mu\text{m}$
$k_0$	Initial Dpp degradation rate	$300 \text{h}^{-1}$
$w_0$	Initial Dpp source width	$10^{-10} \mu\text{m}$
$\phi_0$	Initial relative fraction of proliferating cells	1
$\hat{g}$	Maximum growth rate	$0.121 \text{h}^{-1}$
$\eta$	Dpp source parameter	$3.5 \mu\text{m}$
$\nu$	Dpp production rate per unit area	$1800 \mu\text{m}^{-2}\text{h}^{-1}$
$D$	Dpp diffusion coefficient	$0.1 \mu\text{m}^2\text{s}^{-1}$
$\theta$	Parameter of the stochastic temporal rule	9.13 h
$\bar{\alpha}$	Parameter of the deterministic temporal rule	0.587
$\lambda_T$	Parameter of the time-averaged spatial rule	$18.5 \mu\text{m}$
$\tau_\lambda$	Parameter of the time-averaged spatial rule	5 h

**Table 5.2.:** Initial conditions and parameter values used in this chapter, if not stated otherwise. Numerical solutions are determined using the software Mathematica 6.





## 6. Relationship Between Tissue Growth and Mechanical Stresses

In this chapter we study the relationship between proliferation, apoptosis (cell death), and mechanical stresses. As in the previous chapters we focus on the wing imaginal disc, where we estimate that forces of the order of 0.1-1  $\mu\text{N}$  act on the cells (see appendix D). It is not known if forces of this magnitude have a significant effect on proliferation or apoptosis. However there is evidence that mechanical stresses can influence the expression of certain genes during development [56], and that mechanical stresses play an important role in tumour growth [29]. It is thus plausible that mechanical stresses also may have an influence on the growth behaviour of the wing disc. In accordance with this view, it has been proposed that the homogeneity of growth in the wing disc is due to a mechanical effect [152].

In the vertex model the cell interior is described as a homogeneous elastic material. The mechanical pressure  $P_i$  inside cell  $i$  is thus given by

$$P_i = -\frac{\partial \mathcal{F}}{\partial A_i} = K(A_i^{(0)} - A_i) \quad (6.1)$$

and has the dimension force per length. To account for apoptosis in the vertex model, we allow for T2 processes by choosing the mechanical parameters appropriately [58] (see table 6.2 for parameter values). Cells having a sufficiently small area due to high mechanical pressure are removed from the system and replaced by a vertex, which corresponds to the extrusion of an apoptotic cell from the epithelium. The occurrence of T2 processes thus depends on the mechanical stresses in the system. The apoptosis rate  $\Omega$  is defined as the number of T2 processes per cell per unit time (see appendix E)

In section 6.1 we first study how proliferation influences mechanical stresses in the tissue. Here the rate of proliferation is predetermined and independent of mechanical stresses. We consider spatially homogeneous proliferation as well as cases in which the proliferation rate in a small clone is locally increased or decreased with respect to the rest of the tissue. The parameter values used in this section are given in table 6.1 on page 75.

In section 6.2 we explore how mechanical stresses can influence self-organized growth by adding a mechanical feedback to the deterministic temporal growth rule. The parameter values used in this section are given in table 6.2 on page 80. In all figures shown in this chapter, error bars indicate the standard error of the mean.

## 6.1. Influence of Proliferation on Mechanical Stresses

### 6.1.1. Homogeneous Proliferation

Here we choose the proliferation rate to be homogeneous in time and space on average. In this case the pressure distribution does not change significantly while the system grows (see figure 6.1). The mean pressure shows a slight temporal increase in the beginning of the simulation but remains approximately constant for  $N \gtrsim 1000$  (not shown). Increasing the tension of the  $AP$ -interface by increasing the parameter  $\kappa$  leads to a minor increase of the mean pressure  $\bar{P}$ . The apoptosis rate  $\Omega$  is more than one order of magnitude smaller than the growth rate  $g$  (see figure 6.2).

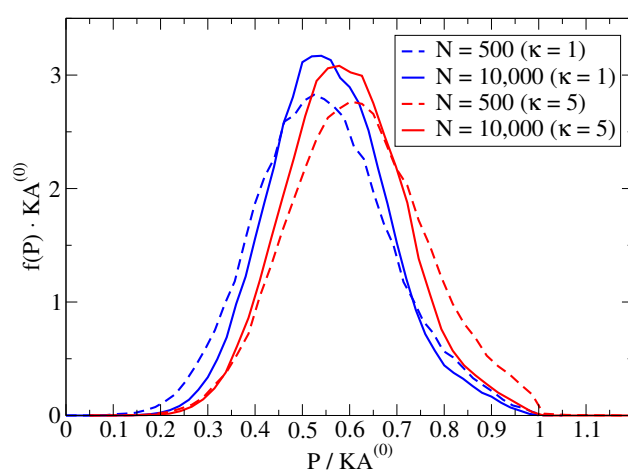


**Figure 6.1.:** Normalized pressure distribution  $f(P)$  in a homogeneously growing system shown for different system sizes  $N$  and different  $AP$ -interface tension factors  $\kappa$ .

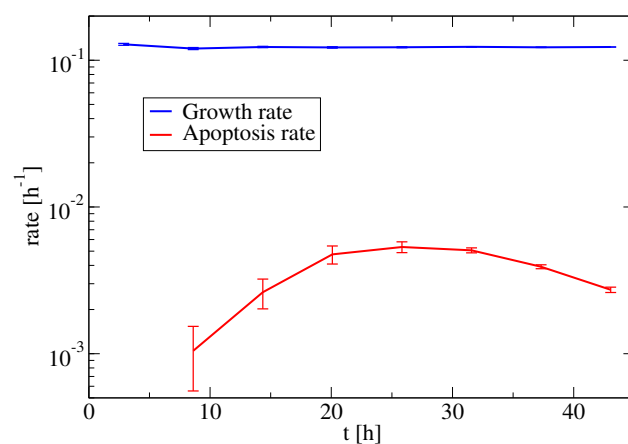


**Figure 6.2.:** Growth rate and apoptosis rate in a homogeneously growing system ( $\kappa = 1$ ).

### 6.1.2. Inhomogeneous Proliferation

Here we study how a locally increased or decreased proliferation rate influences the mechanical stresses and the apoptosis rate in the system. For that purpose we create a small clone that has a different proliferation rate than the rest of the system. The simulations are performed as follows. When the simulation starts we choose a random cell to be the founder of the clone. The clone consists of the progeny of this founder cell. We then let the whole system grow homogeneously until the total number of cells exceeds a threshold  $N_t$ , in order to get a moderate clone size and thus reduce fluctuations. When the number of cells exceeds  $N_t$ , we either stop proliferation in the clone or in the rest of the system to create a difference between the proliferation rates. Proliferation in the respective cells is stopped by halting cell cycle progression in cell cycle state  $C$ .

#### Locally Increased Proliferation Rate in a Clone

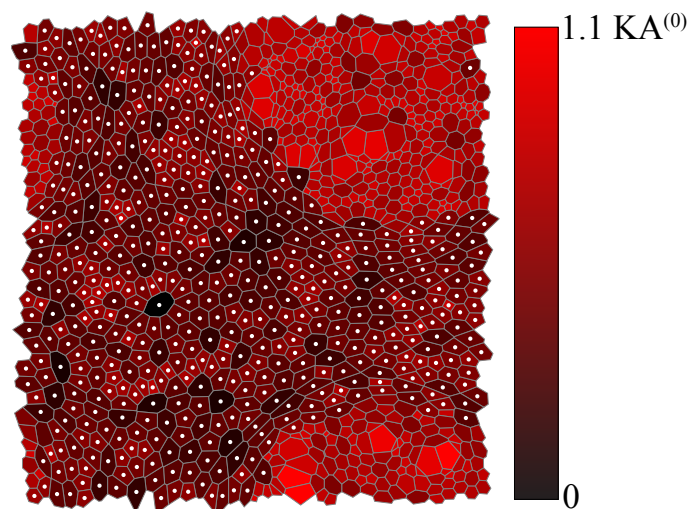


**Figure 6.3.:** Snapshot of a system consisting of  $N = 1000$  cells. The mechanical pressure  $P_i$  is indicated for each cell by a color code. Here only the clone cells proliferate, which are shown without dots. The mechanical pressure and the apoptosis rate in the clone is increased as a result. The other, non-proliferating cells are indicated by white dots.

Here the clone cells proliferate with constant rate, whereas the other cells stop to proliferate when  $N$  exceeds the threshold  $N_t$ . The result of the locally increased proliferation rate in the clone with respect to the rest of the system is a local increase in the pressure and apoptosis rate (see figures 6.4 and 6.5). In contrast, the pressure and apoptosis rate in the rest of the system is decreased (see figures 6.4 and 6.5).

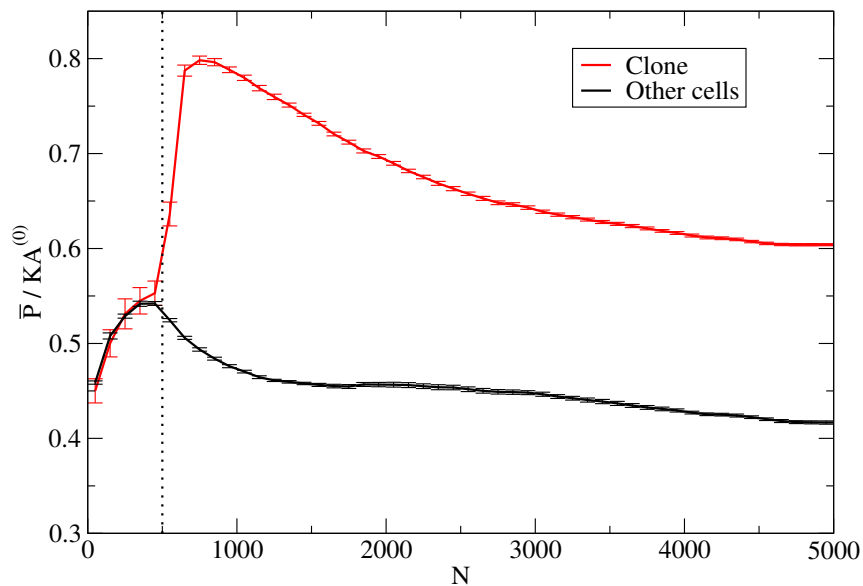


**Figure 6.4.:** Mean pressure  $\bar{P}$  in the clone and in the other cells, shown as a function of the number of cells  $N$ . Here the cells not belonging to the clone stop to proliferate when  $N$  exceeds  $N_t = 500$ .

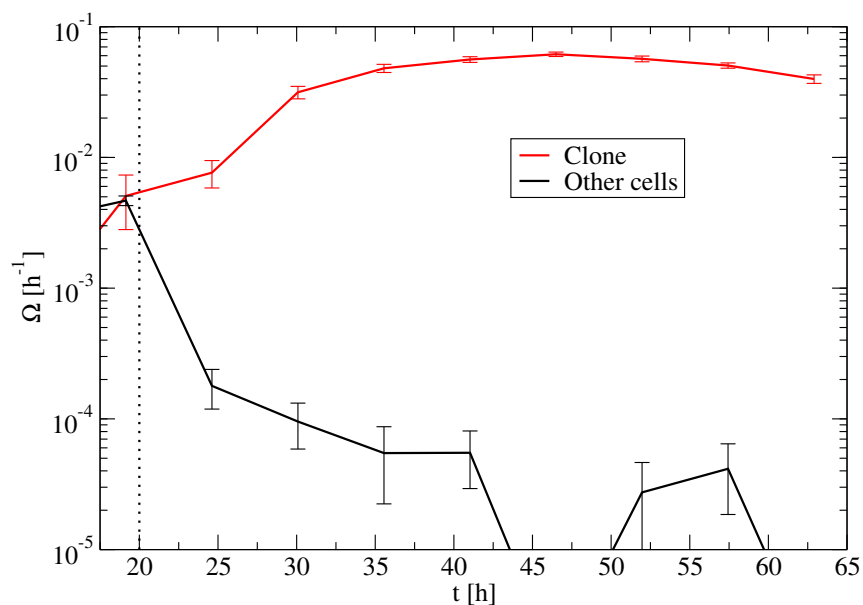


**Figure 6.5.:** Average apoptosis rate  $\Omega$  in the clone and in the other cells, shown as a function of time. Here the cells not belonging to the clone stop to proliferate when the number of cells  $N$  exceeds  $N_t = 500$ , which corresponds to  $t \approx 20$  h.

### Locally Decreased Proliferation Rate in a Clone

Here the clone cells stop to proliferate when  $N$  exceeds  $N_t$ , whereas the other cells continue to proliferate. When the clone cells stop to proliferate, the pressure inside the clone drops (see figure 6.6). As a result the apoptosis rate in the clone is reduced (not shown). Actually, for our choice of the parameter values, the apoptosis rate in the clone drops to zero when the clone cells stop to proliferate.

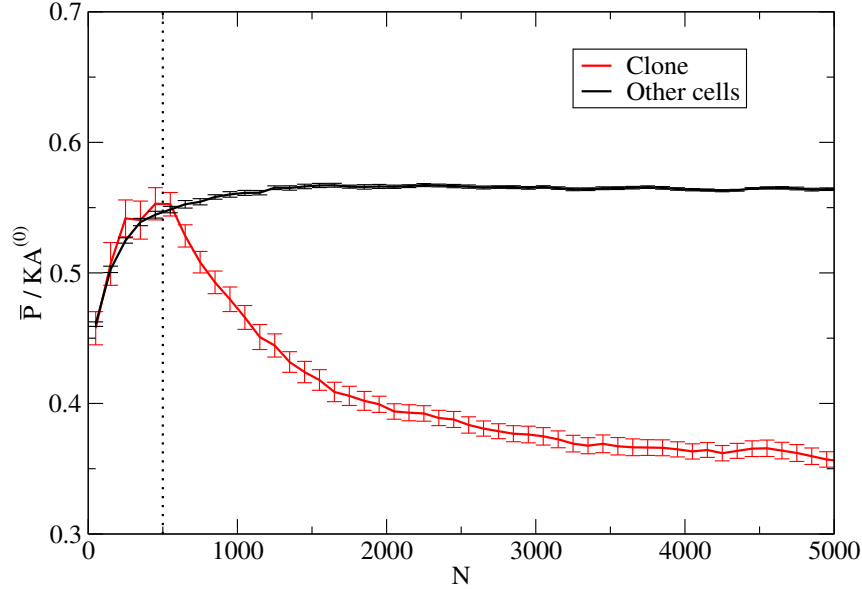


**Figure 6.6.:** Mean pressure  $\bar{P}$ , shown as a function of the number of cells  $N$ . Here the clone cells stop to proliferate when  $N$  exceeds  $N_t = 500$ .

Parameter	Meaning	Value
$\Gamma / KA^{(0)}$	Dimensionless cell perimeter stiffness	0.04
$\Lambda / K(A^{(0)})^{3/2}$	Dimensionless cell bond tension	0.12
$\kappa$	$AP$ -interface tension factor	1
$N_0$	Initial number of cells	36
$N_t$	Cell number threshold for inhomogeneous growth	500
$\bar{\tau}_M$	Mean residence time in cell cycle state $M$	0.75 h
$\bar{\tau}_I$	Mean residence time in cell cycle state $I$	5 h
$\tau_C$	Residence time in cell cycle state $C$	0 h
$\xi$	Gamma distribution shape parameter	25

**Table 6.1.:** Parameter values used in section 6.1 if not stated otherwise. The values for the mechanical parameters are taken from the paper [58]. The global relaxation method is used here (see appendix F), and all results are averages over 25 simulations.

## 6.2. Influence of Mechanical Stresses on Self-organized Growth

In this section we explore how mechanical stresses can influence self-organized growth. Cells that grow in size prior to a cell division have to perform mechanical work against the pressure they are exposed to. Because cell growth and cell division are coupled in the wing imaginal disc, we expect that sufficiently high mechanical pressures can inhibit proliferation. To study this effect, we extend the deterministic temporal growth rule with a mechanical feedback that inhibits proliferation at high pressures and stimulates proliferation at low pressures. For this purpose the parameter  $\alpha$ , which was introduced in equation (4.1) on page 39, is replaced by a variable  $\alpha(P_i)$  that depends on the local pressure,

$$\alpha(P_i) = \alpha^{(0)} + \chi(P_i - P^{(0)}). \quad (6.2)$$

Here  $\alpha^{(0)}$ ,  $\chi$ , and  $P^{(0)}$  are parameters. The relative increase of the Dpp level necessary to trigger a cell division thus increases linearly with the pressure  $P_i$  inside the cell. The parameter  $P^{(0)}$  is chosen close to the mean pressure in the system. The strength of the mechanical feedback is determined by  $\chi$  and can be estimated by considering that the mean and standard deviation of  $\alpha(P_i)$  are approximately given by  $\alpha^{(0)}$  and  $\chi\sigma_P$ . Here,  $\sigma_P$  denotes the standard deviation of the pressure distribution. Its magnitude is given by  $\sigma_P \approx 10^{-1}KA^{(0)}$  (see figure 6.1). The mechanical feedback is weak if  $\chi\sigma_P \ll \alpha^{(0)}$ , and it is strong if  $\chi\sigma_P \approx \alpha^{(0)}$ .

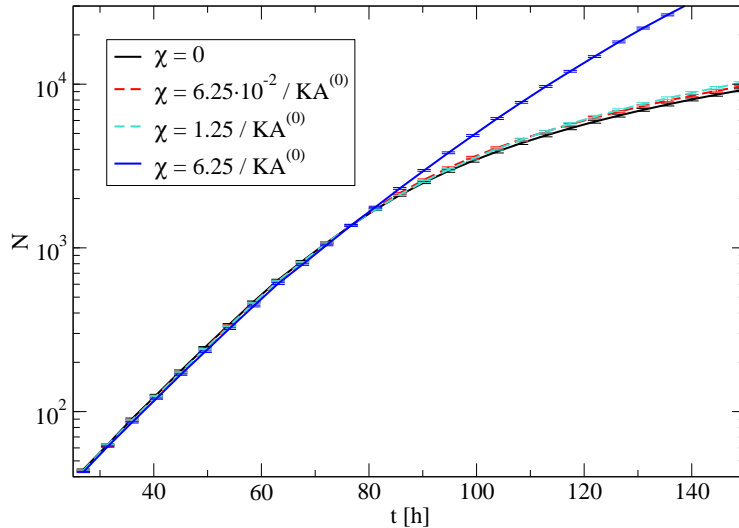


**Figure 6.7.:** Number of cells  $N$  shown as a function of time for different choices of the parameter  $\chi$ . The growth rule is switched on at  $t \approx 55$  h ( $N_g = 360$ ).

As long as the mechanical feedback is weak, the growth curves do not differ much from each other (see figure 6.7). However, if the mechanical feedback is strong, the

growth rate decays slower and the system becomes significantly larger (blue curve in figure 6.7). The reason for this overgrowth is that, if the feedback is strong, then those cells that are exposed to sufficiently low pressure divide regardless of the dynamics of the Dpp gradient, because  $\alpha(P_i) \approx 0$  for these cells. The parameter  $\chi$  must thus be chosen sufficiently small in order to maintain the mean behaviour of the system.

The growth asymmetry between the  $A$  and  $P$  population is reduced when the strength of the mechanical feedback is increased (see figure 6.8). However, this effect is weak; even for a strong feedback a significant asymmetry remains. The reason for the stabilizing effect of the mechanical feedback is the following: due to the asymmetry of the Dpp source, the deterministic temporal rule generates more proliferation in the  $P$  population as compared to the  $A$  population (see section 4.1.1), which leads to a higher pressure in the  $P$  population (see figure 6.11 and also section 6.1.2). The pressure difference between the  $P$  and  $A$  populations has two effects. Firstly, the apoptosis rate is systematically higher in the  $P$  population as compared to the  $A$  population (see figure 6.9). However, this difference in the apoptosis rate cannot compensate for the growth asymmetry of the two populations because the apoptosis rate is generally too small. Secondly, due to the mechanical feedback in the growth rule, the pressure difference leads to an inhibition of growth in the  $P$  population and a stimulation of growth in the  $A$  population. Therefore, the relative difference between the growth rates of the  $P$  and  $A$  populations is reduced as the strength of the feedback is increased (see figure 6.10).

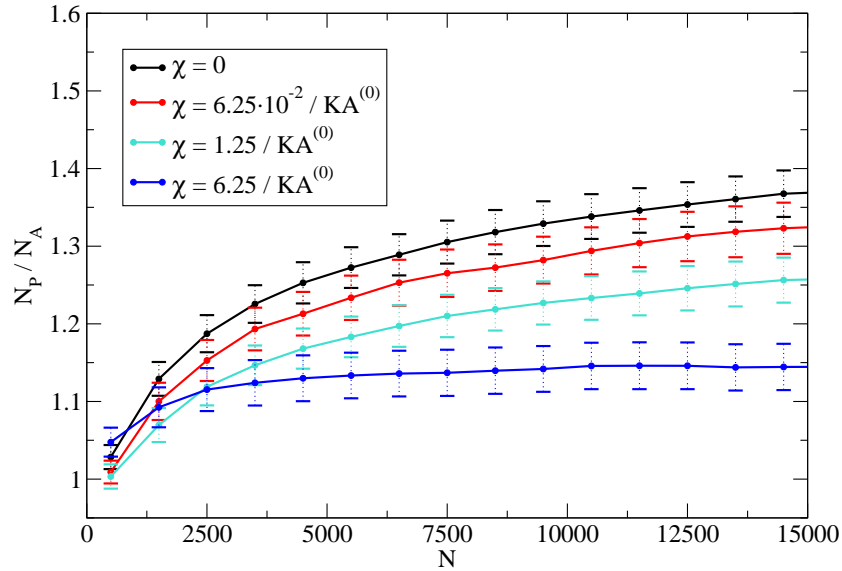


**Figure 6.8.:** Ratio of the cell number in the  $P$  population ( $N_P$ ) to the cell number in the  $A$  population ( $N_A$ ) shown as a function of the total number of cells  $N$ . The growth asymmetry is reduced by the mechanical feedback.

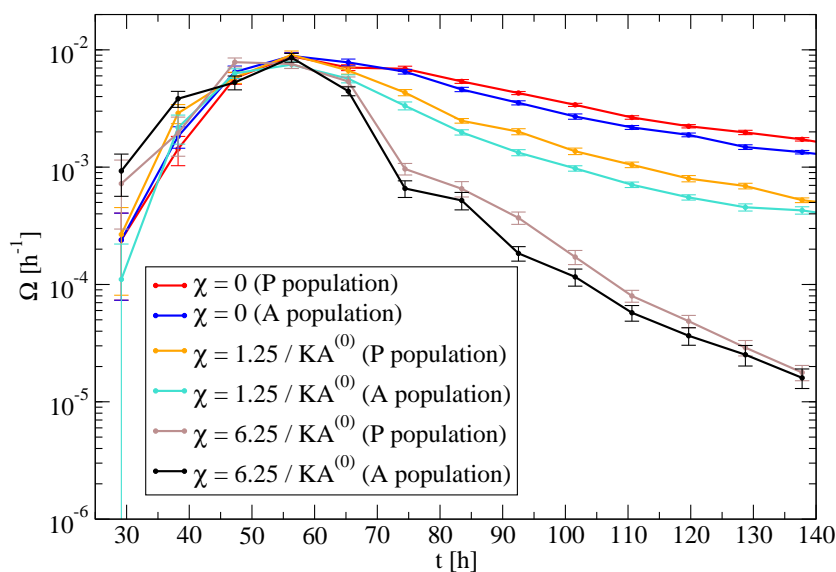


**Figure 6.9.:** Apoptosis rate  $\Omega$  in the  $A$  and  $P$  population, shown as a function of time for different choices of the parameter  $\chi$ . The growth rule is switched on at  $t \approx 55$  h. The apoptosis rate in the  $P$  population is systematically higher due to a higher pressure. The apoptosis rate depends strongly on the strength of the mechanical feedback.

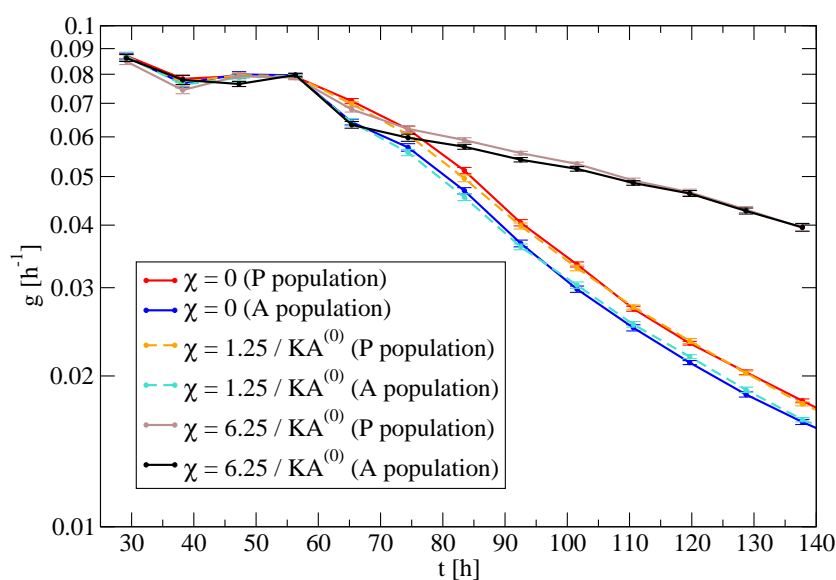


**Figure 6.10.:** Growth rate  $g$  in the  $A$  and  $P$  population, shown as a function of time for different choices of the parameter  $\chi$ . The growth rule is switched on at  $t \approx 55$  h. The relative difference between the growth rates in the  $A$  and  $P$  populations is decreased as the strength of the feedback is increased.



Furthermore the mechanical feedback slightly reduces the mean pressure in the system (figure 6.11). Moreover the standard deviation of the pressure distribution is reduced (figure 6.12). Due to these changes in the pressure distribution, fewer cells are exposed to high pressure which reduces the probability for T2 processes. Consequently, increasing the strength of the mechanical feedback leads to a substantial decrease in the apoptosis rate (see figure 6.9).

In the literature it has been suggested that the spatial homogeneity of growth in the wing disc relies on a mechanical feedback [152, 83, 3]. We indeed find that a mechanical feedback can have a stabilizing effect on the system, as growth inhomogeneities, pressure fluctuations, and the rate of apoptosis are reduced. However, the stabilizing effect concerning the growth asymmetry is weak. Without mechanical feedback, the  $P$  population is approximately 35% bigger than the  $A$  population when the total system size reaches  $N = 1.5 \cdot 10^4$  cells. This asymmetry can be reduced by the mechanical feedback, but if the feedback is too strong, the shape of the growth curve is changed substantially (figure 6.7). However, a moderate feedback strength that maintains the shape of the growth curve is only able to reduce the asymmetry to 25% ( $\chi = 1.25 / KA^{(0)}$ ). In the light of this result, the proposal that a mechanical feedback can ensure the spatial homogeneity of growth in the wing imaginal disc seems implausible.

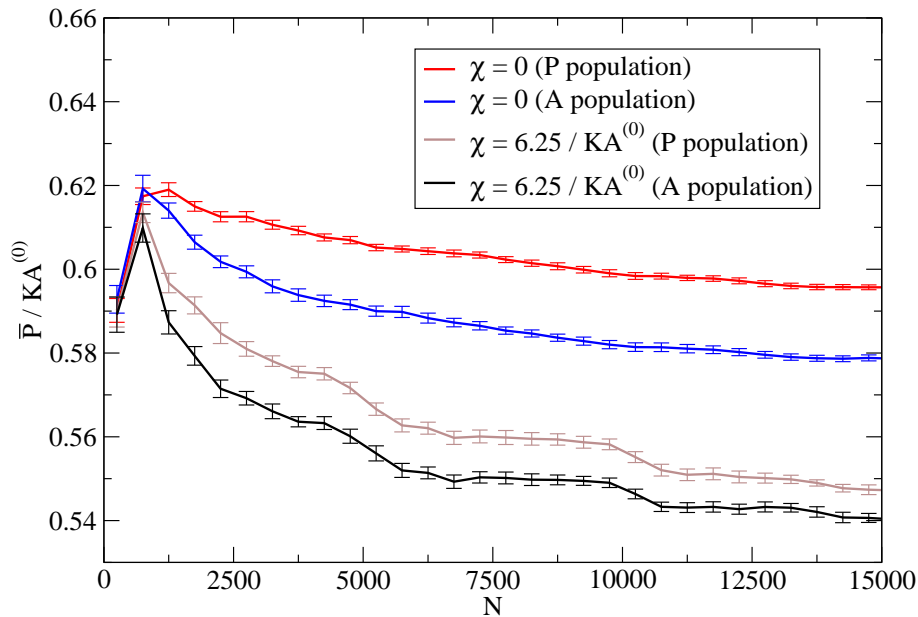


**Figure 6.11.:** Mean pressure  $\bar{P}$  shown as a function of the total number of cells  $N$ . The mechanical feedback decreases the mean pressure in the system and also slightly decreases the pressure difference between the  $A$  and  $P$  populations.

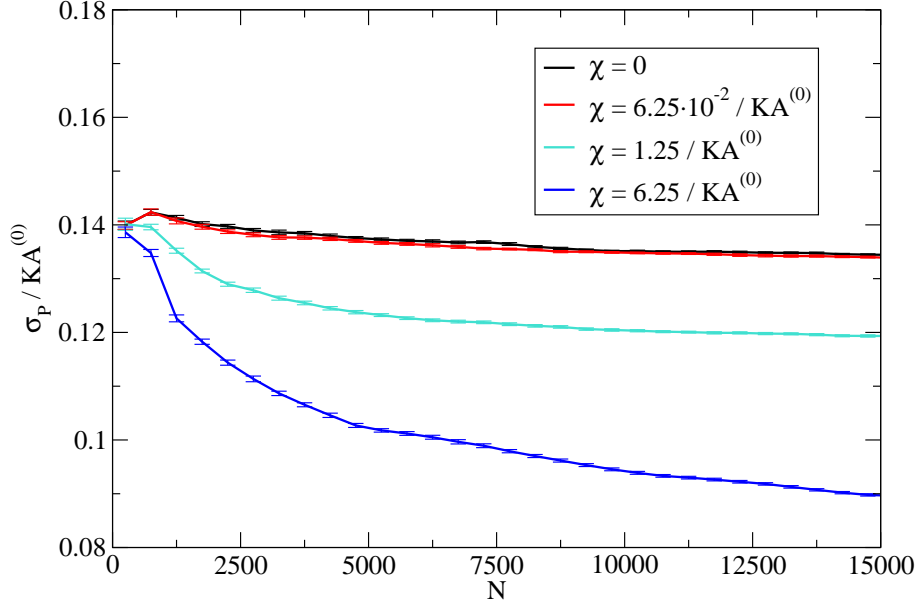


**Figure 6.12.:** Standard deviation  $\sigma_P$  of the pressure distribution in the whole system shown as a function of the total number of cells  $N$ . The standard deviation is decreased as the strength of the feedback is increased.

Parameter	Meaning	Value
$\Gamma / KA^{(0)}$	Dimensionless cell perimeter stiffness	0.04
$\Lambda / K(A^{(0)})^{3/2}$	Dimensionless cell bond tension	0.12
$A^{(0)}$	Preferred cell area	$13.7 \mu\text{m}^2$
$\kappa$	$AP$ -interface tension factor	5
$\bar{\tau}_I$	Mean residence time in cell cycle state $I$	8.3 h
$d^{(D)}$	Parameter describing Dpp diffusion	$3.0 \mu\text{m}^{-1}\text{h}^{-1}$
$D^{(D)}$	Corresponding Dpp diffusion coefficient	$0.01 \mu\text{m}^2\text{s}^{-1}$
$t_0$	Starting time of the simulation	24.6 h
$n_0^{(E)}$	Initial number of expander molecules per cell	$3 \cdot 10^4$
$\gamma$	Dilution scaling mechanism parameter	$9.2 \cdot 10^{-4} \text{h}^{-1}$
$\alpha^{(0)}$	Growth rule parameter	0.64
$P^{(0)} / KA^{(0)}$	Growth rule parameter	0.54

**Table 6.2.:** Parameter values used in section 6.2. For parameters that are not listed, the values in table 4.1 on page 52 are used. The average cell area is given by  $A_c \approx 0.4A^{(0)} \approx 5.5 \mu\text{m}^2$ . The parameter values correspond to the haltere disc (see section 7.1). The dilution scaling mechanism is used, and the global relaxation method is chosen (see appendix F).

**Summary** In this chapter we have studied the relationship between tissue growth and mechanical stresses using the vertex model. We have shown that the pressure distribution in a homogeneously growing system is essentially independent of the system size. We investigated the effect of local deviations from a homogeneous proliferation rate. We found that a locally increased proliferation rate results in a local pressure increase, which in turn leads to a locally increased apoptosis rate. Conversely, a locally decreased proliferation rate results in a local pressure decrease and a locally decreased apoptosis rate. We then explored how mechanical stresses can influence self-organized growth. For this purpose we used the deterministic temporal growth rule and added a mechanical feedback that inhibits proliferation at high pressures and stimulates proliferation at low pressures. We found that this feedback has a stabilizing effect on the system, as growth inhomogeneities, pressure fluctuations, and the rate of apoptosis are reduced.



# 7. Self-organized Growth Under Perturbed Conditions

In this chapter we study self-organized growth under conditions that deviate from the conditions in chapter 4. Most of these new conditions correspond to mutant wing discs for which experimental data is available. The aim of this chapter is to further check the consistency between theory and experiment. We focus on the deterministic temporal growth rule because it has already shown good agreement with experimental data in chapter 4. In section 7.1 we study the growth behaviour under conditions that correspond to the haltere discs. The two haltere discs give rise to the halteres of the fly, which are small organs that help to maintain stability in flight. In section 7.2 we study the effect of cell clones that produce permanently active Dpp receptors, which locally enhance the Dpp signal. The clones in these simulations represent the so-called  $Tkv^{QD}$  clones. Experiments using these clones are particularly interesting because it is possible to control the expression of the permanently active Dpp receptors externally by adding a drug to the food of the larvae [175]. In section 7.3 we study the effects of changes in the maximum growth rate. These simulations correspond to experiments with *Minute* mutants. For a brief description of the *Minute* mutants see section 1.2.2. In section 7.4 we fix the width of the Dpp source, which corresponds to experiments in which the morphogen Hh is replaced by non-diffusible HhCD2 [160]. In section 7.5 we include system-wide Dpp production in the simulations, mimicking ubiquitous Dpp expression with the C765-Gal4 driver [146]. In the last section 7.6 we demonstrate that the growth behaviour generated by the deterministic temporal rule can be stabilized by nonlinear Dpp auto-repression. The experimental growth curves shown in this chapter were measured by Ortrud Wartlick. Error bars indicate the standard error of the mean if not stated otherwise.

## 7.1. Kinetic Parameters Estimated from Haltere Imaginal Discs

The initial size of the haltere disc and the growth rate in the initial, exponential growth phase are smaller as compared to the case of the wing disc (see figure 7.1). If only these parameters are changed but otherwise the parameters estimated from the wing discs are used, the growth curve does not match the experimental haltere data (turquoise curve in figure 7.1). However, we estimate that both the Dpp

diffusion coefficient and degradation rate are approximately one order of magnitude smaller in the haltere disc (see appendix J.2). Changing these two parameters additionally (parameter set 3, see table 7.2) results in growth dynamics consistent with experimental data for both the deterministic temporal rule and the stochastic temporal rule (see figure 7.1).

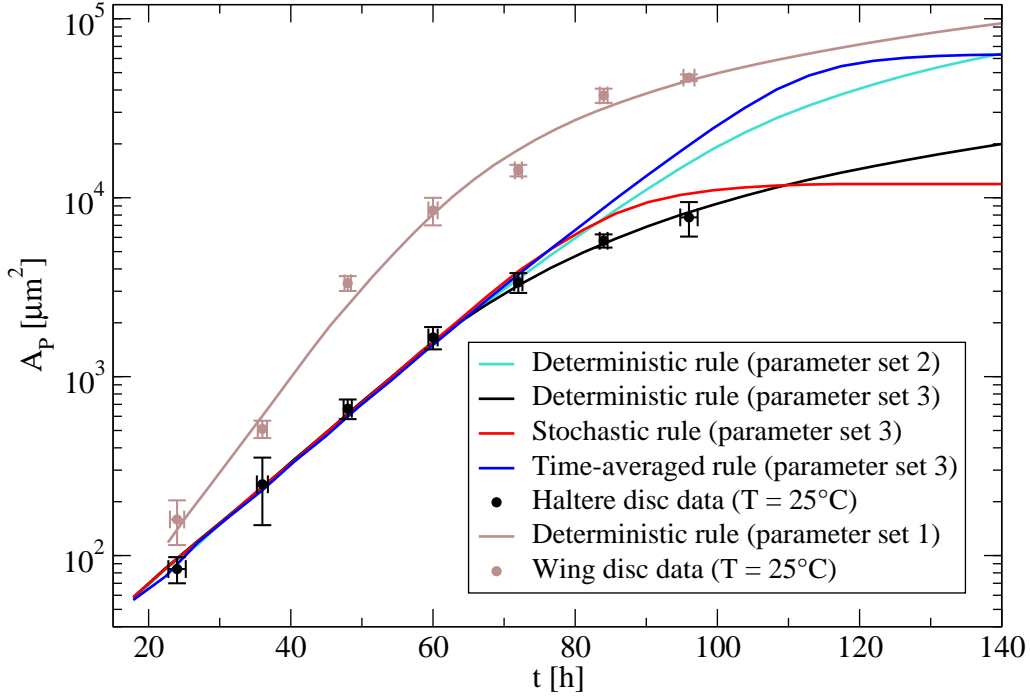


**Figure 7.1.:** Area of the  $P$  population shown as a function of time. Parameter set 1 refers to the parameters values that are used to simulate normal wing discs (see tables 4.1 and 4.3). Parameter set 2 is given in table 7.1, and parameter set 3 is given in table 7.2.

Parameter	Meaning	Value
$N_0$	Initial number of cells	18
$\bar{\tau}_I$	Mean residence time in cell cycle state $I$	8.3 h
$t_0$	Starting time of the simulation	15.6 h

**Table 7.1.:** Parameter set 2, which is used to simulate haltere discs. For parameters not listed here, we take the values from the normal wing disc simulations (see tables 4.1 and 4.3).

Parameter	Meaning	Value
$N_0$	Initial number of cells	18
$\bar{\tau}_I$	Mean residence time in cell cycle state $I$	8.3 h
$t_0$	Starting time of the simulation	15.6 h
$d^{(D)}$	Parameter describing Dpp diffusion	$3.0 \mu\text{m}^{-1}\text{h}^{-1}$
$D^{(D)}$	Corresponding Dpp diffusion coefficient	$0.01 \mu\text{m}^2\text{s}^{-1}$
$\gamma$	Dilution scaling mechanism parameter	$9.2 \cdot 10^{-4} \text{h}^{-1}$

**Table 7.2.:** Parameter set 3, which is used to simulate haltere discs. For parameters not listed here, we take the values from the normal wing disc simulations (see tables 4.1 and 4.3).

## 7.2. Local Production of Permanently Active Dpp Receptors

In this section we discuss simulations in which cell clones produce permanently active Dpp receptors, known as  $\text{TkV}^{\text{QD}}$  receptors [141]. In these simulations each cell is assigned a number of  $\text{TkV}^{\text{QD}}$  receptors  $n_i^{(T)}$ , which obeys

$$\frac{d}{dt}n_i^{(T)} = p_i^{(T)} - k_i^{(T)}n_i^{(T)}. \quad (7.1)$$

Here,  $p_i^{(T)}$  is the production rate and  $k_i^{(T)}$  is the degradation rate of  $\text{TkV}^{\text{QD}}$  receptors in cell  $i$ . When a cell divides, each daughter cell inherits half of the receptors. At the onset of the simulation, one founder cell in the  $P$  population is chosen, whose progeny constitute the  $\text{TkV}^{\text{QD}}$  clone. To study the position dependence of the clone behaviour, we choose the founder cell of the  $\text{TkV}^{\text{QD}}$  clone either adjacent to the Dpp source (medial) or at a maximum distance from the Dpp source (lateral). Only cells that belong to the  $\text{TkV}^{\text{QD}}$  clone produce  $\text{TkV}^{\text{QD}}$  receptors, so that  $n_i^{(T)} = 0$  for all times if cell  $i$  does not belong to the clone. The production rate and degradation rate of the receptors is the same for all cells within the clone,  $p_i^{(T)} = p^{(T)}$ ,  $k_i^{(T)} = k^{(T)}$ . In experiments,  $\text{TkV}^{\text{QD}}$  receptor production is induced by adding a drug to the food of the *Drosophila* larvae [175]. Therefore we choose the production of receptors to be time-dependent in the simulations. Production begins at  $t = t^{(T)}$  and increases linearly within the time interval  $\Delta t^{(T)}$  until the maximum production rate  $\hat{p}^{(T)}$  is reached,

$$p^{(T)}(t) = \begin{cases} 0, & \text{if } t < t^{(T)} \\ \hat{p}^{(T)}(t - t^{(T)})/\Delta t^{(T)}, & \text{if } t^{(T)} \leq t \leq t^{(T)} + \Delta t^{(T)} \\ \hat{p}^{(T)}, & \text{if } t^{(T)} + \Delta t^{(T)} < t. \end{cases} \quad (7.2)$$

We define the Dpp signal  $s_i^{(D)}$  in cell  $i$  by

$$s_i^{(D)} = n_i^{(D)} + n_i^{(T)}, \quad (7.3)$$

where  $n_i^{(D)}$  is the number of Dpp molecules in cell  $i$ . In the simulations presented in this section we use the deterministic temporal growth rule. However, we use a version of this rule in which the Dpp signal  $s_i^{(D)}$  is considered instead of  $n_i^{(D)}$ . To assess the effect of receptor production we compare the behaviour of the  $\text{TkV}^{\text{QD}}$  clones with control clones that do not produce receptors. The parameter values chosen in this section are given in table 7.3.

After the initiation of  $\text{TkV}^{\text{QD}}$  receptor production, Dpp signaling levels in the  $\text{TkV}^{\text{QD}}$  clones become higher than in control clones (see figure 7.2). Due to the temporal increase in Dpp signaling levels, the deterministic temporal growth rule leads to an overgrowth of  $\text{TkV}^{\text{QD}}$  clones with respect to control clones (see figures 7.4 and 7.5). On average, lateral  $\text{TkV}^{\text{QD}}$  clones overgrow by a factor  $4.0 \pm 0.2$  and medial  $\text{TkV}^{\text{QD}}$  clones overgrow by a factor  $2.4 \pm 0.2$  (at  $t = 120$  h). These results are in excellent agreement with experimental observations, where lateral clones overgrow by a factor 3.7 and medial clones by a factor 2.1 [109]. Our simulations suggest the following explanation for the difference between medial and lateral clones: the relative increase in Dpp signaling caused by the  $\text{TkV}^{\text{QD}}$  receptors is larger in lateral clones, because there the normal Dpp levels are low. According to the deterministic temporal growth rule, cell divisions are triggered by relative increases in Dpp signaling. Because the relative increases are higher in lateral clones, these clones overgrow more than medial ones.

In the simulations in this section we use the dilution scaling mechanism with non-diffusible expander molecules. Therefore, the Dpp degradation rate in each cell only depends on the cell generation number. The higher the cell generation number is, the smaller is the Dpp degradation rate. Due to the overgrowth of the  $\text{TkV}^{\text{QD}}$  clones, the Dpp degradation rate in these clones is smaller as compared to control clones. The Dpp degradation rate inside the clone also influences the Dpp levels in the vicinity. This effect can be observed for the lateral  $\text{TkV}^{\text{QD}}$  clones: Dpp signaling levels are higher in cells that surround a lateral  $\text{TkV}^{\text{QD}}$  clone as compared to cells that surround a control clone (see figure 7.3). Due to this effect, the growth rate in cells surrounding lateral  $\text{TkV}^{\text{QD}}$  clones is slightly elevated (see figure 7.6). Increased proliferation in the vicinity of  $\text{TkV}^{\text{QD}}$  clones has indeed been observed experimentally [141]. The deterministic temporal growth rule together with the dilution scaling mechanism provide an explanation for this non-autonomous effect of the  $\text{TkV}^{\text{QD}}$  clones upon proliferation.



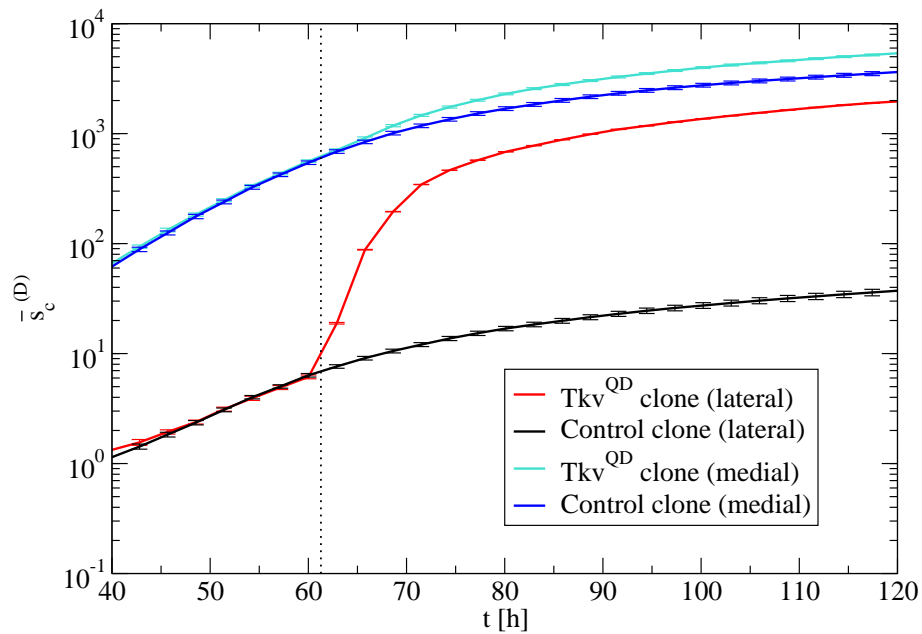


**Figure 7.2.:** Average Dpp signal  $\bar{s}_c^{(D)}$  inside the clone shown as a function of time. The starting time of receptor production is indicated by the dotted line.

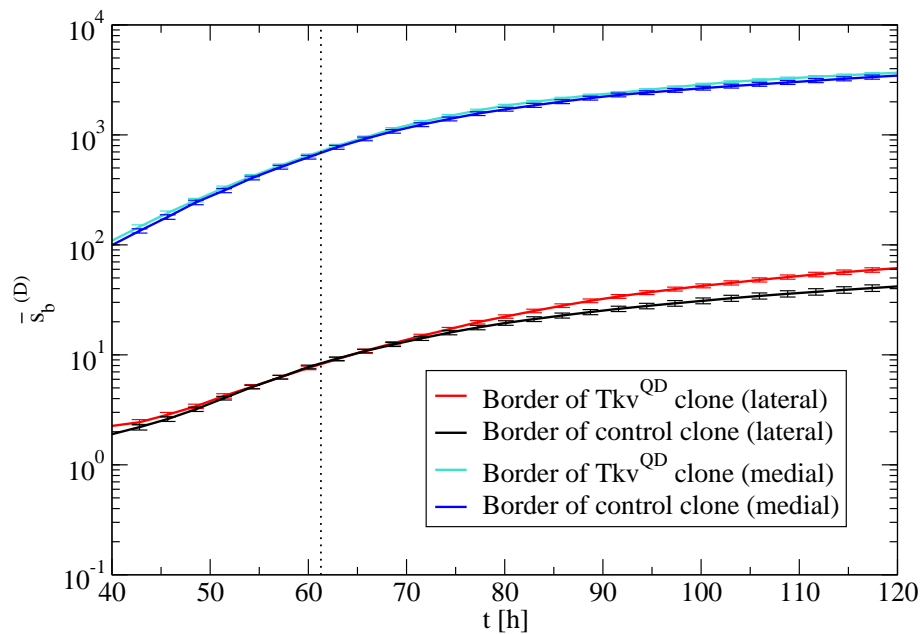


**Figure 7.3.:** Average Dpp signal  $\bar{s}_b^{(D)}$  in the non-Tkv<sup>QD</sup> cells that are bordering the clone, shown as a function of time. The starting time of receptor production is indicated by the dotted line.

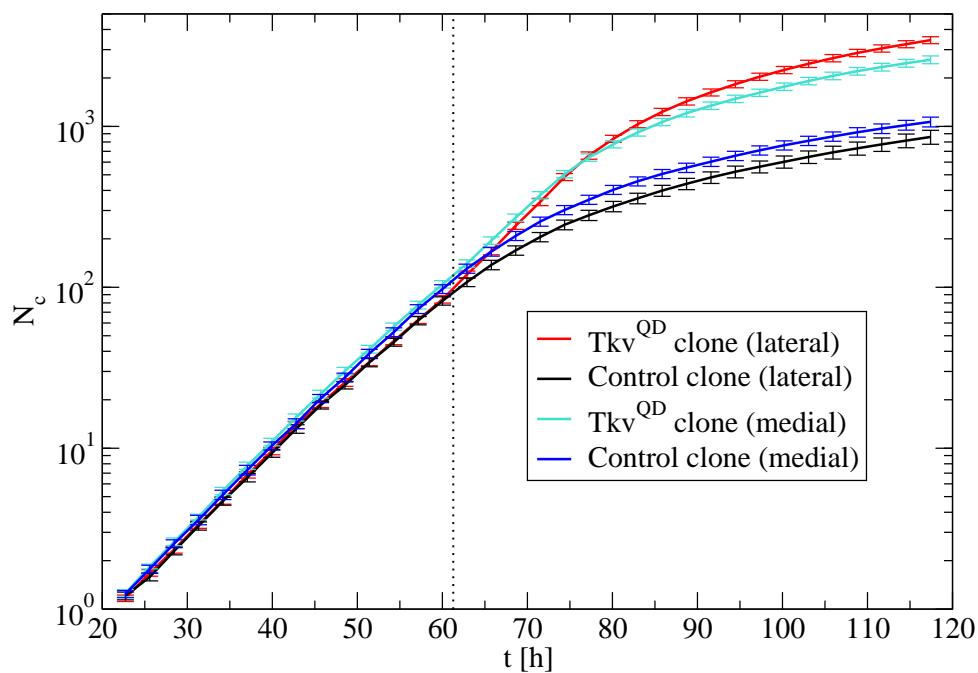


**Figure 7.4.:** Clone size  $N_c$  shown as a function of time. The starting time of receptor production is indicated by the dotted line.

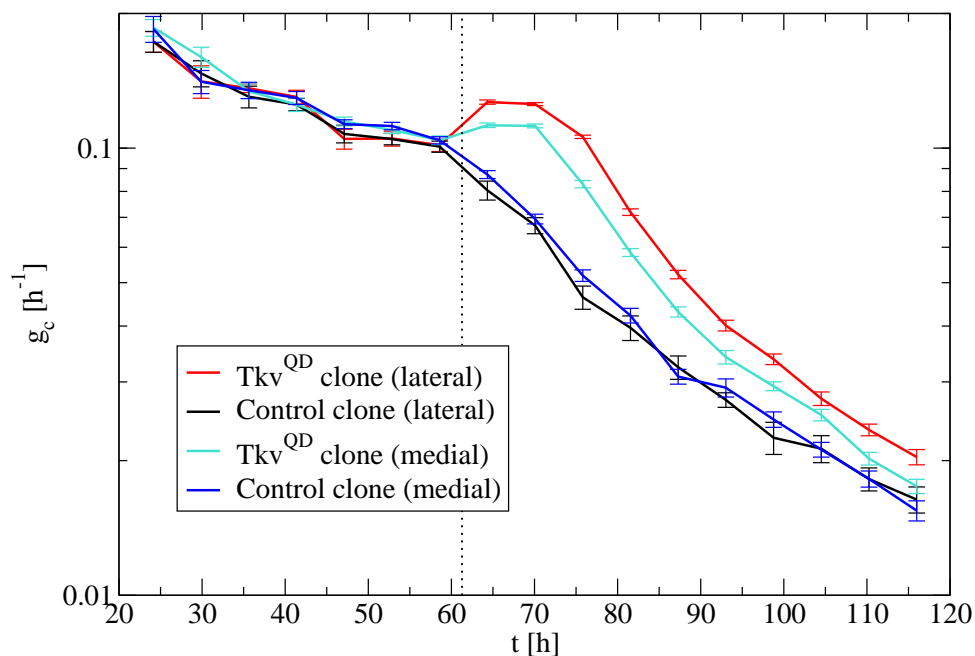


**Figure 7.5.:** Growth rate  $g_c$  of the clone shown as a function of time. The starting time of receptor production is indicated by the dotted line.

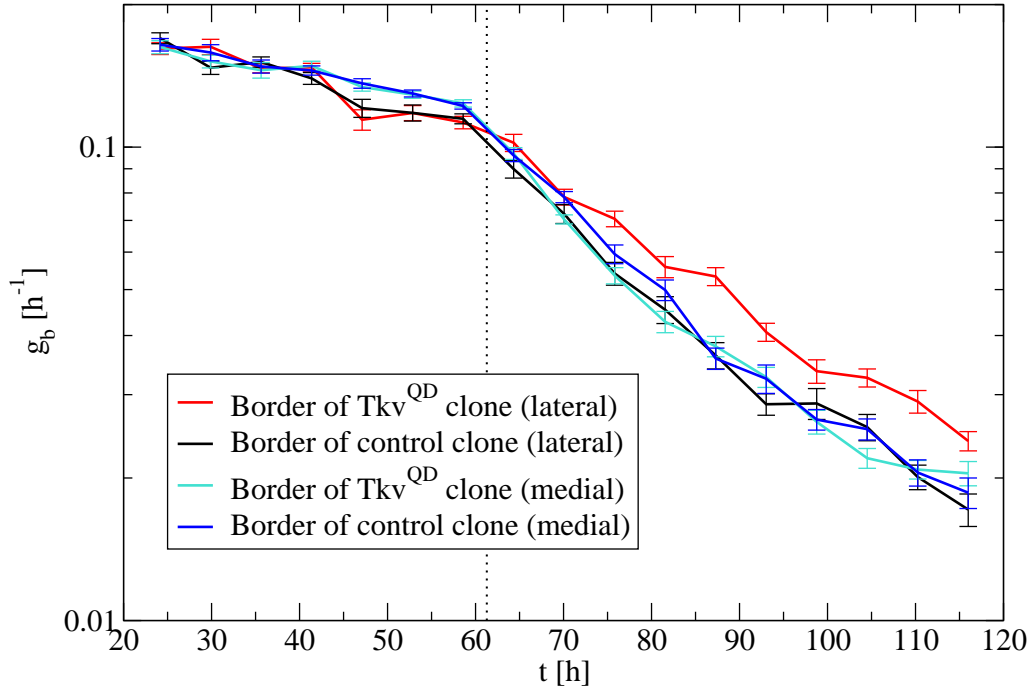


**Figure 7.6.:** Growth rate  $g_b$  of the non-Tkv<sup>QD</sup> cells that are bordering the clone, shown as a function of time. The starting time of receptor production is indicated by the dotted line.

Parameter	Meaning	Value
$t^{(T)}$	Starting time of receptor production	61 h
$\Delta t^{(T)}$	Time interval of increasing receptor production	10 h
$\hat{p}^{(T)}$	Maximum receptor production rate	$10^2 \text{ h}^{-1}$
$k^{(T)}$	Receptor degradation rate	$2 \cdot 10^{-2} \text{ h}^{-1}$
$\alpha$	Deterministic temporal growth rule parameter	68%
$d^{(E)}$	Parameter describing expander diffusion	$0 \mu\text{m}^{-1}\text{h}^{-1}$
$D^{(E)}$	Corresponding expander diffusion coefficient	$0 \mu\text{m}^2\text{s}^{-1}$

**Table 7.3.:** Parameter values used to study Tkv<sup>QD</sup> clones. For parameters not listed here, we take the values from the normal wing disc simulations (see tables 4.1 and 4.3).

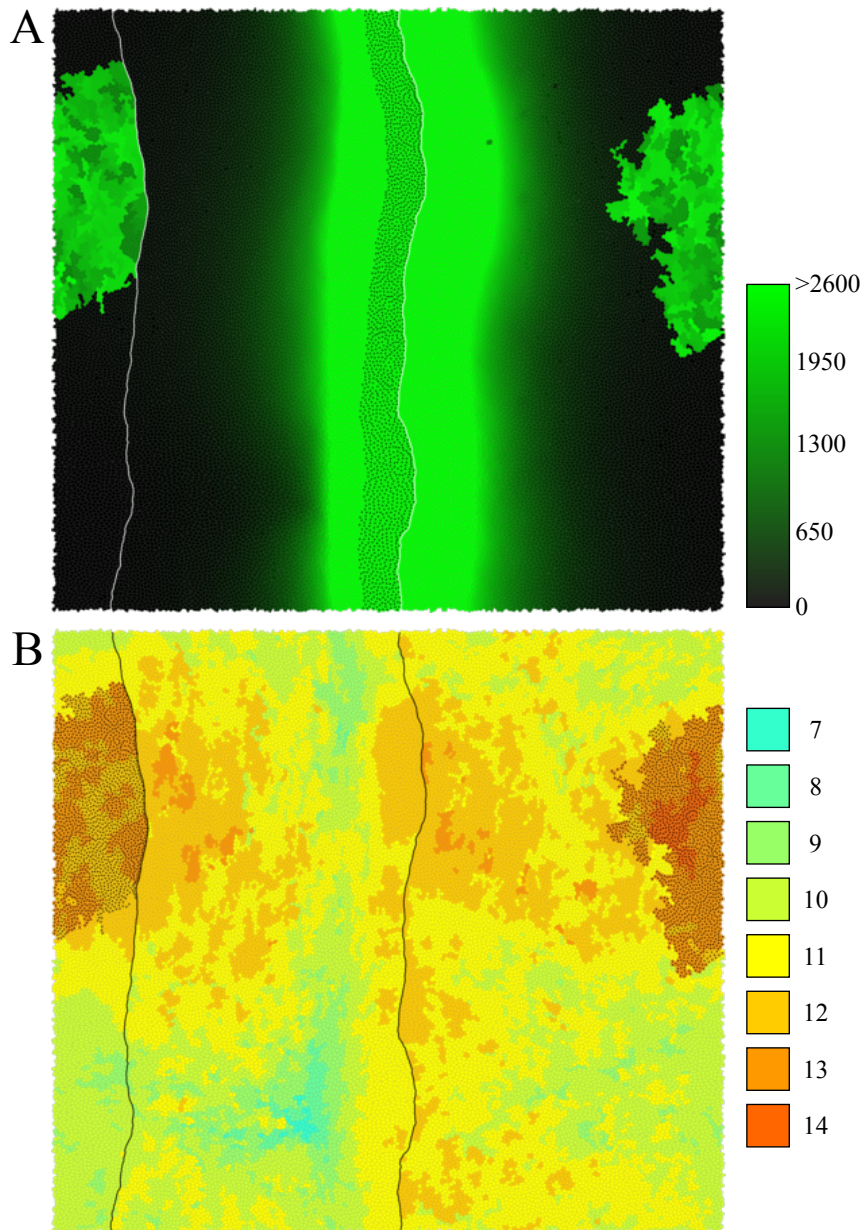


**Figure 7.7.:** Configuration of a system containing a lateral  $Tkv^{QD}$  clone ( $t = 120$  h,  $N = 3 \cdot 10^4$  cells). The  $AP$ -interfaces are indicated by thick lines. (A) Dpp signaling level  $s_i^{(D)}$  shown for each cell by a color code. Dpp producing cells, which are located in the medial region, are indicated by black dots. The  $Tkv^{QD}$  clone in the lateral region is easily recognized by the high signaling levels. (B) Here, the color code indicates the cell generation to which each cell belongs. The starting cells of the simulation belong to generation 1. Each cell division increases the cell generation number by one. The  $Tkv^{QD}$  clone is indicated by black dots.

### 7.3. Changes in the Maximum Growth Rate

Growth is slowed down in cells carrying a *Minute* mutation as compared to non-*Minute* cells due to reduced ribosome levels [119, 144, 112]. To mimic *Minute* mutants in our simulations, we decrease the maximum growth rate by increasing the average residence times in cell cycle state  $M$  and  $I$  (see table 7.4). If the stochastic temporal growth rule is used, the resulting growth curve is inconsistent with experimental data (black line in figure 7.8A). Additionally, the growth rule parameter  $\theta$  has to be changed to match the experimental curve (blue line in figure 7.8A). However, in the case of the deterministic temporal growth rule, the resulting growth curve matches the experimental *Minute* data quantitatively (black line in figure 7.8B).

We therefore further investigate the behaviour of *Minute* mutants using the deterministic temporal growth rule. In the simulations of *minute* wing discs, we choose one cell in the  $P$  population to be the founder of a fast growing non-*Minute* clone. For the non-*Minute* cells we use the same values for  $\bar{\tau}_M$  and  $\bar{\tau}_I$  as for normal wing disc cells (see table 4.1). This non-*Minute* clone does not perturb the growth curve substantially (red line in figure 7.8B).

In experiments it has been observed that non-*Minute* clones created in a *Minute* wing disc can account for a large fraction of a compartment due to their faster growth rate. It has been reported that non-*Minute* clones can account for up to 60% – 90% of a compartment in such experiments [66]. In our simulations we observe a similar effect: although the fraction of non-*Minute* cells is only 2.8% at the onset of the simulation, the non-*Minute* clone accounts for 15% of the total number of cells at the end (red curve in figure 7.9).

To further investigate the behaviour of non-*Minute* clones, we add a mechanical feedback to the growth rule (see section 6.2) and allow for apoptosis by choosing the mechanical parameters appropriately (see table 7.5). In section 6.2 we show that the mechanical feedback and apoptosis have a stabilizing effect on the system. Here, we also observe such a stabilizing effect: the fraction of fast growing non-*Minute* cells is reduced by apoptosis (figure 7.9). However, the effect of the mechanical feedback in the growth rule is not significant (compare the blue and turquoise curves in figure 7.9).

We conclude that the *Minute* mutation is easily described in our simulations if we use the deterministic temporal growth rule. In this case, it is sufficient to decrease the maximum growth rate to account for the growth curve of a pure *Minute* wing disc. Furthermore, the behaviour of simulated fast growing non-*Minute* clones in a *Minute* background is qualitatively the same as in experiments: the relative size of the non-*Minute* clone increases substantially due to its larger maximum growth rate.

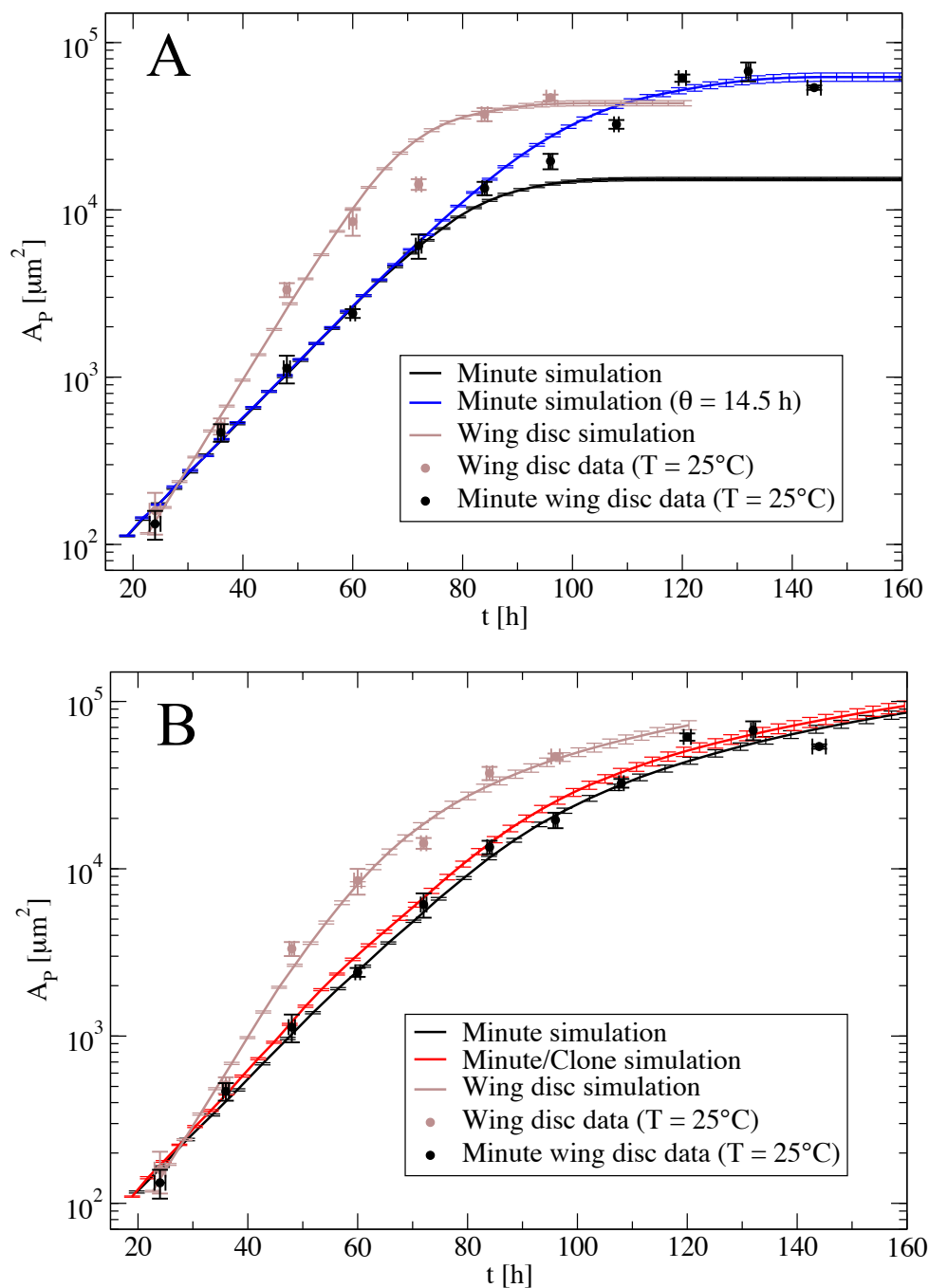


**Figure 7.8.:** Area  $A_P$  of the  $P$  population shown as a function of time. For the Minute and Minute/Clone simulations we use the parameter values given in table 7.4. In the Minute/Clone simulation we create a fast growing non-Minute clone at the onset of the simulation. For the wing disc simulations we use the parameter values given in the tables 4.1 and 4.3. The dilution scaling mechanism is used here. Top (A): Stochastic temporal growth rule. Bottom (B): Deterministic temporal growth rule.

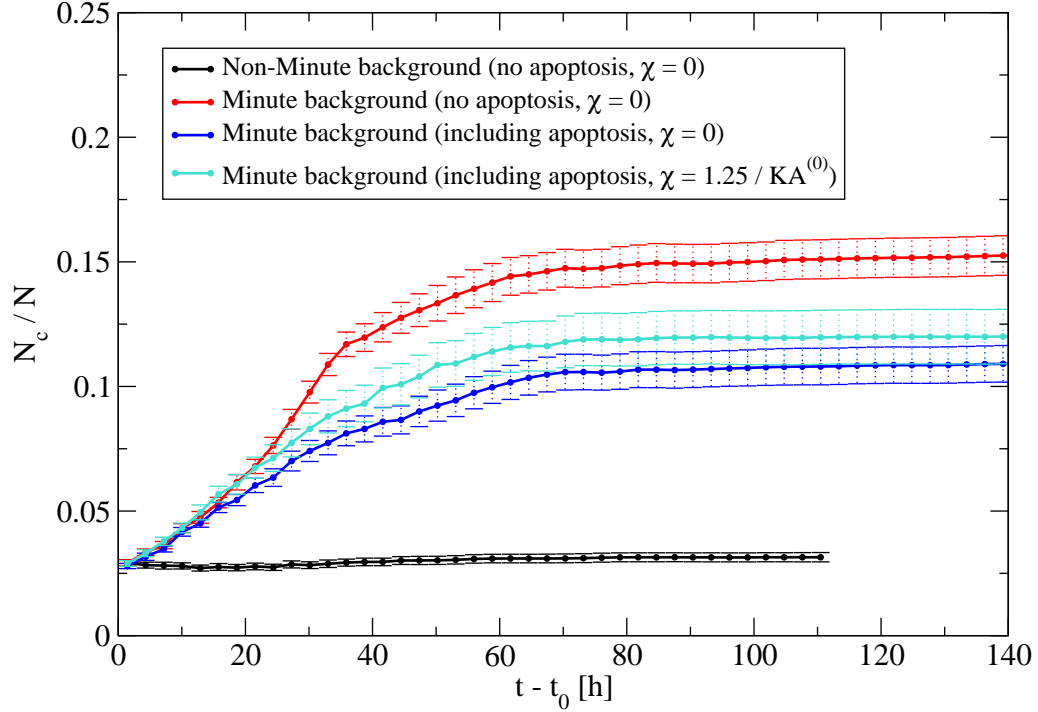


**Figure 7.9.:** Simulations of non-Minute clones in different backgrounds. The number of cells belonging to the non-Minute clone is denoted  $N_c$ , and  $N$  denotes the total number of cells. We use the deterministic temporal growth rule and the dilution scaling mechanism here. The following parameters are used, non-Minute background: see tables 4.1 and 4.3, Minute background without apoptosis: see table 7.4, Minute background with apoptosis: see table 7.5. The parameter value  $\chi = 0$  corresponds to the absence of mechanical feedback;  $\chi = 1.25/KA^{(0)}$  corresponds to the presence of mechanical feedback.

Parameter	Meaning	Value
$\bar{\tau}_I$	Mean residence time in cell cycle state $I$	8 h
$\bar{\tau}_M$	Mean residence time in cell cycle state $M$	1.2 h
$t_0$	Starting time of the simulation	17.5 h

**Table 7.4.:** Parameter values used to simulate Minute mutants. The mean residence times are 1.6 times longer than in the simulations of normal wing discs. For parameters not listed here, we take the values from the normal wing disc simulations (see tables 4.1 and 4.3).

Parameter	Meaning	Value
$\bar{\tau}_I$	Mean residence time in cell cycle state $I$	8 h
$\bar{\tau}_M$	Mean residence time in cell cycle state $M$	1.2 h
$t_0$	Starting time of the simulation	17.5 h
$\Gamma/KA^{(0)}$	Dimensionless cell perimeter stiffness	0.04
$\Lambda/K(A^{(0)})^{3/2}$	Dimensionless cell bond tension	0.12
$\kappa$	$AP$ -interface tension factor	5
$A^{(0)}$	Preferred cell area	$13.7 \mu\text{m}^2$
$\alpha^{(0)}$	Growth rule parameter	0.64
$P^{(0)}/KA^{(0)}$	Growth rule parameter	0.54
$\chi \cdot KA^{(0)}$	Growth rule parameter	0 or 1.25

**Table 7.5.:** Parameter values used to simulate Minute mutants including apoptosis and mechanical feedback (see section 6.2). The parameter  $\chi$  determines the strength of the mechanical feedback. For  $\chi = 0$  there is no feedback, for  $\chi = 1.25/KA^{(0)}$  there is a strong feedback. The mean residence times are 1.6 times longer than in the simulations of normal wing discs. For parameters not listed here, we take the values from the normal wing disc simulations (see tables 4.1 and 4.3).

## 7.4. Fixed Dpp Source Width

In experiments it is possible to replace the diffusible morphogen Hh by membrane-tethered HhCD2 molecules, which are functional but non-diffusible [160]. Therefore, HhCD2 molecules cannot spread in the anterior compartment of the wing disc. Only anterior cells that are bordering the posterior compartment receive a HhCD2 signal, which leads to a one cell diameter wide Dpp source in these mutants. In contrast, the width  $w$  of the Dpp source grows during development in wild type wing discs (see appendix I). The growth rate in the initial, exponential growth phase is smaller in HhCD2 mutant discs as compared to normal discs (see figure 7.10). This difference in the growth rates may be due to a difference in the temperatures at which the larvae are kept, because the speed of development depends on temperature. In the experiments with normal wing discs, the temperature is kept at  $T = 25^\circ\text{C}$ . In contrast, in the experiments with the HhCD2 mutant wing discs, the temperature is kept at  $T = 18^\circ\text{C}$  for the first 48 h after egg laying and at  $T = 30^\circ\text{C}$  for the rest of the time [175]. Furthermore, the ratio between the dad-nRFP decay length  $\lambda_d$  and the width  $L$  of the posterior compartment is different in the HhCD2 mutant disc. A fit of the function  $\lambda_d = m_d L$  using  $m_d$  as fit parameter yields  $m_d = 0.098 \pm 0.004$  in the HhCD2 mutant (not shown) and  $m_d = 0.145 \pm 0.003$  in normal wing discs (see figure 3.1), which suggests that either the diffusion coefficient or the degradation rate of Dpp is different in the HhCD2 mutant.

We perform simulations mimicking HhCD2 mutant wing discs by imposing a Dpp source in the  $A$  population that consists of a given number of cells rows adjacent to



one of the two  $AP$ -interfaces. The morphogen Hh plays no role in these simulations. We use the deterministic temporal growth rule and the dilution scaling mechanism. To match the HhCD2 data, we adjust the growth rate in the initial, exponential growth phase. Although the dad-nRFP decay length in the HhCD2 mutant is different from the wild type, we use the same values for the kinetic Dpp parameters because changing the initial Dpp degradation rate or the Dpp diffusion coefficient does not influence the simulation results significantly.

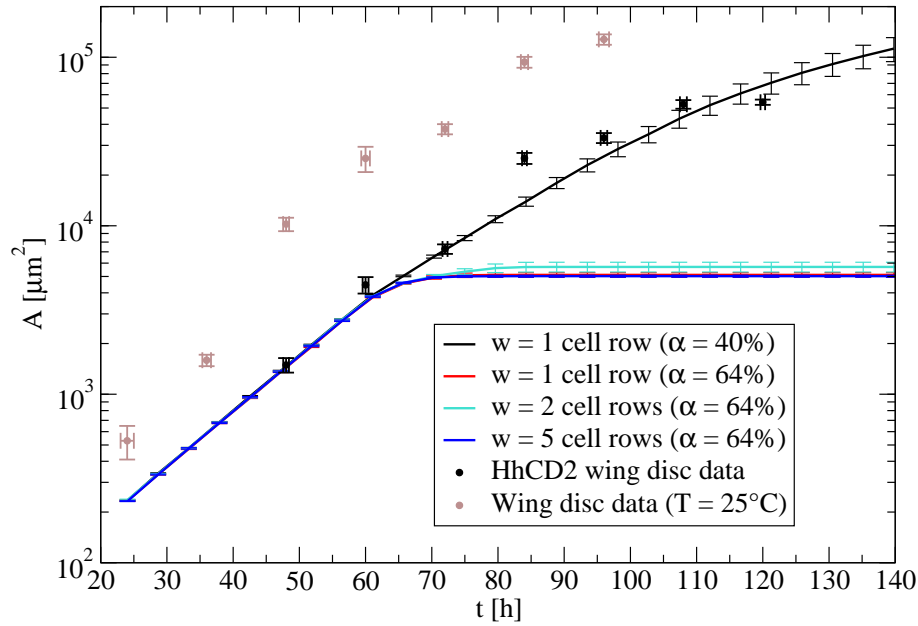


**Figure 7.10.:** Total area  $A$  shown as a function of time. The width of the Dpp source is denoted  $w$ . The parameter values used for the simulations are given in table 7.6.

If the same value for the growth rule parameter  $\alpha$  is used as in the case of the normal wing disc simulation ( $\alpha = 64\%$ ), the simulated HhCD2 mutant stops to grow early (see figure 7.10). Using a broader Dpp source of fixed width does not change this behaviour. The reason for the early termination of growth is that a growing Dpp source in the normal wing disc simulation contributes to an increase of the Dpp level, which stimulates growth. In these simulations the parameter  $\alpha$  is tuned such that the effect of the growing Dpp source is taken into account. Because this effect is missing in the HhCD2 mutant simulation, the parameter  $\alpha$  has to be decreased to match the experimental growth curve.

Although one expects that only Hh molecules are affected in the HhCD2 mutant wing disc, it is conceivable that also the parameter  $\alpha$  must be changed to describe the properties of this mutant correctly. The observation that the ratio between  $\lambda_d$  and  $L$  is different in the HhCD2 mutant as compared to a normal wing disc is already a hint that this mutant is more complex than one would expect.

Parameter	Meaning	Value
$\bar{\tau}_I$	Mean residence time in cell cycle state $I$	8.5 h
$t_0$	Starting time of the simulation	21.7 h

**Table 7.6.:** Parameter values used to simulate HhCD2 mutant wing discs. For parameters not listed here, we take the values from the normal wing disc simulations (see tables 4.1 and 4.3).

## 7.5. System-wide Dpp Production

In experiments the morphogen Dpp can be expressed in the whole wing disc using the so-called C765-Gal4 driver [146]. However, quantitative measurements of the additional Dpp production rate caused by the C765-Gal4 driver are lacking. The growth curves of these C765-Dpp mutant discs differ from the growth curves of normal wing discs (see figure 7.11). During the larval stage of normal wing discs, which ends at the time of pupariation at  $t \approx 110$  h, the C765-Dpp mutant discs are systematically smaller than the normal wing discs (except for the first data point at  $t = 24$  h). However, the larval stage is prolonged by more than 50 hours in the C765-Dpp mutants. The mutant discs continue to grow during this extra time and become larger than normal wing discs in the end.

We mimic the C765-Dpp mutant by adding an extra Dpp production term  $p_+^{(D)}$  to each cell in the vertex model simulation. We perform two different versions of this simulation. In version I, the extra production rate is constant,  $p_+^{(D)} = c$ . In version II, the extra production rate increases linearly with time,  $p_+^{(D)} = r(t - t_0)$ , where  $r$  is the rate of increase and  $t_0$  is the starting time of the simulation. Otherwise, we use the same parameters as in the simulations of normal wing discs (see tables 4.1 and 4.3).

Version I and version II of the C765-Dpp mutant simulation produce similar results. Both the deterministic temporal rule and the time-averaged spatial rule generate growth curves that deviate from the experimental data (see figure 7.11). The additional system-wide Dpp production flattens the Dpp distribution. According to the time-averaged spatial rule, cells only proliferate as long as the relative slope of the Dpp distribution is larger than a threshold (see section 4.2.2). Therefore, the extra Dpp production term reduces the system size if the time-averaged spatial rule is used. In case of the deterministic temporal rule, the system overgrows substantially because the additional Dpp production term leads to faster temporal increases of the Dpp levels.

A plausible explanation for the discrepancy between the simulations and the experimental data is, that the extra Dpp production term introduced in the simulations does not describe the C765-Dpp mutant appropriately. Furthermore, unknown feedbacks, which are not included in the simulation, might stabilize growth of the wing disc against the perturbations induced in the C765-Dpp mutant. In section 7.6 we

discuss an example of such a stabilizing feedback. It is also possible that external factors such as nutrition supply limit the size of the C765-Dpp mutant. Furthermore, the values of the growth rule parameters might have to be changed to describe the properties of the C765-Dpp mutant correctly.

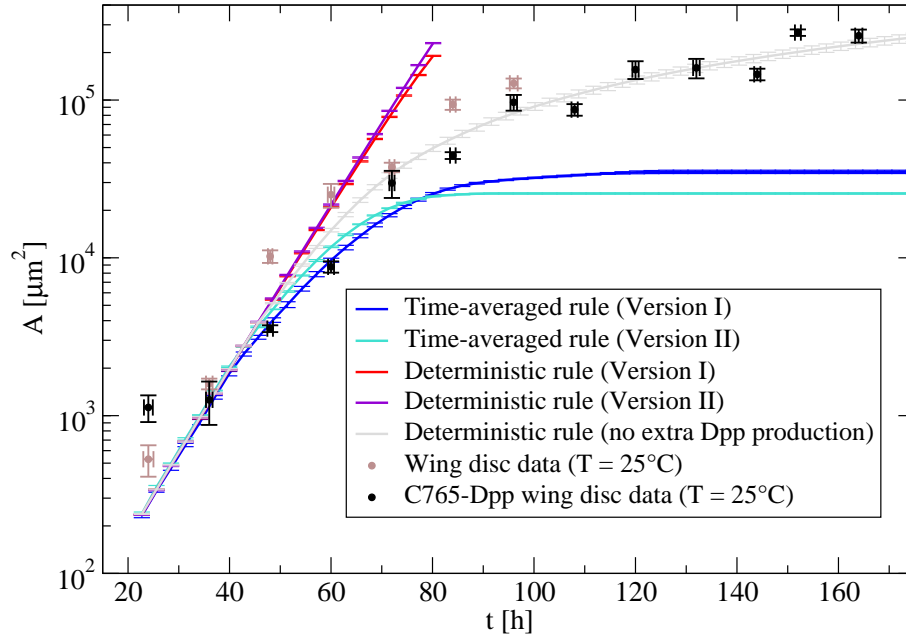


**Figure 7.11.:** Total area  $A$  shown as a function of time. The parameter values used in the simulations are given in the table 7.7. Interestingly, the normal wing disc simulation (no extra Dpp production) matches the C765-Dpp mutant data well.

Parameter	Meaning	Value
$c$	Constant extra Dpp production rate (Version I)	$10^3 \text{ h}^{-1}$
$r$	Rate of increase of extra Dpp production rate (Version II)	$30 \text{ h}^{-2}$

**Table 7.7.:** Parameter values used to study C765-Dpp mutant wing discs. For parameters not listed here, we take the values from the normal wing disc simulations (see tables 4.1 and 4.3).

## 7.6. Nonlinear Dpp Auto-repression

In this section we study the effect of nonlinear Dpp auto-repression on the growth behaviour. To describe Dpp auto-repression, we choose the following rule for the Dpp production rate  $p_i^{(D)}$  in cell  $i$ ,

$$p_i^{(D)} = \begin{cases} p^{(D)} H\left(n_i^{(D)}\right) \Theta\left(n_i^{(H)} - n_T^{(H)}\right) & \text{if } \rho_i = A, \\ 0 & \text{if } \rho_i = P. \end{cases} \quad (7.4)$$

Here,  $n_i^{(D)}$  is the number of Dpp molecules in cell  $i$  and  $n_i^{(H)}$  is the number of Hh molecules in cell  $i$ . The population variable is denoted  $\rho_i$ , the Hh threshold above which Dpp production is switched on in the  $A$  population is denoted  $n_T^{(H)}$ ,  $\Theta$  denotes the Heaviside step function, and  $p^{(D)}$  is the maximum Dpp production rate per cell. The difference between the rule (7.4) and the standard rule (2.6) lies in the term

$$H\left(n_i^{(D)}\right) = \frac{R^h}{\left(n_i^{(D)}\right)^h + R^h}, \quad (7.5)$$

which describes Dpp auto-repression by a Hill-type function with parameters  $h$  and  $R$ . Dpp auto-repression kicks in when the Dpp level in the cell becomes comparable to the repression level  $R$ . Here, we choose the deterministic temporal growth rule and the dilution scaling mechanism. We use the same parameter values as in the normal wing disc simulations if not stated otherwise (see tables 4.1 and 4.3).

The nonlinear feedback has a stabilizing effect on the system. Without auto-repression, the system overgrows if the parameter  $\alpha$  of the deterministic temporal rule is chosen too small (e.g.  $\alpha = 50\%$ ). However, if auto-repression is activated, the growth curves can be tuned to match the experimental data by choosing the repression level  $R$  appropriately, even for small values of  $\alpha$  (see figure 7.12). Dpp levels increase during growth so that Dpp auto-repression becomes important at the end of the growth phase. Therefore, Dpp auto-repression can change the shape of the growth curve at the end of the growth phase without influencing the initial growth phase much. Furthermore, already a small change of the average Dpp production rate due to auto-repression can have a large impact on the growth rate. For example, for  $\alpha = 64\%$ , activation of Dpp auto-repression reduces the average Dpp production rate only by approximately 20% (for  $R = 6000$ , see figure 7.13). However, this reduction substantially changes the shape of the growth curve at late times (compare the black and red curves in figure 7.12).

Nonlinear Dpp auto-repression is an example of a feedback that stabilizes the system and provides a mechanism to fine-tune the shape of the growth curves. It is likely that similar feedbacks stabilize growth in the wing disc.

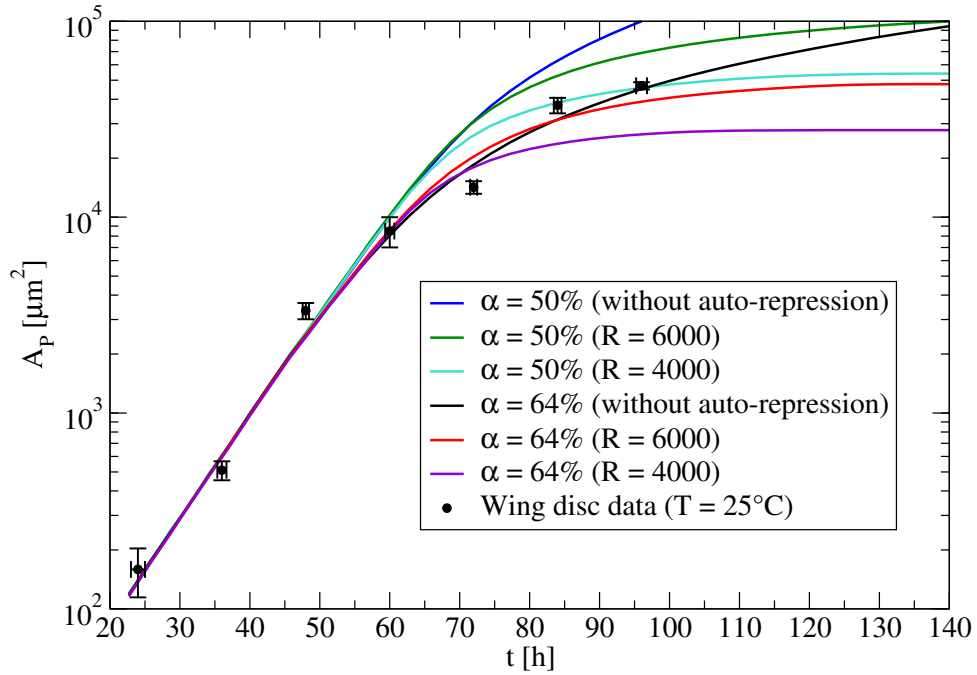


**Figure 7.12.:** Area  $A_P$  of the  $P$  population shown as a function of time. Here we choose the Hill coefficient  $h = 4$ .

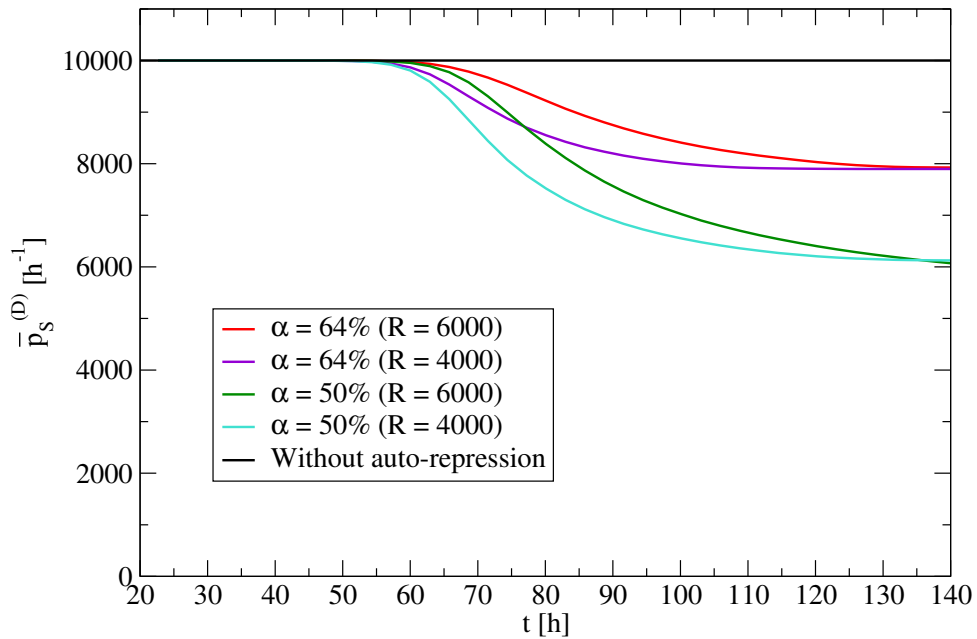


**Figure 7.13.:** Average Dpp production rate  $\bar{p}_S^{(D)}$  in the Dpp source shown as a function of time. The Dpp source consists of all cells that are characterized by a non-zero Dpp production rate. Here we choose the Hill coefficient  $h = 4$ .

**Summary** In this chapter we studied self-organized growth under perturbed conditions to further check the consistency between theory and experiment, focusing on the deterministic temporal growth rule. The first perturbation we applied to the system was to use parameter values estimated from haltere discs. The haltere is an organ important for the stability during flight. It is related to the wing, but it is much smaller. We estimated that the kinetic parameters of Dpp are approximately tenfold smaller in the haltere disc. Using the parameter values estimated for the haltere disc resulted in a growth curve exhibiting good agreement with experimental data. Moreover, we simulated wing discs in which the Dpp source width is fixed to one cell diameter as in the HhCD2 mutant. The growth behaviour is sensitive with respect to this mutation. The resulting growth curve is only in agreement with the experimental data if the growth rule parameter is changed substantially. Another perturbed condition that we simulated is system-wide Dpp production. The system becomes much larger in the simulation as compared to corresponding experiments. However, the corresponding mutant wing disc is not well understood. We argued that the discrepancy between theory and experiment may also be explained by external factors such as limited nutrition supply or by unknown feedbacks that stabilize the wing disc against perturbations. We also studied the effect of producing permanently active Dpp receptors in cell clones. We showed that clones in which the receptor is produced become larger than normal clones. The amount of overgrowth depends on the position of the clone. If the clone is far away from the Dpp source, then the clone overgrows more than if it is close to the source. These results are in good quantitative agreement with experimental measurements. We furthermore investigated the effects of decreasing the maximum growth rate of the system. We found that the deterministic growth rule is robust with respect to this perturbation. The growth curve agrees with experimental data from wing discs in which the maximum growth rate is decreased due to a Minute mutation. We finally discussed a possible stabilizing feedback. We demonstrated that the growth behaviour generated by the deterministic temporal rule can be stabilized by nonlinear Dpp auto-repression.

## 8. Conclusion

In this thesis we have studied self-organized growth in developing tissues from a theoretical viewpoint, focusing on the *Drosophila* wing disc as a model system. In chapter 1 this model system was introduced, and the reader was also familiarized with the necessary biological background, such as the experimental findings that the morphogen Decapentaplegic (Dpp) controls growth in the wing disc, and that growth is approximately homogeneous in space. Furthermore, we presented existing theoretical approaches to describe growth in epithelia, the formation of morphogen gradients, and growth control in the wing disc.

In chapter 2 we introduced a general theoretical description of morphogen gradients and growth in epithelia. This description is based on a two-dimensional vertex model in which cells are represented as polygons and mechanical tissue properties are taken into account. The distribution of morphogens within the cellular network is described by assigning molecule numbers to each cell. The dynamics of these distributions is described by systems of coupled differential equations that allow for molecule exchange between neighbouring cells. Furthermore, the cell cycle is described by introducing a cell cycle variable that can assume three different states. We have applied this model to describe the key features of the wing disc with regard to growth and morphogen distributions.

In chapter 3 we studied scaling of the Dpp distribution. Scaling means that the characteristic decay length of the exponential Dpp distribution is proportional to the width of the wing disc. We analysed experimental data and concluded that scaling is caused by a temporal decrease in the Dpp degradation rate. Using our theoretical description of the wing disc, we studied two mechanisms that may underlie scaling. Both mechanisms rely on an additional molecule species that we call the expander. The expander behaves differently in the two scaling mechanisms, but in both cases the expander ensures that the Dpp degradation rate decreases appropriately while the system grows. In the dilution scaling mechanism, expander molecules are neither degraded nor produced, but they are provided initially and subsequently diluted due to growth. We showed that the Dpp gradient scales if the Dpp degradation rate is proportional to the local expander concentration.

The expansion-repression scaling mechanism relies on a feedback loop between the Dpp distribution and expander production. Expander molecules are not degraded, but they are produced where the Dpp concentration is sufficiently low. The Dpp degradation rate depends on the local expander concentration in such a way that

increasing the expander concentration causes an increase in the Dpp decay length. We demonstrated that this feedback leads to an exponential Dpp distribution that approximately scales, if the diffusion coefficient and the production rate of the expander are sufficiently large. We showed that the required magnitudes of these two quantities depend on the growth rate of the system.

We have not been able to decide if the dilution mechanism or the expansion-repression mechanism describes scaling in the wing disc correctly. Future experiments, in which scaling under perturbed conditions is studied, are required to determine which mechanism operates in the wing disc. In appendix A, we furthermore checked if a nonlinearity in the Dpp degradation term is an alternative explanation for the observed scaling of the Dpp distribution. We concluded that this is not the case.

In chapter 4 we explored how growth of developing tissues can be controlled in a self-organized way. For that purpose we formulated four different growth rules for the vertex model. These growth rules govern cell divisions based on the local Dpp level. In general, the resulting growth behaviour does not only depend on the growth rule but also on the scaling mechanism. Therefore we discussed the resulting growth behaviour for the dilution mechanism as well as the expansion-repression mechanism. Two growth rules, which we denoted spatial rules, depend on the slope of the Dpp distribution. Essentially, these rules impose that cells divide as long as the local relative slope is larger than a threshold. We showed that the system exhibits an instability if the instantaneous slope of the Dpp distribution is considered. In this case, local perturbations of the Dpp gradient caused by cell divisions can trigger further cell divisions nearby, leading to travelling waves of proliferation, which are inconsistent with experimental observations. We demonstrated that this instability can be eliminated by considering the time-averaged slope of the Dpp distribution in the growth rule. In this case, fluctuations are damped and growth stops reliably. However, this rule generates spatially inhomogeneous growth: in the maximum and minimum of the Dpp distribution, almost no cell division occur. Such a striking inhomogeneity has not been reported in experimental studies of the wing disc. Therefore, we argued that the spatial growth rules do not correctly describe growth control in the wing disc.

The two other growth rules studied in chapter 4 have been denoted temporal rules, because they depend on temporal changes in the cellular Dpp concentration. These growth rules are based on the idea that the Dpp signaling pathway is sensitive to relative changes of the input signal. One such growth rule, which we call deterministic temporal rule, imposes that a cell division occurs when the cellular Dpp concentration has increased by a certain relative amount. The other temporal rule, which we call stochastic temporal growth rule, imposes two cell types: proliferating cells and non-proliferating cells. Whether a cell generated by a cell division is a proliferating cell or not depends stochastically on the temporal increase of the Dpp concentration in the precursor cell. We showed that both temporal rules gener-



ate similar growth behaviour. The expansion-repression scaling mechanism leads to strongly inhomogeneous growth that is inconsistent with experimental observations. In contrast, growth is approximately homogeneous and the growth curves agree well with experimental data if the dilution mechanism is chosen to ensure scaling of the Dpp distribution.

Although the deterministic temporal rule and the stochastic temporal rule exhibit many similarities, we found significant differences. At late times corresponding to the end of larval development, the stochastic temporal rule leads to the complete termination of growth, whereas the deterministic temporal rule leads to a finite growth rate. Thus, these two rules could be distinguished by careful experiments that determine if there are mitotic cells in the wing disc immediately before the pupal stage of development. Moreover, we showed that the two growth rules generate different clone size distributions. The deterministic temporal rule generates distributions that exhibit striking peaks at cell numbers that are powers of two, whereas the stochastic temporal rule leads to smooth distributions.

The main result of chapter 4 is the finding that one of the temporal growth rules may correctly describe growth control in the wing disc. However, this finding requires that scaling of the Dpp distribution is caused by a mechanism equivalent to the dilution scaling mechanism.

In chapter 5 we developed mean field approximations of the systems that were studied in chapter 4. We argued that the relaxation time of the Dpp distribution is determined by the Dpp degradation rate. Using this result and taking advantage of the spatial homogeneity of growth, we demonstrated that the vertex model simulations can be approximated by nonlinear dynamical systems. We found that the effective growth rule parameters of these dynamical systems must be renormalized with respect to the parameters of the vertex model simulations.

The interplay between tissue growth and mechanical stresses was investigated in chapter 6. We first studied the impact of proliferation on mechanical stresses. We found that a locally increased proliferation rate results in a local pressure increase, which in turn leads to a locally increased apoptosis rate. Conversely, a locally decreased proliferation rate results in a local pressure decrease and a locally decreased apoptosis rate. We then explored how mechanical stresses can influence self-organized growth. For this purpose we used the deterministic temporal growth rule and added a mechanical feedback that inhibits proliferation at high pressures and stimulates proliferation at low pressures. We found that this feedback has a stabilizing effect on the system, as growth inhomogeneities, pressure fluctuations, and the rate of cell death are reduced.

In chapter 7 we studied self-organized growth under perturbed conditions, most of which corresponded to mutant wing discs for which experimental data is available. The aim of this chapter was to further check the consistency between theory and

experiment. We focused on the deterministic temporal growth rule because it had already shown good agreement with experimental data in chapter 4. We showed that this growth rule results in a growth behaviour that is consistent with experimental data for haltere discs and Minute mutants. Furthermore, this growth rule could explain key features observed in experiments with clones expressing permanently active Dpp receptors. These experiments are particularly important because they allow to externally manipulate the Dpp signaling levels in clones. For two mutant conditions that are less well understood, the HhCD2 mutant and the mutant with ubiquitous Dpp expression, the agreement between simulation and experiment was less good though. We furthermore discussed a possible stabilizing feedback. We demonstrated that the growth behaviour generated by the deterministic temporal rule can be stabilized by nonlinear Dpp auto-repression.

In this work we have proposed a growth rule that governs cell divisions in the *Drosophila* wing imaginal disc. According to this growth rule, a cell division occurs when the cellular Dpp concentration has increased by a certain relative amount. This growth rule can explain many key observations that have not been understood so far, for example the spatial homogeneity of growth, the different sizes of wing and haltere, and the behaviour of clones expressing permanently active Dpp receptors. Future experiments, for example *in vitro* experiments in which cell cultures grow under controlled conditions, will have to show if the suggested growth rule truly captures the essence of growth control in the wing imaginal disc.

## A. Scaling Behaviour of Non-exponential Morphogen Gradients

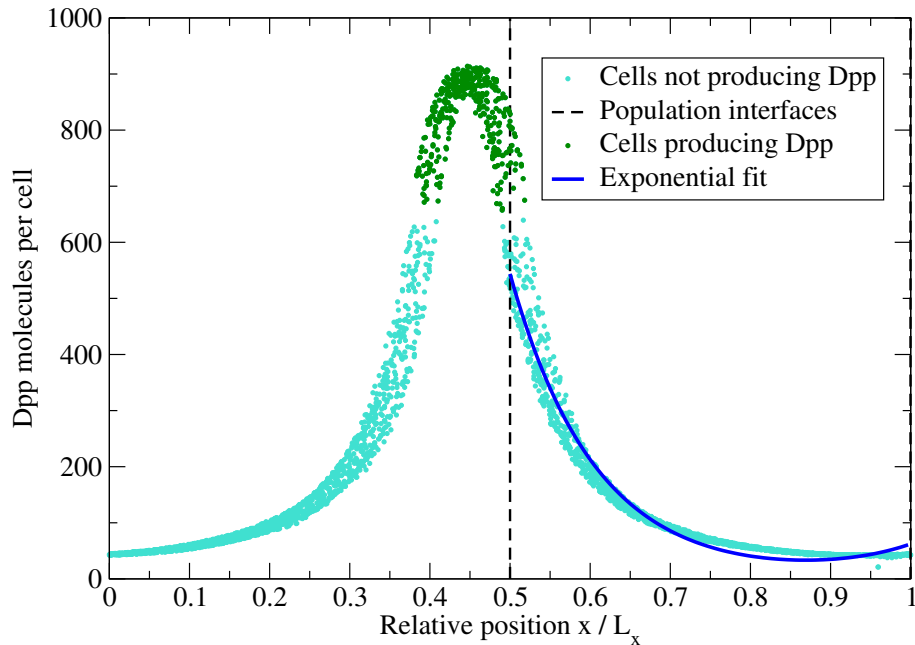


**Figure A.1.:** Projection of a non-exponential Dpp gradient on the  $x$ -axis at  $t = 63$  h ( $N = 3600$ ,  $L_x = 160 \mu\text{m}$ ,  $L = 80 \mu\text{m}$ ,  $k^{(D)} = 0.01 \text{ h}^{-1}$ ,  $m = 2$ ). Each point corresponds to a cell. Due to the nonlinearity, Dpp is degraded slowly when Dpp levels are low. Therefore the Dpp levels are comparably high far from the Dpp source. The exponential fit (see caption of figure 3.5 on page 27) yields  $B_1 = 543 \pm 2$ ,  $B_2 = 0.51 \pm 0.02$ , and  $\lambda = (17.0 \pm 0.1) \mu\text{m}$ .

In this section we show that the assumption of a nonlinear Dpp degradation term does not provide a simple explanation for the experimentally observed scaling of the Dpp gradient. We perform this analysis because we cannot exclude the possibility that the Dpp gradient in the wing disc follows a power law rather than an exponential function (see appendix J). Power law gradients are scale free so that the system size  $L$  would be the only length scale in such a system. Fitting exponential functions to

power law gradients would impose the system size upon the exponential functions and yield values for  $\lambda$  that increase with  $L$ .

To test if a misinterpretation of power law gradients as exponential gradients provides a simple explanation for the observed proportionality between  $\lambda$  and  $L$ , we fit exponential functions to non-exponential Dpp gradients generated in the vertex model, and display the obtained decay length  $\lambda$  as a function of  $L$ . The fitting procedure is explained in the caption of figure 3.5. The non-exponential Dpp gradients are generated using a nonlinear Dpp degradation term, which is proportional to the  $m$ -th power of the cellular Dpp level. In contrast to section 3.2, the coefficient  $k^{(D)}$  of the degradation term is the same for all cells and is kept constant here. The nonlinear dynamic equations governing the Dpp gradient are thus given by

$$\frac{d}{dt}n_i^{(D)} = p_i^{(D)} - k^{(D)} \left(n_i^{(D)}\right)^m + d^{(D)} \sum_j b_{ij} \left(n_j^{(D)} - n_i^{(D)}\right). \quad (\text{A.1})$$

For  $m \neq 1$ , the steady state Dpp gradient outside of the Dpp source follows the power law  $n^{(D)}(x) \sim (x + x_0)^{2/(1-m)}$  in a continuum description with infinite system size. Here,  $x$  is the distance from the Dpp source and  $x_0$  is a constant. We use two different exponents,  $m = 2$  and  $m = 1.65$ , and vary the coefficient  $k^{(D)}$  over three orders of magnitude, respectively. The other parameters are the same as in section 3.2. The parameter value  $m = 1.65$  is obtained by fits of power laws to GFP-Dpp gradients (see appendix J.1.2).

Indeed, the decay lengths  $\lambda$  obtained by exponential fits increase with increasing system size  $L$  (see figure A.2). However, for all parameter values used, the slope of these curves is too small to account quantitatively for the experimental data. We conclude that a nonlinear Dpp degradation term with a fixed rate coefficient does not provide an alternative explanation for the experimentally observed scaling of the Dpp gradient in the wing disc.

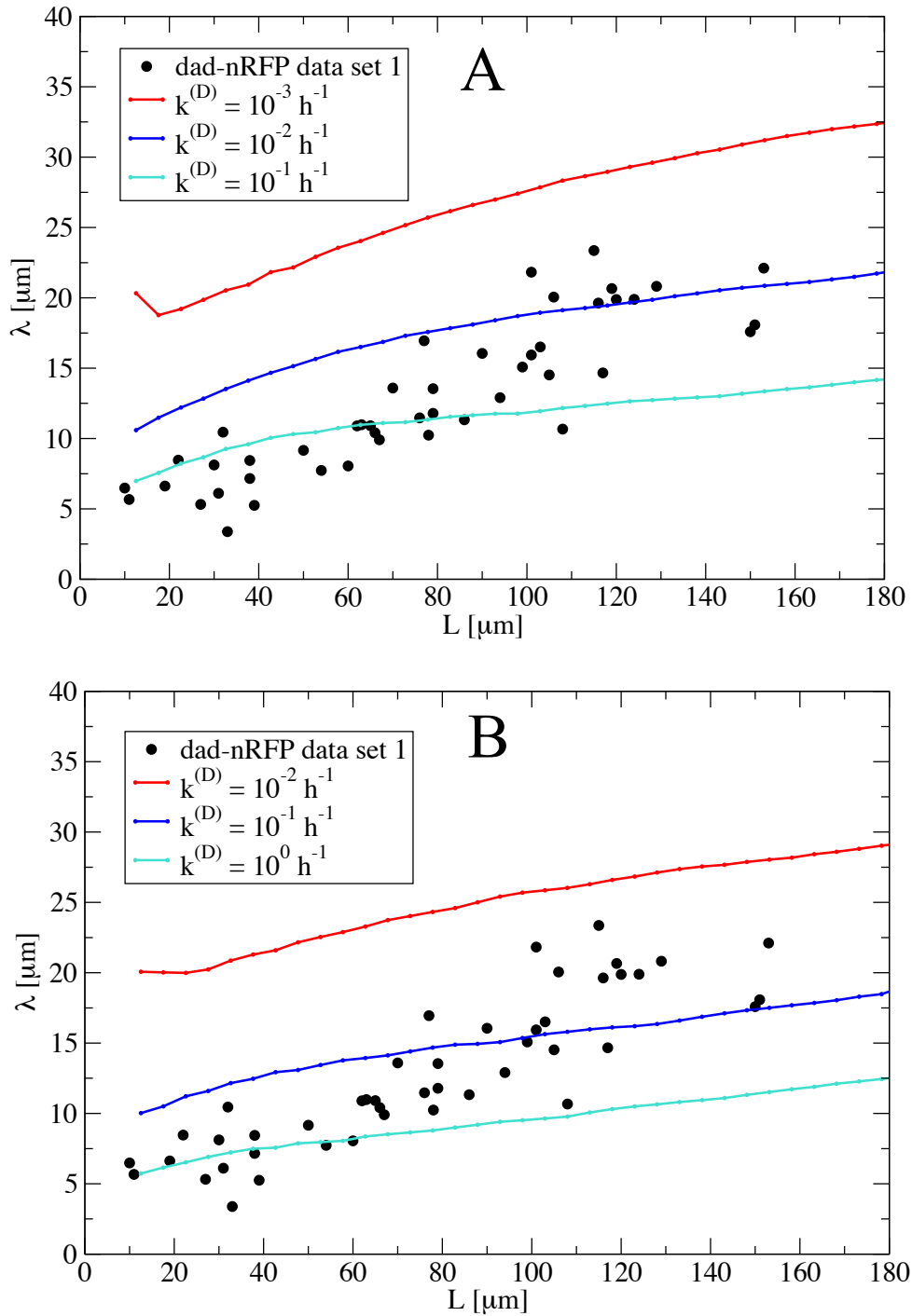


**Figure A.2.:** Decay length  $\lambda$  of non-exponential Dpp gradients shown as a function of  $L$ . Top (A):  $m = 2$ . Bottom (B):  $m = 1.65$ .



## B. Sensitivity of the Growth Rules with Respect to Initial Conditions

Here we investigate how sensitive the growth rules introduced in chapter 4 are with respect to initial conditions. For that purpose we apply the growth rules from the beginning of the simulation on, when the system is small and fluctuations are strong. In chapter 4 the growth rules were not applied from the beginning on, but after a tenfold increase in system size ( $N_g = 360$ ). The parameter  $N_g$  determines when the growth rule is switched on. As long as the number of cells obeys  $N < N_g$ , the system is forced to grow exponentially with the maximum growth rate. If  $N \geq N_g$ , growth is governed by the growth rule. The parameter values used in the simulations are given in the tables 4.1 and 4.3 on pages 52 and 53.

### B.1. Deterministic Temporal Rule

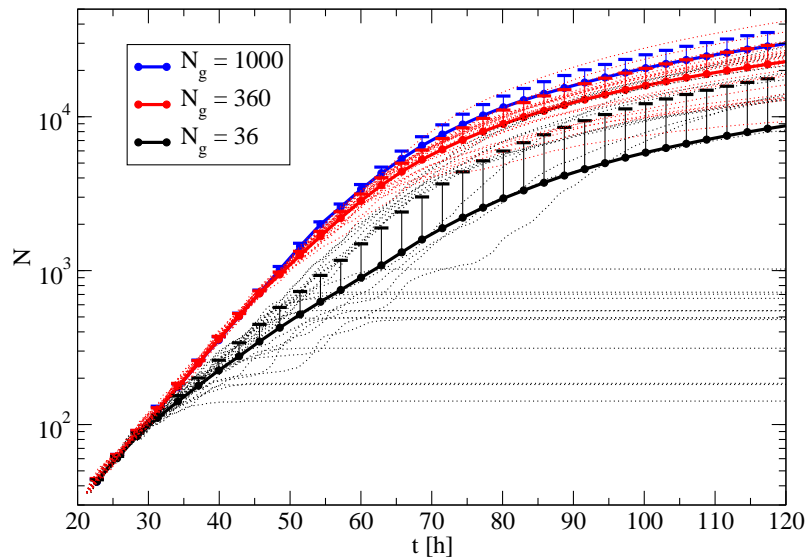


**Figure B.1.:** Mean number of cells  $N$  shown as a function of time, obtained from 25 realizations of the simulation using the deterministic temporal rule with the dilution scaling mechanism ( $\alpha = 64\%$ ). The one-sided error bars indicate the standard deviation. Individual realizations are shown as dotted lines for  $N_g = 36$  and  $N_g = 360$ .

The system behaviour is sensitive to initial conditions. If the growth rule is applied from the onset of the simulation on, the relative variance of the resulting growth curves becomes considerable, and in many realizations of the simulation the system stops to grow early, when consisting of only a few hundred cells (see figure B.1).

If the growth rule is switched on after a tenfold increase in system size, these early terminations of growth do not occur, the system becomes larger, and the relative variance of the growth curves is reduced (see figure B.1). Instead of switching on the growth rule at later times, the relative variance of the growth curves can also be reduced by using a Dpp source that is more regular and exhibits less fluctuations (see figure B.2). Using the stabilized Dpp source described in the caption of figure B.3 has a similar effect as switching on the growth rule after a tenfold increase in system size. The strong effect of Dpp source fluctuations on the variance of the growth curves might be a reason for additional feedbacks in the Hh signaling network that provide robustness to the Dpp source [52, 86]. For vanishing expander diffusion coefficient  $D^{(E)}$  the sensitivity to initial fluctuations is less pronounced (data not shown).

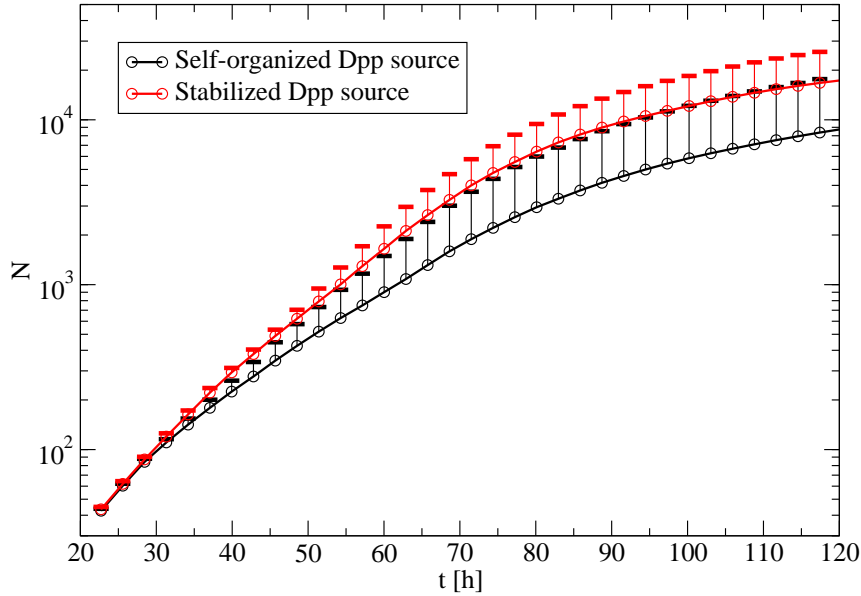


**Figure B.2.:** Mean number of cells  $N$  shown as a function of time, obtained from 25 realizations of the simulation using the deterministic temporal rule with the dilution scaling mechanism ( $\alpha = 64\%$ ). The one-sided error bars indicate the standard deviation. In these simulations, the growth rule is applied from the beginning on ( $N_g = 36$ ). The difference between the two Dpp sources is explained in the caption of figure B.3. The solid black line is the same as in figure B.1.



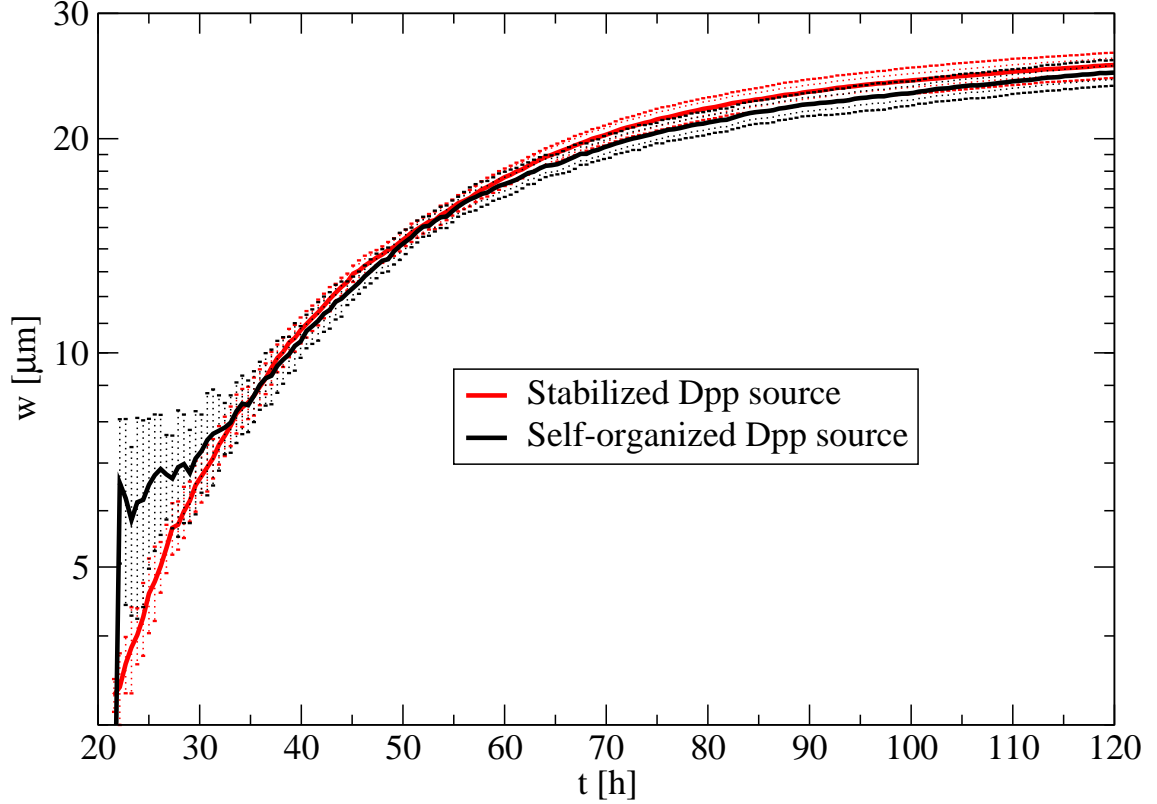


**Figure B.3.:** Mean Dpp source width  $w$  shown as a function of time, obtained from 25 realizations of the simulation using the deterministic temporal rule with the dilution scaling mechanism ( $\alpha = 64\%$ ,  $N_g = 360$ ). The error bars indicate the standard deviation, which is a measure for the fluctuations of the source width. At early times, the width of the self-organized source is significantly bigger, is less smooth as a function of time, and exhibits stronger fluctuations as compared to the width of the stabilized Dpp source. The self-organized Dpp source is generated in response to Hh molecules, see section 2.3.1, and is used in all simulations if not stated otherwise. The stabilized Dpp source obeys the following rule: cell  $i$  produces Dpp molecules with rate  $p^{(D)}$ , if  $\rho_i = A$ , and if the minimum distance from the center of cell  $i$  to any vertex belonging to one particular  $AP$ -interface is smaller than  $f(L) = b_1 \ln(L/b_2)$ . Here,  $L$  is the width of the  $P$  population and  $b_1$  and  $b_2$  are parameters (see table 4.1).

## B.2. Stochastic Temporal Rule

Similar to the case of the deterministic temporal rule, the system behaviour is sensitive to initial conditions. Switching on the growth rule later by increasing  $N_g$  reduces the relative variance of the growth curves, and also increases the system size (see figure B.4). Using a stabilized Dpp source has qualitatively the same effect on the system (see figure B.5), similar to the case of the deterministic temporal rule.

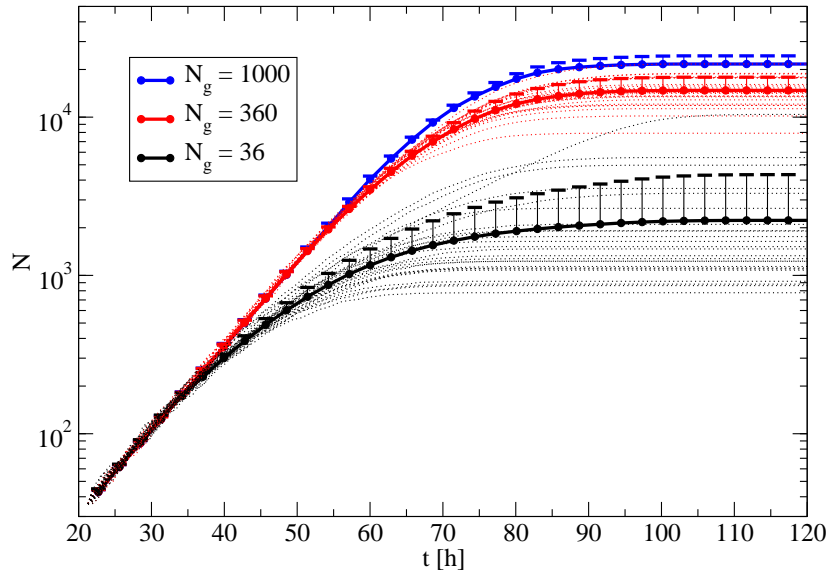


**Figure B.4.:** Mean number of cells  $N$  shown as a function of time, obtained from 25 realizations of the simulation using the stochastic temporal rule with the dilution scaling mechanism ( $\theta = 9$  h). The one-sided error bars indicate the standard deviation. Individual realizations are shown as dotted lines for  $N_g = 36$  and  $N_g = 360$ .

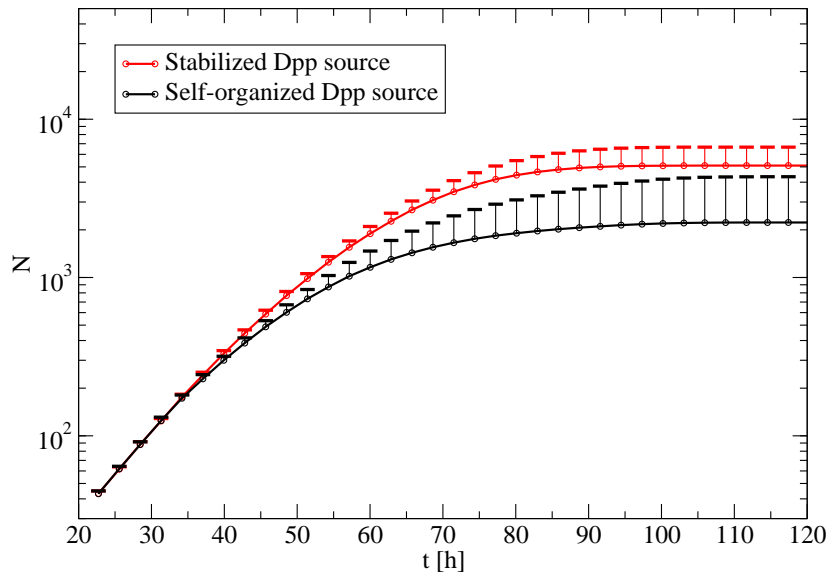


**Figure B.5.:** Mean number of cells  $N$  shown as a function of time, obtained from 25 realizations of the simulation using the stochastic temporal rule with the dilution scaling mechanism ( $\theta = 9$  h). The one-sided error bars indicate the standard deviation. In these simulations, the growth rule is applied from the beginning on ( $N_g = 36$ ). The difference between the two Dpp sources is explained in the caption of figure B.3. The solid black line is the same as in figure B.4.

### B.3. Time-averaged Spatial Rule

The time-averaged spatial rule is insensitive with respect to initial conditions: whether the growth rule is applied from the onset of the simulation on or after a tenfold increase in system size has a negligible effect on the mean and standard deviation of the resulting growth curves (see figure B.6).

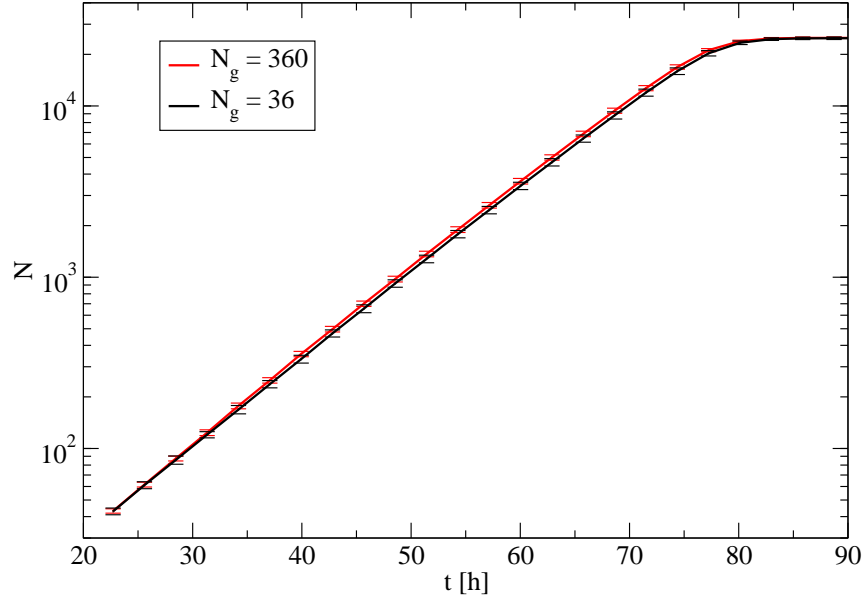


**Figure B.6.:** Mean and standard deviation of the number of cells  $N$  shown as a function of time for the time-averaged spatial rule with the dilution scaling mechanism ( $u_T = 0.375$ ,  $\tau_u = 5$  h). The growth rule is applied if  $N > N_g$ . The coefficients of variation of the final sizes are 1.7% ( $N_g = 36$ ) and 1.2% ( $N_g = 360$ ). The relative difference between the means of the final sizes is 0.5%.



## C. Dynamic Range and Uncertainty of Local Dpp Levels

Growth control by the Dpp gradient requires a signaling system that is able to deal with Dpp concentrations of different orders of magnitude. The dynamic range of Dpp signaling can be estimated by comparing the highest and lowest Dpp levels in the system. We find in our simulations, using the deterministic temporal rule and the dilution scaling mechanism, that the dynamic range increases with time but that it does not exceed three orders of magnitude (figure C.1). The parameter values used in the simulation are given in the tables 4.1 and 4.3 on pages 52 and 53.

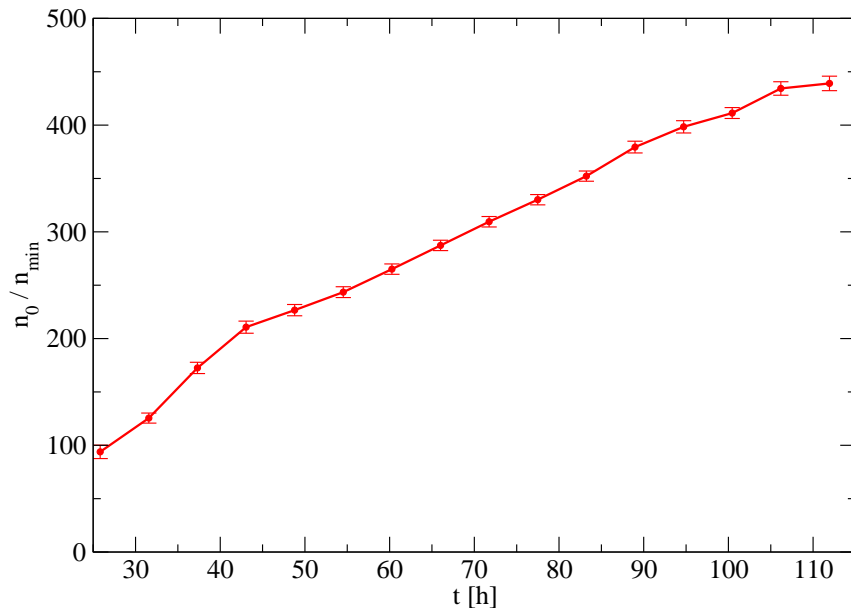


**Figure C.1.:** Dynamic range of the Dpp gradient in the  $P$  population shown as a function of time. The maximum and minimum number of Dpp molecules per cell,  $n_0$  and  $n_{\min}$ , are determined by curve fitting as described in figure 3.5.

Furthermore we estimate the minimal Dpp concentration in the system using simulations. We find that the number of Dpp molecules in the minimum of the gradient is of the order of 10 molecules per cell. Low molecule numbers and finite measurement time lead to an uncertainty in the Dpp signal [17]. The relative uncertainty is

given by

$$\frac{\Delta c}{c} = (5\pi T D c a / 3)^{-1/2}. \quad (\text{C.1})$$

Here,  $\Delta c$  is the concentration uncertainty,  $c$  is the mean concentration,  $T$  is the measurement time,  $D$  is the diffusion coefficient, and  $a$  is the radius of the measurement volume. Using simulations, we estimate  $\Delta c/c$  in lateral regions where Dpp levels are minimal and thus the relative uncertainty maximal. For the measurement time  $T$  we take a typical cell cycle time  $\tau$ , which we estimate from the growth rate  $g$  by the relation  $\tau \approx \ln(2)/g$ , and we choose  $a = 2.5 \mu\text{m}$ ,  $D = 0.1 \mu\text{m}^2/\text{s}$ . Figure C.2 shows that even in lateral regions there are enough molecules to determine the Dpp signal with considerable precision, due to the available measurement time. The relative uncertainty decreases with time because both the available measurement time and the minimal Dpp concentration increase with time. The relative uncertainty is small compared to the parameter  $\alpha$  used in the deterministic temporal rule, which shows that growth can indeed be controlled by the Dpp gradient, in spite of low molecule numbers.

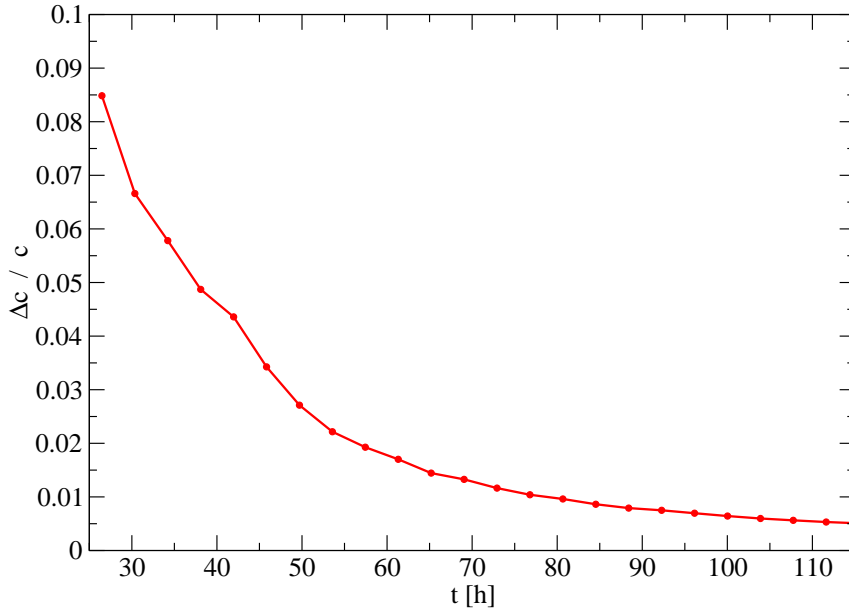


**Figure C.2.:** Estimated relative concentration uncertainty in the minimum of the Dpp gradient, shown as function of time.

## D. Estimation of the Mechanical Forces in the Wing Imaginal Disc

Here we estimate the magnitude of the mechanical forces acting on cells in the wing imaginal disc. The parameter  $K$  of the vertex model (see chapter 2), which describes the elasticity of cells, can be related to the Young's modulus  $E$  [99]. Dimensional analysis yields  $K \simeq hE/A^{(0)}$ , where  $h$  is the height of a cell. The Young's modulus  $E$  has not yet been measured for wing disc cells, but it has been measured for other cell types. These measurements can be used to estimate the magnitude of the parameter  $K$ . The literature provides the following values:  $E = 1 - 50$  kPa for human platelets [137],  $E = 37$  kPa for young human epithelial cells [16],  $E = 1$  kPa for fibroblasts [106]. In general, the Young's modulus is of the order  $1 - 100$  kPa in biological cells [7, 90]. Using the values  $E = 10$  kPa,  $h = 30 \mu\text{m}$ , and  $A^{(0)} = 10 \mu\text{m}^2$ , we estimate

$$K \approx 0.03 \mu\text{N}/\mu\text{m}^3. \quad (\text{D.1})$$

Typical pressures are thus of the order  $KA^{(0)} \approx 0.3 \mu\text{N}/\mu\text{m}$ . Using the values for the dimensionless mechanical parameters given in table 6.1, we get the following estimates for the cell bond tension and cell perimeter stiffness,

$$\Lambda \approx 0.1 \mu\text{N}, \quad \Gamma \approx 0.01 \mu\text{N}/\mu\text{m}. \quad (\text{D.2})$$

Considering these estimates for the parameters  $K$ ,  $\Lambda$ , and  $\Gamma$ , we conclude that forces of the order of  $0.1-1 \mu\text{N}$  act on a cell in the wing imaginal disc.





# E. Growth and Apoptosis Rates

## E.1. Continuous System

### E.1.1. Definitions

In a system where the number of cells is described by a continuous variable  $N$ , we define the growth rate  $g$  by

$$g = \frac{dN_g}{Ndt}, \quad (\text{E.1})$$

where  $dt$  denotes an infinitesimal time interval, and  $dN_g \geq 0$  is the increase in system size within that time interval due to growth. The time-averaged growth rate  $g_T(t)$  we define by

$$g_T(t) = \frac{1}{T} \int_{t-T/2}^{t+T/2} dt' g(t') = \frac{1}{T} \int \frac{dN_g}{N}, \quad (\text{E.2})$$

where  $T$  is the time over which the growth rate is averaged. Analogously, we define the apoptosis rate  $\Omega$  by

$$\Omega = \frac{dN_\Omega}{Ndt}, \quad (\text{E.3})$$

where  $dN_\Omega \geq 0$  is the decrease in system size within the time interval  $dt$  due to cell death. The total change in system size within the time interval  $dt$  is given by  $dN = dN_g - dN_\Omega$ . Thus  $N$  obeys

$$\frac{\dot{N}}{N} = g - \Omega. \quad (\text{E.4})$$

### E.1.2. Relationship Between Doubling Time and Growth Rate

In situations where  $\Omega = 0$ , i.e. growth is the only process that changes the system size, equation (E.4) yields  $g = \dot{N}/N$ . If the growth rate is constant we can integrate this equation and obtain  $N(t) \sim \exp(gt)$ . Thus the growth rate  $g$  and the time  $\tau$  during which the system doubles its size are related by

$$g = \frac{\ln 2}{\tau}. \quad (\text{E.5})$$

## E.2. Discrete System

### E.2.1. Definitions

We now consider a cell population that consists of a discrete number of cells  $N(t)$ . Because the cell number is a discrete variable here, the instantaneous growth rate is a series of  $\delta$ -functions, which is inconvenient to quantify growth. We therefore consider the average over a time interval  $T$ ,

$$g(t) = \frac{1}{T} \sum_{k=1}^K \frac{1}{N_k}, \quad (\text{E.6})$$

which we denote the stochastic growth rate, because it is based on counting stochastic cell division events. The number of cell divisions that occur in the population during the time interval  $(t - T/2, t + T/2]$  is denoted  $K$ , and  $N_k$  is the population size when cell division number  $k$  occurs. If several cell divisions occur at the same time, then the divisions are counted one by one, such that  $N_k$  is increased after each division. Definition (E.6) is the discrete version of equation (E.2), which is obtained by replacing the integral by a sum, and by replacing  $dN_g$  by 1. Analogously, we define the stochastic apoptosis rate by

$$\Omega(t) = \frac{1}{T} \sum_{j=1}^J \frac{1}{N_j}. \quad (\text{E.7})$$

Here the number of T2 processes (cell deaths) that occur during the time interval  $(t - T/2, t + T/2]$  is denoted  $J$ , and  $N_j$  is the population size when T2 process number  $j$  occurs.

In general, the size  $N(t)$  of the considered cell population is not determined by the cell divisions and T2 processes that occur in the population. For example, if one considers the cell population that is constituted by the cells that produce Dpp molecules, then  $N(t)$  is given by the size of the Dpp source, which depends on the Hedgehog distribution. The definitions (E.6) and (E.7) are also applicable to such cases.

### E.2.2. Relationship Between Cell Cycle Time and Growth Rate

#### Deterministic Cell Cycle Time

Here we consider the case in which the cell cycle time  $\tau$  is a constant with zero variance ( $\tau = \bar{\tau}$ ). To obtain a relationship between  $\tau$  and the stochastic growth rate  $g$ , we consider a growing system without apoptosis. Analogous to the continuous case, the system size grows exponentially,  $N(t) \sim \exp(\bar{g}t)$ . The quantity  $\bar{g} = \frac{\ln 2}{\tau}$  is denoted average growth rate. Without apoptosis, equation (E.6) becomes

$$g(t) = \frac{1}{T} \sum_{k=1}^K \frac{1}{N_1 + k - 1}. \quad (\text{E.8})$$

If we average over the duration of one cell cycle,  $T = \tau$ , then each cell divides exactly once within the averaging interval  $(t - T/2, t + T/2]$ . Thus  $K = N_1$ , so that we obtain

$$g(t) = \tau^{-1} \Psi(N_1). \quad (\text{E.9})$$

Here, we introduce the function  $\Psi$ ,

$$\Psi(x) = \psi(2x) - \psi(x), \quad (\text{E.10})$$

where  $\psi(x) = \frac{d}{dx} \ln \Gamma(x)$  is the digamma function, and  $\Gamma(x) = \int_0^\infty t^{x-1} e^{-t} dt$  is the gamma function. The function  $\Psi$  has the following properties,

$$\Psi(1) = 1, \quad (\text{E.11})$$

$$\lim_{x \rightarrow \infty} \Psi(x) = \ln 2. \quad (\text{E.12})$$

Consequently, we obtain

$$g \approx \begin{cases} \frac{1}{\tau} & \text{if } N \approx 1, \\ \frac{\ln 2}{\tau} & \text{if } N \gg 1. \end{cases} \quad (\text{E.13})$$

Thus,  $g$  overestimates the average growth rate of the cell population if the number of cells is of the order 1. However in large cell populations, the stochastic growth rate  $g$  is equal to the average growth rate  $\frac{\ln 2}{\tau}$ .

### Stochastic Cell Cycle Time

We now consider the case in which the cell cycle time  $\tau$  is chosen from a time-independent gamma distribution with probability density function

$$p(\tau) = \tau^{\xi-1} \frac{\exp(-\xi\tau/\bar{\tau})}{(\bar{\tau}/\xi)^\xi \Gamma(\xi)}. \quad (\text{E.14})$$

Here,  $\xi > 0$  is the shape parameter of the gamma distribution and  $\bar{\tau}$  is the mean. The standard deviation is denoted  $\Delta\tau$ . The coefficient of variation is given by  $\Delta\tau/\bar{\tau} = \xi^{-\frac{1}{2}}$ . If  $\xi$  is an integer, then the gamma distribution represents the sum of  $\xi$  independent, exponentially distributed random variables, each of which has a mean of  $\bar{\tau}/\xi$ . If  $\Delta\tau$  is larger than zero, there is generally a transient, non-exponential growth phase at the onset of growth. After this phase, the system grows exponentially,  $N(t) \sim \exp(\bar{g}t)$  (see figure E.2). The average growth rate  $\bar{g}$  in the exponential growth phase depends not only on the mean  $\bar{\tau}$ , but also on the standard deviation  $\Delta\tau$ , which might be surprising at first glance (see figures E.1 and E.2). The growth rate increases with increasing standard deviation. The origin of this behaviour lies in the exponential nature of growth: if a cell divides quickly by chance, then its two daughter cells can immediately contribute to growth after the division. The average growth rate  $\bar{g}$  can be determined using the implicit relation

$$2 \int_0^\infty \exp(-\bar{g}\tau) f(\tau) d\tau = 1, \quad (\text{E.15})$$

where  $f(\tau)$  is the probability density function of the cell cycle times [135]. For gamma distributed cell cycle times, this equation can be solved for  $\bar{g}$ ,

$$\bar{g} = \frac{\xi}{\bar{\tau}}(2^{1/\xi} - 1). \quad (\text{E.16})$$

For fixed  $\bar{\tau}$ , the function  $\bar{g}(\xi)$  is strictly decreasing and behaves as follows,

$$\begin{aligned} \lim_{\xi \rightarrow 0} \bar{g} &= \infty, \\ \lim_{\xi \rightarrow 1} \bar{g} &= \frac{1}{\bar{\tau}}, \\ \lim_{\xi \rightarrow \infty} \bar{g} &= \frac{\ln 2}{\bar{\tau}}. \end{aligned}$$

The product  $\bar{g}\bar{\tau}$  is shown as a function of  $\xi$  in figure E.3. For fixed  $\bar{\tau}$ , the deterministic limit leads thus to the smallest possible growth rate. By increasing the variance of the gamma distribution, the growth rate can be made arbitrarily large. In the figures E.2 and E.3 it is shown that the stochastic growth rate  $g$  converges to the average growth rate  $\bar{g}$  in large systems.

### E.2.3. Temporally and Spatially Resolved Growth Rate

To resolve the growth rate temporally and spatially in vertex model simulations, we divide the system into  $J$  stripes parallel to the Dpp source. The width  $\Delta x$  of each stripe is given by  $\Delta x = L_x/J$ , where  $L_x$  is the linear dimension of the system in the direction perpendicular to the Dpp source. The stripe with index  $j$  corresponds to the spatial interval  $[(j-1)\Delta x, j\Delta x]$ . Analogously, we consider  $K$  time intervals. The time interval with index  $k$  is given by  $[(k-1)\Delta t, k\Delta t]$ , where  $\Delta t$  is the length of the time intervals. The pair of indices  $(j, k)$  determines a space-time interval. Each time a cell divides, the  $x$ -coordinate of the cell center and the time  $t$  are used to allocate the cell division to a space-time interval. The number of cell divisions that occur in the space-time interval  $(j, k)$  is denoted  $\Delta N_{jk}$ . The total number of cells in the system, averaged over the time interval with index  $k$ , is denoted  $N_k$ . The number of cells per stripe at the corresponding time is thus approximately given by  $N_{jk} = N_k/J$ . We approximate the average growth rate  $g_{jk}$  in the space-time interval  $(j, k)$  by the number of cell divisions per cell per unit time,

$$g_{jk} = \frac{\Delta N_{jk}}{N_{jk}\Delta t}. \quad (\text{E.17})$$

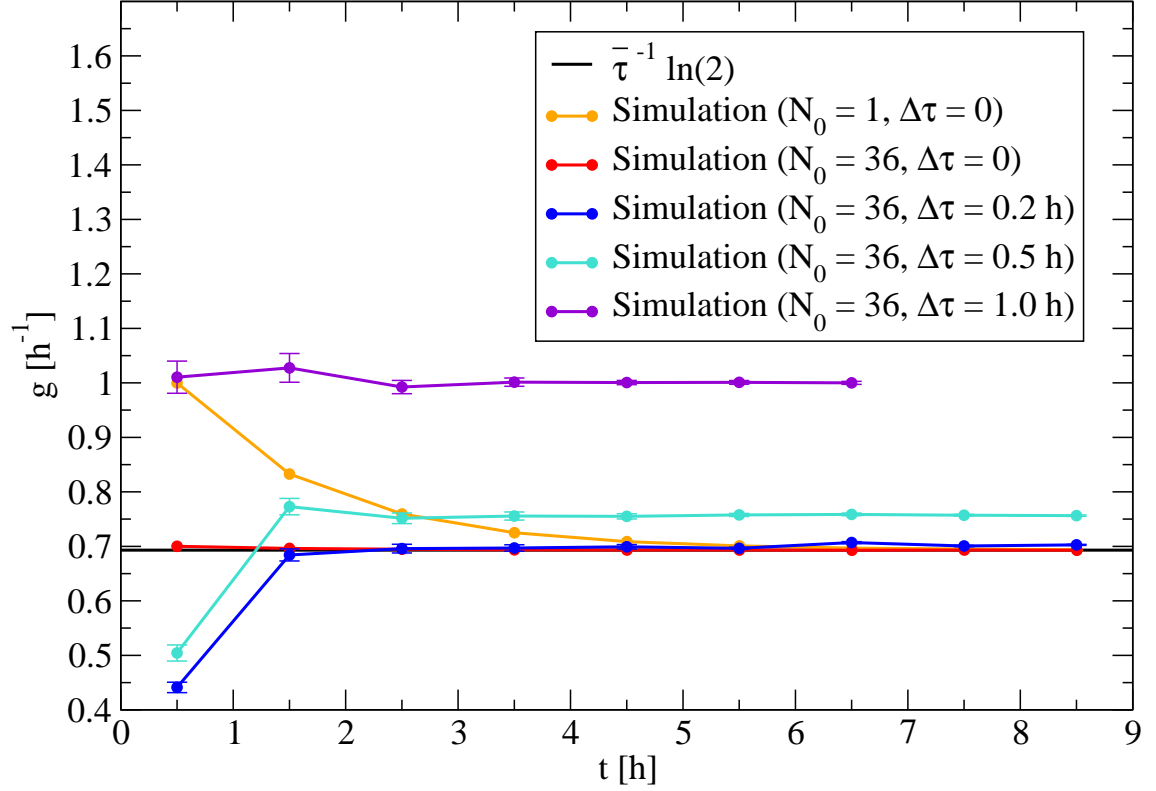


**Figure E.1.:** Stochastic growth rates  $g$  obtained by evaluating the right-hand side of equation (E.6) in simulations. The initial number of cells is denoted  $N_0$ . The cell cycle of these initial cells starts at  $t = 0$ . The cell cycle time  $\tau$  is chosen from a gamma distribution. The mean of the gamma distribution  $\bar{\tau}$  and the averaging time  $T$  are chosen to be 1 hour in all simulations. We show results for different standard deviations  $\Delta\tau$  of the gamma distribution. In the limiting case  $\Delta\tau = 0$ , the cell cycle time is a deterministic quantity. The simulations confirm the result given in equation (E.13): if  $N \gg 1$ , then  $g$  is equal to the average growth rate  $\frac{\ln 2}{\bar{\tau}}$  of the deterministic system (compare the red curve and the black line). However if  $N \approx 1$ , then  $g$  is larger than  $\frac{\ln 2}{\bar{\tau}}$  (compare the orange curve and the black line). If the standard deviation  $\Delta\tau$  of the gamma distribution is larger than zero, the system also grows exponentially after a transient, non-exponential phase in the beginning (see figure E.2). However the growth rate of the system is larger than in the deterministic case, although the mean of the gamma distribution is kept constant. Error bars indicate the standard error of the mean.

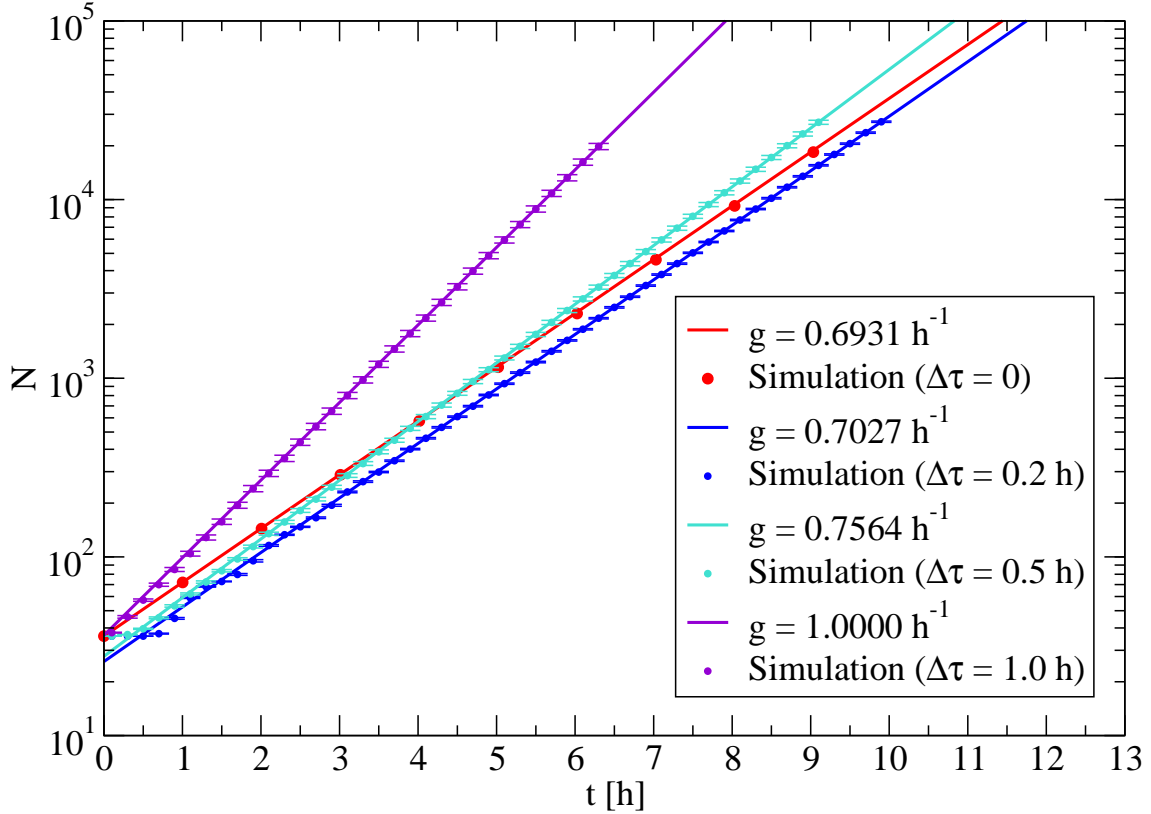


**Figure E.2.:** Number of cells  $N$  shown as a function of time. The simulations are described in the caption of figure E.1. Here we choose  $N_0 = 36$  cells and  $\bar{\tau} = 1$  h in all simulations. For each simulation we determine the stochastic growth rate  $g$  in the exponential growth phase by evaluating the right-hand side of equation (E.6). We plot the function  $f(t) = A \exp(gt)$  (solid lines), where we choose  $A$  such that  $f(t)$  goes through the last data point generated by the simulation. In each case, the function  $f(t)$  matches the exponential part of the growth curve generated by the corresponding simulation, which shows that the stochastic growth rate  $g$  can be used to determine the average growth rate  $\bar{g}$  of the system. Error bars indicate the standard error of the mean.

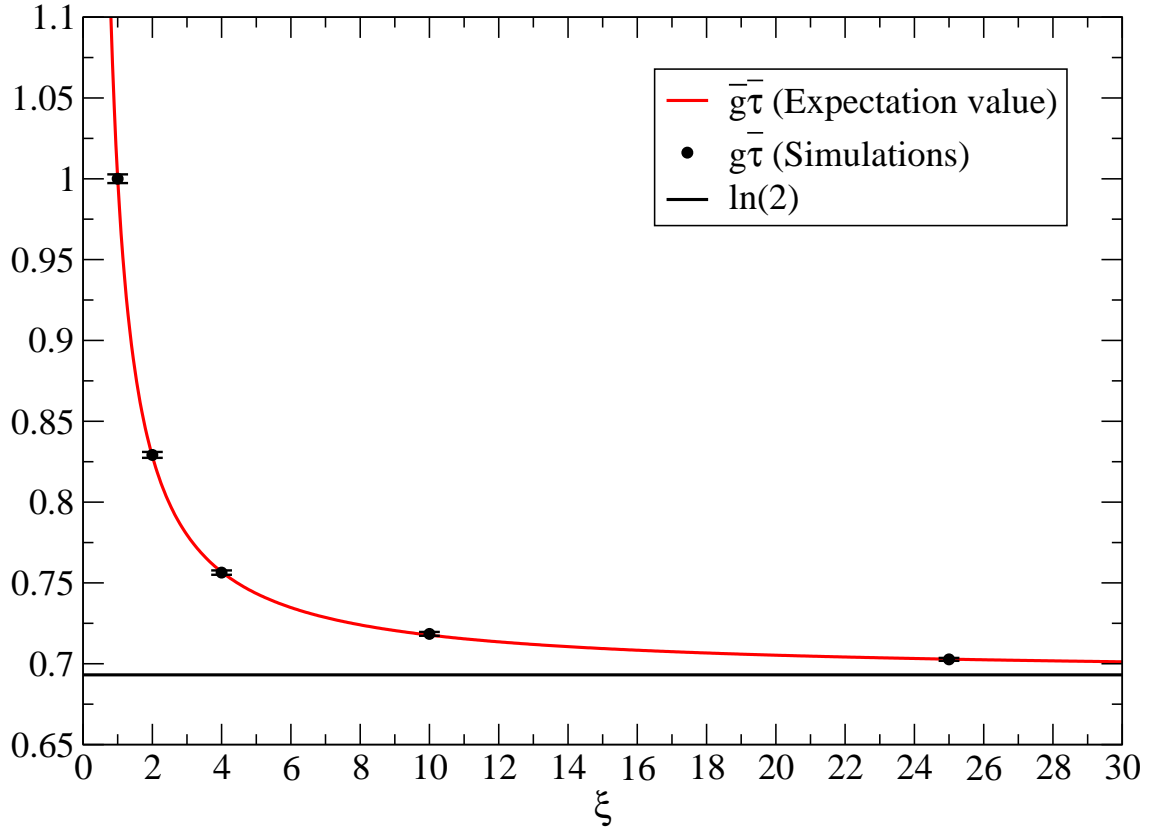


**Figure E.3.:** This figure shows – for gamma distributed cell cycle times – that the stochastic growth rate  $g$  is equal to the average growth rate  $\bar{g}$  in large systems. The solid red line shows the product of average growth rate  $\bar{g}$  and average cell cycle time  $\bar{\tau}$  as a function of the shape parameter  $\xi$  of the gamma distribution, according to equation (E.16). The black dots show the product of stochastic growth rate  $g$  and average cell cycle time  $\bar{\tau}$ . The stochastic growth rate  $g$  is determined in large systems ( $N > 10^4$ ) using simulations, which are described in the caption of figure E.1. The black line indicates the limiting value of  $\bar{g}\bar{\tau}$  for  $\xi \rightarrow \infty$ . Error bars indicate the standard error of the mean.





## F. Relaxation of the Cellular Network in the Vertex Model

The work function (2.1) describing the mechanical properties of the epithelium is a function of the vertex coordinates  $\{(x_v, y_v)\}$  and the connection between the vertices. To relax the cellular network numerically, we introduce normalized vertex coordinates,  $\tilde{x}_v = x_v/L_x, \tilde{y}_v = y_v/L_y$ , where  $L_x$  and  $L_y$  are the linear dimensions of the periodic simulation box (see figure F.1). The normalized coordinates lie in the interval  $[0, 1)$ . The numerical minimization of the work function  $\mathcal{F}$  with respect to the variables  $\{(\tilde{x}_v, \tilde{y}_v), L_x, L_y\}$  is performed using a C-implementation of the Polak-Ribière version of the conjugate gradient algorithm [133, 136]. This algorithm uses successive one-dimensional minimizations to find the minimum. The directions of the one-dimensional minimizations are determined using the gradient of the work function. However, each one-dimensional minimization only requires iterated evaluations of the work function. The numerical computation of the work function is parallelized using the OpenMP interface for shared-memory parallel programming [33].

### F.1. Global Relaxation of the Network

The simultaneous minimization of the work function with respect to all variables  $\{(\tilde{x}_v, \tilde{y}_v), L_x, L_y\}$  is denoted global relaxation. The dimension of the minimization problem is given by  $2N_V + 2$ , where  $N_V$  is the number of vertices. For simulations in which the cellular pressure is analyzed or the growth rule depends on pressure, we have chosen global relaxation for the minimization of the work function. For large systems, global relaxation becomes time consuming because the minimization is performed in a very high-dimensional space and the iterated evaluation of the work function (2.1) is computationally intensive (see figure F.2).

### F.2. Local Relaxation of the Network

Simulations, in which the cellular pressure is neither analyzed nor enters the growth rule, do not require accurate minimization of the work function. To decrease the execution time of such simulations we have used a local relaxation strategy for the cellular network. The local relaxation consists of two steps: relaxation of the cellular neighbourhood and relaxation of the simulation box.

### F.2.1. Relaxation of the Cellular Neighbourhood

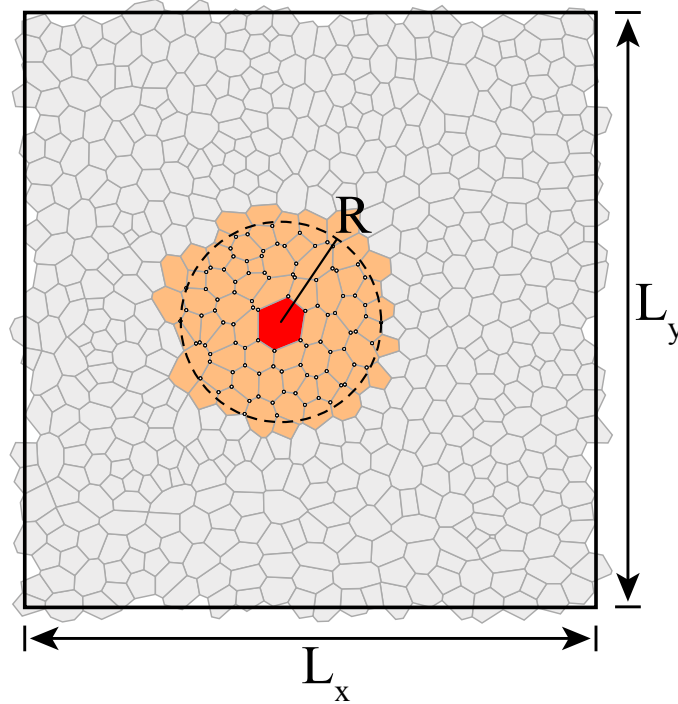


**Figure F.1.:** Schematic of the local relaxation strategy. Here, the preferred area of the red cell was increased. The vertices  $V_R$  lying within the circle with radius  $R$  (dashed line) are indicated by small circles. The corresponding cells  $C_R$  are colored orange.

We start with a globally relaxed cellular network. If the preferred area  $A_i^{(0)}$  of cell  $i$  is changed or cell  $i$  divides we construct a virtual circle with radius  $R$  around the center of cell  $i$ . Next, we identify all vertices  $V_R$  that lie within this circle. Furthermore, we identify all cells  $C_R$  and all bonds  $B_R$  containing at least one such vertex. We subsequently define a local energy which corresponds to the part of the cellular network lying inside the circle,

$$\mathcal{F}_R = \sum_{i \in C_R} \frac{K}{2} \left( A_i - A_i^{(0)} \right)^2 + \sum_{i \in C_R} \frac{\Gamma}{2} L_i^2 + \sum_{\langle v, v' \rangle \in B_R} \Lambda_{vv'} l_{vv'}. \quad (\text{F.1})$$

Here, the first two sums of the right hand side extend over all cells that are elements of the set  $C_R$  and the third sum extends over all bonds which are elements of  $B_R$ . In the next step, the function  $\mathcal{F}_R$  is minimized with respect to the normalized coordinates of the vertices that are elements of  $V_R$ . The variables  $L_x$  and  $L_y$  remain fixed in this step. The speed of this minimization step does not depend on system size because both the dimension of the minimization problem and the effort to compute the local energy  $\mathcal{F}_R$  only depend on the radius  $R$  (for sufficiently small  $R$ ).

### F.2.2. Relaxation of the Simulation Box

In the second step of the local relaxation method, the work function of the whole system (2.1) is minimized with respect to the two variables  $L_x$  and  $L_y$ . In this step, all normalized vertex coordinates  $\{(\tilde{x}_v, \tilde{y}_v)\}$  are fixed. The evaluation of the work function (2.1) is indeed computationally intensive and depends on system size, however the minimization is only two-dimensional. To decrease the execution time of the simulations, we only relax the simulation box when a cell division has occurred.

### F.3. Comparison Between Global and Local Relaxation

We compare the global to the local relaxation method with different circle radii  $R$ , which we measure in units of the average cell diameter  $\delta$ . For that purpose, we let the system grow with a constant average growth rate including some fluctuations. The simulations are run on Intel Xeon quad-core processors (Nehalem X5570) at 2.93 GHz clock speed. On each core of the CPU two threads can be executed in parallel, so that each simulation can use up to eight threads at most. The execution time of the simulation is strongly reduced by the local relaxation method. Using four parallel threads, it takes about 2 weeks to grow a system to 45,000 cells using global relaxation (see figure F.2). Using local relaxation, it takes only 5 hours ( $R = 5\delta$ ). The difference in the energy per cell  $\mathcal{F}/N$  between local and global relaxation is smaller than 3%, even for small radii  $R$  (see figure F.3). The mean pressure is about 10% larger for the global relaxation as compared to local relaxation (see figure F.4). Furthermore, the standard deviation  $\sigma_P$  of the pressure distribution is roughly 20% smaller for the global relaxation (see figure F.5). In simulations, in which the cellular pressure  $P_i$  does not enter the growth rule explicitly, these differences are negligible and do not influence the results significantly.

Parameter	Meaning	Value
$\Gamma/KA^{(0)}$	Dimensionless cell perimeter stiffness	0.04
$\Lambda/K(A^{(0)})^{3/2}$	Dimensionless cell bond tension	0.12
$\kappa$	$AP$ -interface tension factor	1
$N_0$	Initial number of cells	36
$\bar{\tau}_M$	Mean residence time in cell cycle state $M$	0.75 h
$\bar{\tau}_I$	Mean residence time in cell cycle state $I$	5 h
$\xi$	Gamma distribution shape parameter	25
$\tau_C$	Residence time in cell cycle state $C$	0 h

**Table F.1.:** Parameter values used for the simulations in this section.

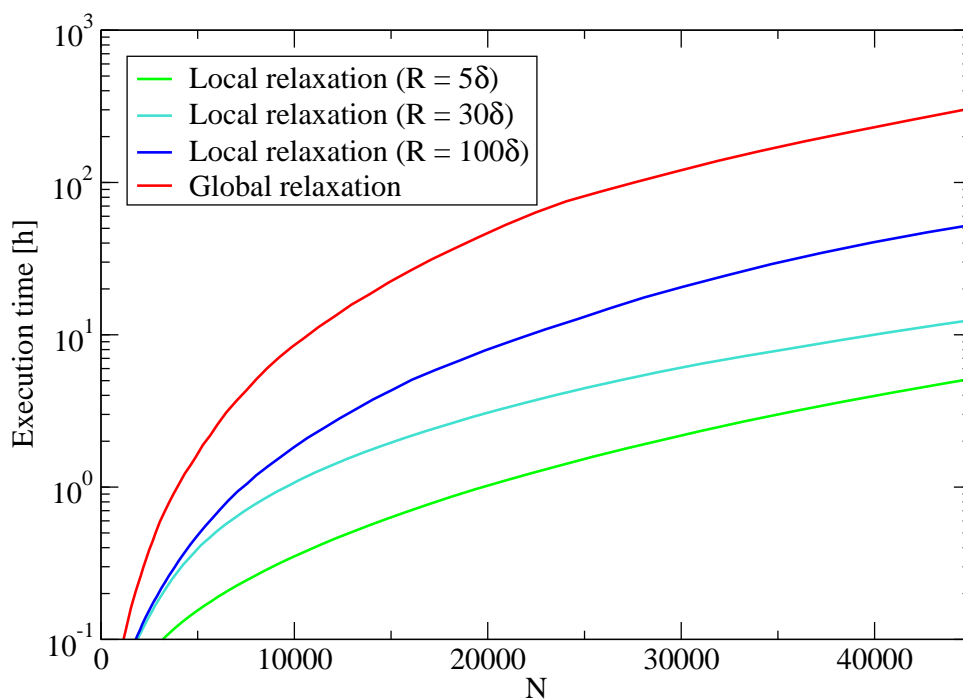


**Figure F.2.:** Execution time of the simulation shown as a function of the number of cells  $N$ . Here, we use four parallel threads for each simulation.

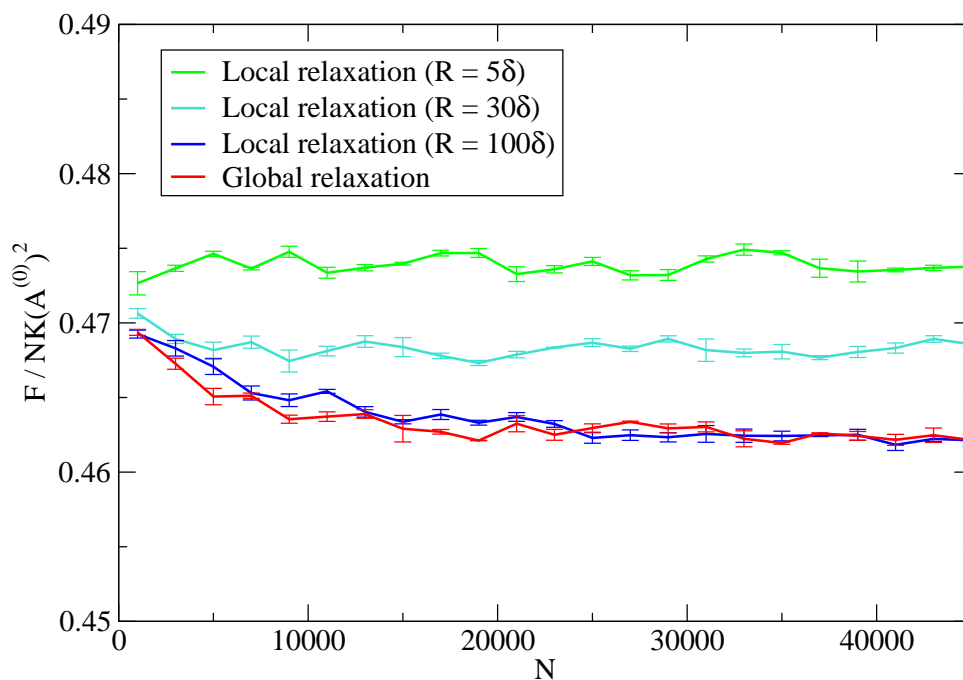


**Figure F.3.:** Average energy per cell  $\mathcal{F}/N$  shown as a function of the number of cells  $N$ .

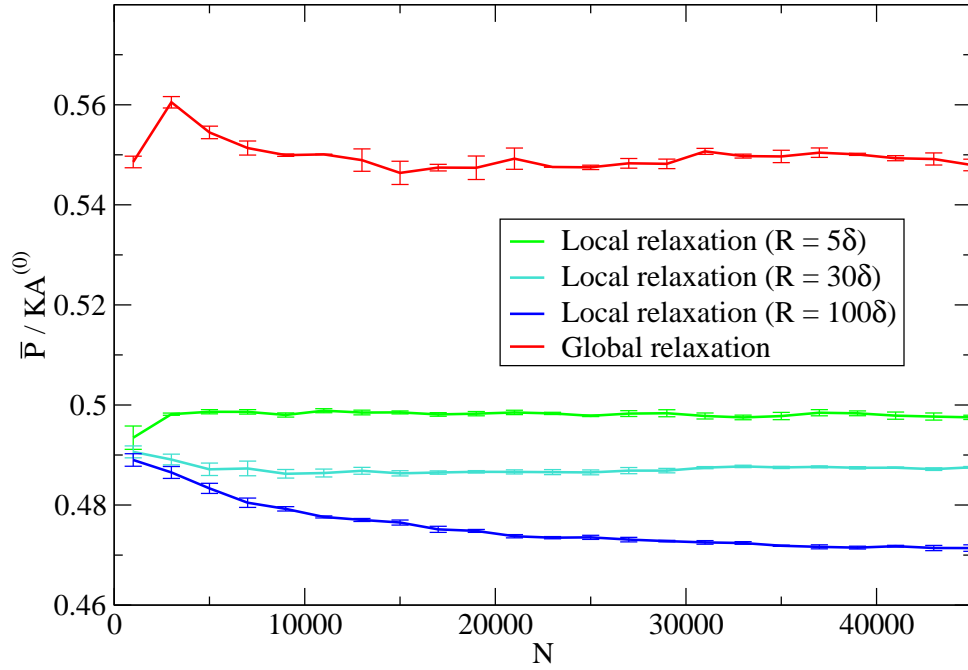


**Figure F.4.:** Average cellular pressure  $\bar{P} = \langle \frac{\partial \mathcal{F}}{\partial A_i} \rangle$  shown as a function of the number of cells  $N$ .

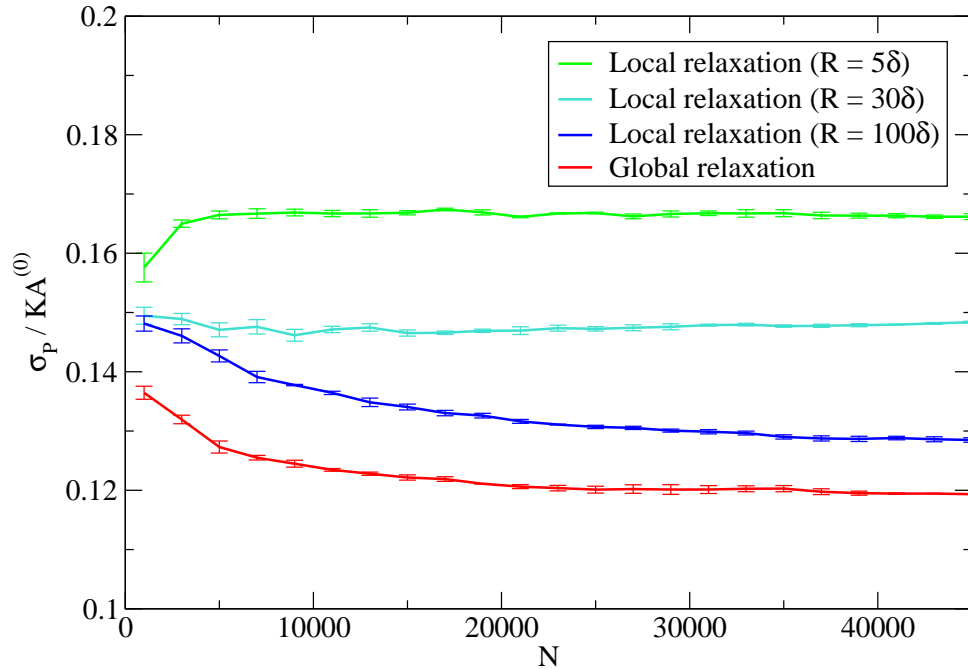


**Figure F.5.:** Standard deviation  $\sigma_P$  of the pressure distribution shown as a function of the number of cells  $N$ .



# G. Continuum Description of the Dpp Morphogen Gradient

The dynamics of the Dpp gradient with constant diffusion coefficient  $D$  and constant degradation rate  $k$  can be described by the partial differential equation

$$\frac{\partial c(x, t)}{\partial t} = D \frac{\partial^2 c(x, t)}{\partial x^2} - kc(x, t) + \nu(x, t). \quad (\text{G.1})$$

Here,  $c(x, t)$  is the Dpp area concentration and  $\nu(x, t)$  is the Dpp production rate per unit area. In this section, the solutions of (G.1) for both finite and infinite system size are discussed.

## G.1. Finite System Size

Equation (G.1) together with the no-flux boundary conditions

$$\frac{\partial c}{\partial x}(-L, t) = 0, \quad \frac{\partial c}{\partial x}(+L, t) = 0, \quad (\text{G.2})$$

describe the dynamics of the Dpp gradient in a finite system of width  $2L$ .

### G.1.1. Time-dependent Solution

#### General Solution

The general solution of (G.1) fulfilling the boundary conditions (G.2) is given by

$$c(x, t) = \int_0^\infty dt' \int_{-L}^{+L} dx' G(x', t'; x, t) \nu(x', t') + \int_{-L}^{+L} dx' G(x', 0; x, t) c(x', 0), \quad (\text{G.3})$$

$$G(x', t'; x, t) = \frac{\Theta(t - t')}{2L} \sum_{j=0}^{\infty} \exp \left\{ - \left( 1 + \left( \frac{j\pi\lambda}{2L} \right)^2 \right) k(t - t') \right\} \times \left\{ (-1)^j \cos \left( \frac{j\pi(x + x')}{2L} \right) + \cos \left( \frac{j\pi(x - x')}{2L} \right) - \delta_{j,0} \right\}. \quad (\text{G.4})$$

This result is obtained by the Green's function method as follows. We first define the following linear operators,

$$\hat{L} = \frac{\partial}{\partial t'} - D \frac{\partial^2}{\partial x'^2} + k, \quad \hat{M} = -\frac{\partial}{\partial t'} - D \frac{\partial^2}{\partial x'^2} + k. \quad (\text{G.5})$$

For any arbitrary function  $G$  the following equation holds,

$$G\hat{L}c - c\hat{M}G = \frac{\partial}{\partial t'}Gc + D \frac{\partial}{\partial x'} \left( c \frac{\partial G}{\partial x'} - G \frac{\partial c}{\partial x'} \right). \quad (\text{G.6})$$

Integration of (G.6) yields

$$\int_0^\infty dt' \int_{-L}^{+L} dx' \left( G\hat{L}c - c\hat{M}G \right) = \int_{-L}^{+L} dx' [Gc]_{t'=0}^{t'=\infty} + D \int_0^\infty dt' \left[ c \frac{\partial G}{\partial x'} - G \frac{\partial c}{\partial x'} \right]_{x'=-L}^{x'=+L}. \quad (\text{G.7})$$

We now require that the function  $G$  satisfies

$$\begin{aligned} \hat{M}G(x', t'; x, t) &= \delta(x - x')\delta(t - t'), \\ \lim_{t' \rightarrow \infty} G(x', t'; x, t) &= 0, \\ \frac{\partial G}{\partial x'}(-L, t'; x, t) &= 0, \quad \frac{\partial G}{\partial x'}(+L, t'; x, t) = 0. \end{aligned} \quad (\text{G.8})$$

Using these properties of  $G$  and equation (G.7) we obtain the formal solution given in equation (G.3). To calculate  $G$  we use the Fourier representations

$$\begin{aligned} G(x', t'; x, t) &= \frac{1}{2\pi} \int_{-\infty}^{+\infty} d\omega \tilde{G}(x', \omega; x, t) e^{i\omega t'}, \\ \delta(t - t') &= \frac{1}{2\pi} \int_{-\infty}^{+\infty} d\omega e^{i\omega(t'-t)}, \end{aligned} \quad (\text{G.9})$$

and transform equation (G.8) into Fourier space,

$$\left( -i\omega - D \frac{\partial^2}{\partial x'^2} + k \right) \tilde{G}(x', \omega; x, t) = e^{-i\omega t} \delta(x - x').$$

The solution of this equation that fulfills the boundary conditions

$$\frac{\partial \tilde{G}}{\partial x'}(-L, \omega; x, t) = 0, \quad \frac{\partial \tilde{G}}{\partial x'}(+L, \omega; x, t) = 0,$$

is given by

$$\tilde{G}(x', \omega; x, t) = \frac{\cosh(\kappa(x + x')) + \cosh(\kappa(2L - |x - x'|))}{2D\kappa \sinh(2L\kappa)} e^{-i\omega t}, \quad \kappa = \sqrt{\frac{k - i\omega}{D}}. \quad (\text{G.10})$$



To obtain  $G$  we insert (G.10) into (G.9). The integral in (G.9) is solved using the residue theorem. For  $t' > t$ , the integration path is closed by a semicircle in the upper half-plane. Because the integrand  $g(\omega) = \tilde{G}(x', \omega; x, t)e^{i\omega t'}$  is holomorphic in the upper half-plane, the integral in (G.9) vanishes for  $t' > t$ . For  $t' < t$ , the integration path is closed by a semicircle in the lower half-plane. There,  $g(\omega)$  has simple poles at

$$\omega = -i\left(\frac{D\pi^2 j^2}{4L^2} + k\right), \quad j \in \mathbb{N} \cap \{0\},$$

and the corresponding residues are given by

$$\begin{aligned} \text{Res}\left(g, \omega = -i\left(\frac{D\pi^2 j^2}{4L^2} + k\right)\right) &= \frac{i}{2L} \exp\left\{-\left(1 + \left(\frac{j\pi\lambda}{2L}\right)^2\right)k(t-t')\right\} \\ &\times \left\{(-1)^j \cos\left(\frac{j\pi(x+x')}{2L}\right) + \cos\left(\frac{j\pi(x-x')}{2L}\right) - \delta_{j,0}\right\}, \end{aligned}$$

where  $\lambda = \sqrt{D/k}$ . The residue theorem finally yields the Green's function given in equation (G.4).

### Solution for a Time-independent Dpp Source of Finite Width

Using equations (G.3) and (G.4), one can calculate the time dependent solution for a Dpp source of finite width  $w$  which is described by

$$\nu(x) = \nu\Theta(-x)\Theta(x+w). \quad (\text{G.11})$$

The solution is given by

$$\begin{aligned} c(x, t) &= \frac{\nu w}{2kL} (1 - e^{-kt}) + \frac{\nu}{\pi k} \sum_{j=1}^{\infty} \frac{1 - \exp\left\{-\left(1 + \left(\frac{j\pi\lambda}{2L}\right)^2\right)kt\right\}}{j\left(1 + \left(\frac{j\pi\lambda}{2L}\right)^2\right)} \\ &\times \left\{((-1)^j - 1) \sin\left(\frac{j\pi x}{2L}\right) - (-1)^j \sin\left(\frac{j\pi(x-w)}{2L}\right) + \sin\left(\frac{j\pi(x+w)}{2L}\right)\right\}, \end{aligned} \quad (\text{G.12})$$

if  $c(x, 0) = 0$  is used as initial condition for the Dpp gradient.

### G.1.2. Steady State Solution

The steady state solution is obtained by taking the limit  $\lim_{t \rightarrow \infty} c(x, t)$  of the time-dependent solution (G.3). For a Dpp source of finite width  $w$  described by equation (G.11), it is however more convenient to obtain the steady state solution by solving

$$D \frac{d^2 c(x)}{dx^2} - kc(x) + \nu\Theta(-x)\Theta(x+w) = 0, \quad \frac{dc}{dx}(-L) = 0, \quad \frac{dc}{dx}(+L) = 0,$$

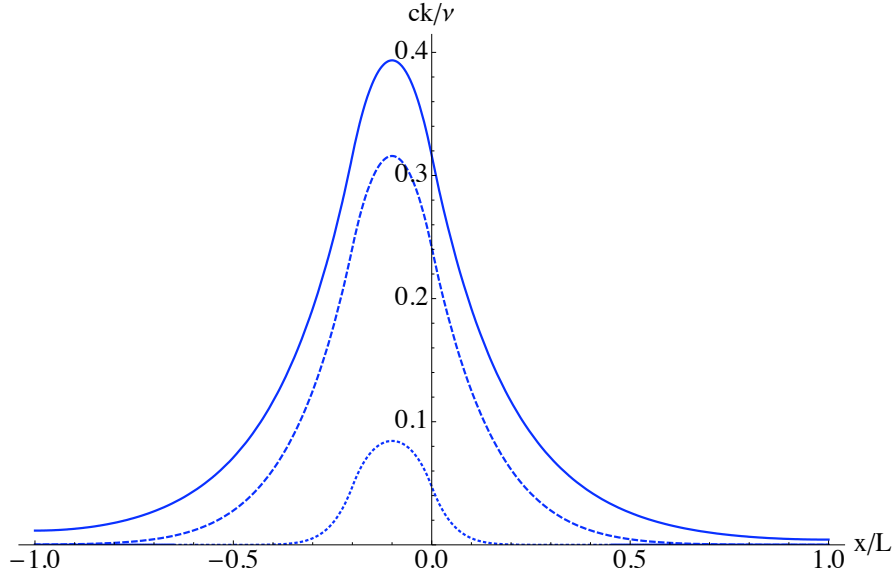


**Figure G.1.:** Dpp gradient described by equation (G.12) shown for three different points in time ( $w = 0.2L$ ,  $\lambda = 0.2L$ ). The series in equation (G.12) is truncated at  $j = 1000$ . Dotted line:  $kt = 0.1$ , dashed line:  $kt = 1$ , solid line:  $kt = 10$ . The Dpp gradient for  $kt = 10$  is so close to the steady state described by equation (G.13) that it is indistinguishable from the steady state in this figure.

with an exponential ansatz. The solution is given by

$$c(x) = \begin{cases} B_1 \exp(-\frac{x}{\lambda}) + B_2 \exp(\frac{x}{\lambda}), & \text{if } 0 \leq x \leq L, \\ B_3 \exp(-\frac{x}{\lambda}) + B_4 \exp(\frac{x}{\lambda}) + C, & \text{if } -w < x < 0, \\ B_5 \exp(-\frac{x}{\lambda}) + B_6 \exp(\frac{x}{\lambda}), & \text{if } -L \leq x \leq -w, \end{cases} \quad (\text{G.13})$$

where  $B_i$  and  $C$  are constant coefficients,

$$\begin{aligned} C &= \frac{\nu}{k}, \quad \tilde{C} = C(2e^{\frac{4L}{\lambda}} - 2)^{-1}, \\ B_1 &= \tilde{C} e^{\frac{2L-w}{\lambda}} (e^{\frac{w}{\lambda}} - 1)(e^{\frac{2L}{\lambda}} + e^{\frac{w}{\lambda}}), \quad B_2 = e^{-\frac{2L}{\lambda}} B_1, \\ B_3 &= \tilde{C} \left(1 - e^{\frac{2L}{\lambda}} - e^{\frac{4L-w}{\lambda}} + e^{\frac{2L+w}{\lambda}}\right), \quad B_4 = \tilde{C} \left(e^{\frac{w}{\lambda}} + e^{\frac{2L}{\lambda}} - e^{\frac{2L-w}{\lambda}} - e^{\frac{4L}{\lambda}}\right), \\ B_5 &= \tilde{C} e^{-\frac{w}{\lambda}} (e^{\frac{w}{\lambda}} - 1)(1 + e^{\frac{2L+w}{\lambda}}), \quad B_6 = e^{\frac{2L}{\lambda}} B_5. \end{aligned}$$

## G.2. Infinite System Size

Equation (G.1) together with the boundary conditions

$$\lim_{x \rightarrow -\infty} c(x, t) = 0, \quad \lim_{x \rightarrow +\infty} c(x, t) = 0, \quad (\text{G.14})$$

describe the dynamics of the Dpp gradient in the limit of an infinitely large system.

## G.2.1. Time-dependent Solution

### General Solution

The general solution of (G.1) fulfilling the boundary conditions (G.14) is given by

$$c(x, t) = \int_0^{\infty} dt' \int_{-\infty}^{+\infty} dx' F(x', t'; x, t) \nu(x', t') + \int_{-\infty}^{+\infty} dx' F(x', 0; x, t) c(x', 0), \quad (\text{G.15})$$

$$F(x', t'; x, t) = \frac{\Theta(t - t') e^{-k(t-t')}}{\sqrt{2\pi} \sqrt{2D(t-t')}} \exp\left(-\frac{1}{2} \left(\frac{x - x'}{\sqrt{2D(t-t')}}\right)^2\right). \quad (\text{G.16})$$

This result is obtained by the Green's function method as follows. Using the definitions (G.5) and integrating equation (G.6), we obtain the identity

$$\int_0^{\infty} dt' \int_{-\infty}^{+\infty} dx' (F \hat{L}c - c \hat{M}F) = \int_{-\infty}^{+\infty} dx' [Fc]_{t'=0}^{t'=\infty} + D \int_0^{\infty} dt' \left[ c \frac{\partial F}{\partial x'} - F \frac{\partial c}{\partial x'} \right]_{x'=-\infty}^{x'=+\infty}. \quad (\text{G.17})$$

Here, we denote the Green's function by  $F$  rather than  $G$  to avoid confusion with the Green's function of the finite system problem. We now require that  $F$  satisfies

$$\begin{aligned} \hat{M}F(x', t'; x, t) &= \delta(x - x') \delta(t - t'), \\ \lim_{t' \rightarrow \infty} F(x', t'; x, t) &= 0, \\ \lim_{x' \rightarrow -\infty} F(x', t'; x, t) &= 0, \quad \lim_{x' \rightarrow +\infty} F(x', t'; x, t) = 0. \end{aligned} \quad (\text{G.18})$$

Using these properties of  $F$  and equation (G.17) we obtain the formal solution given in equation (G.15). To calculate  $F$  we use the Fourier representations

$$\begin{aligned} F(x', t'; x, t) &= \frac{1}{4\pi^2} \int_{-\infty}^{+\infty} dq \int_{-\infty}^{+\infty} d\omega \tilde{F}(q, \omega; x, t) e^{i(qx' + \omega t')}, \\ \delta(t - t') &= \frac{1}{2\pi} \int_{-\infty}^{+\infty} d\omega e^{i\omega(t' - t)}, \\ \delta(x - x') &= \frac{1}{2\pi} \int_{-\infty}^{+\infty} dq e^{iq(x' - x)}, \end{aligned} \quad (\text{G.19})$$

and transform equation (G.18) into Fourier space. This procedure yields

$$\tilde{F}(q, \omega; x, t) = \frac{e^{-i(qx + \omega t)}}{Dq^2 + k - i\omega}. \quad (\text{G.20})$$

Inserting (G.20) into (G.19) results in

$$F(x', t'; x, t) = \frac{1}{4\pi^2} \int_{-\infty}^{+\infty} dq e^{iq(x'-x)} \int_{-\infty}^{+\infty} d\omega f(\omega), \quad f(\omega) = \frac{e^{i\omega(t'-t)}}{Dq^2 + k - i\omega}.$$

The integral over the variable  $\omega$  is solved using the residue theorem. For  $t' > t$ , the integration path is closed by a semicircle in the upper half-plane. Because the integrand  $f(\omega)$  is holomorphic in the upper half-plane, the integral vanishes for  $t' > t$ . For  $t' < t$ , the integration path is closed by a semicircle in the lower half-plane. There,  $f(\omega)$  has a simple pole at  $\omega = -i(Dq^2 + k)$  and the corresponding residue is given by

$$\text{Res}(f, \omega = -i(Dq^2 + k)) = ie^{(Dq^2 + k)(t'-t)}.$$

The remaining integration over the variable  $q$  is carried out directly, so that we finally get the Green's function given in equation (G.16).

### Solution for a Time-independent Dpp Source of Finite Width

Using equations (G.15) and (G.16), one can calculate the time dependent solution for a Dpp source of finite width  $w$  described by (G.11). The solution is given by

$$c(x, t) = \frac{\nu}{2\sqrt{Dk}} \int_{-w}^0 dx' e^{-\frac{|x-x'|}{\lambda}} (1 - \Phi),$$

$$\Phi = \frac{1}{2} \left( \text{erfc}\left(\sqrt{kt} - \frac{|x-x'|}{2\lambda\sqrt{kt}}\right) + e^{\frac{2|x-x'|}{\lambda}} \text{erfc}\left(\sqrt{kt} + \frac{|x-x'|}{2\lambda\sqrt{kt}}\right) \right),$$

if  $c(x, 0) = 0$  is used as initial condition for the Dpp gradient. The relaxation towards the steady state is described by the function  $\Phi$ , which has the following properties,  $\lim_{t \rightarrow 0} \Phi = 1$ ,  $\lim_{t \rightarrow \infty} \Phi = 0$ . The complementary error functions are defined as

$$\text{erfc}(z) = \frac{2}{\sqrt{\pi}} \int_z^{\infty} e^{-t^2} dt = 1 - \text{erf}(z).$$

### Solution for a $\delta$ Dpp Source

For a Dpp source described by  $\nu(x) = r\delta(x - x_0)$  the solution is given by

$$c(x, t) = \frac{re^{-\frac{|x-x_0|}{\lambda}}}{2\sqrt{Dk}} (1 - \phi), \quad (\text{G.21})$$

$$\phi = \frac{1}{2} \left( \text{erfc}\left(\sqrt{kt} - \frac{|x-x_0|}{2\lambda\sqrt{kt}}\right) + e^{\frac{2|x-x_0|}{\lambda}} \text{erfc}\left(\sqrt{kt} + \frac{|x-x_0|}{2\lambda\sqrt{kt}}\right) \right). \quad (\text{G.22})$$

The relaxation towards the steady state is described by the function  $\phi$ , which has the following properties,  $\lim_{t \rightarrow 0} \phi = 1$ ,  $\lim_{t \rightarrow \infty} \phi = 0$ . If the conditions  $\sqrt{kt} \gg 1$  and  $\sqrt{kt} \gg |x - x_0|/\lambda$  hold, the arguments of the complementary error functions are much larger than unity. In this case we can use the approximation [1]

$$\operatorname{erfc}(z) \approx \frac{e^{-z^2}}{z\sqrt{\pi}} \quad \text{for } z \rightarrow \infty,$$

and approximate  $\phi$  as follows,

$$\phi \approx \frac{e^{-kt} e^{\frac{|x-x_0|}{\lambda}}}{\sqrt{\pi kt}}. \quad (\text{G.23})$$

Inserting this approximation into equation (G.21) yields the approximate solution

$$c(x, t) \approx \frac{r e^{-\frac{|x-x_0|}{\lambda}}}{2\sqrt{Dk}} \left( 1 - \frac{e^{-kt} e^{\frac{|x-x_0|}{\lambda}}}{\sqrt{\pi kt}} \right) \quad \text{if } \sqrt{kt} \gg 1, \quad \sqrt{kt} \gg \frac{|x-x_0|}{\lambda}.$$

This approximation shows that the Dpp gradient relaxes exponentially towards the steady state. The time constant of the relaxation is given by the inverse of the degradation rate  $k$ .

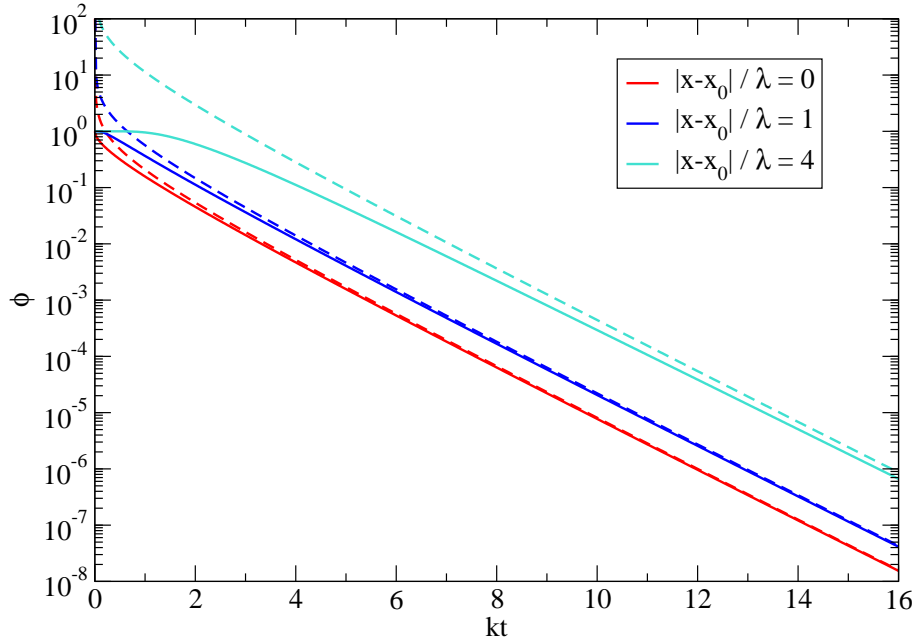


**Figure G.2.:** Comparison of the exact expression of  $\phi$  given by equation (G.22) (solid lines) with the approximation (G.23) (dashed lines).

### G.2.2. Steady State Solution

For a Dpp source of finite width  $w$  described by equation (G.11), the steady state solution can be obtained by taking the limit  $\lambda/L \rightarrow 0$  of solution (G.13). This procedure yields

$$c(x) = \begin{cases} c_0 \exp(-\frac{x}{\lambda}), & \text{if } 0 \leq x, \\ \frac{\nu}{2k} (2 - \exp(-\frac{x+w}{\lambda}) - \exp(\frac{x}{\lambda})), & \text{if } -w < x < 0, \\ c_0 \exp(\frac{x+w}{\lambda}), & \text{if } x \leq -w, \end{cases} \quad (\text{G.24})$$

where the gradient amplitude is given by

$$c_0 = \frac{\nu}{2k} (1 - e^{-\frac{w}{\lambda}}). \quad (\text{G.25})$$

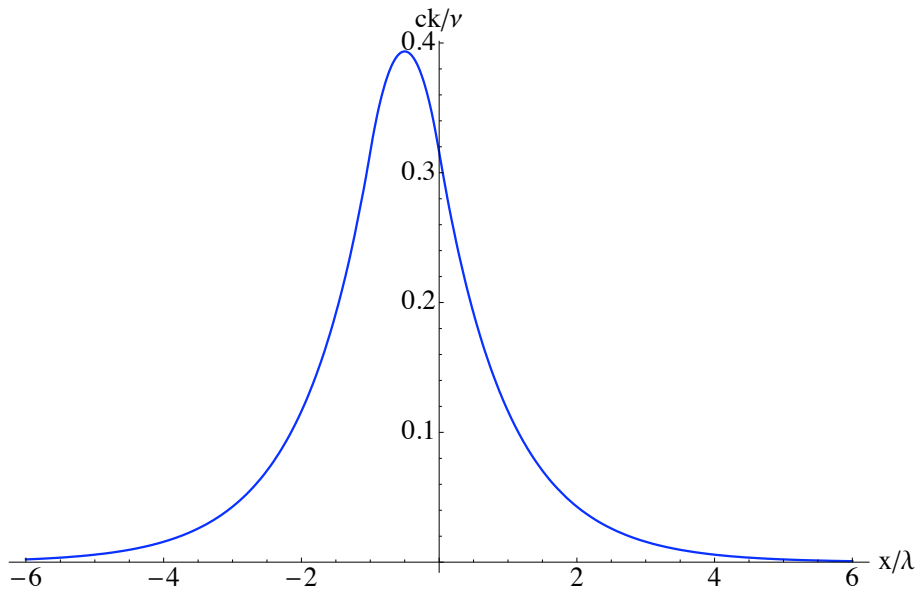


**Figure G.3.:** Steady state of the Dpp gradient described by equation (G.24) shown for  $w = \lambda$ .

# H. The Hedgehog Morphogen Gradient

## H.1. Experimental Observations

The morphogen Hh is only produced in the posterior compartment of the *Drosophila* wing disc in response to the protein Engrailed [78, 60, 134]. From there, Hh spreads into the anterior compartment. In contrast, the Hh receptor Patched (Ptc) is not produced in the posterior but only in the anterior compartment [79, 125, 132]. As a result, only anterior cells are responsive to Hh. The range of Hh in the anterior compartment is limited by Ptc, which binds and sequesters Hh [35, 166].

## H.2. Continuum Description

We describe the Hh gradient by the time-independent diffusion equation with production and degradation terms,

$$0 = D_a \frac{d^2 h(x)}{dx^2} - k_a h(x) \quad \text{if } -L \leq x < 0, \quad (\text{H.1})$$

$$0 = D_p \frac{d^2 h(x)}{dx^2} - k_p h(x) + \nu \quad \text{if } 0 \leq x \leq L. \quad (\text{H.2})$$

We use the no-flux boundary conditions

$$\frac{dh}{dx}(-L) = 0, \quad \frac{dh}{dx}(+L) = 0.$$

The area concentration of Hh is denoted  $h(x)$  and  $\nu$  is the Hh production rate per unit area. The interval  $-L < x < 0$  corresponds to the anterior compartment and  $0 < x < L$  corresponds to the posterior compartment (Hh source). The diffusion coefficient  $D$  and degradation rate  $k$  of Hh can be different in the two intervals. The subscript of  $D$  and  $k$  indicates the interval. The corresponding decay lengths of Hh are given by  $\lambda_a = \sqrt{D_a/k_a}$ ,  $\lambda_p = \sqrt{D_p/k_p}$ . In the following, we discuss the solutions of (H.1) and (H.2) for both a finite and a vanishing Hh degradation rate in the Hh source.

### H.2.1. Finite Hedgehog Degradation in the Hedgehog Source

For  $k_p > 0$ , the solution is given by sums of exponential functions.

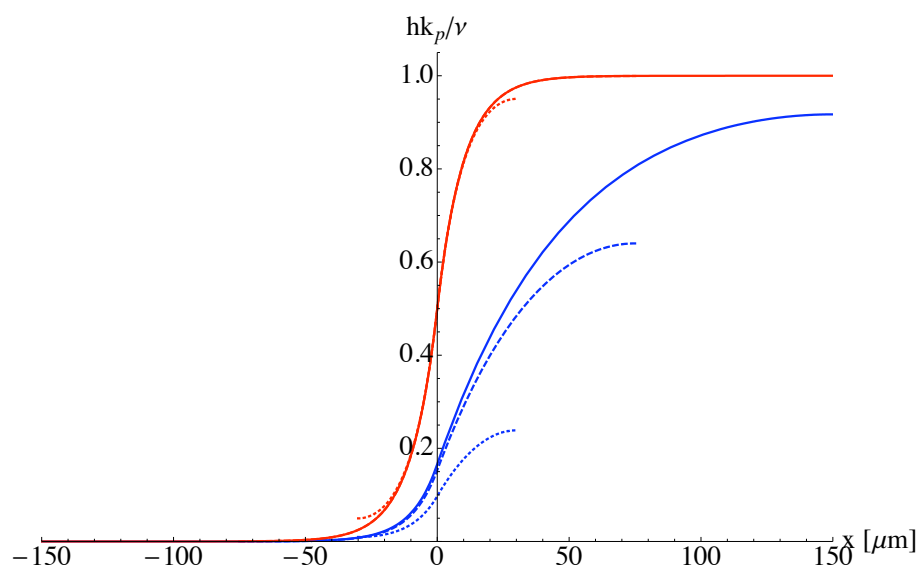


**Figure H.1.:** Hh gradients described by equation (H.3) shown for different system sizes  $L$ . Solid lines:  $L = 150 \mu m$ , Dashed lines:  $L = 75 \mu m$ , Dotted lines:  $L = 30 \mu m$ . Blue lines:  $\lambda_a = 10 \mu m$ ,  $\lambda_p = 50 \mu m$ . Red lines:  $\lambda_a = 10 \mu m$ ,  $\lambda_p = 10 \mu m$ . The shape of the Hh gradient is almost invariant for  $\lambda_a = 10 \mu m$ ,  $\lambda_p = 10 \mu m$ .

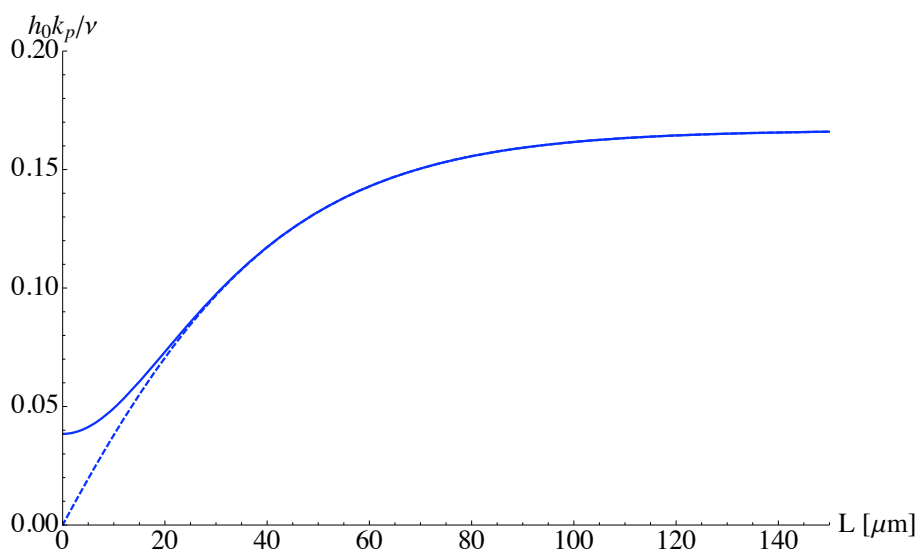


**Figure H.2.:** Hh concentration  $h_0$  at the origin shown for  $\lambda_a = 10 \mu m$ ,  $\lambda_p = 50 \mu m$ . The dependence of  $h_0$  on  $L$  is weak. Solid line: Exact expression given in equation (H.4). Dashed line: Approximation for  $\lambda_a \ll L$  given in (H.7).



### Exact Solution

The exact solution is given by

$$h(x) = \begin{cases} B_1 \exp(-\frac{x}{\lambda_a}) + B_2 \exp(\frac{x}{\lambda_a}) & \text{if } -L \leq x < 0, \\ B_3 \exp(-\frac{x}{\lambda_p}) + B_4 \exp(\frac{x}{\lambda_p}) + C & \text{if } 0 \leq x \leq L, \end{cases} \quad (\text{H.3})$$

$$C = \frac{\nu}{k_p}, \quad B_1 = \frac{\frac{C}{2} \exp(-\frac{L}{\lambda_a})}{\cosh(\frac{L}{\lambda_a}) + \frac{\lambda_p}{\lambda_a} \coth(\frac{L}{\lambda_p}) \sinh(\frac{L}{\lambda_a})}, \quad B_2 = \exp(\frac{2L}{\lambda_a}) B_1,$$

$$B_3 = \frac{-\frac{C}{2} \exp(\frac{L}{\lambda_p})}{\cosh(\frac{L}{\lambda_p}) + \frac{\lambda_a}{\lambda_p} \coth(\frac{L}{\lambda_a}) \sinh(\frac{L}{\lambda_p})}, \quad B_4 = \exp(-\frac{2L}{\lambda_p}) B_3.$$

The hedgehog concentration  $h_0 = h(0)$  at the origin is given by

$$h_0 = \frac{\nu/k_p}{1 + \frac{\lambda_p}{\lambda_a} \coth(\frac{L}{\lambda_p}) \tanh(\frac{L}{\lambda_a})}. \quad (\text{H.4})$$

For  $\lambda_a = \lambda_p$ ,  $h_0$  does not depend on  $L$  and is given by  $h_0 = \nu/2k_p$ .

### Approximate Solution for Large Systems

For  $\lambda_a \ll L$ , the solution can be approximated by

$$h(x) = \begin{cases} h_0 \exp(\frac{x}{\lambda_a}) & \text{if } -L \leq x < 0, \\ B_3 \exp(-\frac{x}{\lambda_p}) + B_4 \exp(\frac{x}{\lambda_p}) + C & \text{if } 0 \leq x \leq L, \end{cases} \quad (\text{H.5})$$

$$C = \frac{\nu}{k_p}, \quad h_0 = \frac{C}{1 + \frac{\lambda_p}{\lambda_a} \coth(\frac{L}{\lambda_p})}, \quad (\text{H.6})$$

$$B_3 = \frac{-\frac{C}{2} \exp(\frac{L}{\lambda_p})}{\cosh(\frac{L}{\lambda_p}) + \frac{\lambda_a}{\lambda_p} \sinh(\frac{L}{\lambda_p})}, \quad B_4 = \exp(-\frac{2L}{\lambda_p}) B_3. \quad (\text{H.7})$$

## H.2.2. Vanishing Hedgehog Degradation in the Hedgehog Source

For  $k_p = 0$ , the Hh morphogen gradient inside the Hh source becomes parabolic.

### Exact Solution

The exact solution is given by

$$h(x) = \begin{cases} B_1 \exp(-\frac{x}{\lambda_a}) + B_2 \exp(\frac{x}{\lambda_a}) & \text{if } -L \leq x < 0, \\ B_3 x^2 + B_4 x + h_0 & \text{if } 0 \leq x \leq L, \end{cases} \quad (\text{H.8})$$

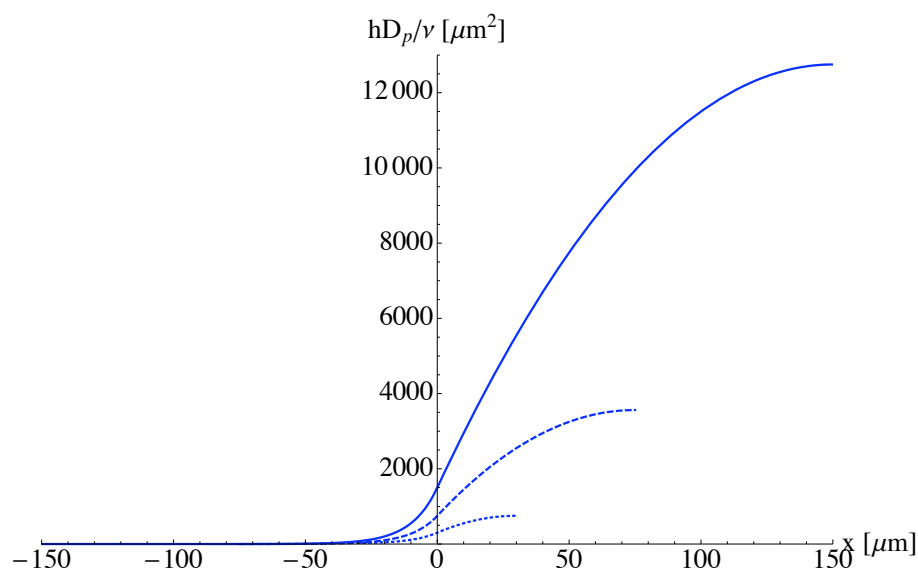


**Figure H.3.:** Hh gradients described by equation (H.8) shown for different system sizes  $L$  and  $\lambda_a = 10 \mu m$ . Solid line:  $L = 150 \mu m$ , Dashed line:  $L = 75 \mu m$ , Dotted line:  $L = 30 \mu m$ .

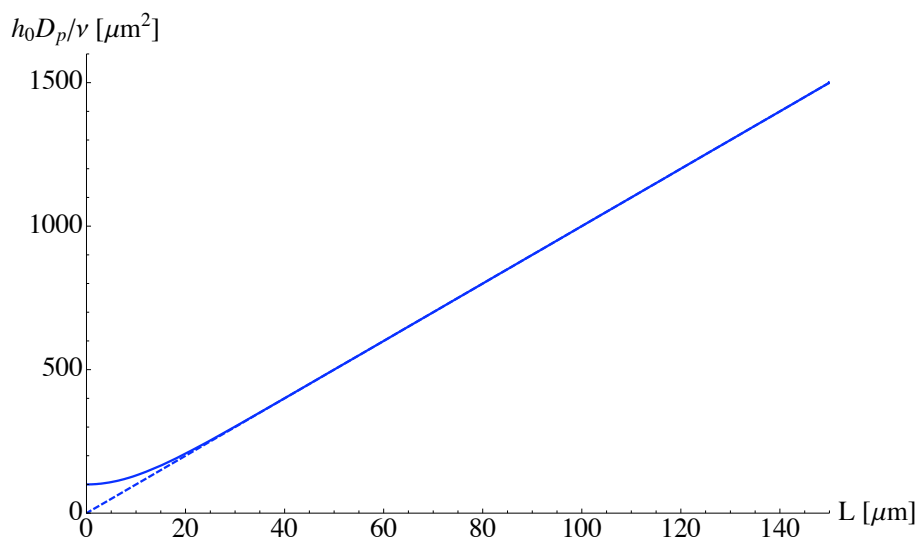


**Figure H.4.:** Hh concentration  $h_0$  at the origin shown for  $\lambda_a = 10 \mu m$ . Solid line: Exact expression given in (H.9). Dashed line: Linear approximation (valid for  $\lambda_a \ll L$ ) given in (H.11).

$$\begin{aligned}
C &= \frac{\nu\lambda_a L}{D_p}, & B_1 &= \frac{C}{\exp(\frac{2L}{\lambda_a}) - 1}, & B_2 &= \exp(\frac{2L}{\lambda_a})B_1, \\
B_3 &= -\frac{C}{2\lambda_a L}, & B_4 &= \frac{C}{\lambda_a}, & h_0 &= C \coth(\frac{L}{\lambda_a}).
\end{aligned} \tag{H.9}$$

### Approximate Solution for Large Systems

For  $\lambda_a \ll L$ , the solution can be approximated by

$$h(x) = \begin{cases} h_0 \exp(\frac{x}{\lambda_a}) & \text{if } -L \leq x < 0, \\ B_3 x^2 + B_4 x + h_0 & \text{if } 0 \leq x \leq L, \end{cases} \tag{H.10}$$

$$h_0 = \frac{\nu\lambda_a L}{D_p}, \quad B_3 = -\frac{h_0}{2\lambda_a L}, \quad B_4 = \frac{h_0}{\lambda_a}. \tag{H.11}$$



# I. The Dpp Source

## I.1. Generation of the Dpp Source in the Wing Imaginal Disc

Cells in the anterior compartment of the *Drosophila* wing disc produce and secrete Dpp if the local Hh level is sufficiently high [12, 85, 183]. Because Hh is only produced in the posterior compartment (see appendix H), the Dpp source consists of a stripe of anterior cells along the anteroposterior compartment boundary.

## I.2. Continuum Description

Using the definitions and results from section H.2, we derive expressions for the width of the Dpp source. If Dpp production is induced when the local Hh concentration  $h(x)$  exceeds the threshold  $h_T$  (for  $-L < x < 0$ ), the width  $w$  of the Dpp source is determined by  $h(-w) = h_T$ . For a finite Hh degradation rate in the Hh source, we obtain

$$w = \lambda_a \ln \left( \frac{\nu}{k_p h_T} \left[ 1 + \frac{\lambda_p}{\lambda_a} \coth\left(\frac{L}{\lambda_p}\right) \right]^{-1} \right) \quad (\text{I.1})$$

using equation (H.5). Here  $\nu$  is the Hh production rate per unit area,  $k_p$  is the Hh degradation rate in the interval  $0 < x < L$ , and  $L$  corresponds to the width of a compartment. The decay length of the Hh gradient is denoted  $\lambda_a$  in the interval  $-L < x < 0$  and  $\lambda_p$  in the interval  $0 < x < L$ . For vanishing Hh degradation in the Hh source we obtain

$$w = \lambda_a \ln \left( \frac{\nu \lambda_a L}{D_p h_T} \right) \quad (\text{I.2})$$

using equation (H.10). Here the diffusion coefficient of Hh in the interval  $0 < x < L$  is denoted  $D_p$ .

## I.3. Comparison of Theory and Experimental Data

To fit expression (I.1) to experimental data, we use  $\lambda_a$ ,  $\lambda_p$ , and  $\nu/k_p h_T$  as fit parameters and  $L$  as the independent variable. The fit yields a large decay length  $\lambda_p$  and is very insensitive to the fit parameters  $\lambda_p$  and  $\nu/k_p h_T$ , which is indicated by the huge standard errors (see table I.1). For the fit of expression (I.2) we use  $\lambda_a$  and

Fit parameter	Optimal value
$\lambda_a$	$(8.7 \pm 2.4) \mu\text{m}$
$\lambda_p$	$(3287 \pm 5 \cdot 10^5) \mu\text{m}$
$\nu/k_p h_T$	$1.1 \cdot 10^5 \pm 4 \cdot 10^7$

**Table I.1.:** Result of the least squares fit of expression (I.1) to experimental data.

Fit parameter	Optimal value
$\lambda_a$	$(8.3 \pm 1.2) \mu\text{m}$
$D_p h_T / \nu \lambda_a$	$(10.1 \pm 3.5) \mu\text{m}$

**Table I.2.:** Result of the least squares fit of expression (I.2) to experimental data.

$D_p h_T / \nu \lambda_a$  as fit parameters. The resulting fit is nearly indistinguishable from the fit of expression (I.1), offering a simpler description with only two fit parameters. These results suggest that the decay length of Hh is much larger in the posterior compartment than in the anterior one. A plausible explanation is provided by the expression pattern of the Hh receptor Ptc, which is only produced in the anterior compartment [35, 79, 125, 132]. Upon binding to the receptor Ptc, Hh is internalized into the cell and degraded [166]. Because Ptc is absent in the posterior compartment, a much smaller Hh degradation rate is expected there.

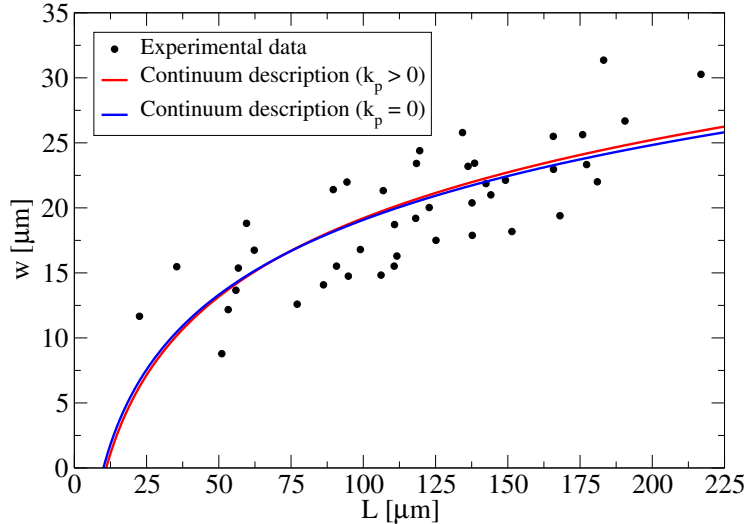


**Figure I.1.:** Dpp source width  $w$  shown as a function of the width  $L$  of the posterior compartment. The source width was measured by Ortrud Wartlick using in situ hybridization against dpp-mRNA, and expressing GFP-Dpp under the control of dpp-GAL4 in the wing disc. Red line: fit of expression (I.1). Blue line: fit of expression (I.2).

# J. Analysis of Experimental Data

## J.1. Analysis of GFP-Dpp and Dad-nRFP Gradients

### J.1.1. Measurement of the Gradients

The experimental measurements of the GFP-Dpp and dad-nRFP gradients were performed by Ortrud Wartlick as follows.

A fluorescent GFP-Dpp fusion protein [53, 163] expressed in the endogenous Dpp source with the dpp-Gal4 driver was used to quantify GFP-Dpp profiles in the posterior compartment as a function of distance  $x$  from the Dpp source at different times  $t$  during larval development. To ensure that the fluorescence intensity originating from GFP-Dpp molecules is proportional to the GFP-Dpp concentration, previously established linear GFP-Dpp imaging conditions were used [93]. The fixation, mounting, and imaging conditions were the same for all imaginal discs of a given dataset. The GFP-Dpp profiles were quantified with the software ImageJ using maximum projections of z-stacks comprising the apical most 7  $\mu\text{m}$  of the wing disc epithelium. Maximum projections were used to reduce effects of varying cell density and disc thickness on the gradient profile. The measurement of the GFP-Dpp concentration was complicated by auto-fluorescence of the tissue, which means that the tissue is fluorescent even if no GFP-Dpp molecules are present. The background signal due to auto-fluorescence was measured in non-GFP-Dpp expressing discs fixed at the same time in the same sample, and subtracted from the intensity measured in GFP-Dpp expressing discs in order to obtain the GFP-Dpp signal.

Dad-nRFP is a transcriptional reporter construct expressing red fluorescent protein (RFP) in the cell nucleus under the control of the promoter of *daughters against dpp* (dad), which is a Dpp target gene [169, 111, 165, 178]. The dad-nRFP gradients, quantified as a function of distance  $x$  from the Dpp source at different times  $t$  during larval development, serve as a representative readout of the Dpp signal. The gradient profiles were quantified with the software ImageJ using maximum projections of z-stacks through the nuclei of the disc epithelium. The proportionality between nRFP fluorescence intensity and nRFP concentration was confirmed using a stepwise bleaching assay [175]. The background signal due to auto-fluorescence was determined by a measurement outside of the cell nucleus, because RFP is only present inside the cell nucleus.

## J.1.2. Data Fitting

### Fit Functions

We fit four different functions to the GFP-Dpp and dad-nRFP gradients. The first three fit functions are given by

$$c^{(1)}(x) = B_1 \exp(-x/\lambda), \quad (\text{J.1})$$

$$c^{(2)}(x) = B_1 \exp(-x/\lambda) + B_2 \exp(x/\lambda), \quad (\text{J.2})$$

$$c^{(3)}(x) = A(x + x_0)^{-\beta}. \quad (\text{J.3})$$

The analytical form of the fourth fit function is unknown because it is determined numerically (see below). The first two fit functions  $c^{(1)}$  and  $c^{(2)}$  are solutions of the time-independent diffusion equation with a linear degradation term (see appendix G.1.2 and G.2.2). The third fit function  $c^{(3)}$  is a special solution of the time-independent diffusion equation with a nonlinear degradation term,

$$0 = D \frac{d^2}{dx^2} c - kc^m, \quad (\text{J.4})$$

satisfying the boundary condition  $\lim_{x \rightarrow \infty} c(x) = 0$ . The parameters  $A$  and  $\beta$  are given by

$$A = \left( \frac{2D(m+1)}{k(m-1)^2} \right)^{\frac{1}{m-1}}, \quad \beta = \frac{2}{m-1}, \quad (\text{J.5})$$

and  $x_0$  is an integration constant. The fourth fit function  $c^{(4)}$  is the general solution of equation (J.4). To determine this solution, we define

$$\Lambda = \sqrt{D/k}, \quad v = \frac{dc}{dx}, \quad (\text{J.6})$$

and write equation (J.4) as a two-dimensional system of first order differential equations,

$$\frac{d}{dx} \begin{pmatrix} c \\ v \end{pmatrix} = \begin{pmatrix} v \\ \Lambda^{-2} c^m \end{pmatrix}. \quad (\text{J.7})$$

The solution of (J.7) is determined numerically using the Matlab routine *ode113*, which is a variable order Adams-Bashforth-Moulton predictor-corrector solver [149]. The so obtained solution  $c^{(4)}$  is fit to the data using  $c(0)$ ,  $v(0)$ ,  $\Lambda$ , and  $m$  as fit parameters.

The optimization of the fits with respect to the fit parameters is performed by minimizing the sum of squared residuals,

$$\chi^2 = \sum_i \left( \frac{c_i - c(x_i)}{\sigma_i} \right)^2, \quad (\text{J.8})$$

using the Matlab routine *lsqnonlin*, which is an implementation of the Levenberg-Marquardt algorithm. In equation (J.8), the sum extends over all data points  $i$ ,  $c_i$



is the measured concentration at position  $x_i$ ,  $c(x_i)$  is the value of the fit function at that position, and  $\sigma_i$  is a weighting factor that is proportional to the measurement error. In case of the GFP-Dpp gradients we choose  $\sigma_i = 1$ , corresponding to constant absolute measurement errors, because we are unable to determine the background fluorescence with high precision. In case of the dad-nRFP gradients, the background fluorescence can be determined with higher precision. Therefore we choose  $\sigma_i = c_i$  for the dad-nRFP gradients, corresponding to constant fractional measurement errors.

### Results for the GFP-Dpp Gradients

The fits of  $c^{(1)}$  and  $c^{(2)}$  to the GFP-Dpp gradients yield values for the decay length  $\lambda$  that increase with the width  $L$  of the posterior compartment, consistent with a linear relationship between  $\lambda$  and  $L$  (figure J.1A). The GFP-Dpp gradient scales. The gradient amplitude  $c_0 = c(0)$  also increases as the wing discs grow (figure J.1B).

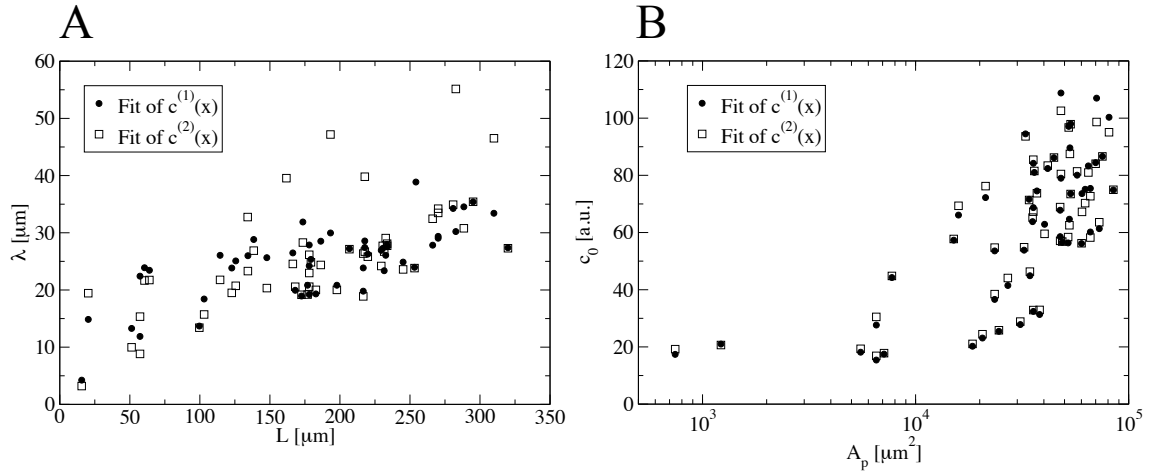


**Figure J.1.:** Results obtained by fitting the functions  $c^{(1)}$  and  $c^{(2)}$  to the GFP-Dpp gradients. (A) Decay length  $\lambda$  shown for different values of  $L$ . (B) Gradient amplitude  $c_0 = c(0)$  shown for different areas  $A_p$  of the posterior compartment.

The fits of  $c^{(3)}$  to the GFP-Dpp gradients yield clustered values for  $\beta$  (figure J.2A). This result suggests that the GFP-Dpp gradients can also be described by power laws with a constant exponent  $\beta$ , which corresponds to a constant exponent  $m$  of the nonlinear degradation term in equation (J.4). However, there are some gradient profiles that yield values for  $\beta$  which differ significantly from the average (figure J.2A). Those GFP-Dpp gradients that result in  $\beta < 2$  are treated as outliers and disregarded in the calculation of the average. The average value is  $\beta = 3.09$ , corresponding to  $m = 1.65$ . We repeat the fits of  $c^{(3)}$  to the GFP-Dpp gradients with the parameter  $\beta$  fixed to the average value 3.09. Figure J.2C shows that in the majority of the cases the fit of the single exponential function  $c^{(1)}$  is superior to the fit of  $c^{(3)}$

with fixed  $\beta$ . We also calculate  $\Lambda = \sqrt{D/k}$  for the fits with fixed parameter  $\beta$  from the fit results for  $A$  using equations (J.5). We find an approximately linear relationship between  $\Lambda$  and  $L$  (figure J.2B). This result shows, that the GFP-Dpp gradients cannot be described with constant parameters  $D$  and  $k$  throughout development, even if nonlinear Dpp degradation with a constant exponent is assumed.

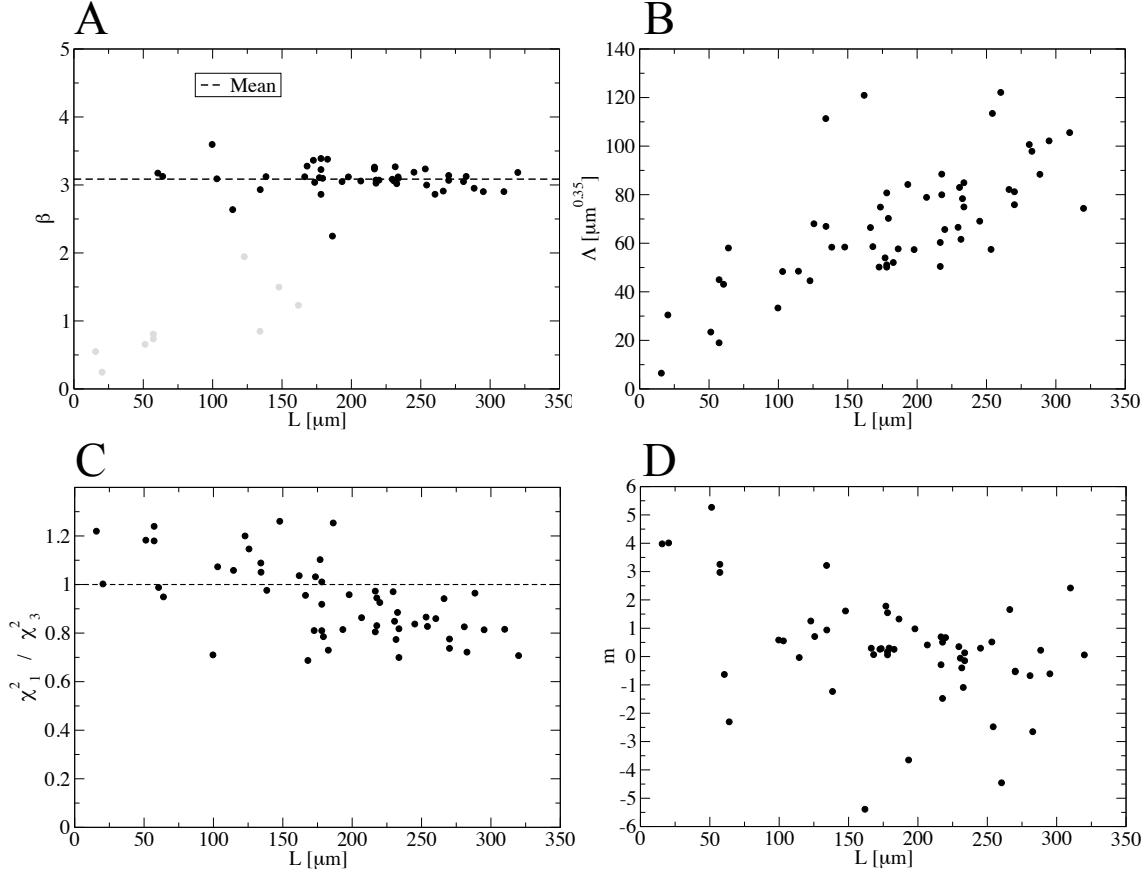


**Figure J.2.:** Results obtained by fitting the functions  $c^{(3)}$  and  $c^{(4)}$  to the GFP-Dpp gradients. (A) Power law exponent  $\beta$  obtained by fits of  $c^{(3)}$  shown for different values of  $L$ . The data points shown in grey are treated as outliers and are disregarded in the calculation of the mean (3.09), which is indicated by the dashed line. (B) Results for  $\Lambda = \sqrt{D/k}$  obtained by fitting  $c^{(3)}$  with a fixed exponent  $\beta = 3.09$  to the gradients. (C) If  $\chi_1^2 / \chi_3^2 < 1$ , the function  $c^{(1)}$  describes the gradient better than the function  $c^{(3)}$ . Here,  $\chi_1^2$  and  $\chi_3^2$  denote the sum of squared residuals, defined in equation (J.8), for the fit of  $c^{(1)}$  and the fit of  $c^{(3)}$ , respectively. (D) Exponent  $m$  obtained by fitting the function  $c^{(4)}$  to the gradients shown for different values of  $L$ .

The fits of  $c^{(4)}$  always yield the smallest value for  $\chi^2$  and are thus the best fits. This result follows from the definition of  $c^{(4)}$  because the three other fit functions are a subset of the general solution of equation (J.4). However, fits of the function

$c^{(4)}$ , which involve four fit parameters, are inappropriate to obtain meaningful information about the exponent  $m$  from the GFP-Dpp gradients. The obtained values for  $m$  are neither constant nor do they show a systematic trend (figure J.2D).

### Results for the Dad-nRFP Gradients

The fit results for the dad-nRFP gradients are similar to the results obtained for the GFP-Dpp gradients. The fits of  $c^{(1)}$  and  $c^{(2)}$  to the dad-nRFP gradients yield values for the decay length  $\lambda$  that are consistent with a linear relationship between  $\lambda$  and  $L$  (figure J.3A). Like the GFP-Dpp gradient, the dad-nRFP gradient scales. The gradient amplitude  $c_0 = c(0)$  increases significantly as the wing discs grow (figure J.3B).

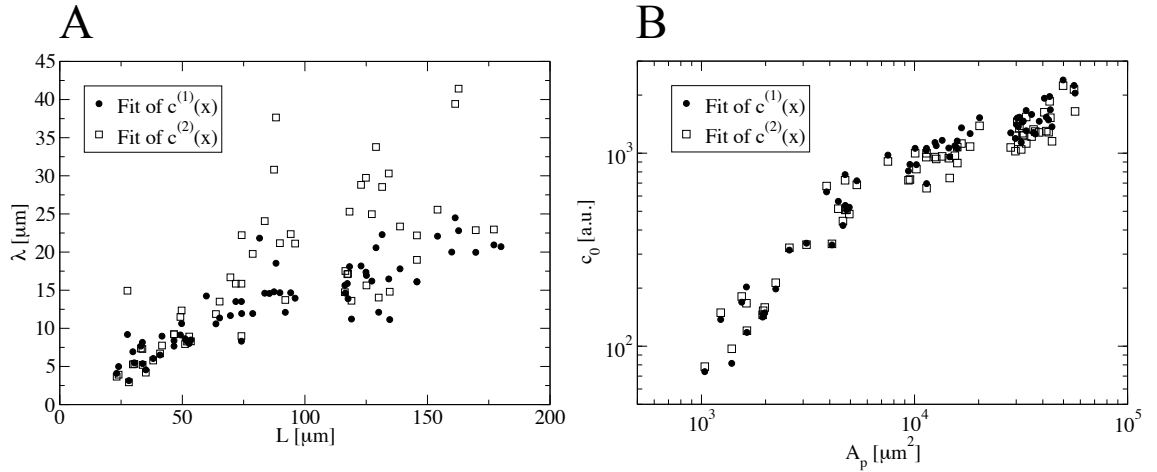


**Figure J.3.:** Results obtained by fitting the functions  $c^{(1)}$  and  $c^{(2)}$  to the dad-nRFP gradients. (A) Decay length  $\lambda$  shown for different values of  $L$ . (B) Gradient amplitude  $c_0 = c(0)$  shown for different areas  $A_p$  of the posterior compartment.

Fitting the function  $c^{(3)}$  to the dad-nRFP gradients yields values for  $\beta$  between 2.5 and 5 (figure J.4A). The average value is  $\beta = 3.26$ . Fits of  $c^{(3)}$  with the parameter  $\beta$  fixed to the average value 3.26 are in almost all cases inferior to fits of the single exponential function  $c^{(1)}$  (figure J.4C). Calculating  $\Lambda = \sqrt{D/k}$  for the fits with fixed parameter  $\beta$ , we find an approximately linear relationship between  $\Lambda$  and  $L$ , like in the case of the GFP-Dpp gradients (figure J.4B). We conclude that exponential functions describe the dad-nRFP gradients better than power laws.

Fits of the function  $c^{(4)}$  are unsuitable to obtain meaningful information about the exponent  $m$  from the dad-nRFP gradients. The obtained values for  $m$  scatter strongly (figure J.4D).

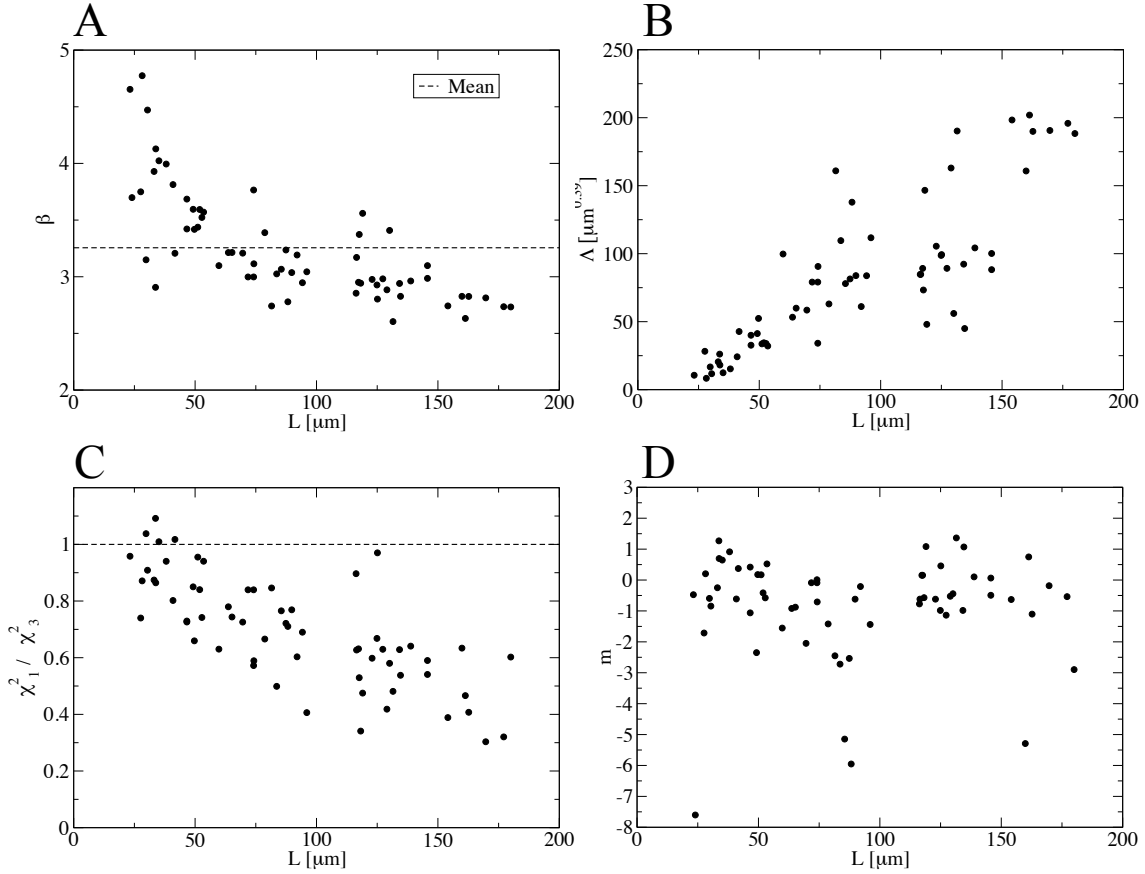


**Figure J.4.:** Results obtained by fitting the functions  $c^{(3)}$  and  $c^{(4)}$  to the dad-nRFP gradients. (A) Power law exponent  $\beta$  obtained by fits of  $c^{(3)}$  shown for different values of  $L$ . The mean (3.26) is indicated by the dashed line. (B) Results for  $\Lambda = \sqrt{D/k}$  obtained by fitting  $c^{(3)}$  with a fixed exponent  $\beta = 3.26$  to the gradients. (C) If  $\chi_1^2/\chi_3^2 < 1$ , the function  $c^{(1)}$  describes the gradient better than the function  $c^{(3)}$ . Here,  $\chi_1^2$  and  $\chi_3^2$  denote the sum of squared residuals, defined in equation (J.8), for the fit of  $c^{(1)}$  and the fit of  $c^{(3)}$ , respectively. (D) Exponent  $m$  obtained by fitting the function  $c^{(4)}$  to the gradients shown for different values of  $L$ .

## J.2. Estimation of the Temporal Variation of Kinetic Dpp Parameters

We used dad-nRFP and blk-nGFP reporter constructs to investigate whether a temporal decrease of the degradation rate  $k$  or a temporal increase of the diffusion coefficient  $D$  is the reason for the scaling of the Dpp gradient (experiments performed by Ortrud Wartlick). Blk-nGFP is a transgenic construct expressing nuclear GFP under the control of the *blk* promoter, the regulatory element responsible for expression of Dpp in the imaginal discs [121]. The fluorescence of nuclear GFP can therefore be used to estimate the Dpp production rate. We measured the nGFP fluorescence intensity in the Dpp source, using maximum projections of z-stacks comprising all nuclei. From the intensity profiles, the source width  $w$  was estimated by eye, using a fluorescence intensity cut-off. The nGFP fluorescence intensity was integrated over the Dpp source and divided by the source width  $w$  to obtain the average fluorescence intensity  $I^{(G)}$  per unit area. As a rough approximation we assumed that the Dpp production rate per unit area  $\nu$  is proportional to the average fluorescence intensity of nuclear GFP,

$$\nu = f_1 I^{(G)}, \quad (\text{J.9})$$

where  $f_1$  is a constant.

The dad-nRFP reporter is described in section J.1.1. We fit the function  $I^{(R)}(x) = I_0^{(R)} \exp(-x/\lambda^{(R)})$  to the dad-nRFP gradients to obtain the gradient amplitude  $I_0^{(R)}$  and the decay length  $\lambda^{(R)}$ . In order to obtain estimates for the kinetic parameters, we assume that the fluorescence intensity  $I^{(R)}(x)$  is proportional to the Dpp concentration  $c(x)$ . In this approximation, the Dpp and dad-nRFP decay lengths are equal,

$$\lambda = \lambda^{(R)}. \quad (\text{J.10})$$

Furthermore, we obtain

$$c_0 = f_2 I_0^{(R)}, \quad (\text{J.11})$$

where  $f_2$  is a constant and  $c_0 = \frac{\nu}{2k} \left(1 - \exp(-\frac{w}{\lambda})\right)$ , is the Dpp gradient amplitude according to equation (G.24). Here,  $k$  is the Dpp degradation rate. Combining equations (J.9), (J.10), and (J.11), we obtain the following estimates for the Dpp degradation rate and diffusion coefficient,

$$k = f \frac{I^{(G)}}{2I_0^{(R)}} \left(1 - \exp(-\frac{w}{\lambda^{(R)}})\right), \quad (\text{J.12})$$

$$D = k(\lambda^{(R)})^2, \quad (\text{J.13})$$

where  $f = f_1/f_2$  is a constant.

### J.2.1. Wing Imaginal Disc

Figure J.5 shows the estimates for the parameters  $\nu$ ,  $\lambda$ ,  $k$ , and  $D$  describing the Dpp gradient in the wing disc. The production rate  $\nu$  is largely constant, apart from an increase in the beginning of development (figure J.5A). The decay length  $\lambda$  is approximately proportional to the width  $L$  of the posterior compartment (figure J.5B). The degradation rate  $k$  decreases by more than two orders of magnitude. We find that the degradation rate and the disc area  $A$  are related by a power law,  $k \sim A^\gamma$ . A fit yields the exponent  $\gamma = -1.05 \pm 0.03$  (figure J.5C). The diffusion coefficient decreases by less than one order of magnitude during development (figure J.5D). We conclude that a decrease of the Dpp degradation rate  $k$  is most likely the reason for the scaling of the Dpp gradient.

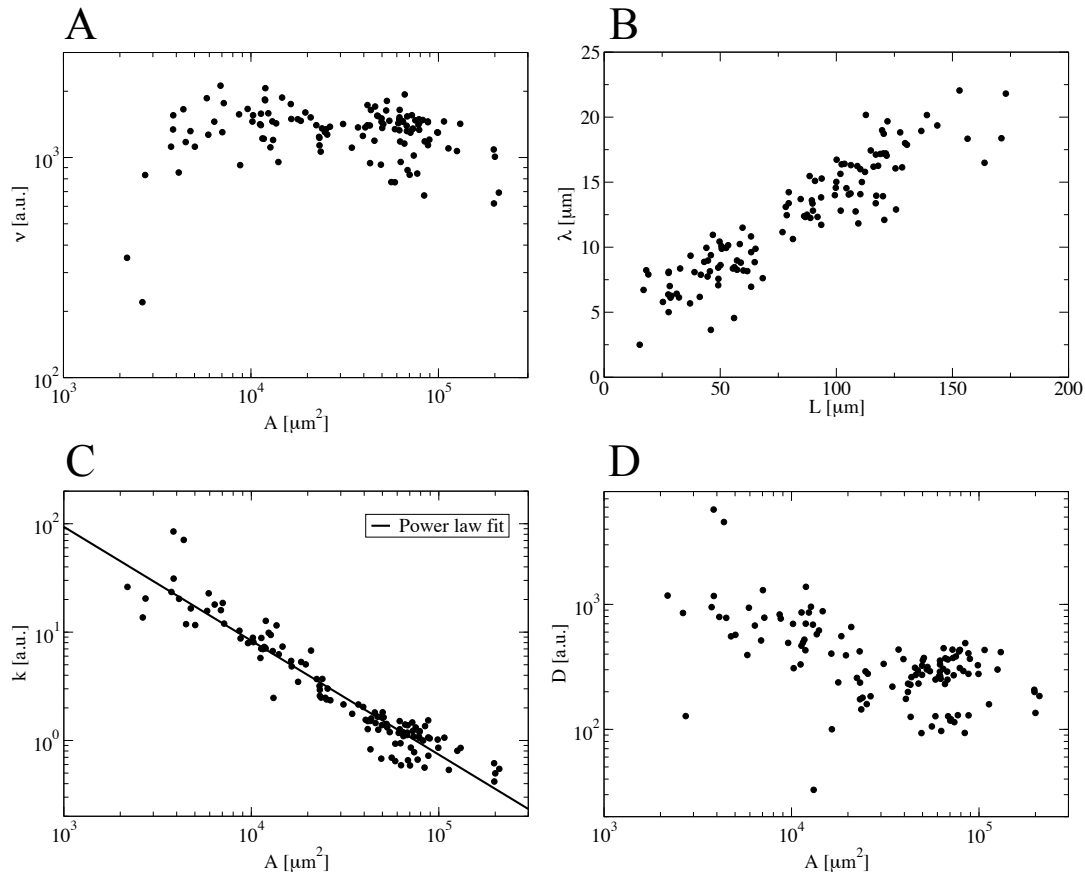


**Figure J.5.:** Estimates for the parameters  $\nu$ ,  $\lambda$ ,  $k$ , and  $D$  describing the Dpp gradient in the wing disc. The disc area is denoted  $A$  and the width of the posterior compartment is denoted  $L$ . (A) Production rate  $\nu$  shown for different values of  $A$ . (B) Decay length  $\lambda$  shown for different values of  $L$ . (C) Degradation rate  $k$  shown for different values of  $A$ . A fit of the power law  $k \sim A^\gamma$  is indicated by the solid line ( $\gamma = -1.05 \pm 0.03$ ). (D) Diffusion coefficient  $D$  shown for different values of  $A$ .

### J.2.2. Haltere Imaginal Disc

For the haltere imaginal discs we obtain results that are qualitatively the same as for the wing disc. In the haltere, the estimated Dpp degradation rate is also inversely proportional to the area,  $k = (sA)^{-1}$ , where  $s$  is a constant. However, for imaginal discs of the same size, the estimated degradation rate is smaller in the haltere disc than in the wing disc. The ratio is given by  $k_h/k_w = s_w/s_h$ , where the subscript indicates the imaginal disc type. We determine  $s_w$  and  $s_h$  by fitting straight lines to  $k^{-1}$  plotted as a function of  $A$ , and obtain  $k_h/k_w = 0.09$  (figure J.6A). To estimate the ratio of the diffusion coefficients, we assume that they are constant in the wing and haltere discs throughout development. We fit the function  $\lambda = rL$  to the experimental data and determine the slope  $r$  for wing and haltere discs (figure J.6B). As an estimate for the ratio of the diffusion coefficients we obtain  $D_h/D_w = s_w r_h^2 / s_h r_w^2 = 0.12$ . These results suggest that the degradation rate and diffusion coefficient of Dpp are approximately one order of magnitude smaller in haltere discs than in wing discs of the same size.

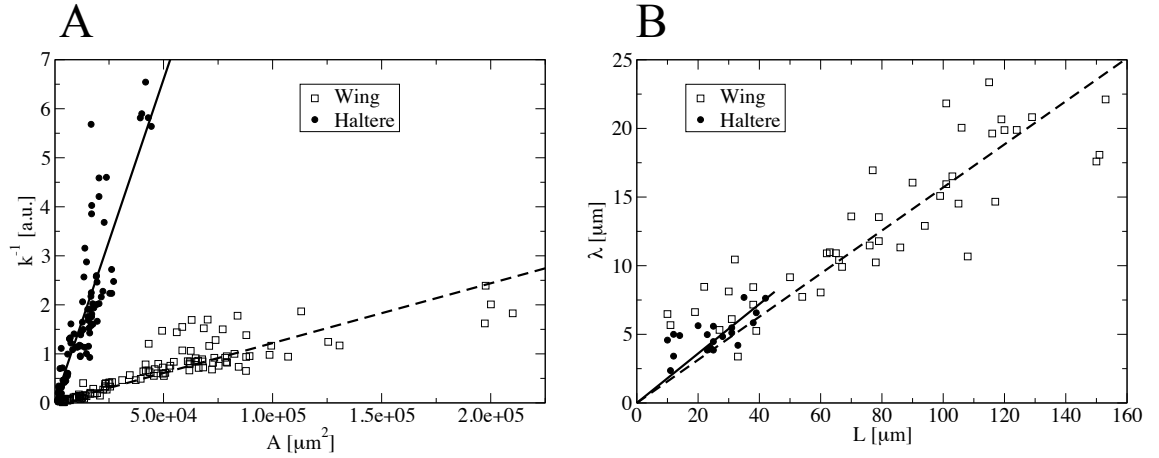


**Figure J.6.:** Estimation of the difference between kinetic Dpp parameters in wing and haltere discs. (A) Inverse of the degradation rate  $k^{-1}$  shown as a function of the disc area  $A$ . The slopes of the linear fits are given by  $s_w = 1.22 \cdot 10^{-5} \mu\text{m}^{-2}$  for the wing discs, and  $s_h = 1.32 \cdot 10^{-4} \mu\text{m}^{-2}$  for the haltere discs. (B) Decay length  $\lambda$  shown as a function of  $L$ . The slopes of the linear fits are given by  $r_w = 0.157$  for the wing discs, and  $r_h = 0.18$  for the haltere discs.





# Bibliography

- [1] M. Abramowitz and I. A. Stegun. *Handbook of Mathematical Functions*. Dover Publications, 1972.
- [2] M. D. Adams et al. The genome sequence of *Drosophila melanogaster*. *Science*, 287(5461):2185–2195, 2000.
- [3] T. Aegerter-Wilmsen, C. M. Aegerter, E. Hafen, and K. Basler. Model for the regulation of size in the wing imaginal disc of *Drosophila*. *Mechanisms of Development*, 124(4):318–326, 2007.
- [4] M. Affolter and K. Basler. The Decapentaplegic morphogen gradient: From pattern formation to growth regulation. *Nature Reviews Genetics*, 8(9):663–674, 2007.
- [5] B. Alberts, A. Johnson, J. Lewis, M. Raff, K. Roberts, and P. Walter. *Molecular Biology of the Cell, Fourth Edition*. Garland Science, 2002.
- [6] U. Alon, M. G. Surette, N. Barkai, and S. Leibler. Robustness in bacterial chemotaxis. *Nature*, 397(6715):168–171, 1999.
- [7] J. L. Alonso and W. H. Goldmann. Feeling the forces: atomic force microscopy in cell biology. *Life Sciences*, 72(23):2553–2560, 2003.
- [8] D. Angeli, J. E. Ferrell Jr., and E. D. Sontag. Detection of multistability, bifurcations, and hysteresis in a large class of biological positive-feedback systems. *Proceedings of the National Academy of Sciences of the United States of America*, 101(7):1822–1827, 2004.
- [9] L. A. Baena-López, A. Baonza, and A. García-Bellido. The orientation of cell divisions determines the shape of *Drosophila* organs. *Current Biology*, 15(18):1640–1644, 2005.
- [10] N. Barkai and D. Ben-Zvi. 'Big frog, small frog' – maintaining proportions in embryonic development. *FEBS Journal*, 276(5):1196–1207, 2009.
- [11] N. Barkai and S. Leibler. Robustness in simple biochemical networks. *Nature*, 387(6636):913–917, 1997.

- [12] K. Basler and G. Struhl. Compartment boundaries and the control of *Drosophila* limb pattern by hedgehog protein. *Nature*, 368(6468):208–214, 1994.
- [13] T. Y. Belenkaya, C. Han, D. Yan, R. J. Opoka, M. Khodoun, H. Liu, and X. Lin. *Drosophila* Dpp morphogen movement is independent of Dynamin-mediated endocytosis but regulated by the glypican members of heparan sulfate proteoglycans. *Cell*, 119(2):231–244, 2004.
- [14] D. Ben-Zvi and N. Barkai. Scaling of morphogen gradients by an expansion-repression integral feedback control. *Proceedings of the National Academy of Sciences of the United States of America*, 107(15):6924–6929, 2010.
- [15] D. Ben-Zvi, B.-Z. Shilo, A. Fainsod, and N. Barkai. Scaling of the BMP activation gradient in *Xenopus* embryos. *Nature*, 453(7199):1205–1211, 2008.
- [16] T. K. Berdyeva, C. D. Woodworth, and I. Sokolov. Human epithelial cells increase their rigidity with ageing in vitro: direct measurements. *Physics in Medicine and Biology*, 50(1):81–92, 2005.
- [17] H. C. Berg and E. M. Purcell. Physics of chemoreception. *Biophysical Journal*, 20(2):193–219, 1977.
- [18] U. S. Bhalla and R. Iyengar. Emergent properties of networks of biological signaling pathways. *Science*, 283(5400):381–387, 1999.
- [19] T. Bittig. *Morphogenetic signaling in growing tissues*. PhD thesis, Technische Universität Dresden, 2008.
- [20] T. Bittig, O. Wartlick, M. González-Gaitán, and F. Jülicher. Quantification of growth asymmetries in developing epithelia. *European Physical Journal E*, 30(1):93–99, 2009.
- [21] T. Bittig, O. Wartlick, A. Kicheva, M. González-Gaitán, and F. Jülicher. Dynamics of anisotropic tissue growth. *New Journal of Physics*, 10(6):063001, 2008.
- [22] M. Block, E. Schöll, and D. Drasdo. Classifying the expansion kinetics and critical surface dynamics of growing cell populations. *Physical Review Letters*, 99(24):248101, 2007.
- [23] T. Bollenbach. *Formation of morphogen gradients*. PhD thesis, Technische Universität Dresden, 2005.
- [24] T. Bollenbach, K. Kruse, P. Pantazis, M. González-Gaitán, and F. Jülicher. Robust formation of morphogen gradients. *Physical Review Letters*, 94(1):018103, 2005.

- [25] T. Bollenbach, K. Kruse, P. Pantazis, M. González-Gaitán, and F. Jülicher. Morphogen transport in epithelia. *Physical Review E*, 75(1):011901, 2007.
- [26] P. J. Bryant and P. Levinson. Intrinsic growth control in the imaginal primordia of *Drosophila*, and the autonomous action of a lethal mutation causing overgrowth. *Developmental Biology*, 107(2):355–363, 1985.
- [27] P. J. Bryant and P. Simpson. Intrinsic and extrinsic control of growth in developing organs. *Quarterly Review of Biology*, 59(4):387–415, 1984.
- [28] R. Burke and K. Basler. Dpp receptors are autonomously required for cell proliferation in the entire developing *Drosophila* wing. *Development*, 122(7):2261–2269, 1996.
- [29] D. T. Butcher, T. Alliston, and V. M. Weaver. A tense situation: Forcing tumour progression. *Nature Reviews Cancer*, 9(2):108–122, 2009.
- [30] J. Capdevila and I. Guerrero. Targeted expression of the signaling molecule decapentaplegic induces pattern duplications and growth alterations in *Drosophila* wings. *EMBO Journal*, 13(19):4459–4468, 1994.
- [31] J. R. Cash and A. H. Karp. A variable order Runge-Kutta method for initial value problems with rapidly varying right-hand sides. *ACM Transactions on Mathematical Software*, 16(3):201–222, 1990.
- [32] J. Cayuso, F. Ulloa, B. Cox, J. Briscoe, and E. Marti. The Sonic hedgehog pathway independently controls the patterning, proliferation and survival of neuroepithelial cells by regulating Gli activity. *Development*, 133(3):517–528, 2006.
- [33] B. Chapman, G. Jost, and R. van der Pas. *Using OpenMP: Portable Shared Memory Parallel Programming*. The MIT Press, 2007.
- [34] Y. Chen and A. F. Schier. The zebrafish Nodal signal Squint functions as a morphogen. *Nature*, 411(6837):607–610, 2001.
- [35] Y. Chen and G. Struhl. Dual roles for Patched in sequestering and transducing Hedgehog. *Cell*, 87(3):553–563, 1996.
- [36] I. Conlon and M. Raff. Size control in animal development. *Cell*, 96(2):235–244, 1999.
- [37] F. Crick. Diffusion in embryogenesis. *Nature*, 225(5231):420–422, 1970.
- [38] C. Dahmann and K. Basler. Compartment boundaries – at the edge of development. *Trends in Genetics*, 15(8):320–326, 1999.

- [39] S. J. Day and P. A. Lawrence. Measuring dimensions: the regulation of size and shape. *Development*, 127(14):2977–2987, 2000.
- [40] E. Dessaud, L. L. Yang, K. Hill, B. Cox, F. Ulloa, A. Ribeiro, A. Mynett, B. G. Novitsch, and J. Briscoe. Interpretation of the sonic hedgehog morphogen gradient by a temporal adaptation mechanism. *Nature*, 450(7170):717–720, 2007.
- [41] F. J. Diaz-Benjumea and S. M. Cohen. Interaction between dorsal and ventral cells in the imaginal disc directs wing development in *Drosophila*. *Cell*, 75(4):741–752, 1993.
- [42] J. E. Dittmer, R. J. Goss, and C. E. Dinsmore. The growth of infant hearts grafted to young and adult rats. *American Journal of Anatomy*, 141(1):155–160, 1974.
- [43] D. Drasdo. Coarse graining in simulated cell populations. *Advances in Complex Systems*, 8(2-3):319–363, 2005.
- [44] D. Drasdo and S. Höhme. A single-cell-based model of tumor growth in vitro: monolayers and spheroids. *Physical Biology*, 2(3):133–147, 2005.
- [45] W. Driever and C. Nusslein-Volhard. The bicoid protein determines position in the *Drosophila* embryo in a concentration-dependent manner. *Cell*, 54(1):95–104, 1988.
- [46] W. Driever and C. Nusslein-Volhard. A gradient of bicoid protein in *Drosophila* embryos. *Cell*, 54(1):83–93, 1988.
- [47] W. Driever and C. Nusslein-Volhard. The bicoid protein is a positive regulator of hunchback transcription in the early *Drosophila* embryo. *Nature*, 337(6203):138–143, 1989.
- [48] W. Driever, G. Thoma, and C. Nusslein-Volhard. Determination of spatial domains of zygotic gene expression in the *Drosophila* embryo by the affinity of binding sites for the bicoid morphogen. *Nature*, 340(6232):363–367, 1989.
- [49] M. Duman-Scheel, L. Weng, S. Xin, and W. Du. Hedgehog regulates cell growth and proliferation by inducing Cyclin D and Cyclin E. *Nature*, 417(6886):299–304, 2002.
- [50] R. Ransom (Ed.). *A Handbook of Drosophila Development*. Elsevier Biomedical Press, 1982.
- [51] A. Eldar, R. Dorfman, D. Weiss, H. Ashe, B.-Z. Shilo, and N. Barkal. Robustness of the BMP morphogen gradient in *Drosophila* embryonic patterning. *Nature*, 419(6904):304–308, 2002.

- [52] A. Eldar, D. Rosin, B.-Z. Shilo, and N. Barkai. Self-enhanced ligand degradation underlies robustness of morphogen gradients. *Developmental Cell*, 5(4):635–646, 2003.
- [53] E. V. Entchev, A. Schwabedissen, and M. González-Gaitán. Gradient formation of the TGF- $\beta$  homolog Dpp. *Cell*, 103(6):981–991, 2000.
- [54] C. Estella, D. J. McKay, and R. S. Mann. Molecular integration of Wingless, Decapentaplegic, and autoregulatory inputs into Distalless during Drosophila leg development. *Developmental Cell*, 14(1):86–96, 2008.
- [55] M. J. Fain and B. Stevens. Alterations in the cell cycle of Drosophila imaginal disc cells precede metamorphosis. *Developmental Biology*, 92(1):247–258, 1982.
- [56] E. Farge. Mechanical induction of twist in the Drosophila foregut/stomodaeal primordium. *Current Biology*, 13(16):1365–1377, 2003.
- [57] R. Farhadifar. *Dynamics of Cell Packing and Polar Order in Developing Epithelia*. PhD thesis, Technische Universität Dresden, 2009.
- [58] R. Farhadifar, J.-C. Röper, B. Aigouy, S. Eaton, and F. Jülicher. The influence of cell mechanics, cell-cell interactions, and proliferation on epithelial packing. *Current Biology*, 17(24):2095–2104, 2007.
- [59] E. L. Ferguson and K. V. Anderson. Decapentaplegic acts as a morphogen to organize dorsal-ventral pattern in the Drosophila embryo. *Cell*, 71(3):451–461, 1992.
- [60] A. Fjose, W. J. McGinnis, and W. J. Gehring. Isolation of a homoeo box-containing gene from the engrailed region of Drosophila and the spatial distribution of its transcripts. *Nature*, 313(6000):284–289, 1985.
- [61] G. Forgacs, R. A. Foty, Y. Shafrir, and M. S. Steinberg. Viscoelastic properties of living embryonic tissues: a quantitative study. *Biophysical Journal*, 74(5):2227–2234, 1998.
- [62] B. M. Friedrich and F. Jülicher. Chemotaxis of sperm cells. *Proceedings of the National Academy of Sciences of the United States of America*, 104(33):13256–13261, 2007.
- [63] A. Garcia-Bellido. Larvalentwicklung transplantierte Organe von Drosophila melanogaster im Adultmilieu. *Journal of Insect Physiology*, 11(8):1071 – 1076, IN1, 1077–1078, 1965.
- [64] A. Garcia-Bellido and J. R. Merriam. Parameters of the wing imaginal disc development of Drosophila melanogaster. *Developmental Biology*, 24(1):61–87, 1971.

- [65] A. Garcia-Bellido, P. Ripoll, and G. Morata. Developmental compartmentalization of the wing disk of *Drosophila*. *Nature New Biology*, 245(147):251–253, 1973.
- [66] A. Garcia-Bellido, P. Ripoll, and G. Morata. Developmental compartmentalization in the dorsal mesothoracic disc of *Drosophila*. *Developmental Biology*, 48(1):132–147, 1976.
- [67] M. C. Gibson, A. B. Patel, R. Nagpal, and N. Perrimon. The emergence of geometric order in proliferating metazoan epithelia. *Nature*, 442(7106):1038–1041, 2006.
- [68] A. Gierer and H. Meinhardt. A theory of biological pattern formation. *Kybernetik*, 12(1):30–39, 1972.
- [69] M. González-Gaitán, M. P. Capdevila, and A. García-Bellido. Cell proliferation patterns in the wing imaginal disc of *Drosophila*. *Mechanisms of Development*, 46(3):183–200, 1994.
- [70] J. B. A. Green, H. V. New, and J. C. Smith. Responses of embryonic *Xenopus* cells to activin and FGF are separated by multiple dose thresholds and correspond to distinct axes of the mesoderm. *Cell*, 71(5):731–739, 1992.
- [71] J. B. Gurdon and P.-Y. Bourillot. Morphogen gradient interpretation. *Nature*, 413(6858):797–803, 2001.
- [72] J. B. Gurdon, P. Harger, A. Mitchell, and P. Lemaire. Activin signalling and response to a morphogen gradient. *Nature*, 371(6497):487–492, 1994.
- [73] T. E. Haerry, O. Khalsa, M. B. O'Connor, and K. A. Wharton. Synergistic signaling by two BMP ligands through the SAX and TKV receptors controls wing growth and patterning in *Drosophila*. *Development*, 125(20):3977–3987, 1998.
- [74] B. D. Harfe, P. J. Scherz, S. Nissim, H. Tian, A. P. McMahon, and C. J. Tabin. Evidence for an expansion-based temporal Shh gradient in specifying vertebrate digit identities. *Cell*, 118(4):517–528, 2004.
- [75] Y. Hatwalne, S. Ramaswamy, M. Rao, and R. A. Simha. Rheology of active-particle suspensions. *Physical Review Letters*, 92(11):118101, 2004.
- [76] L. I. Held. *Imaginal Discs – The Genetic and Cellular Logic of Pattern Formation*. Cambridge University Press, 2002.
- [77] C.-H. Heldin, K. Miyazono, and P. ten Dijke. TGF- $\beta$  signalling from cell membrane to nucleus through SMAD proteins. *Nature*, 390(6659):465–471, 1997.

- [78] A. Hidalgo. Three distinct roles for the engrailed gene in *Drosophila* wing development. *Current Biology*, 4(12):1087–1098, 1994.
- [79] J. E. Hooper and M. P. Scott. The *Drosophila* patched gene encodes a putative membrane protein required for segmental patterning. *Cell*, 59(4):751–765, 1989.
- [80] J. E. Hooper and M. P. Scott. Communicating with hedgehogs. *Nature Reviews Molecular Cell Biology*, 6(4):306–317, 2005.
- [81] B. Houchmandzadeh, E. Wieschaus, and S. Leibler. Establishment of developmental precision and proportions in the early *Drosophila* embryo. *Nature*, 415(6873):798–802, 2002.
- [82] F. Hsiung, F.-A. Ramírez-Weber, D. D. Iwaki, and T. B. Kornberg. Dependence of *Drosophila* wing imaginal disc cytonemes on Decapentaplegic. *Nature*, 437(7058):560–563, 2005.
- [83] L. Hufnagel, A. A. Teleman, H. Rouault, S. M. Cohen, and B. I. Shraiman. On the mechanism of wing size determination in fly development. *Proceedings of the National Academy of Sciences of the United States of America*, 104(10):3835–3840, 2007.
- [84] A. Hunding and P. G. Sørensen. Size adaptation of Turing prepatterning. *Journal of Mathematical Biology*, 26(1):27–39, 1988.
- [85] P. W. Ingham and M. J. Fietz. Quantitative effects of hedgehog and decapentaplegic activity on the patterning of the *Drosophila* wing. *Current Biology*, 5(4):432–440, 1995.
- [86] D. J. Irons, A. Wojcinski, B. Glise, and N. A. M. Monk. Robustness of positional specification by the Hedgehog morphogen gradient. *Developmental Biology*, 342(2):180–193, 2010.
- [87] S. Ishihara and K. Kaneko. Turing pattern with proportion preservation. *Journal of Theoretical Biology*, 238(3):683–693, 2006.
- [88] L. A. Johnston and A. L. Sanders. Wingless promotes cell survival but constrains growth during *Drosophila* wing development. *Nature Cell Biology*, 5(9):827–833, 2003.
- [89] P. Jones and B. D. Simons. Epidermal homeostasis: do committed progenitors work while stem cells sleep? *Nature Reviews Molecular Cell Biology*, 9(1):82–88, 2008.
- [90] S. Kasas and G. Dietler. Probing nanomechanical properties from biomolecules to living cells. *Pflügers Archiv European Journal of Physiology*, 456(1):13–27, 2008.

- [91] M. Kerszberg and L. Wolpert. Mechanisms for positional signalling by morphogen transport: a theoretical study. *Journal of Theoretical Biology*, 191(1):103–114, 1998.
- [92] O. Khalsa, J.-W. Yoon, S. Torres-Schumann, and K. A. Wharton. TGF- $\beta$ /BMP superfamily members, Gbb-60A and Dpp, cooperate to provide pattern information and establish cell identity in the Drosophila wing. *Development*, 125(14):2723–2734, 1998.
- [93] A. Kicheva, P. Pantazis, T. Bollenbach, Y. Kalaidzidis, T. Bittig, F. Jülicher, and M. González-Gaitán. Kinetics of morphogen gradient formation. *Science*, 315(5811):521–525, 2007.
- [94] D. Kimelman and M. Kirschner. Synergistic induction of mesoderm by FGF and TGF- $\beta$  and the identification of an mRNA coding for FGF in the early Xenopus embryo. *Cell*, 51(5):869–877, 1987.
- [95] A. M. Klein, D. P. Doupé, P. H. Jones, and B. D. Simons. Kinetics of cell division in epidermal maintenance. *Physical Review E*, 76(2):021910, 2007.
- [96] S. Kondo and R. Asai. A reaction-diffusion wave on the skin of the marine angelfish Pomacanthus. *Nature*, 376(6543):765–768, 1995.
- [97] K. Kruse, J. F. Joanny, F. Jülicher, J. Prost, and K. Sekimoto. Generic theory of active polar gels: a paradigm for cytoskeletal dynamics. *European Physical Journal E*, 16(1):5–16, 2005.
- [98] K. Kruse, P. Pantazis, T. Bollenbach, F. Jülicher, and M. González-Gaitán. Dpp gradient formation by dynamin-dependent endocytosis: Receptor trafficking and the diffusion model. *Development*, 131(19):4843–4856, 2004.
- [99] L. D. Landau and E. M. Lifschitz. *Lehrbuch der theoretischen Physik, Band VII, Elastizitätstheorie, 7. Auflage*. Akademie Verlag, 1991.
- [100] A. D. Lander, Q. Nie, and F. Y. M. Wan. Do morphogen gradients arise by diffusion? *Developmental Cell*, 2(6):785–796, 2002.
- [101] K. P. Landsberg, R. Farhadifar, J. Ranft, D. Umetsu, T. J. Widmann, T. Bittig, A. Said, F. Jülicher, and C. Dahmann. Increased cell bond tension governs cell sorting at the Drosophila anteroposterior compartment boundary. *Current Biology*, 19(22):1950–1955, 2009.
- [102] T. Lecuit, W. J. Brook, M. Ng, M. Calleja, H. Sun, and S. M. Cohen. Two distinct mechanisms for long-range patterning by decapentaplegic in the Drosophila wing. *Nature*, 381(6581):387–393, 1996.



- [103] F. T. Lewis. The effect of cell division on the shape and size of hexagonal cells. *The Anatomical Record*, 33(5):331–355, 1926.
- [104] F. T. Lewis. The correlation between cell division and the shapes and sizes of prismatic cells in the epidermis of Cucumis. *The Anatomical Record*, 38(3):341–376, 1928.
- [105] M. M. Madhavan and H. A. Schneiderman. Histological analysis of the dynamics of growth of imaginal disks and histoblast nests during the larval development of *Drosophila melanogaster*. *Wilhelm Roux's Archives of Developmental Biology*, 183(4):269–305, 1977.
- [106] R. E. Mahaffy, C. K. Shih, F. C. MacKintosh, and J. Käs. Scanning probe-based frequency-dependent microrheology of polymer gels and biological cells. *Physical Review Letters*, 85(4):880–883, 2000.
- [107] F. A. Martín, S. C. Herrera, and G. Morata. Cell competition, growth and size control in the *Drosophila* wing imaginal disc. *Development*, 136(22):3747–3756, 2009.
- [108] F. A. Martín and G. Morata. Compartments and the control of growth in the *Drosophila* wing imaginal disc. *Development*, 133(22):4421–4426, 2006.
- [109] C. Martín-Castellanos and B. A. Edgar. A characterization of the effects of Dpp signaling on cell growth and proliferation in the *Drosophila* wing. *Development*, 129(4):1003–1013, 2002.
- [110] A. Martínez Arias. Wnts as morphogens? The view from the wing of *Drosophila*. *Nature Reviews Molecular Cell Biology*, 4(4):321–325, 2003.
- [111] T. Marty, B. Müller, K. Basler, and M. Affolter. Schnurri mediates Dpp-dependent repression of brinker transcription. *Nature Cell Biology*, 2(10):745–749, 2000.
- [112] S. J. Marygold, J. Roote, G. Reuter, A. Lambertsson, M. Ashburner, G. H. Millburn, P. M. Harrison, Z. Yu, N. Kenmochi, T. C. Kaufman, S. J. Leever, and K. R. Cook. The ribosomal protein genes and Minute loci of *Drosophila melanogaster*. *Genome Biology*, 8(10):R216, 2007.
- [113] H. Meinhardt. *Models of Biological Pattern Formation*. Academic Press, 1982.
- [114] D. Metcalf. The autonomous behaviour of normal thymus grafts. *Australian Journal of Experimental Biology and Medical Science*, 41:437–448, 1963.
- [115] M. Milán, S. Campuzano, and A. García-Bellido. Cell cycling and patterned cell proliferation in the wing primordium of *Drosophila*. *Proceedings of the National Academy of Sciences of the United States of America*, 93(2):640–645, 1996.

- [116] M. Milán, S. Campuzano, and A. García-Bellido. Developmental parameters of cell death in the wing disc of *Drosophila*. *Proceedings of the National Academy of Sciences of the United States of America*, 94(11):5691–5696, 1997.
- [117] J. C. M. Mombach, R. M. C. de Almeida, and J. R. Iglesias. Mitosis and growth in biological tissues. *Physical Review E*, 48(1):598–602, 1993.
- [118] G. Morata and P. A. Lawrence. The development of wingless, a homeotic mutation of *Drosophila*. *Developmental Biology*, 56(2):227–240, 1977.
- [119] G. Morata and P. Ripoll. Minutes: mutants of *Drosophila* autonomously affecting cell division rate. *Developmental Biology*, 42(2):211–221, 1975.
- [120] T. H. Morgan. Sex limited inheritance in *Drosophila*. *Science*, 32(812):120–122, 1910.
- [121] B. Müller and K. Basler. The repressor and activator forms of Cubitus interruptus control Hedgehog target genes through common generic Gli-binding sites. *Development*, 127(14):2999–3007, 2000.
- [122] J. D. Murray. How the leopard gets its spots. *Scientific American*, 258(3):80–87, 1988.
- [123] J. D. Murray. *Mathematical Biology, Second, Corrected Edition*. Springer, 1993.
- [124] T. Nagai, K. Kawasaki, and K. Nakamura. Vertex dynamics of two-dimensional cellular patterns. *Journal of the Physical Society of Japan*, 57(7):2221–2224, 1988.
- [125] Y. Nakano, I. Guerrero, A. Hidalgo, A. Taylor, J. R. Whittle, and P. W. Ingham. A protein with several possible membrane-spanning domains encoded by the *Drosophila* segment polarity gene patched. *Nature*, 341(6242):508–513, 1989.
- [126] D. Nellen, R. Burke, G. Struhl, and K. Basler. Direct and long-range action of a DPP morphogen gradient. *Cell*, 85(3):357–368, 1996.
- [127] T. P. Neufeld, A. F. de la Cruz, L. A. Johnston, and B. A. Edgar. Coordination of growth and cell division in the *Drosophila* wing. *Cell*, 93(7):1183–1193, 1998.
- [128] C. J. Neumann and S. M. Cohen. A hierarchy of cross-regulation involving Notch, wingless, vestigial and cut organizes the dorsal/ventral axis of the *Drosophila* wing. *Development*, 122(11):3477–3485, 1996.
- [129] M. Ng, F. J. Diaz-Benjumea, J.-P. Vincent, J. Wu, and S. M. Cohen. Specification of the wing by localized expression of wingless protein. *Nature*, 381(6580):316–318, 1996.

- [130] H. G. Othmer and E. Pate. Scale-invariance in reaction-diffusion models of spatial pattern formation. *Proceedings of the National Academy of Sciences of the United States of America*, 77(7):4180–4184, 1980.
- [131] K. J. Painter, P. K. Maini, and H. G. Othmer. Stripe formation in juvenile *Pomacanthus* explained by a generalized Turing mechanism with chemotaxis. *Proceedings of the National Academy of Sciences of the United States of America*, 96(10):5549–5554, 1999.
- [132] R. G. Phillips, I. J. Roberts, P. W. Ingham, and J. R. Whittle. The *Drosophila* segment polarity gene *patched* is involved in a position-signalling mechanism in imaginal discs. *Development*, 110(1):105–114, 1990.
- [133] E. Polak. *Computational Methods in Optimization*. Academic Press, New York, 1971.
- [134] S. J. Poole, L. M. Kauvar, B. Drees, and T. Kornberg. The engrailed locus of *Drosophila*: structural analysis of an embryonic transcript. *Cell*, 40(1):37–43, 1985.
- [135] E. O. Powell. Growth rate and generation time of bacteria, with special reference to continuous culture. *Journal of General Microbiology*, 3(15):492–511, 1956.
- [136] W. H. Press, B. P. Flannery, S. A. Teukolsky, and W. T. Vetterling. *Numerical Recipes in C: The Art of Scientific Computing, Second Edition*. Cambridge University Press, 2002.
- [137] M. Radmacher, M. Fritz, C. M. Kacher, J. P. Cleveland, and P. K. Hansma. Measuring the viscoelastic properties of human platelets with the atomic force microscope. *Biophysical Journal*, 70(1):556–567, 1996.
- [138] F.-A. Ramírez-Weber and T. B. Kornberg. Cytonemes: cellular processes that project to the principal signaling center in *Drosophila* imaginal discs. *Cell*, 97(5):599–607, 1999.
- [139] J. Ranft, M. Basan, J. Elgeti, J.-F. Joanny, J. Prost, and F. Jülicher. Fluidization of tissues by cell division and apoptosis. *Proceedings of the National Academy of Sciences of the United States of America*, 107(49):20863–20868, 2010.
- [140] R. D. Riddle, R. L. Johnson, E. Laufer, and C. Tabin. Sonic hedgehog mediates the polarizing activity of the ZPA. *Cell*, 75(7):1401–1416, 1993.
- [141] D. Rogulja and K. Irvine. Regulation of cell proliferation by a morphogen gradient. *Cell*, 123(3):449–461, 2005.

- [142] D. Rogulja, C. Rauskolb, and K. D. Irvine. Morphogen control of wing growth through the Fat signaling pathway. *Developmental Cell*, 15(2):309–321, 2008.
- [143] B. Schmierer, A. L. Tournier, P. A. Bates, and C. S. Hill. Mathematical modeling identifies Smad nucleocytoplasmic shuttling as a dynamic signal-interpreting system. *Proceedings of the National Academy of Sciences of the United States of America*, 105(18):6608–6613, 2008.
- [144] J. Schultz. The Minute reaction in the development of *Drosophila melanogaster*. *Genetics*, 14(4):366–419, 1929.
- [145] G. Schwank and K. Basler. Regulation of organ growth by morphogen gradients. *Cold Spring Harbor Perspectives in Biology*, 2(1), 2010.
- [146] G. Schwank, S. Restrepo, and K. Basler. Growth regulation by Dpp: an essential role for Brinker and a non-essential role for graded signaling levels. *Development*, 135(24):4003–4013, 2008.
- [147] T. Schwann. *Microscopical Researches into the Accordance of Structure and Growth in Animals and Plants*. Sydenham Society, 1847.
- [148] N. Serrano and P. H. O’Farrell. Limb morphogenesis: connections between patterning and growth. *Current Biology*, 7(3):R186–R195, 1997.
- [149] L. F. Shampine and M. K. Gordon. *Computer Solution of Ordinary Differential Equations: The Initial Value Problem*. W. H. Freeman, 1975.
- [150] R. P. Sharma and V. L. Chopra. Effect of the wingless ( $wg^1$ ) mutation on wing and haltere development in *Drosophila melanogaster*. *Developmental Biology*, 48(2):461–465, 1976.
- [151] Y. Shi and J. Massagué. Mechanisms of TGF- $\beta$  signaling from cell membrane to the nucleus. *Cell*, 113(6):685–700, 2003.
- [152] B. I. Shraiman. Mechanical feedback as a possible regulator of tissue growth. *Proceedings of the National Academy of Sciences of the United States of America*, 102(9):3318–3323, 2005.
- [153] S. J. Silber. Growth of baby kidneys transplanted into adults. *Archives of Surgery*, 111(1):75–77, 1976.
- [154] P. Simpson, P. Berreur, and J. Berreur-Bonnenfant. The initiation of pupariation in *Drosophila*: dependence on growth of the imaginal discs. *Journal of Embryology and Experimental Morphology*, 57:155–165, 1980.
- [155] P. Simpson and G. Morata. Differential mitotic rates and patterns of growth in compartments in the *Drosophila* wing. *Developmental Biology*, 85(2):299–308, 1981.

- [156] F. A. Spencer, F. M. Hoffmann, and W. M. Gelbart. Decapentaplegic: a gene complex affecting morphogenesis in *Drosophila melanogaster*. *Cell*, 28(3):451–461, 1982.
- [157] D. B. Staple, R. Farhadifar, J.-C. Röper, B. Aigouy, S. Eaton, and F. Jülicher. Mechanics and remodelling of cell packings in epithelia. *The European Physical Journal E*, 33(2):117–127, 2010.
- [158] J. Stavans. The evolution of cellular structures. *Reports on Progress in Physics*, 56(6):733–789, 1993.
- [159] C. Stern and C. Tokunaga. On cell lethals in *Drosophila*. *Proceedings of the National Academy of Sciences of the United States of America*, 68(2):329–331, 1971.
- [160] M. Strigini and S. M. Cohen. A Hedgehog activity gradient contributes to AP axial patterning of the *Drosophila* wing. *Development*, 124(22):4697–4705, 1997.
- [161] M. Strigini and S. M. Cohen. Wingless gradient formation in the *Drosophila* wing. *Current Biology*, 10(6):293–300, 2000.
- [162] T. Tabata and T. B. Kornberg. Hedgehog is a signaling protein with a key role in patterning *Drosophila* imaginal discs. *Cell*, 76(1):89–102, 1994.
- [163] A. A. Teleman and S. M. Cohen. Dpp gradient formation in the *Drosophila* wing imaginal disc. *Cell*, 103(6):971–980, 2000.
- [164] O. Thoumine and A. Ott. Time scale dependent viscoelastic and contractile regimes in fibroblasts probed by microplate manipulation. *Journal of Cell Science*, 110(17):2109–2116, 1997.
- [165] J. Torres-Vazquez, S. Park, R. Warrior, and K. Arora. The transcription factor Schnurri plays a dual role in mediating Dpp signaling during embryogenesis. *Development*, 128(9):1657–1670, 2001.
- [166] C. Torroja, N. Gorfinkiel, and I. Guerrero. Patched controls the Hedgehog gradient by endocytosis in a dynamin-dependent manner, but this internalization does not play a major role in signal transduction. *Development*, 131(10):2395–2408, 2004.
- [167] G. J. Tortora and S. R. Grabowski. *Principles of Anatomy and Physiology*, 10<sup>th</sup> Edition. Wiley, 2003.
- [168] M. Towers, R. Mahood, Y. Yin, and C. Tickle. Integration of growth and specification in chick wing digit-patterning. *Nature*, 452(7189):882–886, 2008.

- [169] K. Tsuneizumi, T. Nakayama, Y. Kamoshida, T. B. Kornberg, J. L. Christian, and T. Tabata. Daughters against dpp modulates dpp organizing activity in *Drosophila* wing development. *Nature*, 389(6651):627–631, 1997.
- [170] A. M. Turing. The chemical basis of morphogenesis. *Philosophical Transactions of the Royal Society of London. Series B, Biological Sciences*, 237(641):37–72, 1952.
- [171] V. C. Twitty and J. L. Schwind. The growth of eyes and limbs transplanted heteroplastically between two species of *Amblystoma*. *Journal of Experimental Zoology*, 59(1):61–86, 1931.
- [172] J. M. G. Vilar, R. Jansen, and C. Sander. Signal processing in the TGF- $\beta$  superfamily ligand-receptor network. *PLoS Computational Biology*, 2(1):0036–0045, 2006.
- [173] R. Vuilleumier, A. Springhorn, L. Patterson, S. Koidl, M. Hammerschmidt, M. Affolter, and G. Pyrowolakis. Control of Dpp morphogen signalling by a secreted feedback regulator. *Nature Cell Biology*, 12(6):611–617, 2010.
- [174] O. Wartlick. *Control of Proliferation by the Dpp Gradient in the Wing Imaginal Disc of Drosophila Melanogaster*. PhD thesis, University of Geneva, 2010.
- [175] O. Wartlick, P. Mumcu, A. Kicheva, T. Bittig, C. Seum, F. Jülicher, and M. González-Gaitán. Dynamics of Dpp signaling and proliferation control. *Science*, 331(6021):1154–1159, 2011.
- [176] D. Weaire and J. P. Kermode. Computer simulation of a two-dimensional soap froth – I. Method and motivation. *Philosophical Magazine B: Physics of Condensed Matter; Electronic, Optical and Magnetic Properties*, 48(3):245–259, 1983.
- [177] K. Weigmann, S. M. Cohen, and C. F. Lehner. Cell cycle progression, growth and patterning in imaginal discs despite inhibition of cell division after inactivation of *Drosophila* Cdc2 kinase. *Development*, 124(18):3555–3563, 1997.
- [178] A. Weiss, E. Charbonnier, E. Ellertsdóttir, A. Tsirigos, C. Wolf, R. Schuh, G. Pyrowolakis, and M. Affolter. A conserved activation element in BMP signaling during *Drosophila* development. *Nature Structural & Molecular Biology*, 17(1):69–76, 2010.
- [179] K. A. Wharton, R. P. Ray, and W. M. Gelbart. An activity gradient of decapentaplegic is necessary for the specification of dorsal pattern elements in the *Drosophila* embryo. *Development*, 117(2):807–822, 1993.

- 
- [180] K. A. Wharton, G. H. Thomsen, and W. M. Gelbart. Drosophila 60A gene, another transforming growth factor  $\beta$  family member, is closely related to human bone morphogenetic proteins. *Proceedings of the National Academy of Sciences of the United States of America*, 88(20):9214–9218, 1991.
- [181] L. Wolpert. Positional information and the spatial pattern of cellular differentiation. *Journal of Theoretical Biology*, 25(1):1–47, 1969.
- [182] L. Wolpert, R. Beddington, T. Jessell, P. Lawrence, E. Meyerowitz, and J. Smith. *Principles of Development, Second Edition*. Oxford University Press, 2005.
- [183] M. Zecca, K. Basler, and G. Struhl. Sequential organizing activities of engrailed, hedgehog and decapentaplegic in the Drosophila wing. *Development*, 121(8):2265–2278, 1995.
- [184] M. Zecca, K. Basler, and G. Struhl. Direct and long-range action of a Wingless morphogen gradient. *Cell*, 87(5):833–844, 1996.





# Versicherung

Hiermit versichere ich, dass ich die vorliegende Arbeit ohne unzulässige Hilfe Dritter und ohne Benutzung anderer als der angegebenen Hilfsmittel angefertigt habe; die aus fremden Quellen direkt oder indirekt übernommenen Gedanken sind als solche kenntlich gemacht. Die Arbeit wurde bisher weder im Inland noch im Ausland in gleicher oder ähnlicher Form einer anderen Prüfungsbehörde vorgelegt. Die vorliegende Arbeit wurde am Max-Planck-Institut für Physik komplexer Systeme angefertigt und von Prof. Dr. Frank Jülicher betreut.

Dresden, den 9.6.2011, Peer Mumcu